



**HAL**  
open science

# Planning and guidance of ultrasound guided High Intensity Focused Ultrasound cardiac arrhythmia therapy

Zulma Sandoval Niño

► **To cite this version:**

Zulma Sandoval Niño. Planning and guidance of ultrasound guided High Intensity Focused Ultrasound cardiac arrhythmia therapy. Signal and Image processing. Université de Rennes, 2015. English. NNT: 2015REN1S044 . tel-01241529v2

**HAL Id: tel-01241529**

**<https://inserm.hal.science/tel-01241529v2>**

Submitted on 6 Jan 2016

**HAL** is a multi-disciplinary open access archive for the deposit and dissemination of scientific research documents, whether they are published or not. The documents may come from teaching and research institutions in France or abroad, or from public or private research centers.

L'archive ouverte pluridisciplinaire **HAL**, est destinée au dépôt et à la diffusion de documents scientifiques de niveau recherche, publiés ou non, émanant des établissements d'enseignement et de recherche français ou étrangers, des laboratoires publics ou privés.

ANNÉE 2015



**THÈSE / UNIVERSITÉ DE RENNES 1**

*sous le sceau de l'Université Européenne de Bretagne*

pour le grade de

**DOCTEUR DE L'UNIVERSITÉ DE RENNES 1**

*Mention : Traitement du Signal et Télécommunications*

**École doctorale Matisse**

présentée par

**Zulma Liliana SANDOVAL NIÑO**

Préparée à l'unité de recherche INSERM, U1099  
Laboratoire de Traitement du Signal et de l'Image  
UFR ISTIC: Informatique et Électronique

---

**Planning and  
guidance of ul-  
trasound guided  
High Intensity  
Focused Ultra-  
sound cardiac  
arrhythmia the-  
rapy**

**Thèse soutenue à Rennes le 02 Juillet 2015**

devant le jury composé de :

**Patrick CLARYSSE**

Directeur de Recherche CNRS / *Président*

**Jean-François AUBRY**

Directeur de Recherche CNRS / *Rapporteur*

**Jean-Philippe THIRAN**

Professeur de l'École Polytechnique Fédérale de Lau-  
sanne / *Rapporteur*

**Francis BESSIÈRE**

Cardiologue de l'Université Claude Bernard / *Examineur*

**Mireille GARREAU**

Professeur de l'Université de Rennes 1 / *Examinatrice*

**Cyril LAFON**

Directeur de Recherche INSERM / *Examineur*

**Jean-Louis DILLESEGER**

Maître de conférences de l'Université de Rennes 1 /  
*Directeur de thèse*



# Remerciements

Je voudrais tout d'abord remercier mon directeur de thèse, Jean-Louis Dillenseger, qui m'a encouragée et motivée à planifier et à développer mon projet de recherche dans une atmosphère cordiale. Ses remarques et corrections opportunes ont encadré ma thèse en la conduisant à une conclusion heureuse et valorisante. Grâce à son soutien, j'ai eu l'occasion de participer à des collaborations et des échanges scientifiques pluridisciplinaires en France et à l'étranger. Je tiens également à le remercier pour son accueil chaleureux pour moi et ma petite famille.

Je remercie Jean-Philippe Thiran et Jean-François Aubry qui ont acceptés d'être rapporteurs de ce manuscrit. Leurs commentaires ont amélioré la qualité de ce travail. De même, les concepts et idées exprimés lors de la soutenance par les autres membres du jury, Francis Bessière, Patrick Clarysse, Mireille Garreau et Cyril Lafon, me donnent le ton pour les futures publications et perspectives du travail.

Je suis également reconnaissante de la possibilité qui m'a été donnée de travailler au Laboratoire Traitement du Signal et de l'Image, LTSI, de l'Université de Rennes 1. Le directeur Monsieur Lotfi Senhadji et l'équipe de gestion, Patricia Gerouard, Soizic Charpentier, Muriel Diop et Guillaume Jehenne, m'ont offert les meilleures conditions de travail possible et m'ont aidé dans les différentes procédures administratives avec beaucoup de gentillesse et de sympathies.

Je tiens à adresser un remerciement spécial au Professeur Javad Alirezaie qui m'a accueillie dans le laboratoire Computer Vision and Image Processing, CVIP, lors de mon séjour de mobilité internationale à l'Université Ryerson à Toronto.

Je remercie Oscar Acosta, maître de conférences à l'Université de Rennes 1, pour sa collaboration et ses bons conseils. Je tiens également à remercier Miguel Castro, qui m'a beaucoup aidée pendant l'acquisition des données dans la salle TheraImage de l'hôpital Pontchaillou, CHU de Rennes.

Je pense également à mes collègues du laboratoire Hélène Feuillâtre, Ahmed Oukili, Ke Wu, David Ojeda, Juan Mantilla, Ricardo Gutierrez, Richard Rios, et les remercie pour leur aide, leur soutien scientifique et technique, et surtout leur bonne humeur et leur amabilité. Je remercie également Stephanie Ortega, Xavier Navarro et Juan David Ospina, pour leur amitié inconditionnelle,

et Mariam Lee qui m'a aidée avec la correction de l'anglais dans les différents documents produits.

Je remercie vivement ma famille pour ses encouragements et sa bonne humeur. J'exprime ma gratitude à mes parents pour leurs conseils, enseignements et soins affectueux. Aussi à mes frères, qui ont toujours été à mes côtés et m'ont donné leur appui.

Mes derniers remerciements vont à Julian, mon mari et Helena ma fille, qui remplissent ma vie d'amour, d'espoir et de bonheur. En plus de son soutien au quotidien, Julian m'a aussi apporté sa connaissance scientifique ainsi que son expertise technique. Merci donc pour ses remarques scientifiques, ses bons conseils et les discussions intéressantes que nous avons partagées tout au long de ma thèse.

# Résumé étendu de la Thèse en français



# Partie I : Contexte de l'étude

## Contexte médical

### Fibrillation auriculaire

La fibrillation auriculaire est caractérisée par des contractions rapides, irrégulières et inorganisées du muscle cardiaque de l'oreillette. Elle est causée par des perturbations de la fonction électrique cardiaque.

Dans des conditions normales, l'activité électrique qui conduit à la contraction du cœur naît dans le nœud sinusal situé anatomiquement dans le haut de l'oreillette droite. Cette activité se propage au travers de l'oreillette droite jusqu'au nœud auriculo-ventriculaire. L'influx électrique se propage ensuite le long du faisceau de His et du réseau de Purkinje dans les ventricules. Cette propagation d'activité électrique entraîne la dépolarisation (et donc la contraction) des myocytes (fibres musculaires) de la partie supérieure du cœur jusqu'aux ventricules assurant ainsi le cycle cardiaque. Après une dépolarisation, les cellules entrent dans un état réfractaire pendant lequel elles sont inexcitables. Si un groupe de cellules n'a pas été excité durant la propagation initiale de l'influx il peut se dépolariser à n'importe quel moment. La dépolarisation de ces cellules, postérieure au passage du front initial de propagation, peut entraîner l'activation des cellules voisines qui sont sorties de leur période réfractaire. Ce phénomène est appelé une *réentrée*.

Tous les mécanismes qui entraînent la fibrillation auriculaire ne sont pas connus. Toutefois cette dernière est caractérisée par l'apparition de multiples boucles de réentrée dans les oreillettes. Il se produit alors une désorganisation des contractions de l'oreillette pouvant entraîner jusqu'à 300 pulsations/min au lieu des 60 pulsations/min d'une oreillette normale. Même si le nœud auriculo-ventriculaire limite cette conduction, la fibrillation auriculaire entraîne toutefois une fibrillation des ventricules de l'ordre de 150 pulsations/min. Les conséquences d'une fibrillation auriculaire peuvent à terme être l'insuffisance cardiaque chronique, l'accident vasculaire cérébral (du fait de la non circulation continue du sang), une fatigue, des problèmes supplémentaires du rythme cardiaque et une vascularisation insuffisante.

Comme nous l'avons écrit précédemment, les mécanismes qui entraînent la fibrillation auriculaire sont encore relativement mal connus. Toutefois certaines théories ont été proposées



pour expliquer l'initiation et le maintien d'une fibrillation auriculaire. Selon les travaux de Haïssaguerre (HAÏSSAGUERRE et al. 1998), des extrasystoles et des rythmes auriculaires rapides au niveau des veines pulmonaires pourraient entraîner la fibrillation. Cette défibrillation serait maintenue par des décharges continues de foyers à haute fréquence localisées dans et autour des veines pulmonaires. Selon la théorie du rotor (JALIFE 2003), la séquence de battements ectopiques générée au niveau des veines pulmonaires provoquerait une onde rotationnelle à haute fréquence, le rotor, sur la paroi postérieure de l'oreillette gauche. Les ondes émergeant de ce rotor seraient alors fragmentées et distribuées spatialement pour donner lieu à de nouvelles réentrées maintenant ainsi la fibrillation auriculaire. Dans tous les cas, il semblerait que les régions de l'oreillette gauche, au niveau des veines pulmonaires seraient impliquées dans la génération des fibrillations auriculaires.

## Traitements de la fibrillation auriculaire

Les fibrillations auriculaires sont classiquement traitées en première intention par voies médicamenteuses. Toutefois, celles-ci peuvent présenter des effets secondaires ou des incompatibilités rendant nécessaire un traitement radical par ablation. Deux approches sont généralement utilisées :

- La voie épicardique. L'idée de cette approche proposée par Cox en 1987 est de procéder à des incisions dans la paroi de l'oreillette. Ces incisions, une fois recousues et cicatrisées ont pour objectif de bloquer les réentrées et de guider les impulsions électriques vers le nœud auriculo-ventriculaire. Cette procédure a reçu plusieurs améliorations. La plus récente est appelée « minimaze » (Figure 1) (COX 2004). Elle consiste à 1) isoler les veines pulmonaires, 2) pratiquer une incision entre les veines pulmonaires inférieures et l'anneau mitral, 3) une lésion dans sinus coronaire et 4) une incision entre le sinus coronaire et la valve tricuspide.

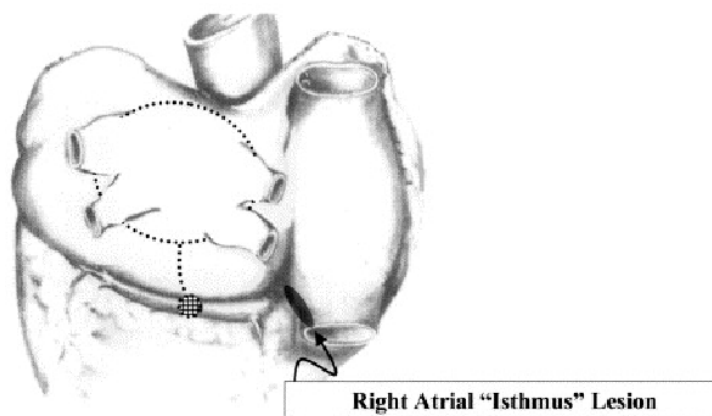


Figure 1: Approche « minimaze » pour le traitement des fibrillations auriculaires par ablation (COX 2004).

Cette trajectoire d'ablation est maintenant considérée comme un standard, les recherches sont concentrées sur des techniques de réalisation de lésions transmurales moins invasives que l'incision de la paroi et par des abords à accès minimal comme la radiofréquence (RF), les micro-ondes, le laser, la cryothérapie ou les ultrasons focalisés (HIFU).

- La voie endocavitaire. De nombreuses équipes ont essayé de reproduire les procédures d'ablation par voie épicaudique dans le contexte endocavitaire (généralement à l'aide de radiofréquences) (CALKINS et al. 1999; JAÏS et al. 1998; KOCHERIL et al. 2005; NATALE et al. 2000). L'équipe d'Haïssaguerre (HAÏSSAGUERRE et al. 2000) a été la première à montrer que l'isolation électrique par ablation des veines pulmonaires de l'oreillette gauche était généralement efficace à court terme pour traiter les fibrillations auriculaires paroxystiques. Dans un second temps, d'autres ablations sont réalisées, se rapprochant des trajectoires de lésions proposées dans minimaze. Ces lésions sont réalisées par une approche électro-physiologiques (mesures des potentiels et ablations en fonction de cette carte des potentiels). Plusieurs principes physiques ont été employés pour procéder à cette ablation par voie endocavitaire : les radiofréquences (AHMED et al. 2009), la cryothérapie (CESARIO et al. 2007) ou les HIFU. En dehors du côté invasif de la procédure, le problème de ce type d'approches endocavitaires est que malgré les progrès technologiques il est encore difficile d'obtenir des lignes d'ablation continues et surtout transmurales. L'autre problème de ces approches intracavitaires est qu'elles peuvent entraîner des lésions sur des tissus à l'extérieur du cœur (nerf phrénique, œsophage).

### **Traitements de la fibrillation auriculaire par ultrason focalisé haute intensité par voie transœsophagienne.**

Pour palier aux problèmes liés aux approches épicaudiques ou endocavitaires, une alternative semble être l'approche transœsophagienne (YIN et al. 2006). L'idée est de placer un transducteur HIFU au bout d'un endoscope afin de traiter la paroi de l'oreillette gauche au travers de l'œsophage (Figure 2<sup>1</sup>). Les avantages d'une telle approche sont multiples : la paroi de l'oreillette gauche est très proche de l'œsophage offrant ainsi une bonne fenêtre acoustique pour un traitement HIFU, elle est beaucoup moins invasive qu'une approche intracavitaire, le risque d'endommager des tissus adjacents est pratiquement nul du fait de la présence d'un ballon de refroidissement de la sonde préservant ainsi l'œsophage et du refroidissement de la paroi cardiaque par la circulation sanguine intracardiaque,...

---

1. <http://www.caehealthcare.com/eng/courseware/iccu-e-learning-solution-for-ultrasound>

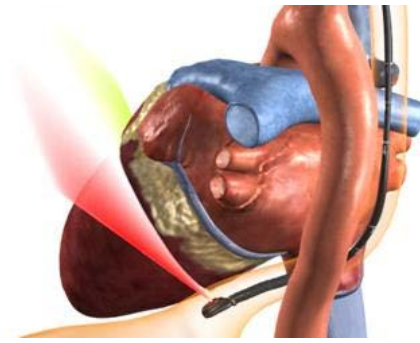


Figure 2: Approche transœsophagienne pour le traitement des fibrillations auriculaires.

Une telle approche a été étudiée dans le cadre du projet ANR TECSAN CardioUSgHIFU (ANR-11-TECS-0004). Durant ce projet, un prototype de sonde HIFU transœsophagienne a été étudié (CONSTANCIEL et al. 2013). Cette sonde est composée d'un transducteur multi-éléments de thérapie avec à son milieu une sonde d'imagerie échographique transœsophagienne (ETO) classique (Figure 3).

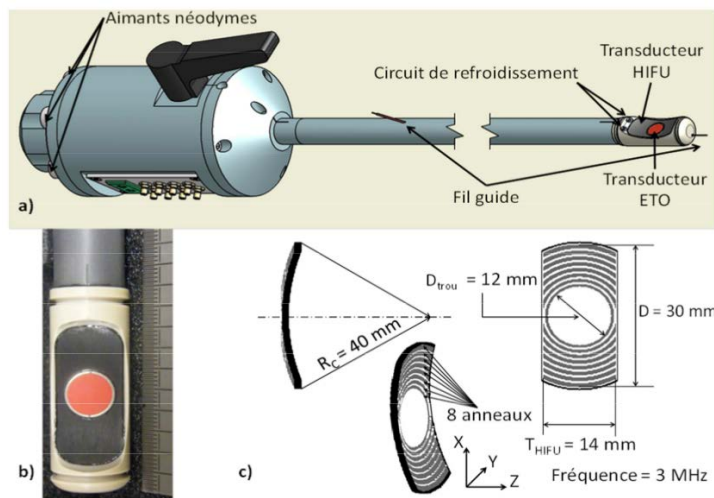


Figure 3: Prototype de sonde transœsophagienne pour le traitement des fibrillations auriculaires (CONSTANCIEL et al. 2013).

La procédure envisagée consiste à se guider vers la zone de thérapie à l'aide de l'image ETO, puis de réaliser la lésion selon la trajectoire prévue par le planning préopératoire (trajectoire du type « minimaze » par exemple) à l'aide de la sonde de thérapie sous guidage ETO. La faisabilité de réaliser l'ablation à l'aide d'une telle approche a été étudiée dans un premier temps par simulation, puis sur des modèles ex-vivos (CONSTANCIEL 2014; CONSTANCIEL et al. 2013).

## **Guidage d'un traitement de la fibrillation auriculaire par ultrason focalisé haute intensité par voie transœsophagienne. Schéma global et justification des travaux de recherche de la Thèse.**

### **Contexte des travaux de Thèse**

Les travaux menés durant la Thèse ont été réalisés dans le cadre du projet ANR TECSAN CardioUSgHIFU (ANR-11-TECS-0004) déjà évoqué précédemment. Ce projet avait pour objectif de proposer l'instrumentation et de mener les premières validations sur modèle animal de deux approches HIFU pour l'ablation dans contexte des thérapies de la fibrillation auriculaire. Dans la première approche, un transducteur HIFU a été miniaturisé afin de pouvoir espérer une utilisation par voie endocardiaque.

L'idée était également de pouvoir monitorer la thérapie à l'aide de nouvelles approches ultrasonores en élastographie à onde de cisaillement.

La deuxième approche est plus prospective. L'idée est de réaliser l'ablation par voie transœsophagienne. Dans ce paragraphe nous avons déjà présenté le prototype développé au LabTau de Lyon (CONSTANCIEL et al. 2013). Nos travaux de thèses se sont insérés dans cette approche en collaboration avec cette équipe. Le projet comprenait plusieurs sous-problèmes :

1. le design de la sonde par simulation de ces effets ;
2. la réalisation physique de la sonde ;
3. l'évaluation de la sonde par :
  - a) la simulation sur fantôme numérique de la faisabilité de l'ablation ;
  - b) la validation en ex-vivo des caractéristiques de la sonde et de sa faculté à produire des lésions ;
  - c) la validation en in-vivo, sur modèle animal, de sa faculté de la sonde à produire des lésions et à produire le protocole ;
4. la mise en place de la chaîne de traitements d'images pour :
  - a) la définition sur les données du patient du planning de l'ablation ;
  - b) le suivi et le contrôle durant la thérapie du planning défini au stade préopératoire ;

Les travaux liés à la Thèse se sont focalisés sur ce dernier point, c'est-à-dire le *planning* et le *guidage de l'intervention*.

### **Choix et justification des travaux de recherche de la Thèse**

Les objectifs des travaux liés à la Thèse sont présentés dans la Figure 4.

**Planning de l'intervention.** L'objectif est ici de proposer une aide au chirurgien pour la planification de l'intervention en se basant de la morphologie spécifique du patient. Cette

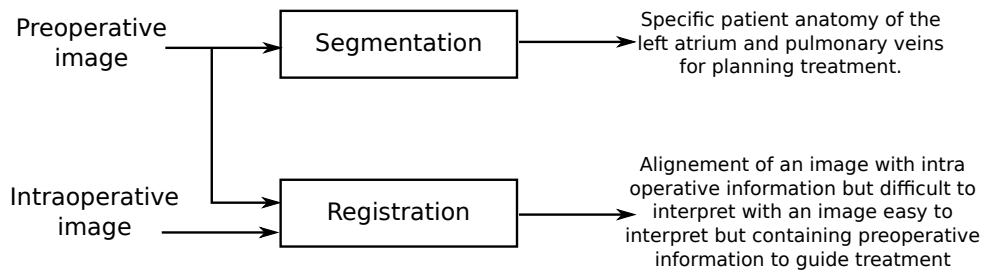


Figure 4: Objectifs des travaux liés à la Thèse.

planification va porter sur deux aspects du geste opératoire : 1) l'élaboration, sur l'anatomie du patient, des différentes zones à nécroser en suivant un schéma du type *minimize* ; 2) la préparation des données utiles au médecin lors du geste proprement dit. Dans ces deux cas, l'imagerie de référence servant à la planification de la défibrillation auriculaire est l'angiographie par scanner X multisources multibarrettes après injection de produit de contraste ou l'angiographie par Résonance Magnétique. Le cœur ayant un mouvement cyclique, des acquisitions synchronisées sur le signal électrocardiographique (ECG) permettent d'obtenir de 10 à 20 volumes à différents instants du cycle cardiaque.

1. La première étape de la définition des trajectoires de thérapie consiste à extraire, par *segmentation*, le *volume de l'oreillette gauche et les départs des veines pulmonaires* (ou du moins de la cavité auriculaire, car la paroi est relativement fine). Après une étude bibliographique des différentes méthodes de segmentation et après l'analyse des données et des attentes des médecins, nous avons choisi d'utiliser, dans le cas statique, une méthode de *segmentation basée sur des atlas*. Le choix de la méthode est justifié par la très grande variabilité inter-individus de l'oreillette gauche et particulièrement des départs des veines pulmonaires. Cette première segmentation donnera le cadre anatomique pour la définition par le médecin de la trajectoire d'ablation.
2. Une des particularités du geste interventionnel est qu'il se déroule dans un contexte transœsophagien. Les images per-opératoires et le futur guidage sont donc directement contraints par l'anatomie de l'œsophage, en particulier par sa localisation, sa forme et sa topologie dans l'espace du corps humain. Une des hypothèses fortes de notre travail est que l'œsophage va contraindre la trajectoire de l'endoscope dans le corps humain. Nous proposons donc de *reconstruire le volume du patient en prenant comme référentiel l'anatomie de l'œsophage*. L'idée est alors de trouver, par segmentation, l'axe de l'œsophage dans le volume préopératoire. Cet axe est alors utilisé pour rééchantillonner le volume préopératoire afin de proposer des plans images avec les mêmes positions et orientations que les futures images échographiques utilisées pour le guidage de la thérapie. Le planning pourra alors être projeté dans un contexte proche de l'intervention.

**Guidage de l'intervention.** Lors de l'intervention, les trajectoires d'ablation HIFU par voie transœsophagienne sont localisées et ciblées grâce aux images échographiques fournies par

la sonde d'imagerie intégrée dans la sonde de thérapie. Par contre, il reste extrêmement difficile de localiser une information 3D à l'aide d'images 2D. L'idée est alors de se référencer par rapport à une modalité intermédiaire qui est l'image 3D préopératoire (scanner X ou IRM). Nous nous proposons donc de *localiser la position de la coupe échographique dans le volume préopératoire par recalage 2D/3D*. Contrairement aux nombreux travaux de recalage 2D/3D présentés dans la bibliographie qui parlent d'images 2D projectives (fluoroscopie), l'objectif du recalage est de trouver la pose (position, orientation) du plan de coupe échographique dans le volume 3D. Le recalage peut alors se décomposer en deux problèmes distincts :

1. Comment comparer l'information contenue dans l'échographie à celle contenue dans la modalité préopératoire, scanner X ou IRM. Nous sommes donc confrontés à la définition d'un *modèle de similarité* entre une échographie et une autre modalité. De manière classique, deux classes de modèles sont généralement utilisées : les approches iconiques et les approches basées intensités. Nous avons écarté les approches iconiques. Ces approches nécessitent une extraction de l'information utilisée par le recalage pour chaque image 2D. Or la segmentation d'images échographiques reste relativement difficile et l'information qui peut être potentiellement extraite est assez peu discriminative. Nous nous sommes donc focalisés sur des *méthodes de similarités basées intensités*. L'utilisation d'une métrique basée intensités n'est pas immédiate, car les différents organes dans l'image ultrasonore sont décrits par une distribution spatiale de speckle et non par une distribution spatiale d'intensités. La première question est alors : une mesure de similarités basées intensités peut-elle s'appliquer pour recalibrer une échographie transœsophagienne sur une image 2D scanner X ou IRM ? Si oui, parmi les différentes métriques, quelle est la plus adaptée à notre problématique clinique ? Nous proposons donc d'étudier la faisabilité d'une *solution de recalage entre une échographie 2D et une coupe d'image scanner X ou IRM*. Cette étude couvrira le *choix de la métrique la mieux adaptée aux images de notre problématique clinique dans un contexte de recalage rigide et/ou élastique*.
2. Trouver la pose de la coupe échographique dans le volume du patient. Dans un premier temps se pose le choix de la transformation utilisée pour le recalage (élastique ou rigide). Même si le cœur est un organe en mouvement, nous avons choisi de procéder à un recalage rigide du fait de la synchronisation de l'imagerie 3D et ultrasonore sur l'ECG. Nous supposons que pour une phase donnée du cycle cardiaque, le cœur aura toujours la même forme. Nous supposons aussi que l'impact sur la zone à traiter du mouvement et des déformations du cœur dues à la respiration est négligeable. Un *recalage rigide* peut alors être considéré. Le problème revient donc à trouver *la coupe oblique du volume 3D la plus ressemblante à l'image échographique en utilisant la métrique choisie*. Sans hypothèse a priori, la pose de la coupe échographique dans le volume préopératoire du patient est contrôlée par 6 paramètres (3 de translation et 3 de rotation). Afin de diminuer le nombre de paramètres nous avons choisi de *prendre*

en compte l'hypothèse de la contrainte de la trajectoire de l'endoscope par l'œsophage.

## Schéma global des travaux de la Thèse

Le schéma global des différentes méthodes étudiées durant la Thèse est le suivant (Figure 5) :

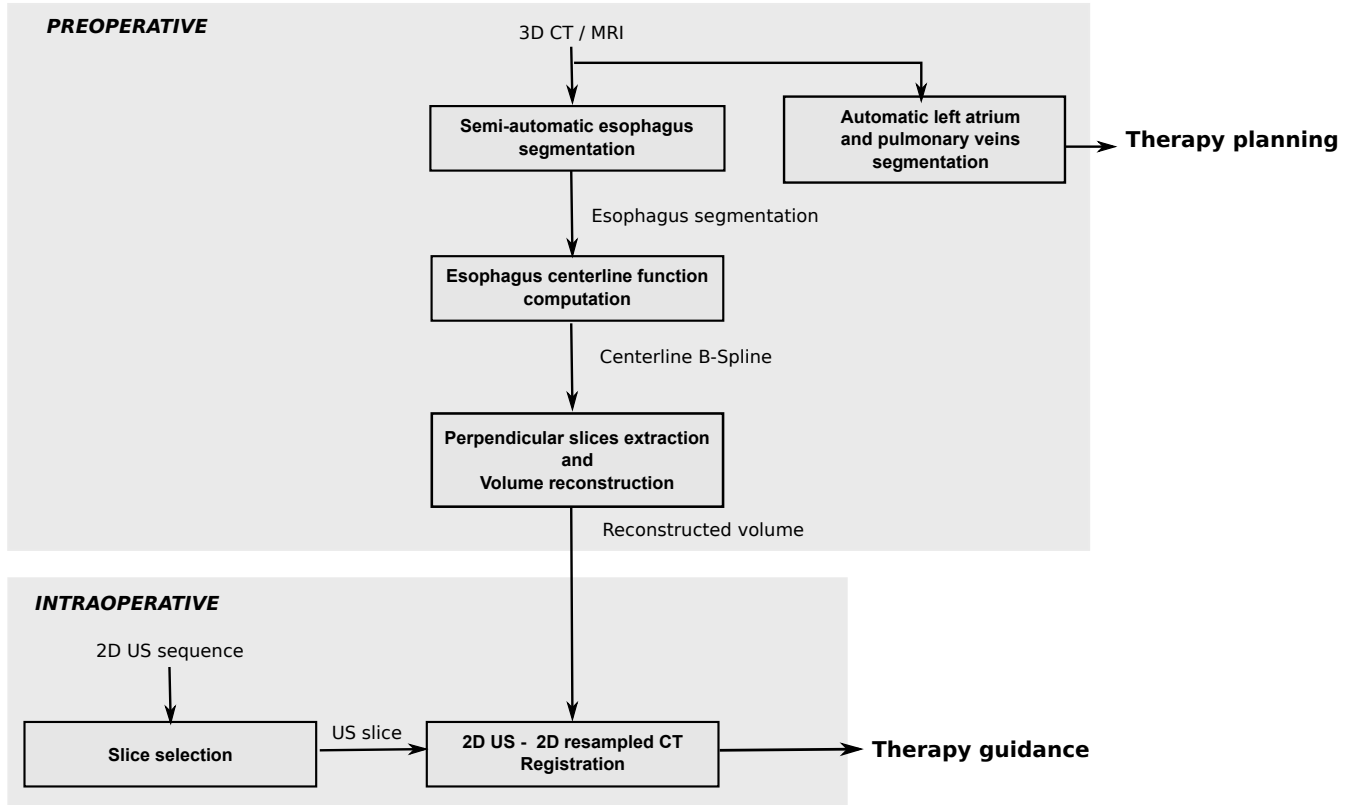


Figure 5: Méthodes étudiées durant la Thèse.

- Le référentiel anatomique spécifique patient est établi à l'aide d'une méthode de *segmentation multi-atlas de l'oreillette gauche et des veines pulmonaires* en Scanner X et en IRM (SANDOVAL et al. 2014). Le planning de la future ablation pourra être établi sur le volume ainsi extrait.
- Afin de projeter le planning dans un contexte proche de l'intervention, nous avons décidé de *rééchantillonner le volume préopératoire en fonction de la future trajectoire de la sonde transœsophagienne*. Cette étape est basée sur une première segmentation et extraction de la ligne centrale de l'œsophage. Cette ligne centrale formera le référentiel du rééchantillonnage.
- Deux étapes cruciales du recalage entre l'échographie 2D et l'imagerie préopératoire 3D ont été étudiées :
  - Le *choix et l'évaluation de métriques de similarité* basées intensités entre une image échographique et une coupe 2D issue de l'imagerie préopératoire (SANDOVAL et al. 2013a; SANDOVAL et al. 2013b). Les métriques sont au cœur du futur schéma recalage 2D/3D.

- *L'estimation de la pose de l'image échographique 2D dans le référentiel de l'imagerie préopératoire 3D.* Ce type de problématique est encore peu étudié. L'originalité de notre méthode consiste à utiliser le volume 3D précédent rééchantillonné par rapport aux futures images per-opératoires. Le problème de recalage se simplifie alors à une recherche dans ce volume de la coupe la plus ressemblante à l'image échographique.



## Partie II : Planning préopératoire

### Segmentation de l'oreillette gauche et des veines pulmonaires

#### Méthodologies de la segmentation

Le processus global de la segmentation de l'oreillette gauche et des départs des veines pulmonaires se fait en deux étapes : 1) une méthode multi-atlas qui permet de prendre en compte la très grande variabilité inter-individus du cœur et du réseau vasculaire ; suivi 2) d'une méthode de raffinement basée sur la croissance de régions pour ajuster localement le résultat de la première étape à la morphologie particulière du patient.

Les points les plus originaux de la Thèse concernent 1) la démarche globale qui consiste à raffiner le résultat de la méthode multi-atlas avec une croissance de région, 2) à la méthodologie de choix des paramètres de la méthode multi-atlas et 3) le choix de la méthode de fusion entre les atlas.

#### Méthode multi-atlas

L'approche multi-atlas a été utilisée dans d'autres cas présentant une grande variabilité interindividuelle comme le cerveau (LEUNG et al. 2011), la prostate (ACOSTA et al. 2011), ou le cœur entier et les grands vaisseaux (ZULUAGA et al. 2013).

Dans notre cas, en données d'entrées, nous avons  $I$  le volume scanner X ou IRM à segmenter et  $A_1, A_2, \dots, A_N$ , une série de  $N$  atlas composés chacun d'une image d'intensités  $I_i$  et d'une vérité terrain  $GT_i$ , ainsi  $A_i(I_i, GT_i)$ ,  $i = 1, 2, \dots, N$ .

La segmentation multi-atlas est basée sur 3 étapes (Figure 6): 1) le choix des atlas les plus proches du volume à segmenter, 2) l'ajustement de ces atlas sur le volume à segmenter et 3) la fusion entre les atlas ajustés.

1. Le choix des atlas les plus proches du volume à segmenter se fait après un recalage affine entre chaque image d'intensités  $I_i$  des  $N$  atlas avec l'image  $I$  (Figure 7). Ce recalage est mené en se basant sur un critère de similarité. Les différents atlas sont ensuite ordonnés en fonction de la valeur du critère de similarité. Les  $M$  atlas présentant les mesures les plus élevées sont ensuite utilisés pour l'étape suivante.
2. L'ajustement des atlas. Les images d'intensités  $I_i$  de ces  $M$  atlas sont ensuite ajustées sur  $I$  en utilisant une méthode de recalage élastique (Figure 8). Le champ de déformations estimé entre chaque  $I_i$  et  $I$  permet de propager cet ajustement aux vérités terrains  $GT_i$  des

$M$  atlas choisis sous la forme d'une série de  $M$  volumes étiquetés  $L_i$ .

3. La segmentation finale de  $I$  est issue de la fusion entre les  $L_i$  ajustés à  $I$  obtenues dans l'étape précédente. Nous avons exploré deux grandes stratégies de fusion :
  - a) La majorité après vote. Un voxel de  $I$  appartiendra à l'oreillette gauche ou aux veines pulmonaires si aux moins la moitié des  $L_i$  l'étiquettent ainsi (voir un exemple Figure 9).
  - b) L'estimateur STAPLE (Simultaneous Truth And Performance Level Estimation). La donnée d'entrée de cet algorithme est une collection de segmentations. Il estime ensuite, en utilisant la maximisation de l'espérance, la combinaison de ces segmentations qui optimise simultanément la sensibilité et la spécificité du résultat (WARFIELD et al. 2004).

Considérons une image de  $P$  voxels et un ensemble de  $R$  segmentations de cette image. Nous pouvons former une matrice  $D = P \times R$  qui décrit la décision binaire faite par chaque segmentation à chaque voxel de l'image. Soit  $T$ , vecteur de  $P$  éléments, qui représente de manière cachée la vérité de segmentation. Ceci nous donne donc les données complètes  $(D, T)$  avec une fonction de masse pour ces données complètes  $f(D, T / \text{sensitivity}, \text{specificity})$ .

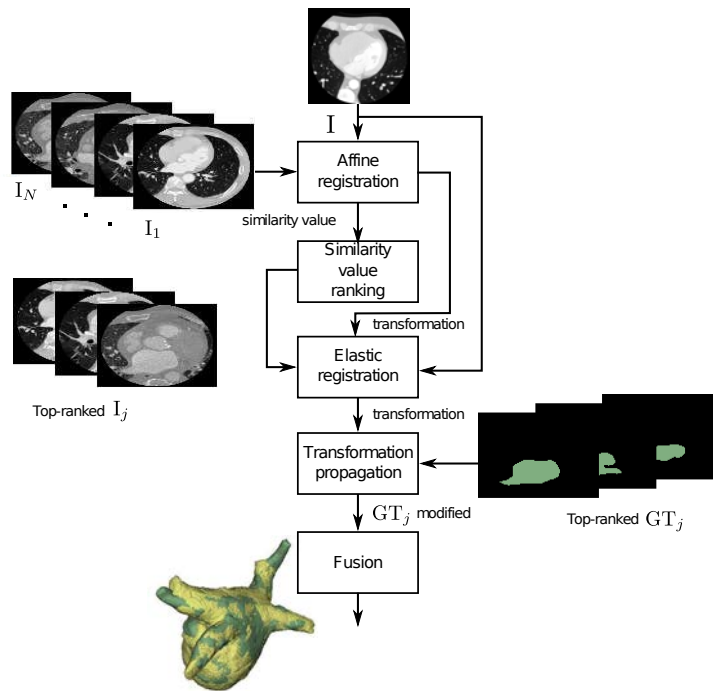


Figure 6: Approche de segmentation multi-atlas. 1) Choix des atlas les plus proches du volume à segmenter après un recalage affine, 2) l'ajustement des atlas les plus proches par recalage élastique et 3) la fusion entre les atlas ajustés.

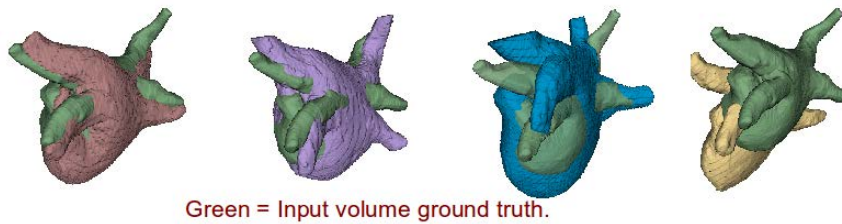


Figure 7: Exemples de recalage affine de différents atlas (en vert la vérité terrain).

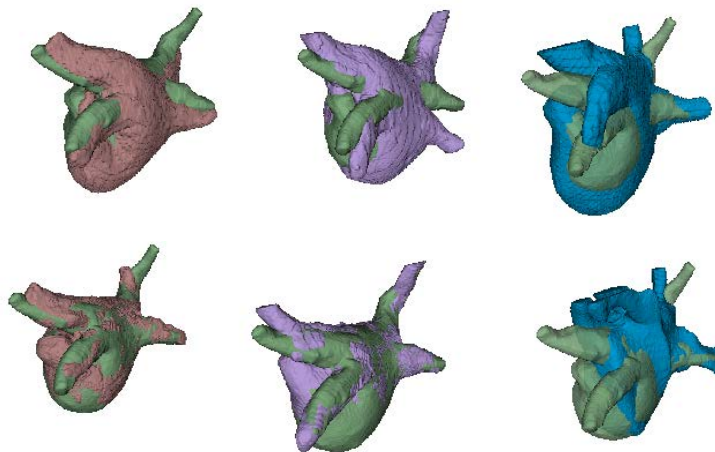


Figure 8: Trois exemples d'alignements avant (haut) et après (bas) le recalage élastique.

L'objectif de STAPLE est d'estimer la performance de la segmentation (caractérisée par la sensibilité et la spécificité) qui maximise la fonction log de la vraisemblance des données complètes :

$$(\widehat{sensitivity}, \widehat{specificity}) = \arg \max \ln f(D, T / sensitivity, specificity)$$

### Raffinement basée sur la croissance de régions

Dans un premier temps, le résultat de la segmentation issue de la méthode multi-atlas est érodé de 2 mm afin d'être sûr d'être à l'intérieur de l'oreillette gauche et des veines pulmonaires. Ce volume érodé sert d'une part de volume germe pour la croissance de région et d'autre part à établir le critère d'intensités utilisé pour la croissance de région. Ainsi le critère d'intensités sera égal à deux écarts-types autour de la valeur moyenne des intensités des voxels inclus dans le volume germe.

De même, le résultat de la segmentation issue de la méthode multi-atlas est dilaté de 2 mm afin de proposer un critère d'arrêt spatial qui évitera les fuites de la croissance de régions (Figure 10).

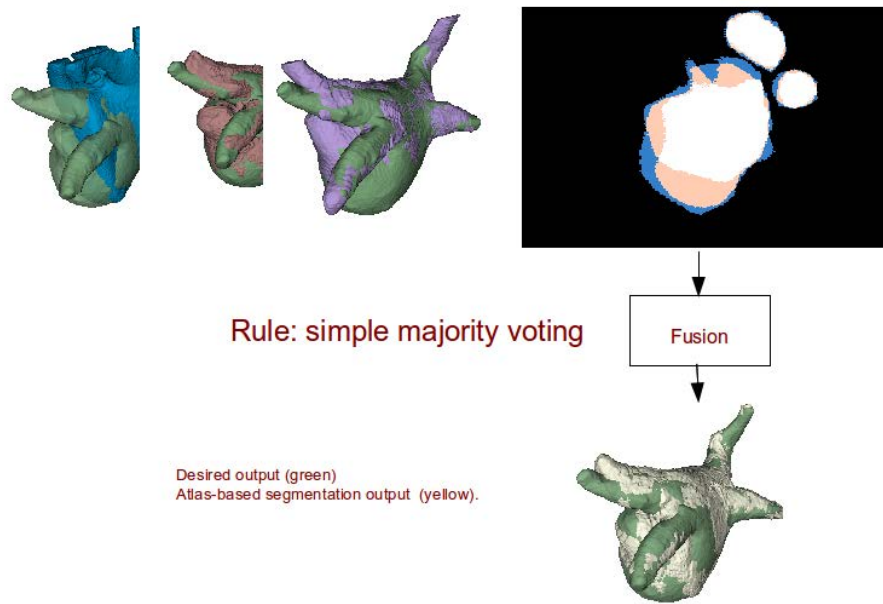


Figure 9: Processus de fusion avec 3 volumes. Résultat de la majorité après vote.

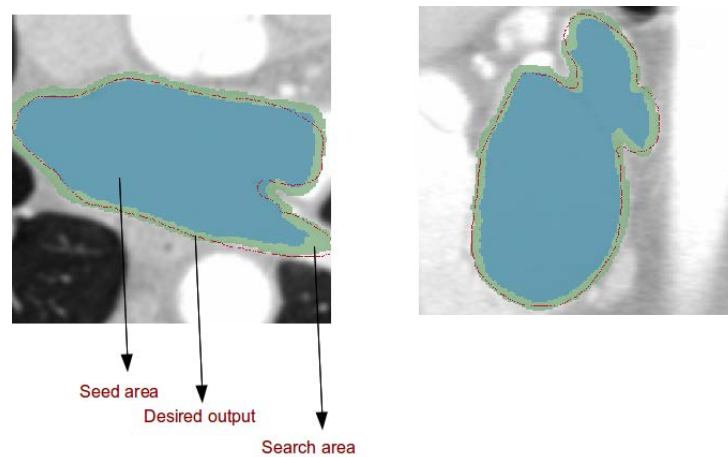


Figure 10: Région de recherche pour la croissance de régions.

## Données et Résultats

### Contexte de l'évaluation et données

L'évaluation de notre méthodologie a été effectuée dans le cadre du challenge de segmentation de l'oreillette gauche (Left Atrial Segmentation Challenge - LASC) du workshop STACOM'13 satellite de MICCAI'13 (TOBON-GOMEZ et al. 2013) pour le scanner X suivi d'une étude de comparaison multicentrique de méthodes de segmentation pour l'IRM (TOBON-GOMEZ et al. 2015).

Le challenge et l'étude multicentrique ont fourni 30 volumes scanner X et 30 volumes IRM.

Les données scanner X et IRM étaient des images synchronisées sur l'ECG en fin de systole. Ces données présentaient des variabilités en résolution et en qualité d'images.

Pour chaque modalité, 10 volumes ont été fournis avec une vérité terrain pour servir de base d'apprentissage et d'ajustement des paramètres aux différentes méthodes de segmentation (et dans notre cas, ces 10 volumes et vérités terrains ont servi également d'atlas à notre méthodologie). L'évaluation a ensuite porté sur les 20 autres volumes, sans connaissance de la vérité terrain de notre part.

### Choix des options et ajustement des paramètres

Les tests suivants ont eu pour but de sélectionner les paramètres de la méthode, c'est-à-dire : 1) la meilleure initialisation des procédures de recalage. En effet, le recalage peut être effectué sur l'ensemble du volume ou à l'intérieur d'une région d'intérêt (region of interest, ROI), un cube qui entoure l'oreillette gauche ; 2) Le choix des mesures de similarités utilisées dans les deux phases de recalage affine et élastique. Dans notre cas, trois mesures classiques de mesure de similarité ("Somme des Erreurs Quadratiques", "Information mutuelle" et la "Corrélation Croisée Normalisée" évaluées ; 3) Le nombre optimal  $M$  de volumes utilisés pour la fusion.

La performance de ces paramètres sera évaluée de la manière suivante : parmi les 10 volumes de la base d'apprentissage, nous segmenterons un des volumes et utiliserons les 9 autres en tant que bases d'atlas. La performance sera mesurée grâce au score de Dice entre  $V_1$ , le résultat du traitement à évaluer, et  $V_2$ , la vérité terrain<sup>2</sup>.

Nous avons évalué séparément les différents paramètres de la méthode puis leur influence conjointe. Si l'on considère l'ensemble de la procédure (recalage affine, choix des  $M$  atlas utilisés pour la fusion, recalage élastique et croissance de région), les meilleurs scores de Dice ont été obtenus avec des recalages effectués sur l'ensemble du volume avec une fusion de  $M = 5$  atlas. Nous avons toutefois un peu différencié les méthodes en adaptant la métrique de similarité utilisée par les deux phases de recalage à la modalité d'imagerie. La métrique "Somme des Erreurs Quadratiques" donnait les meilleurs scores pour la segmentation de volume scanner X alors que pour l'IRM, c'est la métrique "Information mutuelle" qui a été privilégiée.

### Évaluation en scanner X et IRM : résultat des challenges

Le challenge de segmentation de l'oreillette gauche (Left Atrial Segmentation Challenge - LASC) du workshop STACOM'13 satellite de MICCAI'13 (TOBON-GOMEZ et al. 2013) encourageait les participants à proposer une méthode de segmentation de l'oreillette gauche et de la partie proximale des veines pulmonaires. Le rôle du comité d'organisation de ce challenge était de proposer un cadre d'évaluation (données, vérité terrain, critère de standardisation des résultats

2. Pour rappel le score de Dice entre les volumes  $V_1$  et  $V_2$  est :  $Dice = \frac{2|V_1 \cap V_2|}{|V_1| + |V_2|}$

et métrique) des différentes méthodes soumises (TOBON-GOMEZ et al. 2015).

Nous avons participé à ce challenge en proposant nos deux versions de notre méthode de segmentation : 1) la méthode multi-atlas avec une fusion basée sur le vote majoritaire et 2) celle avec une fusion basée sur l'estimateur STAPLE. Ces deux versions ont été testées sur des images scanner X et IRM.

Concernant l'évaluation de méthodes, les résultats des participants sont dans un premier temps standardisés, c'est-à-dire que les différentes veines pulmonaires sont tronquées de façon identique. Deux métriques ont été proposées pour comparer les résultats des participants aux vérités terrains établis par des experts : le score de Dice (DC) et la distance inter-surfaces (S2S). Cette distance est obtenue par le cumul des distances entre points correspondants des surfaces des résultats des participants et des vérités terrains. Après normalisation, ces deux métriques ont été fusionnées afin de proposer un score unifié  $S_p = \frac{Z_{S2S_{OG,p}} + Z_{(1-DC)_{VP,p}}}{2}$  avec, pour le participant  $p$ ,  $Z_{S2S_{OG,p}}$  la normalisation de la métrique S2S sur le seul corps de l'oreillette gauche et  $Z_{(1-DC)_{VP,p}}$  celle de la métrique DC mesurée aux seules veines pulmonaires.

Onze algorithmes différents, développés par sept groupes internationaux, ont été proposés. Ces algorithmes se différencient par : 1) le pré-traitement (sans traitements, normalisation d'histogrammes, définition de régions d'intérêt, ...), 2) la procédure de segmentation principale (méthode multi-atlas, croissance de régions, modèle de formes, ...), 3) l'optimisation de cette segmentation (croissance de régions, snake sur l'ensemble ou sur les seules veines pulmonaires, ...) et 4) le post-traitement (remplissage de trous, graph cuts, ...).

**Résultats sur les IRM.** Les figures 11 et 12 montrent respectivement les résultats de la segmentation sur des IRM de haute et basse qualité (TOBON-GOMEZ et al. 2015). Si la segmentation des IRM des hautes qualités donne de très bons résultats, les zones de faibles contrastes des IRM de basses qualités peuvent entraîner des sur-segmentations par notre méthode. Cette sur-segmentation semble être due au module de recalage élastique sensible aux faibles contrastes.

Les scores médians de DICE et S2S montrent une supériorité de la fusion par vote majoritaire par rapport à celle utilisant l'estimateur STAPLE (voir table 1), sans doute due à une plus grande sensibilité à une mauvaise initialisation.

Le score unifié nous a permis de comparer nos méthodes (LTSI\_VRG pour la variante avec fusion par vote majoritaire et LTSI\_VSRG pour la fusion par STAPLE dans la figure 13). La variante avec fusion par vote majoritaire obtient le meilleur score. Il est à noter que ce score est très proche de celui d'un second observateur humain OBS\_2 utilisé pour définir la variabilité inter-observateurs.

**Résultat sur les scanner X.** Le comportement de la segmentation des volumes scanner X est

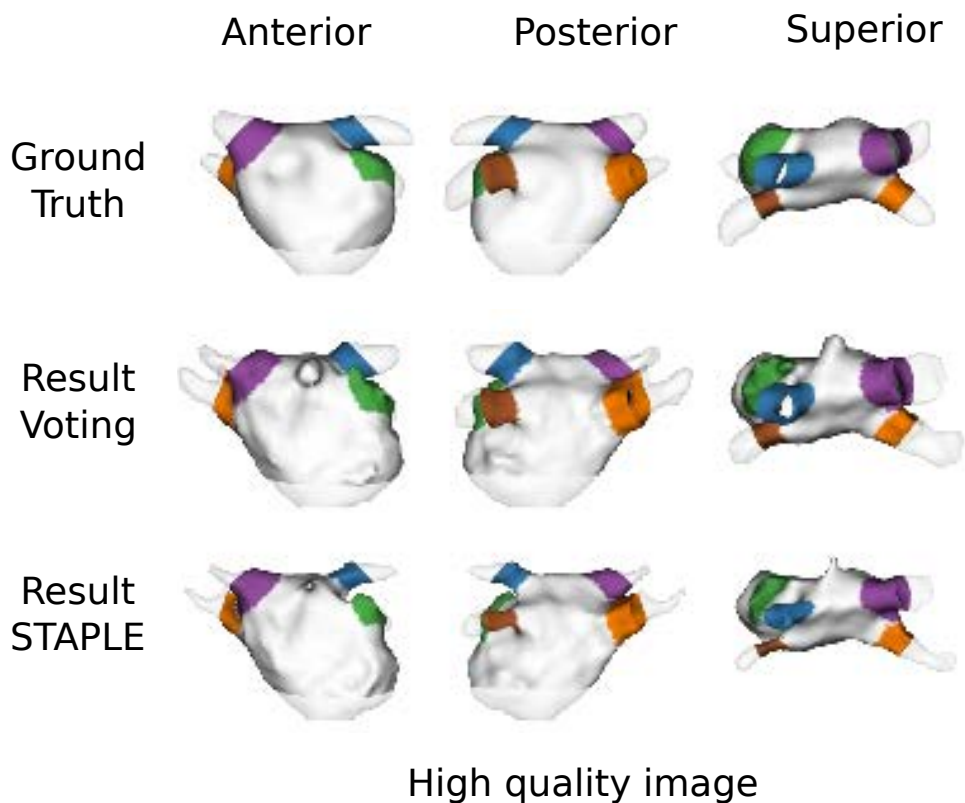
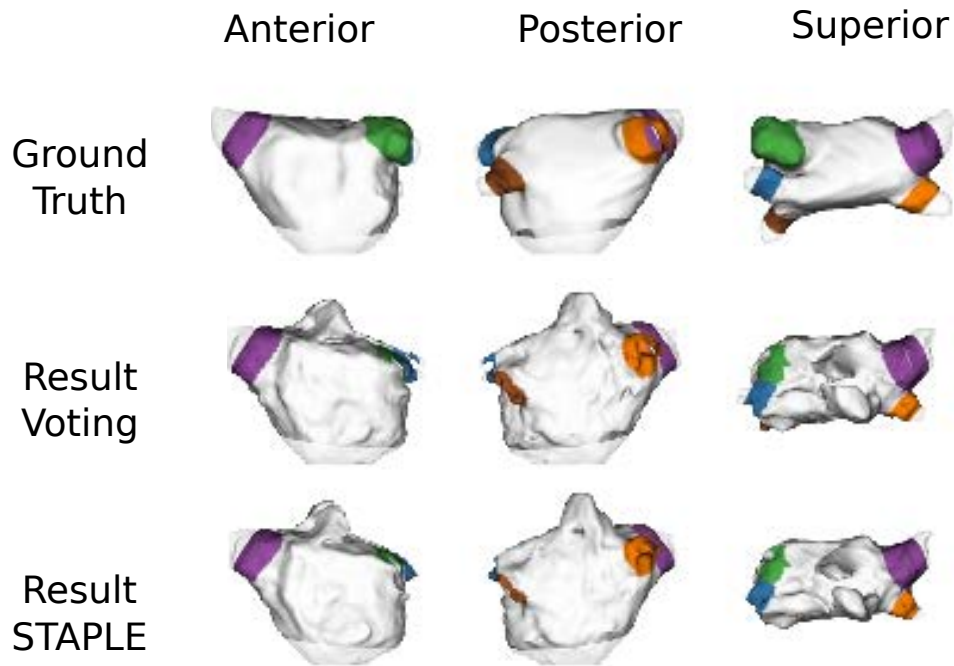


Figure 11: Résultats de la segmentation sur une IRM de bonne qualité. La vérité terrain est sur la ligne supérieure (TOBON-GOMEZ et al. 2015).

Table 1: Scores médians de DICE et S2S entre le résultat de la segmentation et la vérité terrain pour l'oreillette et les veines pulmonaires (TOBON-GOMEZ et al. 2015). Idéalement S2S = 0mm et le score de Dice = 1.

Méthode	Métrique	oreillette gauche	veines pulm.
Multi-atlas (vote maj.)	S2S (mm)	$0.886 \pm 2.18$	$1.199 \pm 2.34$
	Dice	$0.931 \pm 0.04$	$0.696 \pm 0.16$
Multi-atlas (STAPLE)	S2S (mm)	$2.091 \pm 1.59$	$2.251 \pm 1.84$
	Dice	$0.881 \pm 0.02$	$0.507 \pm 0.19$



### Low quality image

Figure 12: Résultats de la segmentation sur une IRM de basse qualité. La vérité terrain est sur la ligne supérieure (TOBON-GOMEZ et al. 2015).

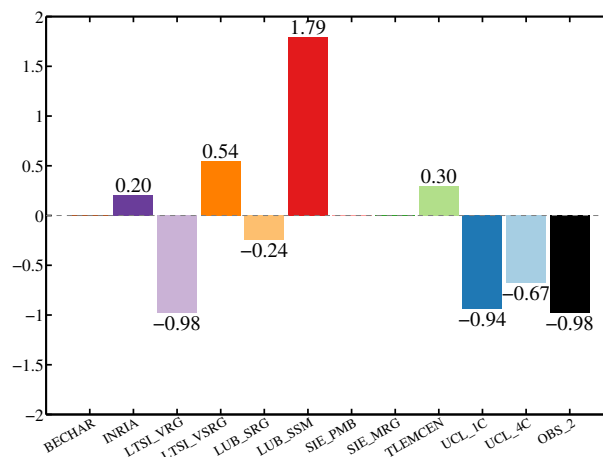


Figure 13: Score unifié pour l'IRM. Comparaison entre méthodes (TOBON-GOMEZ et al. 2015). Les scores les plus faibles (les plus négatifs) sont les meilleurs. Nos méthodes sont : LTSI\_VRG pour la variante avec fusion par vote majoritaire et LTSI\_VSRG pour la fusion par STAPLE. OBS\_2 est un second observateur humain qui permet de définir la variabilité inter-observateurs.



proche de celui observé en IRM avec de très bons scores pour les images de bonne qualité et quelques faiblesses lorsque les volumes présentent des fortes inhomogénéités de contraste.

Les scores montrent également une légère supériorité ou une plus grande robustesse de la fusion par vote majoritaire par rapport à celle utilisant l'estimateur STAPLE.

## Volume préopératoire adapté à la thérapie

L'idée générale de ce chapitre est d'adapter le volume préopératoire (scanner X ou IRM) à la future thérapie. En effet, la thérapie se fait de manière transœsophagienne. Ceci veut dire que toutes les images échographiques acquises durant la thérapie seront liées (ou contraintes) par la topologie de l'œsophage du patient. En d'autres termes, les futures images sur lesquelles se guideront les médecins sont toutes perpendiculaires à l'axe de l'œsophage et les organes vus par ces images seront explorés selon un certain ordre lors du déplacement de l'endoscope dans l'œsophage (Figure 14). Afin de nous mettre dans ce contexte et de préparer la future intervention, nous nous proposons donc de reconstruire le volume préopératoire du patient en prenant comme référentiel l'anatomie de l'œsophage, c'est-à-dire sous la forme d'une suite de coupes perpendiculaires à l'axe de l'œsophage.

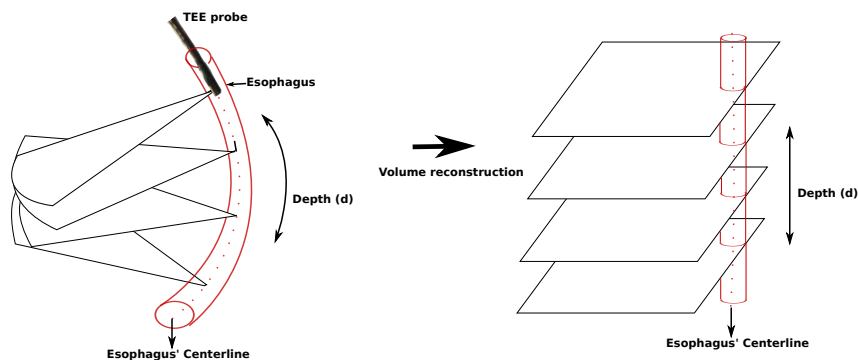


Figure 14: Volume préopératoire adapté à la thérapie.

### Méthode de reconstruction.

La construction du volume préopératoire adapté à la thérapie se fait en trois étapes :

1. La segmentation semi-automatique de l'œsophage dans le volume scanner X. Pour cela, nous avons utilisé l'implémentation des contours actifs du logiciel ITKSNAP<sup>3</sup> après une sélection manuelle d'une région d'intérêt par l'utilisateur et un seuillage des niveaux de gris.
2. L'estimation de la ligne centrale de l'œsophage. Des points de la ligne centrale sont déterminés pour chaque coupe à partir de la segmentation précédente. Une courbe spline (smoothing spline (DE BOOR 1978)) est ensuite ajustée sur ces points. Le paramètre de lissage de cette courbe peut être contrôlé par l'utilisateur. Au final, cette courbe est échantillonnée de manière régulière à l'aide de son paramètre naturel.
3. La création de coupes perpendiculaires à la ligne centrale. Pour chaque point échantillonné sur la ligne centrale, nous pouvons déterminer le plan perpendiculaire à la tangente  $\vec{w}$  de

3. <http://www.itksnap.org>

la courbe à ce point (Figure 15). Ce plan est alors échantillonné de manière régulière et les intensités de ces échantillons sont estimés par interpolation des voxels voisins du volume scanner X.

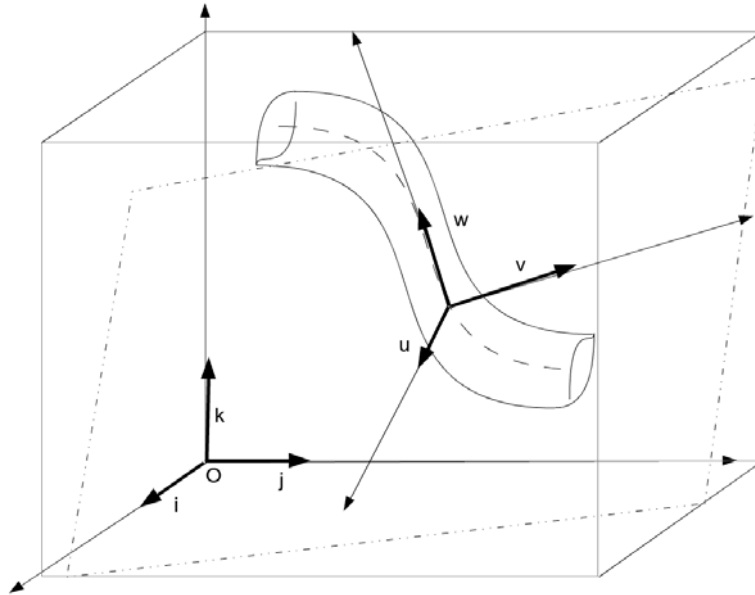


Figure 15: Systèmes de référence entre le volume scanner X et les coupes le long de l'œsophage.

### Validation sur fantôme physique

L'hypothèse de départ est que les coupes du volume reconstruit ont les mêmes orientations que les images de l'échographie transœsophagienne. L'idée de la validation est donc de créer un fantôme physique mimant le cœur et l'œsophage. Ce fantôme peut alors être imagé à l'aide d'un scanner X. Cette acquisition permet de construire le volume préopératoire adapté à la thérapie en utilisant la méthode décrite précédemment. Nous faisons ensuite l'acquisition d'images échographiques transœsophagiennes. La comparaison de ces images avec le volume reconstruit devra permettre de valider la reconstruction.

### Création du fantôme et acquisition des images

Pour fabriquer le fantôme physique nous avons adapté le fantôme commercial des ventricules du cœur PVAH-01 Medical Imaging Technologies, de SHELLEY Automation Inc. London, Canada. Nous lui avons ajouté un tuyau simulant l'œsophage (Figure 16). L'œsophage étant opaque aux ultrasons, nous avons aménagé 3 fenêtres de tir. L'ensemble est immergé dans de l'eau afin d'assurer une bonne propagation des ultrasons. Trois marqueurs en caoutchouc, visibles dans les deux modalités, ont également été fixés le long de la paroi du cœur afin de proposer une référence spatiale au fantôme.

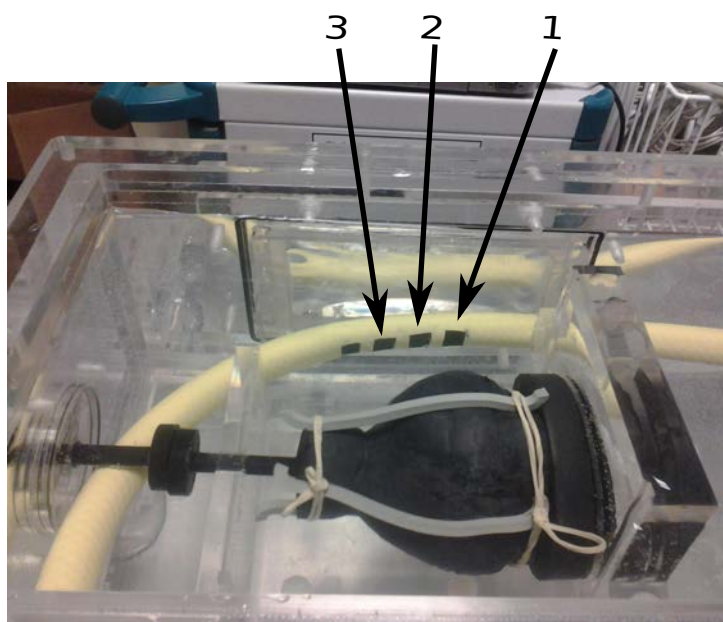


Figure 16: Fantôme physique du cœur et de l'œsophage. Trois fenêtres (1, 2 et 3) sont ouvertes dans l'œsophage pour permettre l'acquisition échographique. Deux des 3 marqueurs externes de référence sont également visibles sur la face externe du cœur.

L'acquisition des échographies transœsophagiennes a été réalisée à l'aide de l'échographe Vivid Q 2D (General Electric, Healthcare, Wauwatosa, USA) avec une sonde 6VT-D 4D. La sonde a été bloquée à l'orientation 0, perpendiculaire à l'axe de l'endoscope.

Le volume préopératoire correspond à un Cone Beam CT acquis en utilisant un C-arm robotisé Artis zeego (Siemens AG, Erlangen, Allemagne). Afin d'ajuster au mieux les images échographiques et le volume préopératoire, nous avons acquis un volume CBCT pour chaque position de la sonde transœsophagienne.

### Évaluation de la reconstruction

Dans un premier temps, nous avons segmenté, pour chaque volume CBCT, de manière semi-automatique, le myocarde, les 3 marqueurs externes et la tête de la sonde échographique (et donc une information sur la localisation spatiale du centre de l'image échographique correspondante). Pour chaque volume ainsi segmenté, nous avons créé un volume préopératoire adapté à la thérapie en utilisant la méthode décrite précédemment.

Au final, nous avons, pour chaque image échographique notée  $I_{US}$  : a) un volume CBCT original, noté  $V_{or}$ , qui contient en plus la position 3D du centre de l'image échographique et la position 3D des marqueurs externes et b) un volume reconstruit pour s'adapter à la thérapie, noté  $V_{rec}$ , qui contient en plus les positions 3D reprojetées du centre de l'image échographique et des marqueurs externes.

Selon notre hypothèse de départ,  $V_{rec}$  est composé de coupes parallèles ayant potentiellement la même localisation spatiale que les images échographiques. L'objectif de l'évaluation est de vérifier cette hypothèse. Pour cela, nous allons comparer 1) la pose 3D de  $I_{US}$  en se basant sur les coupes parallèles de  $V_{rec}$  avec 2) la pose 3D de  $I_{US}$  estimée directement dans  $V_{or}$ . Ces deux poses sont estimées respectivement par :

1. Nous retenons la coupe parallèle de  $V_{rec}$  qui porte le centre de l'échographe trouvée par la segmentation. Dans cette coupe, l'orientation de  $I_{US}$  est obtenue par l'estimation de la matrice de rotation 2D centrée sur la position de l'échographe à l'aide d'une technique de recalage rigide 2D-2D basée sur les marqueurs externes (Figure 17). Connaissant la pose de l'image échographique dans la coupe parallèle de  $V_{rec}$  et la transformation géométrique de cette coupe par rapport  $V_{or}$ , nous pouvons estimer une matrice de transformation  $T_{RecEval}$  qui estime la pose 3D de l'image échographique en se basant sur notre volume reconstruit.

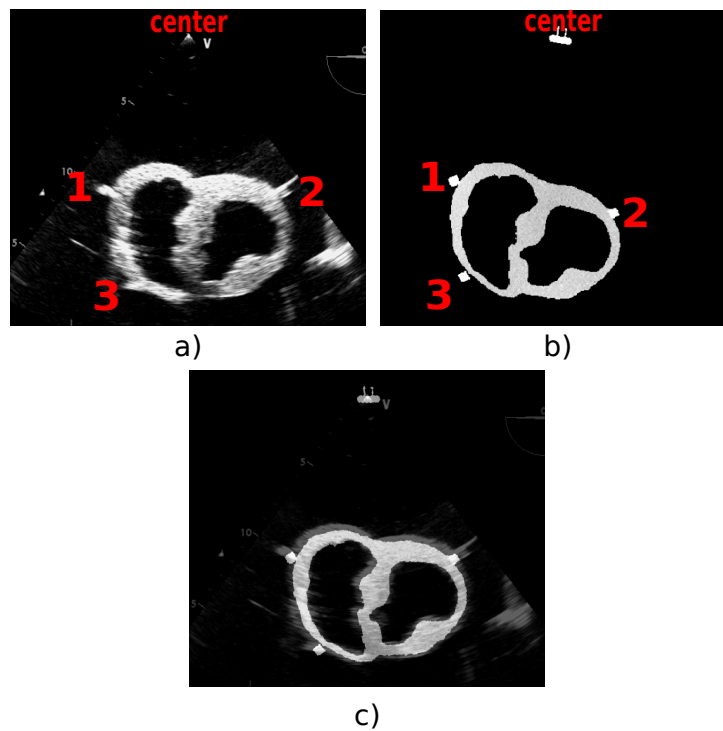


Figure 17: a) Image échographique. b) Coupe du volume reconstruit à l'aide de notre méthode et présentant le myocarde et les marqueurs segmentés. c) Résultat du recalage en rotation 2D autour de la position du centre de l'échographe.

2. dans un premier temps, nous connaissons dans  $V_{or}$  la position du centre de l'échographe trouvée par la segmentation. Autours de cette position, nous allons effectuer un recalage rigide *manuel* entre  $I_{US}$  et  $V_{or}$ . L'utilisateur peut faire varier manuellement les paramètres de la transformation rigide (3 translations et 3 rotations). L'estimation du meilleur recalage est effectuée visuellement en se basant sur les marqueurs externes et le myocarde. Pour

chaque image échographique, cette procédure est répétée 3 fois. Les paramètres moyens de ce recalage sont considérés comme référence et donnent une transformation  $T_{ref}$  qui estime la pose 3D de l'image échographique dans le volume  $V_{or}$ .

La précision de notre méthode de volume préopératoire adapté à la thérapie sera estimée par l'erreur de recalage (FITZPATRICK et al. 2001) :  $TRE(P_{landmark}^i) = |T_{Ref}P_{landmark}^i - T_{RecEval}P_{landmark}^i|$ , avec  $P_{landmark}^i$  des points caractéristiques de l'image échographique. Les  $TREs$  permettent de définir un indice global de précision, l'erreur moyenne de recalage :  $mTRE = \frac{1}{n} \sum_{i=1}^n TRE(P_{landmark}^i)$ .

L'évaluation de la méthode a été menée pour les 3 images échographiques correspondant aux trois fenêtres de tir. Chaque point caractéristique de l'image échographique a été sélectionné manuellement 10 fois afin de prendre en compte la variabilité interindividuelle.

Une des tendances des différentes évaluations est que l'erreur de recalage augmente (et donc la validité de notre hypothèse décroît) lorsque la distance entre l'œsophage et la cible augmente (Figure 18). Dans cette figure la fenêtre 1 est la plus proche du cœur et la fenêtre 3 la plus éloignée. Les  $mTRE$  se répartissent entre 3mm et 5,5mm. Ces erreurs sont du même ordre de grandeur que celles mesurées par les méthodes de recalage entre scanner X et échographies transœsophagiennes décrites dans (GAO et al. 2012; LANG et al. 2013).

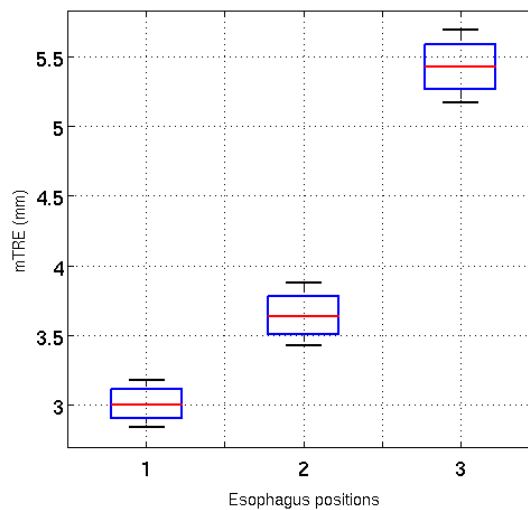


Figure 18: Boîtes à moustaches des  $TREs$  pour les 3 fenêtres d'échographies transœsophagiennes. La fenêtre 1 est la plus proche du cœur et la fenêtre 3 la plus éloignée.

Ce résultat nous conforte dans le choix d'utiliser un volume préopératoire adapté à la thérapie. En effet, les erreurs qu'il entraîne sont du même ordre de grandeur qu'un recalage direct entre

scanner X et échographie transcesophagienne. L'impact des erreurs est d'autant plus faible que l'oreillette gauche est très proche de l'œsophage.

## Partie III : Guidage de la thérapie

### Évaluation de métriques pour le recalage US/scanner X

Un des points clés des techniques de recalage est la métrique de comparaison entre les images des différentes modalités. Dans le cas de recalage d'images échographiques avec une autre modalité, généralement cette métrique est iconique mais nécessite une première étape de segmentation. Pour des raisons de précision nous souhaitons utiliser une métrique basée sur l'intensité. Le problème d'une telle métrique est le suivant. Pour les images scanner X, les différents tissus sont caractérisés par une intensité spécifique. Par contre, dans les échographies, les tissus sont caractérisés par une distribution spatiale de speckle et non par une intensité fixe rendant difficile une métrique basée sur l'intensité. Toutefois, Huang a proposé une méthode de recalage entre des échographies cardiaques et du scanner X qui utilise l'information mutuelle pour conduire l'alignement (HUANG et al. 2009). Dans cette méthode, l'information mutuelle est appliquée sur l'image échographique après un filtrage médian et un seuillage. Les résultats de cette méthode nous ont confortés dans le choix d'utiliser une métrique basée sur l'intensité pour conduire notre recalage. Les questions que nous nous posons alors sont :

1. Est ce que l'information mutuelle est la meilleure des métriques ? D'autres métriques basées sur l'intensité ont été proposées dans la littérature. Quelle est la plus adaptée à notre problématique ?
2. Dans quelles mesures les prétraitements proposés par Huang (filtrage et seuillage) améliorent-ils la précision du recalage ?

L'évaluation que nous proposons a pour objectifs de répondre à ces deux questions en testant l'impact de *différentes métriques* sur la *précision* et l'*efficacité* du recalage.

#### Matériel et méthode

L'évaluation nécessite une vérité terrain. Nous avons décidé de créer des fantômes numériques pour lesquels des structures bien définies (une ellipse et deux coupes du Visible Human Project<sup>4</sup> - une de la base de l'homme et l'autre de la base de la femme) sont utilisées pour simuler des images échographiques (DILLESEGER et al. 2009) et scanner X correspondantes. Pour chaque image scanner X, deux images échographiques à des orientations différentes ont été simulées. La Figure 19 montre des exemples des fantômes numériques.

Nous avons établi une procédure de recalage 2D/2D qui utilise une métrique de similarité basée sur l'intensité. Dans cette expérimentation, nous avons évalué 8 mesures de similarité, 6 basées sur les histogrammes des images (l'information mutuelle -MI- (MAES et al. 1997), l'information mutuelle normalisée -NMI- (STUDHOLME et al. 1999), le coefficient de corrélation d'entropie -ECC- (MAES et al. 1997), l'entropie conjointe -H- (MAES et al. 1997), l'énergie

4. [http://www.nlm.nih.gov/research/visible/visible\\_gallery.html](http://www.nlm.nih.gov/research/visible/visible_gallery.html)



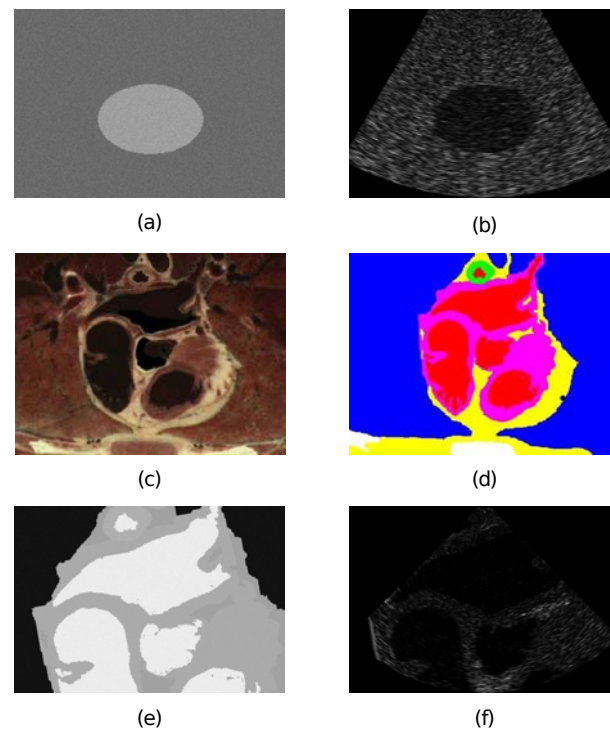


Figure 19: Images des fantômes numériques. Ellipse: images simulées de scanner X (a) et d'échographie (b). Coupe de l'oreillette gauche et des veines pulmonaires : section du thorax de l'homme du Visible Human (c); image segmentée et étiquetée : air, graisse, os, muscle (dont le myocarde), eau et sang (d); images simulées de scanner X (e) et d'échographie (f).

d'histogramme -E- (BRO-NIELSEN 1997) et le ratio de corrélation -CoR- (ROCHE et al. 1998)) et 2 basées à la fois sur les valeurs d'intensités et sur une information spatiale (la mesure de similarité de points basée sur la MI -PSMI- (ROGELJ et al. 2003) et le critère de Woods -WC- (WOODS et al. 1993)).

Nous voulons étudier l'influence de la mesure de similarité non seulement sur le résultat du recalage mais également sur son comportement durant la recherche de la solution. Pour cela nous avons utilisé le protocole imaginé par Skerl (SKERL et al. 2006) qui permet d'évaluer la performance de la mesure de similarité indépendamment du processus d'optimisation. Ce protocole nécessite la connaissance de la vérité terrain c'est-à-dire la vraie transformation géométrique (2 paramètres de translation et 1 paramètre de rotation dans le cas de recalage 2D) entre les images à recalcr. Cette vérité terrain sera le centre d'un espace des paramètres. Toute autre transformation sera localisée sous la forme d'un point dans cet espace des paramètres. Le protocole d'évaluation se décompose en 3 étapes : 1) la définition aléatoire dans l'espace de paramètres de points (donc de transformations géométriques) autour de la vérité terrain; 2) le calcul de la mesure de similarité pour chaque transformation géométrique défini dans l'étape précédente ; et 3) l'analyse de l'évolution de la mesure de similarité autour de la vérité terrain. Cinq propriétés sont estimées : la précision du recalage (ACC), le nombre de minimaux locaux

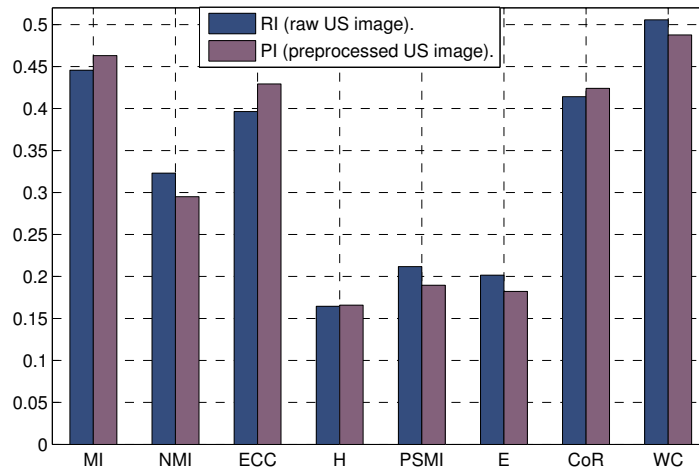


Figure 20: Indice de composition des différentes mesures de similarité.

autour l'optimum (NOM), le risque de non convergence vers l'optimum (RON), l'horizon de capture vers le maximum global (CR) et la discrimination de l'optimum (DO).

## Résultats

Pour chaque paire d'images (1 paire sur l'ellipse et 4 paires sur l'oreillette gauche - 2 paires de la base de l'homme et 2 de la base de la femme du Visible Human Project), nous avons réalisé le recalage en utilisant l'image échographique brute et l'image échographique après le prétraitement proposé par Huang (HUANG et al. 2009). Les paramètres du protocole de Skerl ont été ajustés en fonction de la taille et la résolution des images.

Les résultats de ces différents tests montrent que globalement le *critère de Woods* donne de meilleures performances que les autres mesures de similarités, particulièrement en ce qui concerne la précision du recalage et la discrimination de l'optimum. Le *prétraitement améliore le résultat* en termes de précision. Comme l'analyse de performance est difficile à mener en comparant 5 critères de nature différente, nous avons essayé de combiner ces critères à l'aide d'une analyse des composantes principales. Le coefficient de la première composante servira de critère de qualité (MISHRA 2009). La Figure 20 monte ce coefficient pour les différentes mesures de similarité. Le *critère de Woods* donne également les meilleurs résultats devant l'information mutuelle. Même si globalement dans la Figure 20, les prétraitements ne semblent pas améliorer l'indice, nous allons toutefois retenir l'*utilisation de prétraitements* du fait de la précision du recalage.

## Recalage échographie 2D vers scanner X 3D

Dans ce dernier chapitre nous allons présenter la solution de recalage entre images échographiques 2D et volume préopératoire scanner X 3D. Cette étape est essentielle pour le guidage de la thérapie. Notre problématique est différente des méthodes de recalage 2D/3D généralement décrites dans la littérature qui parlent d'images projectives (radiologie numérique). Dans notre cas de recalage rigide (cf. le chapitre sur la Justification des méthodes), il s'agit trouver la pose de l'image 2D, c'est-à-dire sa position et son orientation, dans le volume 3D. Si l'on reprend le schéma classique du recalage, la méthode proposée devra chercher le jeu optimal de paramètres géométriques (3 translations et 3 rotations) qui maximise la métrique de similarité entre l'image échographique 2D et la section 2D du volume 3D extraite en considérant ces paramètres géométriques.

Afin de diminuer le nombre de paramètres à optimiser, nous allons utiliser l'hypothèse posée précédemment sur le fait que les images échographiques sont toutes perpendiculaires à l'axe de l'œsophage (voir le chapitre sur le Volume préopératoire adapté à la thérapie). Nous allons donc modifier le schéma classique du recalage en intégrant le volume préopératoire adapté à la thérapie (voir Figure 21). En suivant ce schéma, nous n'aurons donc plus qu'à estimer la coupe  $d$  du volume reconstruit qui porte l'image échographique et l'orientation  $\theta$  de l'image échographique dans cette coupe du volume reconstruit. Pour plus de précision, nous pourrions également estimer une petite translation 2D du centre de l'image échographique par rapport à l'axe de l'œsophage.

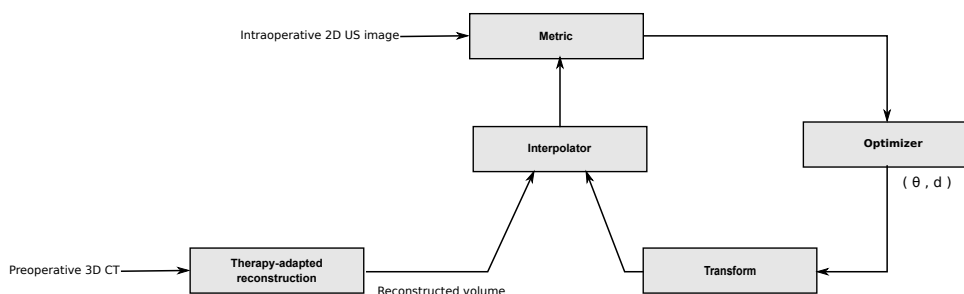


Figure 21: Schéma fonctionnel de la technique de recalage 2D/3D.

La démarche de la méthode de recalage est alors la suivante :

1. Nous prenons un volume préopératoire à un certain moment du cycle cardiaque (75% de l'intervalle R-R dans notre cas) et nous le reformatons en suivant la méthodologie décrite dans le chapitre "Volume préopératoire adapté à la thérapie" afin de créer un volume  $V_{rec}$  composé de coupes perpendiculaires à l'axe de l'œsophage.
2. Nous prenons une image échographique correspondant au même moment du cycle cardiaque que nous positionnons dans une zone initiale dans  $V_{rec}$ . Cette zone peut être estimée grossièrement, par exemple par la longueur et l'orientation de l'endoscope dans l'œsophage.
3. L'image échographique est comparée à la coupe correspondante de  $V_{rec}$  à l'aide d'une mesure de similarité. Nous avons déterminé que le Critère de Woods donnait les meilleurs

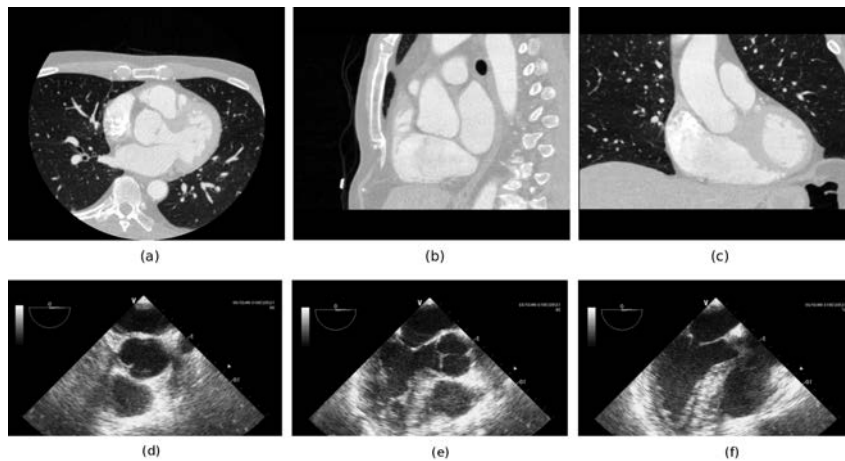


Figure 22: Volume préopératoire, vues a) axiale, b) sagittale et c) coronale. Échographies per-opératoires à 3 positions (d-f) de l'endoscope.

résultats, mais comme il est peu implémenté dans les bibliothèques de fonctions de recalage, nous avons opté pour la seconde métrique en termes de performance, l'Information Mutuelle.

4. Le processus d'optimisation cherche alors les paramètres de la transformation maximisant la similarité entre l'échographie et l'information de  $V_{rec}$ . Dans un premier temps l'orientation  $\theta$  de l'image échographique et la position de cette image selon l'axe  $d$  de  $V_{rec}$ , puis en relâchant les contraintes sur le centre de rotation qui peut être décalé par rapport au centre de l'œsophage.
5. Connaissant la pose estimée par la méthode de recalage et la matrice de transformation de la coupe de coordonnées  $d$  vers le volume préopératoire, il est alors facile de mettre en correspondance l'image échographique et le volume préopératoire.

### Mise en œuvre sur un jeu de données cliniques

Nous avons évalué notre méthode sur un jeu de données cliniques provenant du CHU Louis Pradel de Lyon (Figure 22). Ce jeu était composé d'un volume scanner préopératoire avec injection de produit de contraste, synchronisé à 75% de l'intervalle R-R, de  $512 \times 512 \times 395$  voxels de taille  $0.546875 \times 0.546875 \times 0.44998169\text{mm}^3$  et de trois séquences de 46 images échographiques transœsophagiennes de  $636 \times 420$  pixels de taille  $0.35278 \times 0.35278\text{mm}^2$ . Les trois séquences sont enregistrées à trois positions différentes le long de l'œsophage. Les images des séquences correspondant à 75% de l'intervalle R-R ont été sélectionnées par un expert.

Le volume scanner X préopératoire a été traité afin de créer le volume  $V_{rec}$  composé de coupes perpendiculaires à l'axe de l'œsophage. Pour cela, la surface interne de l'œsophage est extraite en utilisant l'implémentation des contours actifs du logiciel ITKSNAP (YUSHKEVICH et al. 2006). Cette surface nous a permis de définir des points candidats de l'axe central de l'œsophage. Ces points ont servi de base pour la définition de la ligne centrale de l'œsophage par une courbe

spline (Figure 23). Cette ligne centrale est ensuite échantillonnée de manière régulière. Pour ces points, les plans perpendiculaires à la ligne centrale permettent de créer  $V_{rec}$ .

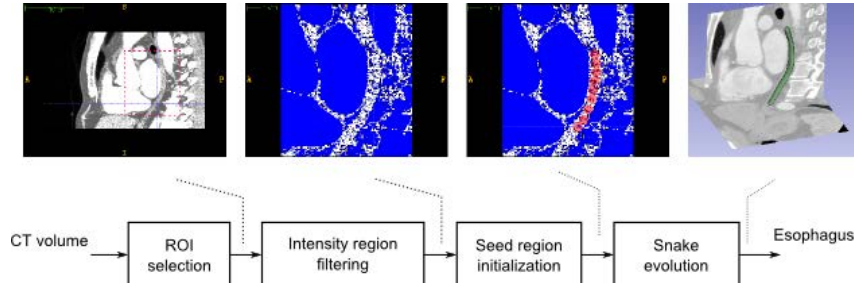


Figure 23: Segmentation de l'œsophage.

En fonction de la configuration de l'endoscope (longueur insérée, suite des images,...), une zone candidate pour la position de l'endoscope peut être définie. Cette zone peut représenter une vingtaine de coupes de  $V_{rec}$ . Un recalage 2D/2D est effectué entre l'image échographique et chacune des coupes de la zone candidate de  $V_{rec}$ . Ce recalage estime l'orientation  $\theta$  de l'image échographique et le décalage du centre de rotation  $(t_x, t_y)$  par rapport à l'axe central. La coupe de coordonnée  $d$  qui présente la mesure de similarité la plus élevée après recalage sera considérée comme la coupe correspondante de l'image échographique.

La Figure 24 montre en exemple le recalage de la première image échographique sur  $V_{rec}$ . La superposition entre les deux images montre visuellement une bonne correspondance entre les deux images.

La Figure 25 montre les poses, estimées par notre méthode, des 3 images échographiques dans le volume préopératoire.

Le temps de calcul moyen pour recalcr une image échographique est de 5,11s avec une déviation de 0,98s.

## Évaluation du recalage

Comme nous ne disposons que du jeu de données cliniques, nous avons évalué les résultats du recalage à l'aide de la méthodologie décrite précédemment pour valider le volume reconstruit.

- Notre méthode permet d'estimer une matrice de transformation  $T_{SliceVolRegis}$  entre l'image échographique et le volume préopératoire.
- De manière interactive un expert essaie de trouver directement la pose de la même image échographique dans le volume préopératoire à l'aide du logiciel Slicer. Afin de tenir compte de la variabilité intra-individu, cette pose est estimée trois fois par cet expert. La moyenne de ces poses sera considérée comme vérité terrain et permet de définir une matrice de transformation de référence  $T_{Ref}$ .

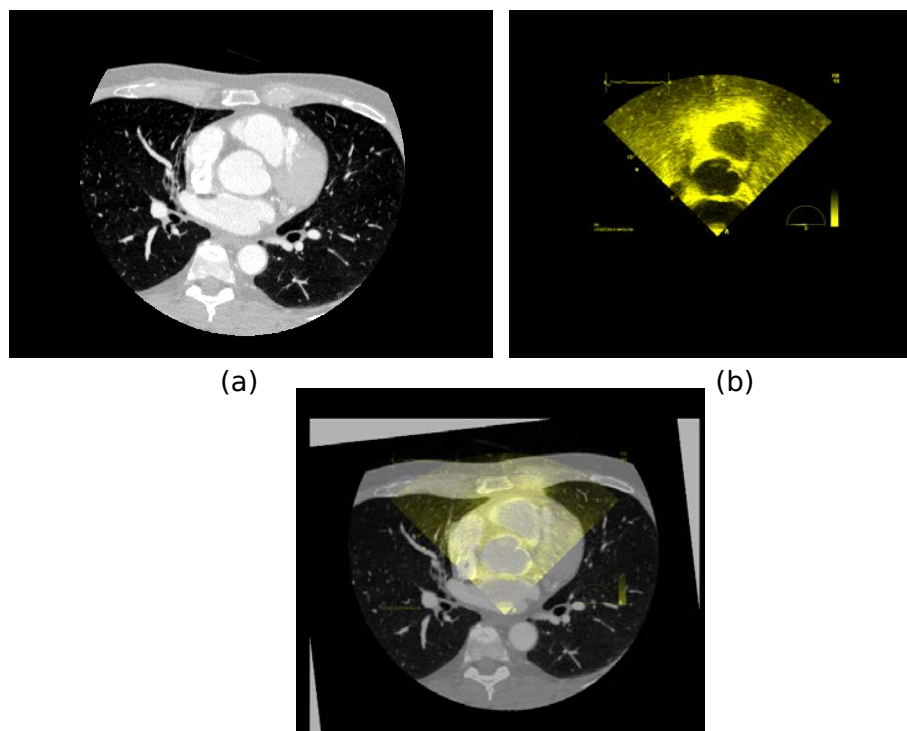


Figure 24: Exemple de recalage 2D/3D. a) Coupe scanner X correspondante du volume reconstruit. b) Image échographique 1. c) Superposition des images après recalage.

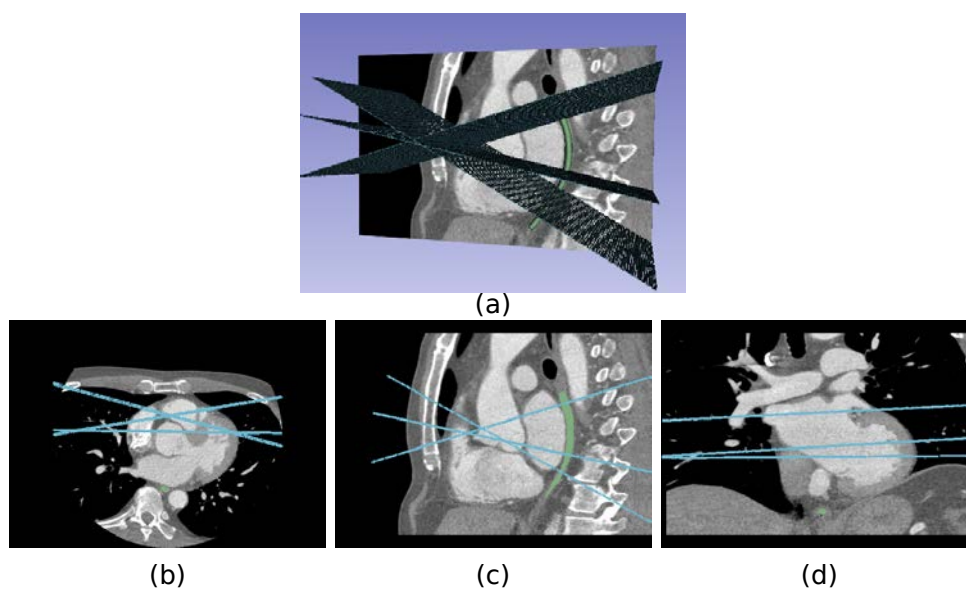


Figure 25: Visualisation 3D de la pose des 3 images échographiques dans le volume préopératoire.

- Afin d'évaluer la précision du recalage, nous définissons des points caractéristiques  $P_{landmark}^i$  sur l'image échographique. Ces points sont reprojétés sur le volume préopératoire à l'aide de respectivement  $T_{SliceVolRegis}$  et  $T_{Ref}$ . L'erreur de recalage est définie par  $TRE(P_{landmark}^i) = |T_{Ref}P_{landmark}^i - T_{SliceVolRegis}P_{landmark}^i|$ . L'erreur moyenne de recalage :  $mTRE = \frac{1}{n} \sum_{i=1}^n TRE(P_{landmark}^i)$  donne une mesure quantitative de cette précision.

Nous avons utilisé cette méthodologie pour les 3 images échographiques. Pour chaque image, 5 points caractéristiques ont été définis 10 fois de manière interactive. La Figure 26 montre les boîte à moustaches des  $TREs$  pour les trois images échographiques.

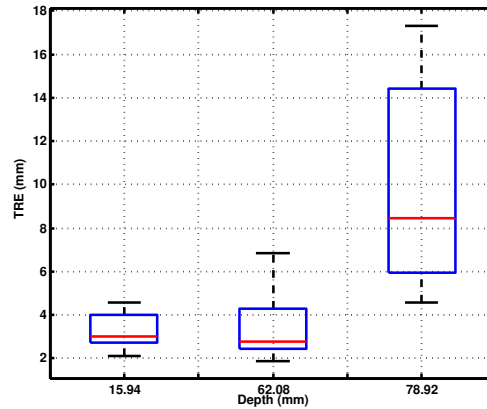


Figure 26: Boîte à moustaches de l'erreur de recalage ( $TRE$ ) pour a) Image 1, b) Image 2 et c) Image 3.

La  $mTRE$  est de l'ordre de 3,5mm pour les deux premières images et de 9,6mm pour la troisième image. La  $mTRE$  globale est de 5,6mm. Cette erreur moyenne est du même ordre de grandeur que celles reportées dans les articles traitant de recalage échographique/scanner X sur données cliniques: 1,5-4,2mm pour (GAO et al. 2012) et 5mm pour (LANG et al. 2013). Il est à noter que ces deux dernières méthodes effectuaient un recalage avec plus d'information (2 coupes images se croisant ou échographies 3D) que dans notre cas et que l'initialisation nécessitait l'intervention d'un expert.

## Conclusion

Dans le contexte clinique du traitement de la fibrillation auriculaire par ablation HIFU par voie transœsophagienne, cette Thèse a porté sur différentes méthodes de traitements d'images permettant d'établir un *planning spécifique patient* de la future thérapie et le *guidage de la thérapie* proprement dite.

Un des objectifs du planning est de permettre de définir l'emplacement des différentes zones à nécroser sur la paroi de l'oreillette gauche en se basant sur l'anatomie du patient. Pour cela, nous avons développé une *méthode de segmentation de l'oreillette gauche et des veines pulmonaires*. Cette méthode se base sur une approche multi-atlas qui permet de prendre en compte la variabilité anatomique des différents patients, suivie d'un raffinement local par croissance de région. Cette méthode a été évaluée et comparée à d'autres méthodes dans le cadre d'une étude multicentrique. Les résultats de cette étude ont montré que, par rapport aux autres méthodes, notre approche donnait de très bons résultats pour la segmentation d'images IRM et des résultats corrects pour la segmentation d'images scanner X.

La phase de planning peut également servir à préparer les données qui seront utiles au médecin lors du geste proprement dit. Nous avons proposé de représenter les images anatomiques préopératoires (un volume scanner X dans notre cas) selon la même pose (position et orientation) que les futures images échographiques qui seront fournies par la sonde transœsophagienne. Cette représentation se présente sous la forme d'un *volume préopératoire adapté à la thérapie*. La création de ce volume a nécessité une estimation de la ligne centrale de l'œsophage suivi d'un rééchantillonnage du volume original en se basant sur la topologie de cette ligne centrale. L'étude de validation de cette méthode, menée sur un fantôme physique, a montré une précision du rééchantillonnage du même ordre que celle des méthodes classiques de recalage citées dans la littérature.

Le guidage de la thérapie nécessite un report de l'information du planning sur les images échographiques utilisées durant la thérapie. Ce report se fait par recalage de l'information 2D des images échographiques avec le volume préopératoire 3D. Afin de réaliser ce recalage, nous avons, dans un premier temps, mené une *étude systématique permettant de choisir la mesure de similarité la plus efficace pour comparer l'information des images échographiques et celle du scanner X*. Ce choix est ensuite intégré dans une *méthode originale de recalage entre les échographies 2D et le scanner X 3D*. L'originalité de cette méthode consiste à utiliser le volume préopératoire adapté à la thérapie en tant que base de recherche pour le recalage. Cette méthode a été appliquée sur des données cliniques réelles avec des résultats qui donnent visuellement un bon alignement entre l'information des images échographiques et celle du scanner X. Ces résultats ont été confirmés lors d'une première évaluation plus formelle.



## References

- ACOSTA, O., A. SIMON, F. MONGE, F. COMMANDEUR, C. BASSIROU, G. CAZOULAT, R. DE CREVOISIER, and P. HAIGRON (2011). “Evaluation of multi-atlas-based segmentation of CT scans in prostate cancer radiotherapy”. In: *8th IEEE International Symposium on Biomedical Imaging (ISBI)*. Chicago, pp. 1966–1969.
- AHMED, H. and V. Y. REDDY (2009). “Technical advances in the ablation of atrial fibrillation”. In: *Heart Rhythm* 6.8 Suppl, S39–S44.
- BRO-NIELSEN, M. (1997). “Rigid registration of CT, MR and cryosection images using a GLCM framework”. In: *CVRMed-MRCAS'97*. Grenoble: Springer, pp. 171–180.
- CALKINS, H., J. HALL, K. ELLENBOGEN, G. WALCOTT, M. SHERMAN, W. BOWE, J. SIMPSON, T. CASTELLANO, and G. N. KAY (1999). “A new system for catheter ablation of atrial fibrillation.” In: *American Journal of Cardiology* 83.5B, pp. 227D–236D.
- CESARIO, D. A., A. MAHAJAN, and K. SHIVKUMAR (2007). “Lesion-forming technologies for catheter ablation of atrial fibrillation”. In: *Heart Rhythm* 4.3 Suppl, S44–S50.
- CONSTANCIEL, E. (2014). “Développement d’un applicateur transoesophagien à Ultrasons Focalisés de Haute Intensité à guidage échographique intégré pour le traitement de la fibrillation atriale”. PhD thesis. Université Claude Bernard, Lyon, France.
- CONSTANCIEL, E., W. N'DJIN, F. BESSIERE, F. CHAVRIER, D. GRINBERG, A. VIGNOT, P. CHEVALIER, J. CHAPELON, and C. LAFON (2013). “Design and evaluation of a transesophageal HIFU probe for ultrasound-guided cardiac ablation: simulation of a HIFU mini-maze procedure and preliminary ex vivo trials”. In: *IEEE Transactions on Ultrasonics, Ferroelectrics, and Frequency Control* 60.9, pp. 1868–1883.
- COX, J. L. (2003). “Atrial fibrillation II: rationale for surgical treatment”. In: *Journal of Thoracic and Cardiovascular Surgery* 126.6, pp. 1693–1699.
- COX, J. L. (2004). “The standard maze-III procedure”. In: *Operative Techniques in Thoracic and Cardiovascular Surgery* 9.1. Surgical Options for Treating Atrial Fibrillation During Mitral Valve Surgery, pp. 3–23.
- DE BOOR, C. (1978). *A practical guide to splines*. Springer-Verlag New York.
- DILLENSEGER, J.-L., S. LAGUITTON, and E. DELABROUSSE (2009). “Fast simulation of ultrasound images from a CT volume.” In: *Computers In Biology and Medicine* 39.2, pp. 180–186.
- FITZPATRICK, J. and J. WEST (2001). “The distribution of target registration error in rigid-body point-based registration”. In: *IEEE Transactions on Medical Imaging* 20.9, pp. 917–927.
- FUSTER, V., L. E. RYDÉN, D. S. CANNOM, H. J. CRIJNS, A. B. CURTIS, K. A. ELLENBOGEN, J. L. HALPERIN, J.-Y. LE HEUZEY, G. N. KAY, J. E. LOWE, S. B. OLSSON, E. N. PRYSTOWSKY, J. L. TAMARGO, S. WANN, S. C. SMITH JR, A. K. JACOBS, C. D. ADAMS, J. L. ANDERSON, E. M. ANTMAN, S. A. HUNT, R. NISHIMURA, J. P. ORNATO, R. L. PAGE, B. RIEGEL, S. G. PRIORI, J.-J. BLANC, A. BUDAJ, A. J. CAMM, V. DEAN, J. W. DECKERS, C. DESPRES, K. DICKSTEIN, J. LEKAKIS, K. MCGREGOR, M. METRA, J. MORAIS, A. OSTERPEY, and J. L. ZAMORANO (2006). “ACC/AHA/ESC 2006 guidelines for the

- management of patients with atrial fibrillation—executive summary: a report of the American College of Cardiology/American Heart Association Task Force on Practice Guidelines and the European Society of Cardiology Committee for Practice Guidelines (Writing Committee to Revise the 2001 Guidelines for the Management of Patients With Atrial Fibrillation).” eng. In: *Journal of the American College of Cardiology* 48.4, pp. 854–906.
- GAO, G., G. PENNEY, Y. MA, N. GOGIN, P. CATHIER, A. ARUJUNA, G. MORTON, D. CAULFIELD, J. GILL, C. ALDO RINALDI, J. HANCOCK, S. REDWOOD, M. THOMAS, R. RAZAVI, G. GIJSBERS, and K. RHODE (2012). “Registration of 3D trans-esophageal echocardiography to X-ray fluoroscopy using image-based probe tracking”. In: *Medical Image Analysis* 16.1, pp. 38–49.
- HAÏSSAGUERRE, M., P. JAÏS, D. C. SHAH, A. TAKAHASHI, M. HOCINI, G. QUINIOU, S. GARRIGUE, A. LE MOUROUX, P. LE MÉTAYER, and J. CLÉMENTY (1998). “Spontaneous initiation of atrial fibrillation by ectopic beats originating in the pulmonary veins”. In: *New England Journal of Medicine* 339.10, pp. 659–666.
- HAÏSSAGUERRE, M., D. C. SHAH, P. JAÏS, M. HOCINI, T. YAMANE, I. DEISENHOFER, S. GARRIGUE, and J. CLÉMENTY (2000). “Mapping-guided ablation of pulmonary veins to cure atrial fibrillation”. In: *American Journal of Cardiology* 86.9, Supplement 1. Converging Electrical Therapies for the Heart, K9–K19.
- HUANG, X., J. MOORE, G. GUIRAUDON, D. JONES, D. BAINBRIDGE, J. REN, and T. PETERS (2009). “Dynamic 2D ultrasound and 3D CT image registration of the beating heart”. In: *IEEE Transactions on Medical Imaging* 28.8, pp. 1179–1189.
- JAÏS, P., D. C. SHAH, A. TAKAHASHI, M. HOCINI, M. HAÏSSAGUERRE, and J. CLÉMENTY (1998). “Long-term follow-up after right atrial radiofrequency catheter treatment of paroxysmal atrial fibrillation”. In: *Pacing and Clinical Electrophysiology* 21.11 Pt 2, pp. 2533–2538.
- JALIFE, J. (2003). “Rotors and spiral waves in atrial fibrillation”. In: *Journal of Cardiovascular Electrophysiology* 14.7, pp. 776–780.
- KOCHERIL, A. G., H. CALKINS, A. D. SHARMA, D. CHER, H. STUBBS, and J. E. BLOCK (2005). “Hybrid therapy with right atrial catheter ablation and previously ineffective antiarrhythmic drugs for the management of atrial fibrillation”. In: *Journal of Interventional Cardiac Electrophysiology* 12.3, pp. 189–197.
- LANG, P., M. CHU, D. BAINBRIDGE, G. GUIRAUDON, D. JONES, and T. PETERS (2013). “Surface-Based CT-TEE Registration of the Aortic Root”. In: *IEEE Transactions on Biomedical Engineering* 60.12, pp. 3382–3390.
- LEUNG, K., J. BARNES, M. MODAT, G. RIDGWAY, J. BARTLETT, N. FOX, and S. OURSELIN (2011). “Automated brain extraction using Multi-Atlas Propagation and Segmentation (MAPS)”. In: *8th IEEE International Symposium on Biomedical Imaging (ISBI)*. Chicago, pp. 2053–2056.
- MAES, F., A. COLLIGNON, D. VANDERMEULEN, G. MARCHAL, and P. SUETENS (1997). “Multi-modality image registration by maximization of mutual information”. In: *IEEE Transactions on Medical Imaging* 16.2, pp. 187–198.

- MISHRA, S. (2009). “On construction of robust composite indices by linear aggregation”. In: *The IUP Journal of Computational Mathematics* 2.3, pp. 24–44.
- NATALE, A., F. LEONELLI, S. BEHEIRY, K. NEWBY, E. PISANO, D. POTENZA, K. RAJKOVICH, B. WIDES, L. CROMWELL, and G. TOMASSONI (2000). “Catheter ablation approach on the right side only for paroxysmal atrial fibrillation therapy: long-term results”. In: *Pacing and Clinical Electrophysiology* 23.2, pp. 224–233.
- ROCHE, A., G. MALANDAIN, X. PENNEC, and N. AYACHE (1998). “The correlation ratio as a new similarity measure for multimodal image registration”. In: *Medical Image Computing and Computer-Assisted Intervention - MICCAI'98*. Ed. by W. WELLS, A. COLCHESTER, and S. DELP. Vol. 1496. Lecture Notes in Computer Science. Springer Berlin Heidelberg, pp. 1115–1124.
- ROGELJ, P., S. KOVAČIČ, and J. C. GEE (2003). “Point similarity measures for non-rigid registration of multi-modal data”. In: *Computer vision and image understanding* 92.1, pp. 112–140.
- SANDOVAL, Z. and J.-L. DILLENSEGER (2013a). “Intensity-based similarity measures evaluation for CT to ultrasound 2D registration”. In: *IRBM* 34.4–5, pp. 278–282.
- SANDOVAL, Z. and J.-L. DILLENSEGER (2013b). “Evaluation of computed tomography to ultrasound 2D image registration for atrial fibrillation treatment”. In: *Computing in Cardiology Conference (CinC)*. Zaragossa, pp. 245–248.
- SANDOVAL, Z., J. BETANCUR, and J.-L. DILLENSEGER (2014). “Multi-atlas-Based Segmentation of the Left Atrium and Pulmonary Veins”. In: *Statistical Atlases and Computational Models of the Heart. Imaging and Modelling Challenges*. Vol. 8330. Lecture Notes in Computer Science. Nagoya: Springer Berlin Heidelberg, pp. 24–30.
- SKERL, D., B. LIKAR, and F. PERNUS (2006). “A protocol for evaluation of similarity measures for rigid registration”. In: *IEEE Transactions on Medical Imaging* 25.6, pp. 779–791.
- STUDHOLME, C., D. HILL, and D. HAWKES (1999). “An overlap invariant entropy measure of 3D medical image alignment”. In: *Pattern Recognition* 32.1, pp. 71–86.
- TOBON-GOMEZ, C., A. GEERS, J. PETERS, J. WEESE, K. PINTO, R. KARIM, M. AMMAR, A. DAOUDI, J. MARGETA, Z. SANDOVAL, B. STENDER, Y. ZHENG, M. ZULUAGA, J. BETANCUR, N. AYACHE, M. CHIKH, J. DILLENSEGER, M. KELM, S. OURSELIN, A. SCHLAEFER, T. SCHAEFFTER, R. RAZAVI, and K. RHODE (2015). “Benchmark for algorithms segmenting the left atrium from 3D CT and MRI datasets”. In: *IEEE Transactions on Medical Imaging* PP.99, pp. 1–1.
- TOBON-GOMEZ, C., J. PETERS, J. WEESE, K. PINTO, R. KARIM, T. SCHAEFFTER, R. RAZAVI, and K. S. RHODE (2013). “Left Atrial Segmentation Challenge: a unified benchmarking framework.” In: *Statistical Atlases and Computational Models of the Heart. Imaging and Modelling Challenges*. Ed. by O. CAMARA, T. MANSI, M. POP, K. S. RHODE, M. SERMESANT, and A. A. YOUNG. Vol. 8330. Lecture Notes in Computer Science. Nagoya: Springer, pp. 1–13.

- WARFIELD, S., K. ZOU, and W. WELLS (2004). “Simultaneous truth and performance level estimation (STAPLE): an algorithm for the validation of image segmentation”. In: *IEEE Transactions on Medical Imaging* 23.7, pp. 903–921.
- WOODS, R. P., J. C. MAZZIOTTA, and S. R. CHERRY (1993). “MRI - PET registration with automated algorithm”. In: *Journal of Computer Assisted Tomography* 17.4, pp. 536–546.
- YIN, X., L. EPSTEIN, and K. HYNYNEN (2006). “Noninvasive transesophageal cardiac thermal ablation using a 2-D focused, ultrasound phased array: a simulation study”. In: *IEEE Transactions on Ultrasonics, Ferroelectrics, and Frequency Control* 53.6, pp. 1138–1149.
- YUSHKEVICH, P. A., J. PIVEN, H. CODY HAZLETT, R. GIMPEL SMITH, S. HO, J. C. GEE, and G. GERIG (2006). “User-guided 3D active contour segmentation of anatomical structures: significantly improved efficiency and reliability”. In: *Neuroimage* 31.3, pp. 1116–1128.
- ZONI-BERISSO, M., F. LERCARI, T. CARAZZA, and S. DOMENICUCCI (2014). “Epidemiology of atrial fibrillation: European perspective.” eng. In: *Clin Epidemiol* 6, pp. 213–220.
- ZULUAGA, M. A., M. J. CARDOSO, M. MODAT, and S. OURSELIN (2013). “Multi-atlas propagation whole heart segmentation from MRI and CTA using a local normalised correlation coefficient criterion”. In: *Functional Imaging and Modeling of the Heart, Proceedings of the 7th International Conference on. FIMH’13*. London, UK: Springer-Verlag, pp. 174–181.

## Références des papiers liés aux travaux de Thèse

### Articles publiés dans des journeaux

SANDOVAL, Z. and J.-L. DILLENSEGER (2013a). “Intensity-based similarity measures evaluation for CT to ultrasound 2D registration”. In: *IRBM* 34.4–5, pp. 278–282.

TOBON-GOMEZ, C., A. GEERS, J. PETERS, J. WEESE, K. PINTO, R. KARIM, M. AMMAR, A. DAOUDI, J. MARGETA, Z. SANDOVAL, B. STENDER, Y. ZHENG, M. ZULUAGA, J. BETANCUR, N. AYACHE, M. CHIKH, J. DILLENSEGER, M. KELM, S. OURSELIN, A. SCHLAEFER, T. SCHAEFFTER, R. RAZAVI, and K. RHODE (2015). “Benchmark for algorithms segmenting the left atrium from 3D CT and MRI datasets”. In: *IEEE Transactions on Medical Imaging* PP.99, pp. 1–1.

*Explication sur le nombre d’auteurs* : Cet article porte sur un protocole d’évaluation de méthodes de segmentation de l’oreillette gauche. Les 4 premiers auteurs et le dernier ont mis le protocole en œuvre. Les 9 auteurs suivants sont, de *manière égalitaire*, les chercheurs qui ont proposé une méthode originale de segmentation et l’ont testé avec le protocole d’évaluation. Les 10 auteurs restant sont les co-auteurs ou directeurs des auteurs ayant proposé une méthode de segmentation.

### Articles publiés dans des conférences internationales

SANDOVAL, Z. and J.-L. DILLENSEGER (2013b). “Evaluation of computed tomography to ultrasound 2D image registration for atrial fibrillation treatment”. In: *Computing in Cardiology Conference (CinC)*. Zaragossa, pp. 245–248.

SANDOVAL, Z., J. BETANCUR, and J.-L. DILLENSEGER (2014). “Multi-atlas-Based Segmentation of the Left Atrium and Pulmonary Veins”. In: *Statistical Atlases and Computational Models of the Heart. Imaging and Modelling Challenges*. Vol. 8330. Lecture Notes in Computer Science. Nagoya: Springer Berlin Heidelberg, pp. 24–30.

# Contents

<b>Remerciements</b>	<b>i</b>
<b>Résumé étendu de la Thèse en français</b>	<b>iii</b>
<b>Introduction</b>	<b>1</b>
<b>PART I: CONTEXT OF THE PLANING AND GUIDANCE FOR ATRIAL FIBRILLATION HIFU THERAPY</b>	<b>5</b>
<b>1 Medical context</b>	<b>7</b>
1.1 Atrial fibrillation . . . . .	7
1.1.1 Definition . . . . .	7
1.1.2 Epidemiologia . . . . .	11
1.1.3 Electrophysiologic mechanisms . . . . .	12
1.1.3.1 Theory of multiple re-entries . . . . .	12
1.1.3.2 Focus hypothesis . . . . .	13
1.1.3.3 Rotor hypothesis . . . . .	13
1.2 Treatments for atrial fibrillation . . . . .	13
1.2.1 Drugs . . . . .	13
1.2.2 Surgical epicardial ablation . . . . .	15
1.2.3 Surgical endocardial ablation . . . . .	16
1.3 Mini-maze ablation using a transesophageal HIFU probe . . . . .	18
1.3.1 The transesophageal approach . . . . .	19
1.3.2 CardioUSgHIFU project . . . . .	20
1.3.2.1 Treatment procedure . . . . .	20
1.3.2.2 Prototype of a transesophageal HIFU probe integrating TEE imaging . . . . .	21
1.4 Conclusion . . . . .	22
References . . . . .	23
<b>2 Presentation of the proposed framework</b>	<b>29</b>
2.1 Images used in AF therapy . . . . .	31
2.1.1 Cardiac computed tomography (CT) . . . . .	31

2.1.2	Magnetic resonance imaging (MRI) . . . . .	31
2.1.3	Echocardiography (US) . . . . .	33
2.2	Image registration: Background . . . . .	35
2.2.1	Geometrical transform . . . . .	36
2.2.2	Interpolator . . . . .	37
2.2.3	Metric . . . . .	38
2.2.4	Optimizer . . . . .	40
2.3	Intraoperative US image registration: State of the art . . . . .	41
2.4	Left atrium and pulmonary veins segmentation: State of the art . . . . .	45
2.4.1	Data-driven methods . . . . .	45
2.4.2	Model-based methods . . . . .	47
2.4.3	Atlas-based . . . . .	49
2.5	Outlines and justifications of the proposed approaches . . . . .	50
2.5.1	Therapy planning . . . . .	51
2.5.1.1	Segmentation of left atrium and pulmonary veins . . . . .	51
2.5.1.2	Labeling of target lesions on the preoperative volume . . . . .	52
2.5.1.3	Reconstructing a volume following the future navigation of the HIFU probe through the esophagus . . . . .	52
2.5.2	Therapy guidance: Registration of the CT volume and 2D-US images . . . . .	53
2.6	Summary: the contribution of the Thesis . . . . .	56
	References . . . . .	58

## **PART II: THERAPY PLANNING 63**

### **3 Left atrium and pulmonary veins segmentation 65**

3.1	Methods . . . . .	66
3.1.1	Multi-atlas-based segmentation . . . . .	66
3.1.2	Region growing . . . . .	68
3.2	Experiments and results . . . . .	68
3.2.1	Data and ground truth . . . . .	68
3.2.1.1	CT datasets . . . . .	69
3.2.1.2	MRI datasets . . . . .	70
3.2.1.3	Ground truth generation . . . . .	70
3.2.2	Method tuning . . . . .	70
3.2.2.1	Tuning the atlas selection step . . . . .	71
3.2.2.2	Elastic registration . . . . .	73
3.2.2.3	Fusion . . . . .	73
3.2.2.4	Contribution of the region growing . . . . .	74
3.2.2.5	Conclusion on the method tuning . . . . .	76
3.2.3	Evaluation of CT and MRI segmentation: left atrium and pulmonary veins challenge . . . . .	76

3.2.3.1	Evaluation framework . . . . .	77
3.2.3.2	Challenge results . . . . .	78
3.3	Conclusion . . . . .	84
	References . . . . .	84
<b>4</b>	<b>Therapy-adapted preoperative volume reconstruction</b>	<b>87</b>
4.1	Methods . . . . .	88
4.1.1	Semi-automatic esophagus segmentation . . . . .	89
4.1.2	Esophagus centerline curve estimation . . . . .	90
4.1.3	CT slices perpendicular to esophagus centerline . . . . .	91
4.2	Physical phantom experiment . . . . .	95
4.2.1	Image acquisition . . . . .	95
4.2.2	Therapy-adapted preoperative volume reconstruction of the CT phantom	96
4.2.3	Evaluation of the CT reconstruction . . . . .	97
4.2.3.1	Transformation matrix of the CT reconstruction evaluation: $T_{RecEval}$	99
4.2.3.2	Gold standard reference transformation matrix: $T_{Ref}$ . . . . .	100
4.2.4	Results . . . . .	100
4.3	Example of lesion lines definition on 3D model . . . . .	106
4.4	Conclusion . . . . .	107
	References . . . . .	107
	<b>PART III: THERAPY GUIDANCE</b>	<b>109</b>
<b>5</b>	<b>Similarity measures evaluation for CT to US registration</b>	<b>111</b>
5.1	Materials and methods . . . . .	112
5.1.1	Images . . . . .	112
5.1.2	Image simulation parameters . . . . .	112
5.1.3	Registration procedure and similarity measures . . . . .	113
5.1.4	Evaluation protocol . . . . .	114
5.2	Results . . . . .	116
5.3	Conclusion . . . . .	118
	References . . . . .	119
<b>6</b>	<b>3D-CT to 2D-US registration</b>	<b>121</b>
6.1	Global methodology . . . . .	122
6.1.1	Preoperative stage . . . . .	122
6.1.2	Intraoperative stage . . . . .	123
6.2	Experiment: 2D-US to 3D-CT registration of human image datasets . . . . .	125
6.2.1	Data . . . . .	125
6.2.1.1	CT datasets . . . . .	125
6.2.1.2	US datasets . . . . .	125



6.2.2	Results . . . . .	126
6.2.2.1	Preoperative stage . . . . .	126
6.2.2.2	Intraoperative registration . . . . .	129
6.2.3	Evaluation . . . . .	132
6.2.3.1	Transformation matrix of our slice to volume registration approach: $T_{SliceVolRegis}$ . . . . .	132
6.2.3.2	Reference transformation matrix: $T_{Ref}$ . . . . .	133
6.2.3.3	Results of the evaluation . . . . .	134
6.2.4	Conclusion . . . . .	136
	References . . . . .	136
	<b>Conclusion</b>	<b>139</b>
	<b>A List of associated publications</b>	<b>141</b>
	International journals . . . . .	141
	International conferences . . . . .	141
	National conferences . . . . .	141
	<b>List of Figures</b>	<b>143</b>
	<b>List of Tables</b>	<b>149</b>

# Introduction

Atrial fibrillation (AF) is a rapid, irregular and uncoordinated contraction of the cardiac muscle of the atria and is caused by a disturbance of the electrical function of the heart. In normal conditions, the electrical activity triggered at the top of the right atrium propagates throughout the atria to reach the atrio-ventricular node and continues towards the ventricles in a systematic fashion. However, some abnormal electrical activity can be triggered and maintained in the left atrium (LA) during AF. The normal rhythm in the atria can increase from 60 pulsations per minute in normal conditions to 300 pulsations per minute during AF. One of the consequences of these abnormal contractions of the atria is that the blood is not completely squeezed out of the atria, which increases the risk of the formation of blood clots. These blood clots may be pushed from the heart to other areas of the body, resulting in cardioembolic stroke. Atrial fibrillation is also associated with hemorrhagic consequences (due to anticoagulation therapy) and death. Patients with AF have a five-times-higher risk of stroke and two-times-higher risk of death. Heart palpitations, syncope, shortness of breath and/or chest pain are the occasionally-detected symptoms, even if most AF episodes are symptomless.

Atrial fibrillation is the most common cardiac arrhythmia. It is estimated that AF has a prevalence of 2% in Europe (10 millions of patients), with between 100 000 and 200 000 new cases per year being diagnosed (ZONI-BERISSO et al. 2014). Epidemiological studies have shown that AF generally begins in paroxysmal form (i.e. recurrent episodes that stop in less than 7 days), progressing to persistent (i.e. recurrent episodes sustained  $> 7$ days) or permanent (i.e. an ongoing long-term episode) forms. Permanent AF is the most commonly-diagnosed form of AF, occurring in 40% – 50% of patients, followed by paroxysmal and persistent types, which occur in 20% – 30% of cases. Atrial fibrillation is a long and burdensome cardiac pathology covered by different clinical protocols, treatment strategies and outcomes.

The primary means of treating AF is by prescribing medication to prevent thromboembolic risk. However, their efficiency is limited and the risk of secondary effects is high. If medication does not offer a solution, surgical procedures are advised. Ablation procedures have demonstrated to be one of the most effective treatments of AF: they aim to destroy the mechanisms that trigger abnormal electrical charges or to modify the substrate that allows for arrhythmia to be induced or maintained. Two types of ablation procedures are currently used, epicardial and endocardial.

The epicardial approach, proposed by J.L. Cox (COX 2004), consists of dividing the atria into smaller segments according to a precise pattern using multiple incisions. After being stitched up, these incisions are transformed into fibrous scars that act as electrical isolators. Today considered the gold standard for the surgical treatment of AF, the epicardial approach has a 90% success rate. Nevertheless, it is an invasive and complex surgical procedure that requires the patient to be placed under extra-corporal circulation during the intervention; therefore, its practice is rare among surgeons, despite the high success rate (COX 2003). Some modifications have been proposed aiming to simplify this procedure; one of these reduces the number of incisions made to obtain a simplified ablation pattern, known as the “mini-Maze” procedure; another replaces the classical surgical instruments used, performing the incisions using radiofrequency (RF), micro-waves, laser, cryotherapy and High Intensity Focused Ultrasound (HIFU). Despite technological progress, it is still difficult to obtain continuous and transmural ablation lines.

Endocardial ablation using a RF catheter is the most commonly-prescribed procedure. The idea is to electrically isolate the pulmonary veins (PVs) in the left atrium using a circular intracardiac catheter (HAÏSSAGUERRE et al. 2000). The efficiency of catheter ablation is limited, estimated at being little more than 60% for patients with paroxymal AF, decreasing to less than 30% for those with persistent AF. This technique is invasive; some complications with radiofrequency energy delivery have been reported, such as phrenic nerve injury, left atrial-esophageal fistula and the formation of blood clots (FUSTER et al. 2006).

An alternative has been proposed to avoid the problems of epicardial and endocardial approaches: a myocardial ablation using HIFU beamed from the esophagus (CONSTANCIEL et al. 2013; YIN et al. 2006). This is a promising procedure for the minimally-invasive treatment of atria fibrillation. This transesophageal technique allows ablation to be performed using an epicardial approach, without the need for surgery. HIFU technology can be used to create thermal lesions in deep tissues, without damaging intervening tissues. It is a mini-invasive treatment that places the HIFU transducer close to the ablation zone, navigating via the esophagus. The output is controlled from a location near enough to the ablation zone to obtain a satisfactory acoustic window. HIFU waves are delivered from the esophagus to the atrial wall (in the inverse way to the endocavitary approach), minimizing the risk of damage to the esophagus and neighboring organs.

Myocardial ablation using HIFU has been studied as part of the ANR TECSAN CardioUS-gHIFU (ANR-11-TECS-0004) project, which aims to develop novel ultrasound approaches for the minimally-invasive treatment of cardiac arrhythmia. Some interdisciplinary research groups (such as LabTAU<sup>5</sup>, Institut Langevin<sup>6</sup>, LTSI<sup>7</sup>) and a private company (Vermon<sup>8</sup>) are involved in the

---

5. Laboratory of Therapeutic Applications of Ultrasound, <http://labtau.univ-lyon1.fr/>

6. Ondes et images, <http://www.institut-langevin.espci.fr/home?lang=fr>

7. Laboratoire Traitement du Signal et de l'Image, <http://www.ltsi.univ-rennes1.fr/>

8. Piezoelectric Transducers, <http://www.vermon.com/vermon/>

design of probe prototypes and the validation of therapy during ex-vivo/in-vivo experiments. Two approaches are explored: intracardiac and transesophageal.

The work presented in this document is part of the transesophageal approach and was developed in collaboration with the LabTAU team, which developed and reported the design of the first transesophageal probe prototypes and preliminary ex-vivo and in-vivo trials (CONSTANCIEL et al. 2013). The probe in question is a multi-element HIFU therapeutic transducer, which includes in its center a Transesophageal Echocardiograph (TEE) transducer to guide therapy. In fact, other than material aspects, the feasibility of therapy is dependent on the guidance of the HIFU beam on intraoperative images. The research goals presented in this Thesis are, as follows: 1) to process the anatomical information provided by preoperative imaging (MRI or CT) to undertake the planning of the intervention and 2) to process intraoperative ultrasound (US) images to guide therapy according to the planned strategy.

Planning aims to use the high resolution information obtained from CT or MRI to extract patient-specific anatomical details and to define future therapeutic procedures. More specifically, image-processing tools have to recover patient-specific morphology concerning the left atrium and pulmonary veins. All of this will aid the practitioner in defining the future lesion lines on the left atrium and in verifying the feasibility of the planned therapy.

During therapy, the practitioner will use the 2D-US images, acquired by the transducer inserted in the center of the therapy probe for the optimal positioning of the HIFU transducer along the esophagus, in the localization of the atrial wall zone to be treated, and to verify the absence of obstacles in the firing line. Intraoperative ultrasound imaging has lot of advantages, being non-ionizing, portable, low cost and quick enough to capture tissue deformation. However, the information contained in the image is relatively low and its field of view is relatively limited (to the 2D sector) and user-dependent. The registration of preoperative high-resolution information with intraoperative US is a key factor in image-guided interventions. Moreover, it allows the transfer of planning information provided by the clinician to the US-guided intervention and so reduces user-dependency on the interpretation of intraoperative US images.

This Thesis will provide various solutions concerning the planning and guidance of transesophageal HIFU atrial fibrillation therapy. In order to describe our contributions, we have divided the Thesis into three main parts, as follows:

Part I gives the context of the study and justifies the approaches proposed in the Thesis. The first chapter gives the medical application background of the Thesis, based on atrial fibrillation and its treatment. Chapter 2 is focused on our specific problem, first describing the properties of images used for planning and therapy guidance. After describing the state-of-the-art methods used in cardiac segmentation and registration, we will justify the choice of methods proposed

used for preoperative segmentation and intraoperative registration.

Part II presents our contributions for preoperative planning. Chapter 3 discusses a method of segmentation of the left atria and the pulmonary veins, which is based on multi-atlas segmentation followed by a region-growing refinement. This approach has been performed on a multicenter evaluation scheme, which also compared our method with other approaches recently proposed in the literature. The segmented data can now be used to define future lesion lines. In order to prepare for therapy, Chapter 4 deals with a new way of reconstructing preoperative data to adapt it to future therapy, and which can be used to explore data in the same order as future transesophageal imaging.

Part III is mostly devoted to the registration of 2D preoperative ultrasound images and preoperative high-resolution anatomical CT volume. Chapter 5 gives a systematic statistical evaluation of the similarity measures that can be used for our specific US/CT registration problem. This evaluation will take part in the final 2D-US to 3D-CT registration framework, described in Chapter 6. The relevance of this framework will be proved by a quantitative evaluation on one clinical dataset.

Finally, Chapter 7 concludes the work and contributions of this Thesis, and discusses possible future works.

**PART I: CONTEXT OF THE  
PLANING AND GUIDANCE FOR  
ATRIAL FIBRILLATION HIFU  
THERAPY**





# Medical context

## 1.1 Atrial fibrillation

### 1.1.1 Definition

Myocardial cells, known as cardiomyocytes, are specialized cells able to conduct electrical impulses and to shorten and lengthen their fibres in order to perform mechanical contraction (GAZTANAGA et al. 2012). These cells have a membrane made up of different ionic channels and intra-cellular gap junctions that allow ionic exchanges. The electric stimulation of a cell increases permeability of its membrane, resulting in series of ionic changes, mainly involving sodium ( $Na^+$ ), calcium ( $Ca^{2+}$ ) and potassium ( $K^+$ ) ions. The flow of ions through the membrane, which modifies the voltage on both sides of it, is known as membrane potential. Cardiomyocytes contraction and relaxation is a cyclic process controlled by the variation of the membrane potential. The time evolution of the membrane potential permit stand out some characteristic phases. Membrane potential behavior during a cycle (action potential) is presented in Figure 1.1.

**Rapid depolarization** When relaxed, the membrane potential is about -90mV. The entry of positive ions causes the voltage to increase until a threshold is reached which causes the beginning of an action potential. Many ionic channels become suddenly activated resulting in the rapid inversion of polarization. This sudden change is known as depolarization or Phase 0.

**Beginning of repolarization** Phase 1 is characterized by a fast and acute movement to a transitory equilibrium value.

**Plateau** Both input and output currents of positive charges maintain an equilibrium during Phase 2, as the membrane potential value does not change significantly. The myocyte contraction starts at the end of this phase,

**Rapid repolarization** Phase 3 is characterized by a rapid decrease in cardiomyocyte voltage, due to positive output channels being activated.



**Final repolarization** During Phase 4 some positive ionic output channels are closed. The repolarization finishes when the voltage reaches the initial value.

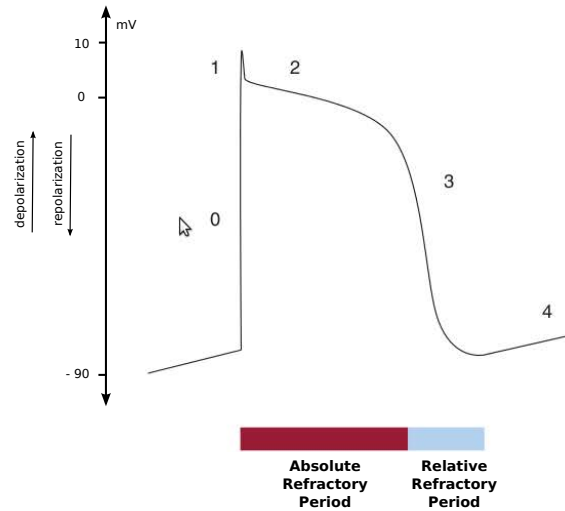


Figure 1.1: Membrane potential over time for a cardiomyocyte. The phases of a complete cycle and the refractory and absolute periods are shown (GAZTANAGA et al. 2012).

After contraction, myocytes must relax in order to contract again, enabling them to repeat this cyclic process. There is a time interval between depolarization and when the cell cannot be stimulated again. This period is known as the refractory period. This period is called absolute when the cell cannot be stimulated, no matter the intensity, and relative when the cell can be stimulated if a greater-than-normal stimulation is applied. Figure 1.1 illustrates the refractory period following depolarization and indicates the absolute and relative intervals.

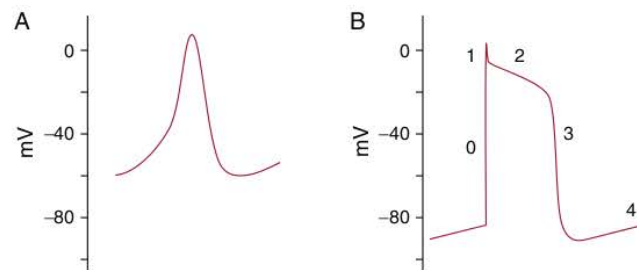


Figure 1.2: Action potential for a cell in the sinus node (A) and a muscle cell (B) (GAZTANAGA et al. 2012).

The characteristic behavior of the membrane potential changes, with regards to the region of the heart. For instance, Figure 1.2 illustrates the membrane potential for a cell in the sinus node and for cells in another region of the heart. Some myocytes that behave automatically (automatism), i.e. they do not need an external stimulation to depolarize. These myocytes behave

like a pacemaker. This is the case for the myocytes in the sino-atrial node, the atrio-ventricular node, the His-Purkinje system and for some cells in the atria (MANGONI et al. 2008). The suppression or stimulation of the automatism can result in clinical arrhythmias.

Under normal conditions, the electrical activity causing the contraction of a healthy heart is triggered at the sino-atrial node (also known as the sinus node) located at the top of the right atrium. This activity propagates throughout the atria to reach the atrio-ventricular node, where it concentrates. The impulse is then sent towards both ventricles. From the atrio-ventricular node, it flows through the Bundle of His. This bundle extends into the interventricular septum and then divides into two branches, each going towards one of the ventricles. The electrical activity follows these branches before finally reaching the Purkinje fibres and propagating towards the ventricle walls. Figure 1.3 illustrates the electrical conduction system of the heart.

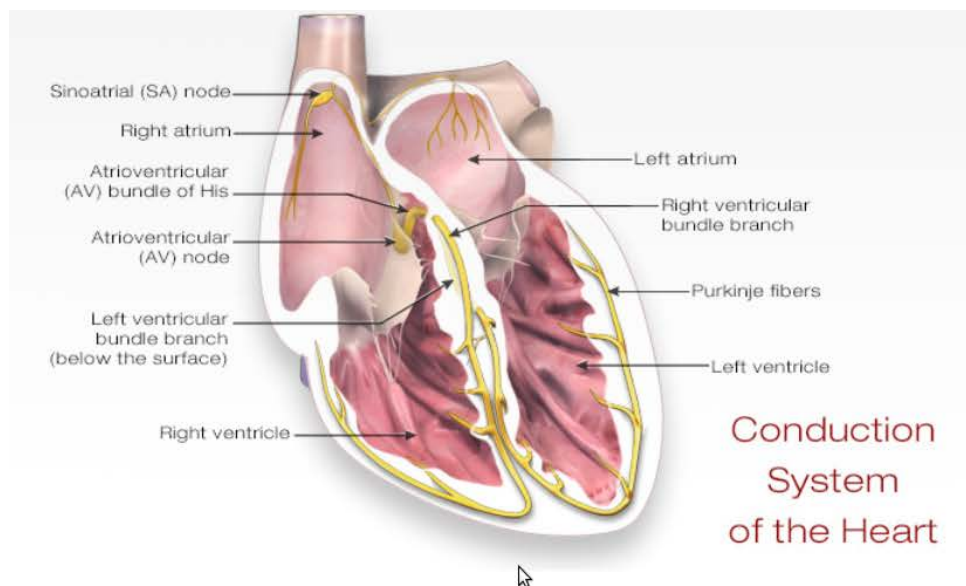


Figure 1.3: The electrical function of a healthy heart, showing the electrical conduction system from the sinus node in the right atrium to the ramifications of the Purkinje fibers in both ventricles.

The arrival of an electrical impulse causes the depolarization and, consequently, the contraction of myocytes from the superior part of the heart (where it generates) to the ventricles, completing a cardiac cycle. After depolarization, cells enter into a refractory state and cannot be reactivated; thus, the electrical impulse vanishes. However, if a group of cells has not been activated during the initial triggering, it can be activated at any time because they are not in a refractory state. The activation of these cells and posterior propagation of their electrical stimuli could activate the other cells that have recovered from the initial repolarization. This phenomenon is known as *re-entry*. The *re-entry* could be anatomic or functional. Figure 1.4 illustrates an anatomic *re-entry*. It is made up of an anatomic obstacle that cannot be stimulated

in only one direction and which is surrounded by a circular path that allows the impulse to re-enter. When the electrical impulse reaches the obstacle, it flows through another path and then propagates through the circular path until once again reaching the blocking point (obstacle), which allows the impulse to flow in a new direction, enabling for re-entry. The anatomical obstacles establish the boundaries of the re-entry circuit in an anatomical re-entry, whereas in a functional re-entry, the circuit is not defined by anatomical obstacles, but by the dynamic heterogeneity of the electro-physiologic properties of tissues involved (GRANT et al. 2007).

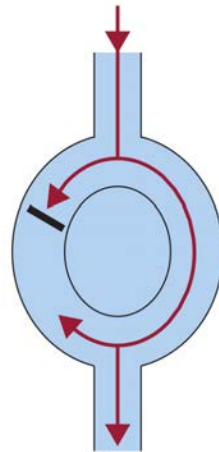


Figure 1.4: Re-entry loop caused by an anatomical blocking of electrical conduction in one direction (GAZTANAGA et al. 2012).

AF requires both a trigger for its initiation and an appropriate anatomic substrate for its maintenance. Although the mechanism triggering AF is still under discussion amongst electro-physiologists, it is characterized by multiple re-entry loops within the atria. This causes the disorganized contraction of the atria, going from 60 pulsations per minute (normal) to about 300 pulsations per minute during AF. Ventricles also contract faster during AF because the electrical stimuli propagate from the atria towards both ventricles, increasing from 60 pulsations per minute (normal) to 150 pulsations per minute. Even if the cardiac rhythm increases in the ventricles during AF, it is not as high as in the atria because the electrical stimuli are concentrated in the atrio-ventricular node before being conducted toward both ventricles. Indeed, the atrioventricular node itself behaves as a fibrillation filter.

AF can cause other health threats including stroke, heart failure, chronic fatigue, additional heart rhythm problems and inconsistent blood supply. It has been reported that AF multiplies the risk of stroke by five (WOLF et al. 1991). This is because the rapid and/or irregular contraction of the atria muscle causes the blood not to be completely squeezed to the other cavities, resulting in the accumulation of remaining blood in various regions of the cavities. Such blood accumulation favors the formation of blood clots that may be pushed from the heart to other areas of the body, e.g. towards the brain, blocking blood flow in the brain arteries, resulting in an embolism or

cardioembolic stroke.

Table 1.1 classifies atrial fibrillation in terms of the duration of episodes. This scheme has been revised and simplified in the 2014 AHA/ACC/HRS Guideline for the Management of Patients with Atrial Fibrillation (JANUARY et al. 2014).

Table 1.1: Classification of atrial fibrillation in terms of the duration of the episodes according to the 2014 AHA/ACC/HRS Guideline for the Management of Patients with Atrial Fibrillation (JANUARY et al. 2014).

	Time
Paroxysmal AF	* AF that terminates spontaneously or with intervention within 7 days of start. * Episodes may recur with variable frequency.
Persistent AF	* Continuous AF that is sustained > 7 days.
Longstanding persistent AF	* Continuous AF of > 12 months duration.
Permanent AF	* The term Permanent AF describes when there has been a joint decision by the patient and the clinician to cease further attempts to restore and/or maintain sinus rhythm. * Accepting AF represents a therapeutic attitude on the part of the patient and clinician rather than an inherent pathophysiological attribute of the AF. * Accepting AF may change as symptoms, the efficacy of therapeutic interventions and patient and clinician preferences evolve.
Nonvalvular AF	* AF in the absence of rheumatic mitral stenosis, a mechanical or bioprosthetic heart valve, or mitral valve repair.

### 1.1.2 Epidemiologia

The prevalence of AF in the USA has been estimated at between 2.7 and 6.1 million people in 2010, and will be between 5.6 and 12 million in 2050 (GO et al. 2014). In the European community, it is estimated that AF has a prevalence of 2% of the population (10 millions of patients) (ZONI-BERISSO et al. 2014).

AF is the most common arrhythmia, causing one third of the hospitalizations for cardiac rhythm disturbances. In fact, these hospitalizations have increased by 66% in the last 20 years. AF is an extremely expensive public health problem costing approximately 3000 EUR annually per patient; the total cost burden approaches 13.5 billion EUR annually in the European Union (FUSTER et al. 2006).

Clinical risk factors for AF include advancing age, diabetes, hypertension, congestive heart failure, rheumatic and nonrheumatic valve disease and myocardial infarction (BENJAMIN et al. 1998).

AF is an independent risk factor for stroke, resulting in an approximate 3- to 5-times excess risk. The risks for stroke associated with AF dramatically increase with age, from 1.5% for those aged from 50 to 59 years to 23.5% for those aged from 80 to 89 years (WOLF et al. 1991).

### 1.1.3 Electrophysiologic mechanisms

The underlying mechanism of AF still continues to be controversial inside the electrophysiologist community. However, it is probably the result of a complex interaction between stimuli causing its apparition and an anatomical substrate which is needed for its maintenance.

In general, three theories are proposed to explain the perpetuation and maintenance of AF, including: (1) multiple independent re-entrant wavelets associated with heterogeneous conduction and refractoriness; (2) more than one rapidly-firing foci, which may be responsive to activities from the cardiac ganglion plexi; and (3) more than one rotor, or spiral wave re-entrant circuits (JANUARY et al. 2014).

#### 1.1.3.1 Theory of multiple re-entries

AF consists of multiple wavelets of functional re-entry that move along the stimulated atrial tissue i.e. they are able to be depolarized when the activation front reaches them (MOE et al. 1959). The theory of multiple re-entries is presented in Figure 1.5, showing re-entries being located throughout the atrial wall.

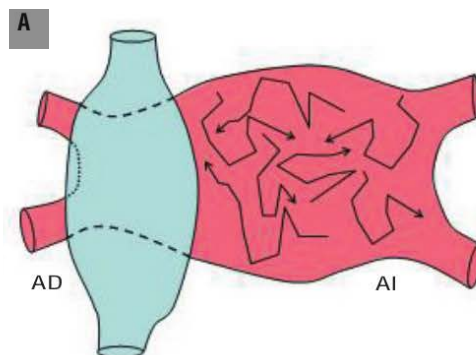


Figure 1.5: Atrial fibrillation is a consequence of wave fronts being propagated in the stimulated atrial tissue (FERNÁNDEZ 2006).

### 1.1.3.2 Focus hypothesis

Extrasystoles and fast atrial rhythms originating in the pulmonary veins could trigger AF. This fibrillation would be maintained by the continuous discharge of a high frequency focus originating in the pulmonary veins. In such a scenario, the generated wave fronts would divide causing the disorganization in the tissue and the fibrillatory conduction (FERNÁNDEZ 2006) (HAÏSSAGUERRE et al. 1998). The focus theory is presented in Figure 1.6. The focus, located in the pulmonary veins, is not only the origin of an episode of AF but also is the mechanism to maintain it.

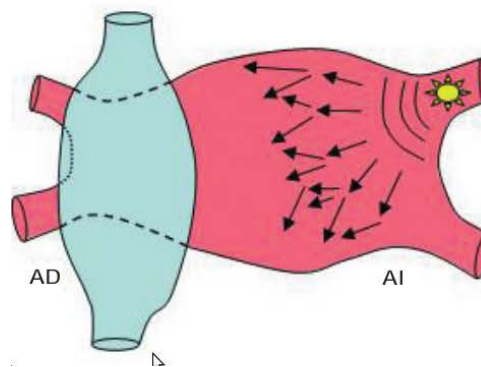


Figure 1.6: Atrial fibrillation is caused and maintained by a focus located in the pulmonary veins (FERNÁNDEZ 2006).

### 1.1.3.3 Rotor hypothesis

AF is triggered by a sequence of ectopic beats originating in the pulmonary veins. The generated wavefronts will fragment when arriving at the curvature of the veno-auricular union, causing two vortices that rotate in opposite directions. Finally, one of these vortex will stabilize in the posterior wall causing the formation of a functional re-entry or rotor. This rotor acts as a preservation mechanism, activating local tissues at a highly regular high frequency and generating new wavefronts that can fragment and propagate at highly recurrent directions (JALIFE 2003). Figure 1.7 demonstrates the rotor hypothesis. Extrasystoles generated in the pulmonary veins trigger the AF episodes and the rotor is the mechanism that maintains it.

## 1.2 Treatments for atrial fibrillation

### 1.2.1 Drugs

According to the consensual recommendations of the American College of Cardiology, the American Heart Association and the European Society of Cardiology, pharmacological options should be accounted for primary intention treatment (FUSTER et al. 2006). Four strategies may

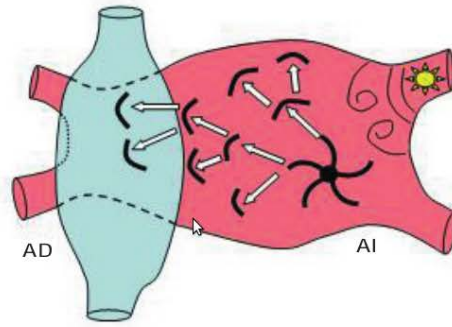


Figure 1.7: Atrial fibrillation is caused by extrasystoles generated in the pulmonary veins, but it is maintained by a rotor generated in the body of the atrium (FERNÁNDEZ 2006).

be considered for treating of AF. They will be described in the following paragraph.

The first strategy focuses on thromboembolic risk prevention. A preventive treatment against the formation of clots (thrombus) in the left atrium can be done if there are risk factors of embolic complications (age, gender, prior occurrence of cerebrovascular accidents, arterial hypertension, diabetes, etc.) evidencing an atrial myopathy. Former generation (AVK) and newer generation (dabigatran, rivaroxaban) of anticoagulants can be used in this scenario.

The second strategy aims at slowing down the cardiac rhythm. If the ventricular frequency is very high, indicating that the atrio-ventricular node is permeable to important fibrillatory activities in the atria, then the clinical tolerance is bad. Palpitations and breathless feeling are among patient symptoms. In this case, the pace of atrio-ventricular conduction channel is needed to be slowed down and beta blockers, calcium channel inhibitors and even digitaline can be used.

The third strategy consists in using cardioversion in order to return the patient to its sinus rhythm. This is needed as soon as AF becomes paroxymal or persistent in order to limit the electrophysiological and mechanical remodelling of the atria. Cardioversion can be obtained using a high dose of anti-arrhythmic pharmacological agents (amiodarone, flecaine, lidocaine) or by administering an external electrical shock (defibrillation). This shock, synchronized with the QRS complex, simultaneously depolarizes myocardial cells and extends their refractory period, enabling the sinus node to take back control of the cardiac rhythm. Both pharmacological and electrical, cardioversion expose the patient to a migration of clots due to the mechanical action and the sinus rhythm restoration. An echocardiographic control of the absence of thrombus in the left atrium must be performed 48 hours after every AF episode, in the absence of effective anticoagulation during the previous 3 months.

The last strategy consists of administering a recurrent preventive dose of an anti-arrhythmic treatment. Once the patient has an effective sinus rhythm the recurring AF episodes must be prevented. Pharmacological agents such as sotalol, amiodarone and dronedarone can be

administered over the long term. These agents can lead to serious secondary effects such as spikes twisting caused by sotalol, thyroidal dysfunction caused by amiodarone or hepatocellular insufficiency caused by dronedarone. Intolerance to these antiarrhythmic agents or their lack of efficiency can lead the clinician to consider a radical treatment for AF: ablation, including epicardial ablation and endocavitary ablation.

### 1.2.2 Surgical epicardial ablation

The epicardial approach was the first used to treat those AF patients not responding to pharmacological treatments. The Maze procedure, as proposed by J.L. Cox in 1987, was the first surgical procedure used to successfully treat AF. It has been evolved into the Maze III procedure, considered today as the Gold Standard for the surgical treatment of AF, with 90% effectiveness. The procedure consists of dividing the atria into smaller segments using multiple incisions (COX 2004). After being stitched up, these incisions will be transformed into fibrous scar that act as electrical isolators. Performed as part of the Maze III scheme (Figure 1.8), they block re-entry circuits and guide the electrical impulses towards the atrio-ventricular node. This procedure is particularly efficient in treating persistent or permanent AF because it aims at modifying the arrhythmogenic substrate in addition to isolating the foci located in the pulmonary veins. Nevertheless, this is a risky and complex procedure that requires the patient to be placed under extra-corporal circulation during the intervention, therefore, its practice is rare among surgeons, despite its high success rate (COX 2003).

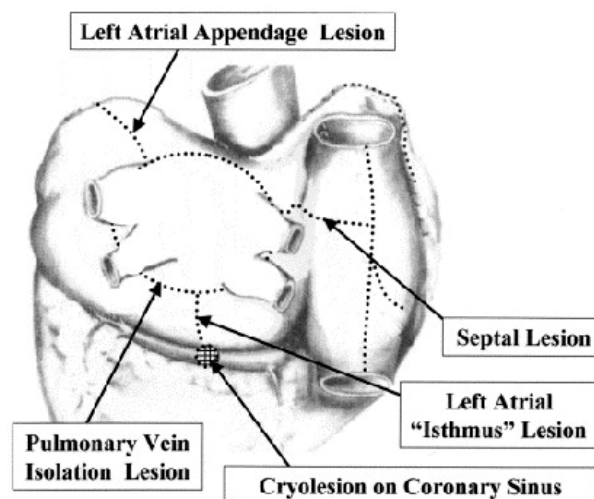


Figure 1.8: Five left atrial lesions as per maze III standard, surgical procedure for atrial fibrillation (Cox 2003).

Some modifications have been proposed, aiming at simplifying this procedure. Based on his experience in 2003, J.L. Cox eliminated some incisions of the Maze III procedure and proposed



the "mini-Maze" procedure (Figure 1.9). It consists of encircling the pulmonary veins ("Box lesion"), before making a second lesion linking the inferior pulmonary veins to the mitral annulus (left atrial isthmus), a third lesion in the coronary sinus and a fourth lesion between the coronary sinus and the tricuspid valve (right atrial isthmus lesion) in order to eliminate the risk of atrial flutter.

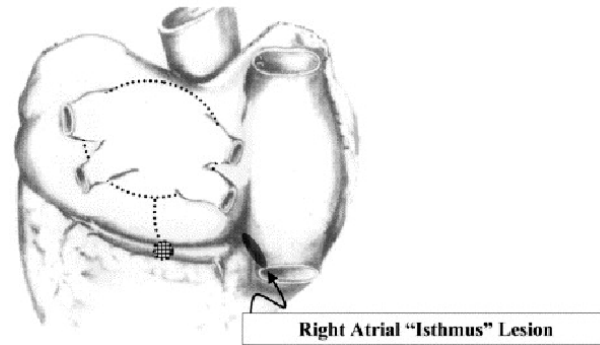


Figure 1.9: The mini-maze procedure for atrial fibrillation (COX 2003).

Another way of simplifying the procedure consists of performing the ablation using other physical techniques such as radiofrequency (RF), micro-waves, LASER, cryotherapy or high-intensity focused ultrasounds (HIFU). The device used for the ablation is set on the epicardium to cause myocardial tissue necrosis along its thickness. The existing technologies can be classified into two categories: those using unipolar sources, i.e. generating energy from one source (unipolar RF, microwaves, laser, HIFU, cryotherapy), and those using bipolar devices. Unipolar RF energy cannot reliably create transmural ablation on the beating heart (PRASAD et al. 2002). The cooling effect of the intracavitary blood flow is often the origin of a non-transmural lesions. The HIFU Epicor Cardiac Ablation System (St. Jude Medical, Maple Grove, MN) stands out from other unipolar devices because of its ability to focus the energy to three different levels of the tissue depth. Thus, the treatment efficiency has a very low dependence on thermal conduction. The limitation of unipolar RF has been overcome by using bipolar RF devices, which have two arms equipped by an electrode. The energy produced is confined between these two arms and then concentrated. Lesion transmuralitity can be also controlled by measuring the conductivity of tissue (PRASAD et al. 2002).

### 1.2.3 Surgical endocardial ablation

Many teams around the world tried to partially reproduce the Maze procedure in the 90s by carry out an endocavitary ablation using RF catheters (CALKINS et al. 1999; JAÏS et al. 1998; KOCHERIL et al. 2005; NATALE et al. 2000). These approaches are used to made ablation lines on the right and left atria. However, the efficiency was restricted by technological limitations, resulting in discontinuous ablation lines and non-transmuralitity at some segments and causing

the recurrence of AF episodes or the apparition of left atrial flutters.

The turning point in treating AF came about in the late 1990s (HAÏSSAGUERRE et al. 1998). This work proved the presence of AF ectopic foci located around pulmonary veins (PV) and that destroying these foci can help patients with paroximal AF. These findings generated great enthusiasm in the healthcare area both for clinicians and industries. According to Haissaguerre's team recommendations, a first step catheter ablation should be used to find and treat PV foci individually. However, there can be many foci and they can be randomly triggered. Haissaguerre thus proposed, in a second step, to electrically isolate PVs in left atrium (LA) using PV segmental ablation (HAÏSSAGUERRE et al. 2000). In this context, they used a 10-electrodes circular mapping catheter (Lasso, Biosense Webster, Diamond Bar, CA, USA). This catheter is inserted into the PV to record the vein voltage at depth of one centimetre. A second RF catheter is inserted into the PV, close to the PV ostium. The zone with the earliest voltage delays corresponding to the PV–LA electric connection zone is the best localization to ablate. Simultaneously, Pappone proposed an electro–mechanical approach for AF treatment (PAPPONE et al. 2000). An electro-anatomical mapping system (CARTO, Biosense Webster, Diamond Bar, CA, USA) was used to obtain a 3D map of the left atrium to locate the PV ostia and to perform a circumferential ablation on them.

Despite technological progress, it is still difficult to obtain continuous and transmural ablation lines. In fact, the efficiency of catheter ablation has been estimated to be more than 60% for patients with paroxymal AF, decreasing to less than 30% for those with persistent AF. For patients with multiple procedures, these rates increase to more than 70% and more than 50%, respectively. However, it has to be noted that these ablation outcome rates were calculated only after one or two years of procedures follow up (CALKINS et al. 2007). Some long term studies, however, have been reported. A five-year study by Haissaguerre's team reported that the success rate in the case of one to three procedures was  $87.7 \pm 3.5\%$  after one year, decreasing to  $62.9 \pm 5.4\%$  after five years (WEERASOORIYA et al. 2011). Bertaglia et al. reported a success rate of 78% after one year for one procedure, decreasing to 45% after four years (BERTAGLIA et al. 2010).

In 2004 Nademanee et al. proposed a treatment adapted to patient-dependent conditions such as the anatomy and the electrophysiology (NADEMANEE et al. 2004). The presence of fragmented atrial potentials (CFAE, Complex Fractionnated Atrial Electrogram) in candidate re-entry zones is described in (KONINGS et al. 1997). In this context, Nademanee proposes to do a mapping of these CFAE to be then treated by RF using a CARTO system. Instead of making a barrier, he proposed to focus on the substrate modification in those zones with electric conduction anomalies. For a population with as many subjects with paroxymal AF as with persistent AF, a success rate of 76% was reported after one year, with one intervention only. However, the efficiency of CFAE ablation in patients with persistent AF was not elucidated by Oral et al. (ORAL et al. 2007). Moreover, Narayan et al. (NARAYAN et al. 2013) proved that the localization of rotors or

source foci do not necessarily correspond to CFAEs position.

Different approaches have been explored to treat AF using catheters. At the same time, catheters themselves have evolved. Today, RF catheters are mainly used. The principle of ablation using a RF catheter is to let electrical current flow from the catheter's tip towards a cutaneous electrode (AHMED et al. 2009; CESARIO et al. 2007). The fact that the tip is smaller than the electrode causes the tip to warm up causing a thermal lesion in contacted tissue when the heat reaches 50°C. Other types of energy are under evaluation.

Cryoablation is the most developed alternative. The principle of this technique is to inject liquid nitrous oxide into the catheter. Cooling tissue below -40°C makes cells freeze, with the apparition of ice in intra-and-extra cellular medium. A sequence of cell freezing/defrosting causes apoptosis and cellular necrosis (MANSOUR et al. 2010).

HIFU catheters have also been developed for pulmonary vein isolation. Here, Ultrasound beams are focused on the target tissue, and due to the significant energy deposit at the focus, the temperature within the tissue can rise to values between 65 °C to 85 °C, destroying tissues by coagulation necrosis.

Steerable HIFU balloon catheters performs circumferential lesions around pulmonary veins (SCHMIDT et al. 2007). After the first clinical trials, the success rate in patients with paroxysmal AF was similar to those obtained using RF ablation. Nevertheless, the complication rate was greater (NEVEN et al. 2012). Among these complications, we can mention esophageal lesions (one causing a mortal atrio-esophageal fistula) and persistent paralysis of the phrenic nerves. These complications caused clinical trials to be stopped.

A transesophageal approach using HIFU energy is also studied in order to reduce the side effects associated with all of these invasive techniques. This approach will be explained in more detail in the next section, 1.3.

### 1.3 Mini-maze ablation using a transesophageal HIFU probe

HIFU energy can be used to create thermal lesions in deep tissue without damaging intervening tissues. The use of HIFU for the treatment of cardiac arrhythmia has been studied since the mid 1990s. Different approaches have been proposed: extracorporeal, extracardiac, intracardiac and transesophageal.

The extracorporeal and extracardiac approaches of (KLUIWSTRA et al. 1995) and (STRICKBERGER et al. 1999), respectively, proved that the therapy is made difficult by the limited acoustic

window due to the presence of ribs and lungs.

In contrast, intracardiac approaches place the HIFU transducer in the cavities of the heart, close to ablation zone, thus improving the acoustic window (CARIAS et al. 2014; GENTRY et al. 2004; SINELNIKOV et al. 2009; ZIMMER et al. 1995). However, the risk of damage for organs and tissues close to the ablation zone is quite high (NEVEN et al. 2012).

Another approach, called the Epicor Cardiac Ablation System, is an epicardial treatment using a probe designed to make ablation lines without needing to be repositioned (NINET et al. 2005). Nevertheless, it is a complex and invasive technique, requiring epicardial surgery.

In contrast, the transesophageal technique as proposed by Yin et al. allows the ablation to be carried out using an epicardial approach without the needing for surgery (YIN et al. 2006). It is a mini-invasive treatment that places the HIFU transducer close to the ablation zone by navigating inside the esophagus. The energy is thus controlled from a location close enough to the ablation zone to obtain a satisfactory acoustic window.

### 1.3.1 The transesophageal approach

The transesophageal technique consists of generating mini-maze incisions using a HIFU transducer placed in the esophagus. The transducer is set on a transesophageal probe that navigates inside the esophagus in order to reach the region that lies just below the posterior wall of the left atrium. The therapy is then generated and controlled from this location. The probe navigation and transducer positioning is carry out using TEE images (Figure 1.10<sup>1</sup>).

The transesophageal technique is advantageous because:

- The esophageal approach results in a good cardiac acoustic window, particularly for the left atrium, which is the ablation zone in the mini-maze therapy.
- It is less invasive than the intracardiac approach.
- TEE probes are routinely used in cardiac interventions.
- An epicardial-like therapy is obtained.
- The blood flow helps to cool the cardiac cavities. In contrast, intracardiac approaches cannot exploit this advantage and the adjacent organs can be damaged.

---

1. <http://www.caehealthcare.com/eng/courseware/iccu-e-learning-solution-for-ultrasound>

- A cooling balloon can be added at the head of the HIFU probe, which cools both transducer and the surrounding tissue, thus avoiding the risk of thermal lesions of the esophagus.

### 1.3.2 CardioUSgHIFU project

The work presented in this document has been developed as part of the ANR TecSan CardioUSgHIFU (ANR-11-TECS-0004) project, as previously mentioned. This project aimed at proposing the instrumentation and carrying out preliminary animal validation of two HIFU-based ablation approaches for the treatment of AF.

In the first approach, a HIFU transducer is miniaturized, enabling an endocardial approach, and also monitoring the therapy using a novel ultrasound technique of shear wave elastography.

The second approach is more prospective. The idea is to perform ablation using a transesophageal approach with the prototype developed at LabTau in Lyon (see Section 1.3). The work presented in this document is part of this approach and was developed in collaboration with the LabTau team.

#### 1.3.2.1 Treatment procedure

The mini-maze procedure seems to be considered using a transesophageal technique because most of the lesions are located on the left atrium. Moreover, different types of AF can be treated by isolating the pulmonary veins (paroxysmic AF) and modifying the arrhythmogenic substrate (persistent AF and permanent AF).

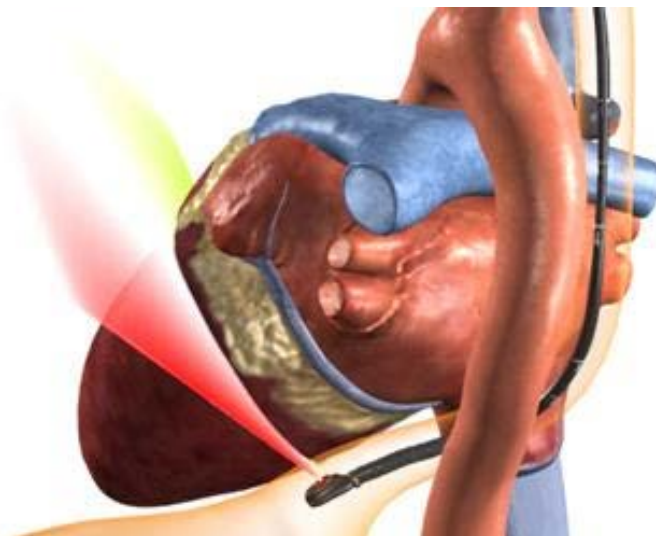


Figure 1.10: Transesophageal approach for atrial fibrillation treatment.

The device used to perform this procedure needs to be able to treat left atrial zones near to the oesophagus (posterior wall) as well as the zones reachable from the oesophagus by crossing the cavity.

However such a therapy need an image guidance. Ultrasound images can be used to guide the TEE probe. The ultrasound images acquired from a TEE probe enables the heart to be viewed from the posterior zone, particularly the region of interest in AF ablation. This allows to asses in real time the deformation of cardiac tissues as caused by the cardiac cycle itself or induced by breathing. In addition, ultrasound imaging can be used to verify the presence of blood clots that may appear after cardiac procedures, including ablation. The abilities of US images to guide HIFU treatments have been proven in (PARMENTIER et al. 2009; PICHARDO et al. 2008; WU et al. 2001). For instance, Ultrasound images can be used to assess the propagation area of HIFU waves in the plane of the image in order to locate the possible obstacles. Unfortunately, it is not easy to identify the HIFU cardiac tissue lesions on a B-Mode ultrasound image. An alternative could be ultrasound elastography to detect the changes in tissue elasticity induced by the HIFU lesion. This would enable real time control of the HIFU lesions in the left atrial wall, as well as in adjacent structures.

### 1.3.2.2 Prototype of a transesophageal HIFU probe integrating TEE imaging

Constancier et al. proposed the design of a transesophageal probe that integrates both therapy and imaging functions for AF treatment using the mini-maze procedure (CONSTANCIEL et al. 2013). The geometrical specifications of the probe and the evaluation of its viability to perform the mini-maze HIFU procedure were made using digital simulations. The first prototype of the transducer was a spherical truncated shape cut into several isosurface concentric rings, as shown in Figure 1.11. This probe was used to perform cardiac ablation from the oesophagus in an ex-vivo pig.

The geometrical specifications of the probe were obtained using an anatomical model of reference from the Visible Human Project dataset (VHP, National Library of Medicine, Bethesda, MD<sup>2</sup>).

The probes use a transducer that can be moved, which enables the focus of the ultrasound beam to be changed and for different depths to be reached. The transducer diameter, curvature radius, frequency and number of rings are defined using an acoustic pressure field model based on the integral method of Rayleigh. The HIFU transducer operates on a frequency of 3MHz which proved to reach the desired depth: the closer and farthest points required by the therapy from the oesophagus are reached using this frequency (Figure 1.12). Finally, a hole with a diameter of 12mm in the middle of the HIFU transducer enables the TEE imaging transducer to be placed.

---

2. [http://www.nlm.nih.gov/research/visible/visible\\_gallery.html](http://www.nlm.nih.gov/research/visible/visible_gallery.html)

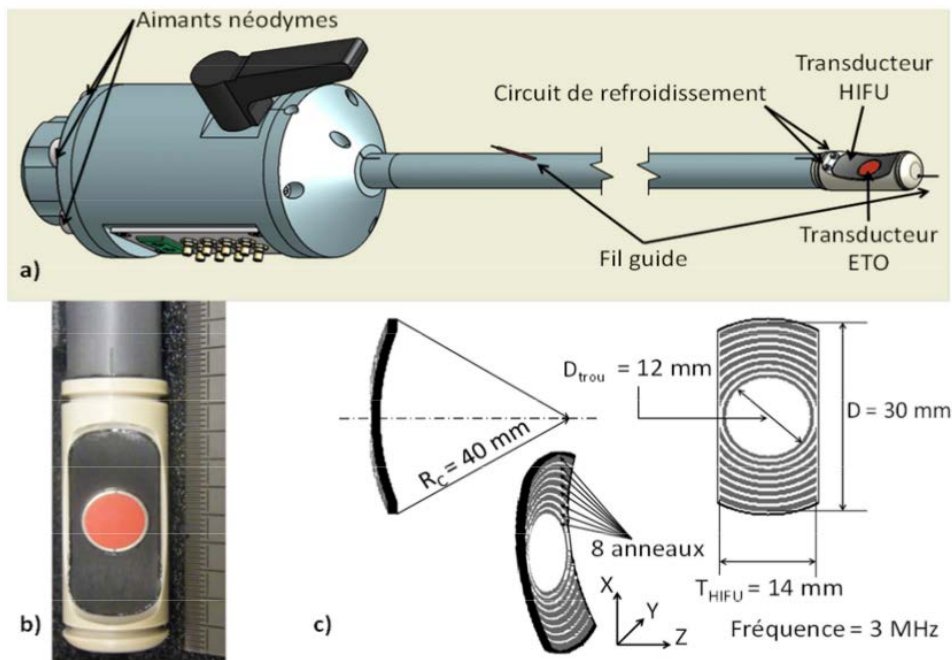


Figure 1.11: The prototype: (a) schematic view of the prototype. (b) Photography of the probe head. (c) Geometrical characteristics of the HIFU transducer (CONSTANCIEL et al. 2013).

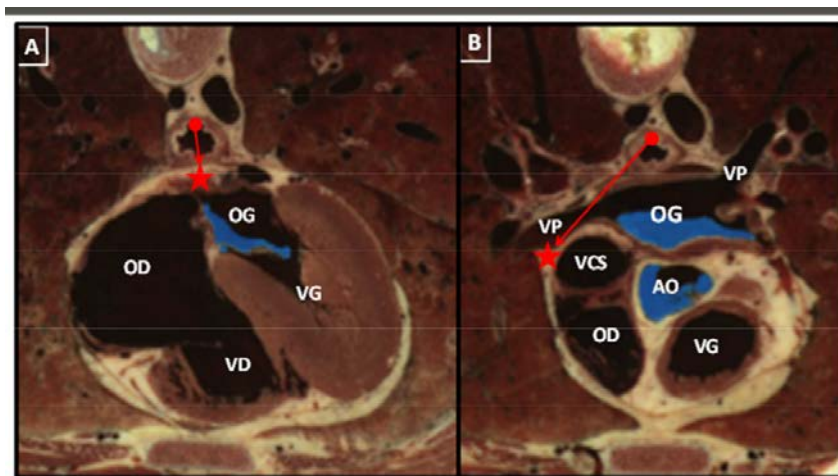


Figure 1.12: Closest and farthest points of the mini-maze therapy from the oesophagus (CONSTANCIEL 2014).

## 1.4 Conclusion

Atrial fibrillation is cardiac arrhythmia with a growing prevalence. It is a long duration pathology that evolves to advanced forms. Ablation therapy is advised when medicaments

are not helpful. Mini-maze procedure using a US guided transesophageal HIFU probe is a promising minimally-invasive approach to obtain transmural lesions reducing the risk of damage of near organs. The ultrasound images acquired to guide the therapy enables the heart to be viewed in real time from the posterior zone, particularly the region of interest in AF ablation.

## References

- AHMED, H. and V. Y. REDDY (2009). “Technical advances in the ablation of atrial fibrillation”. In: *Heart Rhythm* 6.8 Suppl, S39–S44.
- BENJAMIN, E. J., P. A. WOLF, R. B. D’AGOSTINO, H. SILBERSHATZ, W. B. KANNEL, and D. LEVY (1998). “Impact of atrial fibrillation on the risk of death: tThe Framingham Heart Study”. In: *Circulation* 98.10, pp. 946–952.
- BERTAGLIA, E., C. TONDO, A. DE SIMONE, F. ZOPPO, M. MANTICA, P. TURCO, A. IULIANO, G. FORLEO, V. LA ROCCA, and G. STABILE (2010). “Does catheter ablation cure atrial fibrillation? Single-procedure outcome of drug-refractory atrial fibrillation ablation: a 6-year multicentre experience”. In: *Europace* 12.2, pp. 181–187.
- CALKINS, H., J. HALL, K. ELLENBOGEN, G. WALCOTT, M. SHERMAN, W. BOWE, J. SIMPSON, T. CASTELLANO, and G. N. KAY (1999). “A new system for catheter ablation of atrial fibrillation.” In: *American Journal of Cardiology* 83.5B, pp. 227D–236D.
- CALKINS, H., J. BRUGADA, D. L. PACKER, R. CAPPATO, S.-A. CHEN, H. J. G. CRIJNS, R. J. DAMIANO, D. W. DAVIES, D. E. HAINES, M. HAISSAGUERRE, Y. IESAKA, W. JACKMAN, P. JAIS, H. KOTTKAMP, K. H. KUCK, B. D. LINDSAY, F. E. MARCHLINSKI, P. M. MCCARTHY, J. L. MONT, F. MORADY, K. NADEMANEE, A. NATALE, C. PAPPONE, E. PRYSTOWSKY, A. RAVIELE, J. N. RUSKIN, and R. J. SHEMIN (2007). “HRS/EHRA/ECAS expert consensus statement on catheter and surgical ablation of atrial fibrillation: recommendations for personnel, policy, procedures and follow-up. A report of the Heart Rhythm Society (HRS) Task Force on Catheter and Surgical Ablation of Atrial Fibrillation developed in partnership with the European Heart Rhythm Association (EHRA) and the European Cardiac Arrhythmia Society (ECAS); in collaboration with the American College of Cardiology (ACC), American Heart Association (AHA), and the Society of Thoracic Surgeons (STS). Endorsed and approved by the governing bodies of the American College of Cardiology, the American Heart Association, the European Cardiac Arrhythmia Society, the European Heart Rhythm Association, the Society of Thoracic Surgeons, and the Heart Rhythm Society.” In: *Europace* 9.6, pp. 335–379.
- CARIAS, M. and K. HYNYNEN (2014). “The evaluation of steerable ultrasonic catheters for minimally invasive MRI-guided cardiac ablation.” In: *Magnetic Resonance in Medicine* 72.2, pp. 591–598.
- CESARIO, D. A., A. MAHAJAN, and K. SHIVKUMAR (2007). “Lesion-forming technologies for catheter ablation of atrial fibrillation”. In: *Heart Rhythm* 4.3 Suppl, S44–S50.



- CONSTANCIEL, E. (2014). “Développement d’un applicateur transoesophagien à Ultrasons Focalisés de Haute Intensité à guidage échographique intégré pour le traitement de la fibrillation atriale”. PhD thesis. Université Claude Bernard, Lyon, France.
- CONSTANCIEL, E., W. N’DJIN, F. BESSIERE, F. CHAVRIER, D. GRINBERG, A. VIGNOT, P. CHEVALIER, J. CHAPELON, and C. LAFON (2013). “Design and evaluation of a transesophageal HIFU probe for ultrasound-guided cardiac ablation: simulation of a HIFU mini-maze procedure and preliminary ex vivo trials”. In: *IEEE Transactions on Ultrasonics, Ferroelectrics, and Frequency Control* 60.9, pp. 1868–1883.
- COX, J. L. (2003). “Atrial fibrillation II: rationale for surgical treatment”. In: *Journal of Thoracic and Cardiovascular Surgery* 126.6, pp. 1693–1699.
- COX, J. L. (2004). “The standard maze-III procedure”. In: *Operative Techniques in Thoracic and Cardiovascular Surgery* 9.1. Surgical Options for Treating Atrial Fibrillation During Mitral Valve Surgery, pp. 3–23.
- FERNÁNDEZ, F. (2006). “El sustrato de la fibrilación auricular: las venas pulmonares, la pared posterior o ambas.” In: *Revista Española de Cardiología* 59.7, pp. 643–646.
- FERNÁNDEZ, F. A. (2006). “[The atrial fibrillation substrate: pulmonary veins, posterior wall or both].” spa. In: *Rev Esp Cardiol* 59.7, pp. 643–646.
- FUSTER, V., L. E. RYDÉN, D. S. CANNOM, H. J. CRIJNS, A. B. CURTIS, K. A. ELLENBOGEN, J. L. HALPERIN, J.-Y. LE HEUZEY, G. N. KAY, J. E. LOWE, S. B. OLSSON, E. N. PRYSTOWSKY, J. L. TAMARGO, S. WANN, S. C. SMITH JR, A. K. JACOBS, C. D. ADAMS, J. L. ANDERSON, E. M. ANTMAN, S. A. HUNT, R. NISHIMURA, J. P. ORNATO, R. L. PAGE, B. RIEGEL, S. G. PRIORI, J.-J. BLANC, A. BUDAJ, A. J. CAMM, V. DEAN, J. W. DECKERS, C. DESPRES, K. DICKSTEIN, J. LEKAKIS, K. MCGREGOR, M. METRA, J. MORAIS, A. OSTERSEY, and J. L. ZAMORANO (2006). “ACC/AHA/ESC 2006 guidelines for the management of patients with atrial fibrillation—executive summary: a report of the American College of Cardiology/American Heart Association Task Force on Practice Guidelines and the European Society of Cardiology Committee for Practice Guidelines (Writing Committee to Revise the 2001 Guidelines for the Management of Patients With Atrial Fibrillation).” eng. In: *Journal of the American College of Cardiology* 48.4, pp. 854–906.
- GAZTANAGA, L., F. MARCHLINSKI, and B. BETENSKY (2012). “Mechanisms of cardiac arrhythmias”. In: *Revista Española de Cardiología* 65.2, pp. 174–185.
- GENTRY, K. L. and S. W. SMITH (2004). “Integrated catheter for 3-D intracardiac echocardiography and ultrasound ablation.” In: *IEEE Transactions on Ultrasonics, Ferroelectrics, and Frequency Control* 51.7, pp. 800–808.
- GO, A. S., D. MOZAFFARIAN, V. L. ROGER, E. J. BENJAMIN, J. D. BERRY, M. J. BLAHA, S. DAI, E. S. FORD, C. S. FOX, S. FRANCO, H. J. FULLERTON, C. GILLESPIE, S. M. HAILPERN, J. A. HEIT, V. J. HOWARD, M. D. HUFFMAN, S. E. JUDD, B. M. KISSELA, S. J. KITTNER, D. T. LACKLAND, J. H. LICHTMAN, L. D. LISABETH, R. H. MACKEY, D. J. MAGID, G. M. MARCUS, A. MARELLI, D. B. MATCHAR, D. K. MCGUIRE, E. R. MOHLER, C. S. MOY, M. E. MUSSOLINO, R. W. NEUMAR, G. NICHOL, D. K. PANDEY,

- N. P. PAYNTER, M. J. REEVES, P. D. SORLIE, J. STEIN, A. TOWFIGHI, T. N. TURAN, S. S. VIRANI, N. D. WONG, D. WOO, and M. B. TURNER (2014). “Heart disease and stroke statistics-2014 update: a report from the American Heart Association”. In: *Circulation* 129.3, e28–e292.
- GRANT, A. and S. DURRANI (2007). *Mechanisms of cardiac arrhythmias. Textbook of cardiovascular medicine*. Ed. by T. E. Lippincott Williams and Wilkins.
- HAÏSSAGUERRE, M., P. JAÏS, D. C. SHAH, A. TAKAHASHI, M. HOCINI, G. QUINIOU, S. GARRIGUE, A. LE MOUROUX, P. LE MÉTAYER, and J. CLÉMENTY (1998). “Spontaneous initiation of atrial fibrillation by ectopic beats originating in the pulmonary veins”. In: *New England Journal of Medicine* 339.10, pp. 659–666.
- HAÏSSAGUERRE, M., D. C. SHAH, P. JAÏS, M. HOCINI, T. YAMANE, I. DEISENHOFER, S. GARRIGUE, and J. CLÉMENTY (2000). “Mapping-guided ablation of pulmonary veins to cure atrial fibrillation”. In: *American Journal of Cardiology* 86.9, Supplement 1. Converging Electrical Therapies for the Heart, K9–K19.
- JAÏS, P., D. C. SHAH, A. TAKAHASHI, M. HOCINI, M. HAÏSSAGUERRE, and J. CLÉMENTY (1998). “Long-term follow-up after right atrial radiofrequency catheter treatment of paroxysmal atrial fibrillation”. In: *Pacing and Clinical Electrophysiology* 21.11 Pt 2, pp. 2533–2538.
- JALIFE, J. (2003). “Rotors and spiral waves in atrial fibrillation”. In: *Journal of Cardiovascular Electrophysiology* 14.7, pp. 776–780.
- JANUARY, C. T., L. S. WANN, J. S. ALPERT, H. CALKINS, J. C. CLEVELAND, J. E. CIGARROA, J. B. CONTI, P. T. ELLINOR, M. D. EZEKOWITZ, M. E. FIELD, K. T. MURRAY, R. L. SACCO, W. G. STEVENSON, P. J. TCHOU, C. M. TRACY, and C. W. YANCY (2014). “2014 AHA/ACC/HRS guideline for the management of patients with atrial fibrillation: executive summary: a report of the American College of Cardiology/American Heart Association Task Force on practice guidelines and the Heart Rhythm Society”. In: *Circulation*.
- KLUIWSTRA, J. U., Y. ZHANG, P. VANBAREN, S. STRICKBERG, E. EBBINI, and C. CAIN (1995). “Ultrasound phased arrays for noninvasive myocardial ablation: initial studies”. In: *Ultrasonics Symposium (IUS), 1995. Proceedings., 1995 IEEE*. Vol. 2, pp. 1605–1608 v.
- KOCHERIL, A. G., H. CALKINS, A. D. SHARMA, D. CHER, H. STUBBS, and J. E. BLOCK (2005). “Hybrid therapy with right atrial catheter ablation and previously ineffective antiarrhythmic drugs for the management of atrial fibrillation”. In: *Journal of Interventional Cardiac Electrophysiology* 12.3, pp. 189–197.
- KONINGS, K. T., J. L. SMEETS, O. C. PENN, H. J. WELLENS, and M. A. ALLESSIE (1997). “Configuration of unipolar atrial electrograms during electrically induced atrial fibrillation in humans.” In: *Circulation* 95.5, pp. 1231–1241.
- MANGONI, M. E. and J. NARGEOT (2008). “Genesis and regulation of the heart automaticity”. In: *Physiological Reviews* 88.3, pp. 919–982.
- MANSOUR, M., G. FORLEO, A. PAPPALARDO, C. BARRETT, E. HEIST, A. AVELLA, G. BENCARDINO, A. DELLO RUSSO, M. CASELLA, J. RUSKIN, and C. TONDO (2010). “Combined use

- of cryoballoon and focal open-irrigation radiofrequency ablation for treatment of persistent atrial fibrillation: Results from a pilot study”. In: *Heart Rhythm* 7, pp. 452–458.
- MOE, G. K. and J. A. ABILDSKOV (1959). “Atrial fibrillation as a self-sustaining arrhythmia independent of focal discharge”. In: *American Heart Journal* 58.1, pp. 59–70.
- NADEMANEE, K., J. MCKENZIE, E. KOSAR, M. SCHWAB, B. SUNSANEWITAYAKUL, T. VASAVAKUL, C. KHUNNAWAT, and T. NGARMUKOS (2004). “A new approach for catheter ablation of atrial fibrillation: mapping of the electrophysiologic substrate”. In: *Journal of the American College of Cardiology* 43.11, pp. 2044–2053.
- NARAYAN, S. M., K. SHIVKUMAR, D. E. KRUMMEN, J. M. MILLER, and W.-J. RAPPEL (2013). “Panoramic electrophysiological mapping but not electrogram morphology identifies stable sources for human atrial fibrillation: stable atrial fibrillation rotors and focal sources relate poorly to fractionated electrograms”. In: *Circ Arrhythm Electrophysiol* 6.1, pp. 58–67.
- NATALE, A., F. LEONELLI, S. BEHEIRY, K. NEWBY, E. PISANO, D. POTENZA, K. RAJKOVICH, B. WIDES, L. CROMWELL, and G. TOMASSONI (2000). “Catheter ablation approach on the right side only for paroxysmal atrial fibrillation therapy: long-term results”. In: *Pacing and Clinical Electrophysiology* 23.2, pp. 224–233.
- NEVEN, K., A. METZNER, B. SCHMIDT, F. OUYANG, and K.-H. KUCK (2012). “Two-year clinical follow-up after pulmonary vein isolation using high-intensity focused ultrasound (HIFU) and an esophageal temperature-guided safety algorithm”. In: *Heart Rhythm* 9.3, pp. 407–413.
- NINET, J., X. ROQUES, R. SEITELBERGER, C. DEVILLE, J. L. POMAR, J. ROBIN, O. JEGADEN, F. WELLENS, E. WOLNER, C. VEDRINNE, R. GOTTARDI, J. ORRIT, M.-A. BILLES, D. A. HOFFMANN, J. L. COX, and G. L. CHAMPSAUR (2005). “Surgical ablation of atrial fibrillation with off-pump, epicardial, high-intensity focused ultrasound: results of a multicenter trial”. In: *Journal of Thoracic and Cardiovascular Surgery* 130.3, pp. 803–809.
- ORAL, H., A. CHUGH, E. GOOD, A. WIMMER, S. DEY, N. GADEELA, S. SANKARAN, T. CRAWFORD, J. F. SARRAZIN, M. KUHNE, N. CHALFOUN, D. WELLS, M. FREDERICK, J. FORTINO, S. BENLOUCIF-MOORE, K. JONGNARANGSIN, F. PELOSI, F. BOGUN, and F. MORADY (2007). “Radiofrequency catheter ablation of chronic atrial fibrillation guided by complex electrograms”. In: *Circulation* 115.20, pp. 2606–2612.
- PAPPONE, C., S. ROSANIO, G. ORETO, M. TOCCHI, F. GUGLIOTTA, G. VICEDOMINI, A. SALVATI, C. DICANDIA, P. MAZZONE, V. SANTINELLI, S. GULLETTA, and S. CHIERCHIA (2000). “Circumferential radiofrequency ablation of pulmonary vein ostia: a new anatomic approach for curing atrial fibrillation”. In: *Circulation* 102.21, pp. 2619–2628.
- PARMENTIER, H., D. MELODELIMA, A. N’DJIN, S. CHESNAIS, J. Y. CHAPELON, and M. RIVOIRE (2009). “High-intensity focused ultrasound ablation for the treatment of colorectal liver metastases during an open procedure: study on the pig”. In: *Annals of Surgery* 249.1, pp. 129–136.
- PICHARDO, S., A. GELET, L. CURIEL, S. CHESNAIS, and J.-Y. CHAPELON (2008). “New integrated imaging high intensity focused ultrasound probe for transrectal prostate cancer treatment”. In: *Ultrasound in Medicine and Biology* 34.7, pp. 1105–1116.

- PRASAD, S. M., H. S. MANIAR, R. B. SCHUESSLER, and R. J. DAMIANO JR (2002). “Chronic transmural atrial ablation by using bipolar radiofrequency energy on the beating heart”. In: *Journal of Thoracic and Cardiovascular Surgery* 124.4, pp. 708–713.
- SCHMIDT, B., M. ANTZ, S. ERNST, F. OUYANG, P. FALK, J. K. R. CHUN, and K.-H. KUCK (2007). “Pulmonary vein isolation by high-intensity focused ultrasound: first-in-man study with a steerable balloon catheter.” In: *Heart Rhythm* 4.5, pp. 575–584.
- SINELNIKOV, Y. D., T. FJELD, and O. SAPOZHNIKOV (2009). “The mechanism of lesion formation by focused ultrasound ablation catheter for treatment of atrial fibrillation”. In: *Acoust Phys* 55.4-5, pp. 647–656.
- STRICKBERGER, S. A., T. TOKANO, J. U. KLUIWSTRA, F. MORADY, and C. CAIN (1999). “Extracardiac ablation of the canine atrioventricular junction by use of high-intensity focused ultrasound”. In: *Circulation* 100.2, pp. 203–208.
- WEERASOORIYA, R., P. KHAIRY, J. LITALIEN, L. MACLE, M. HOCINI, F. SACHER, N. LELLOUCHE, S. KNECHT, M. WRIGHT, I. NAULT, S. MIYAZAKI, C. SCAVEE, J. CLEMENTY, M. HAISSAGUERRE, and P. JAIS (2011). “Catheter ablation for atrial fibrillation: are results maintained at 5 years of follow-up?” In: *Journal of the American College of Cardiology* 57.2, pp. 160–166.
- WOLF, P, R. ABBOTT, and W. KANNEL (1991). “Atrial fibrillation as an independent risk factor for stroke: the Framingham Study”. In: *Stroke*, pp. 983–988.
- WU, F., W. Z. CHEN, J. BAI, J. Z. ZOU, Z. L. WANG, H. ZHU, and Z. B. WANG (2001). “Pathological changes in human malignant carcinoma treated with high-intensity focused ultrasound”. In: *Ultrasound in Medicine and Biology* 27.8, pp. 1099–1106.
- YIN, X., L. EPSTEIN, and K. HYNYNEN (2006). “Noninvasive transesophageal cardiac thermal ablation using a 2-D focused, ultrasound phased array: a simulation study”. In: *IEEE Transactions on Ultrasonics, Ferroelectrics, and Frequency Control* 53.6, pp. 1138–1149.
- ZIMMER, J. E., K. HYNYNEN, D. S. HE, and F. MARCUS (1995). “The feasibility of using ultrasound for cardiac ablation.” In: *IEEE Transactions on Biomedical Engineering* 42.9, pp. 891–897.
- ZONI-BERISSO, M., F. LERCARI, T. CARAZZA, and S. DOMENICUCCI (2014). “Epidemiology of atrial fibrillation: European perspective.” eng. In: *Clin Epidemiol* 6, pp. 213–220.



# Presentation of the proposed framework

The work presented in this document has been developed as part of the ANR TECSANCardioUSgHIFU (ANR-11-TECS-0004) project, mentioned before. This project aimed to propose the instrumentation and to carry out preliminary animal validation of two HIFU-based ablation approaches for the atrial fibrillation treatment.

In the first approach, a HIFU transducer is miniaturized to enable an endocardial approach. The goal also includes to monitor the therapy using the novel ultrasound technique of shear wave elastography.

The second approach is more prospective. In this approach the idea is to perform the ablation using a transesophageal approach with the prototype developed at LabTau in Lyon (see Section 1.3). The work presented in this document is part of this approach and developed in collaboration with the LabTau team. The project is decomposed into several sub-problems:

1. The geometrical design of the probe using numerical simulation;
2. Manufacturing of the first prototype;
3. The evaluation of the probe by:
  - a) Simulating ablation therapy using a digital phantom;
  - b) Validating the real probe's ablation performance in ex-vivo experiments;
  - c) Validating the probe's ability to ablate and to carry out the protocol during in-vivo animal experiments;
4. The development of image processing tools to:
  - a) Define ablation planning using patient-specific images;

- b) Guide and supervise this planning during treatment.

The contributions presented in this document concern sub-problem number 4. Our goal is to process information from the images available before and during the treatment in order to improve the planning and guidance of the interventional procedure. In our case of a cardiac ablation procedure using the transesophageal HIFU probe, we assumed that two kinds of images would be available: a high-resolution preoperative CT/MR image and, during the intervention itself, a real-time intraoperative 2D-US sequence provided by the US imaging system embedded in the transesophageal probe. Several processing problems will be considered from these images throughout this Thesis:

To plan AF treatment, we need to define the anatomical structures of interest from the preoperative CT/MR. We achieve this by the *automatic segmentation of the left atrium and the proximal parts of the pulmonary veins*. The extracted left atrium and the proximal parts of the pulmonary veins can then be used by the practitioner to study and to *delineate future lesion lines*. We also noted that the field of view of the transesophageal imaging probe is strongly constrained by the patient specific anatomy, especially by the esophagus. In order to prepare for future navigation of the probe and for the intervention itself, we decided to reconstruct *preoperative volume according to future probe positions*.

To guide the probe, we must integrate high-resolution information of the preoperative image inside real-time intraoperative 2D-US images. We achieve this by using *2D/3D registration of 2D-US images acquired by the TEE probe located in the esophagus with the CT/MR volume*.

The general framework of our contributions is presented in Figure 2.1.

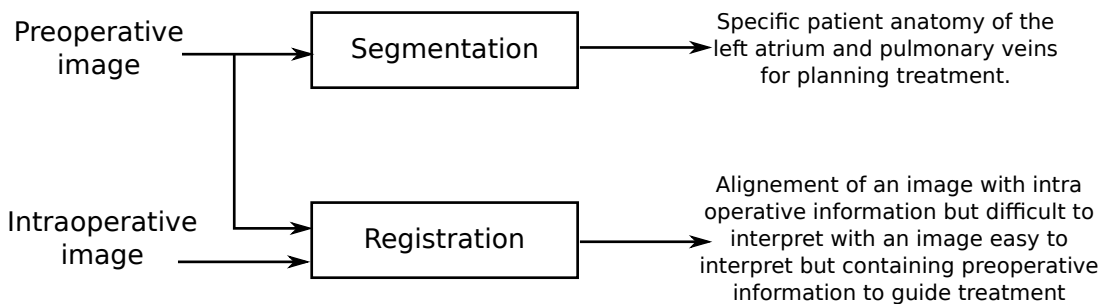


Figure 2.1: Our contributions to the project concerning cardiac arrhythmia treatment using a transesophageal HIFU probe guided by ultrasound imaging.

The medical imaging modalities, the methodological state of the art and the proposed framework of our contributions to the project are presented in this chapter. Three medical imaging modalities were identified for the development of this work: CT, MR and US. A detailed description of each one is presented in Section 2.1. Because the choice of methods of our proposed

framework is mainly constrained by the registration step, we will include a brief formalization of the image registration procedure in Section 2.2. The state of the art of Section 2.3 and Section 2.4 aims at positioning the key methods used in the context of the work according to existing ones. Finally, the proposed framework and the motivation for the choice of each of the methods developed in the context of this Thesis are presented in section 2.5.

## 2.1 Images used in AF therapy

### 2.1.1 Cardiac computed tomography (CT)

X-ray computed tomography is a technology that uses computer-processed X-rays to produce *tomographic images* of some specific areas of the scanned object. Digital geometry processing is used to generate a three-dimensional image of the inside of an object from a large series of two-dimensional radiographic images captured around a single axis of rotation (HERMAN 2009).

CT reconstruction uses multiple X-ray projections, meaning that the intensity of each reconstructed voxel is related to the radiological density of the tissue it belongs, i.e. a measure of its properties of X-ray absorption. The first commercial CT was invented by Sir Godfrey Hounsfield, who gave his name to the unit of absorption coefficients or a *Hounsfield (H)*. For instance, absorption coefficients for air, water (similar to blood) and bones are  $-1000H$ ,  $0H$  and  $1000H$ , respectively. Thus, the differences in X-ray absorption between tissues allow for different organs in the body to be distinguished. *Spiral CT* is the dominant type of CT scanner technology. In this type of machines the patient is placed on a motorized table and moved during CT acquisition while the pair of X-ray emitter-detectors rotates around it, as shown in Figure 2.2. The number of X-ray projections (angular resolution) and the size of the field of view (spatial extent of the object to be imaged), are important parameters defining the CT image resolution.

Cardiac CT image reconstruction needs to "freeze" the moving heart in order to avoid associated artefacts. Most CT systems need more than one heartbeat to reconstruct a 3D image of the heart. Therefore, images acquired at different heartbeats need to be synchronized in order to obtain a meaningful image. Such synchronization is performed using ECG which triggers CT acquisition.

### 2.1.2 Magnetic resonance imaging (MRI)

MRI systems exploit the *nuclear magnetic resonance* of hydrogen nuclei to build an image of biological tissues which can furnish information about the morphology and function of the human organism. The radiation used for MRI is approximately nine orders of magnitude smaller than in X- or  $\gamma$ -rays (used for radioisotope examinations) and is considered biologically safe.



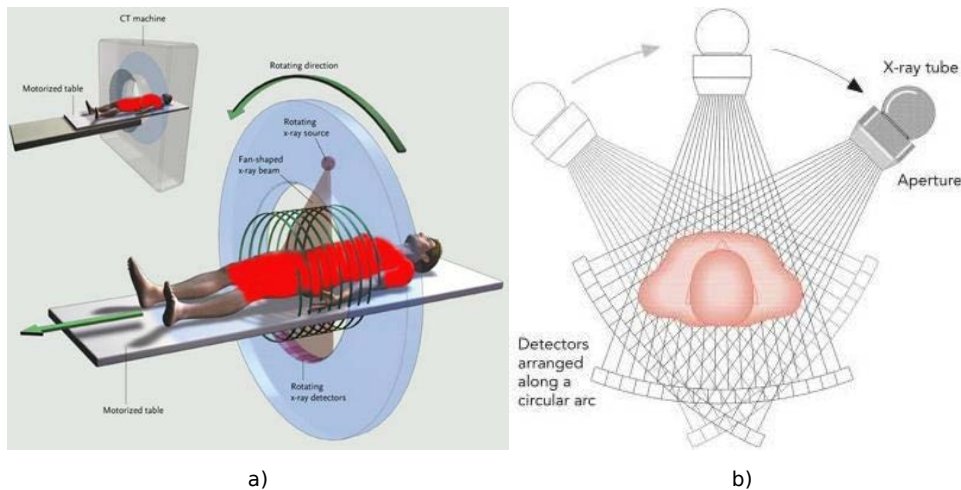


Figure 2.2: Computed tomography. (a) Spiral computed tomography system: the table moves during acquisition while the pair of emitter-detectors rotate around it. (b) X-ray projections used in computed reconstruction.

Hydrogen nuclei (single protons) possess an intrinsic property known as nuclear spin that gives rise to a small magnetic field for each proton, known as a magnetic moment. Normally the magnetic moments (spins) are randomly oriented, causing a global magnetic moment equal to zero. However, in the presence of an externally applied magnetic field, the magnetic moments are aligned towards (low energy state) or against (high energy state) the externally applied field. The protons precess at the Larmor frequency, which is directly proportional to the field (RIDGWAY 2010).

MR systems apply a known magnetic field  $B_0$  to obtain a reference net magnetic moment (moment equilibrium). This equilibrium is perturbed by a radio-frequency field at the corresponding Larmor frequency. Two effects can be seen at this frequency: (1) some protons absorb enough energy to be aligned against the applied field; (2) the spins are synchronized to be in phase each to the other. Immediately after the radio-frequency field is removed, the spin systems starts to return back to its original state, at equilibrium. This process is known as relaxation. The idea is to disturb the system from the equilibrium to another state, and after to measure the process of relaxation or the return to the equilibrium.

There are two distinct relaxation processes which can be measured by MR-systems: T1-relaxation and T2-relaxation. T1-relaxation is a spin to lattice interactions in which the protons lose energy and return to their initial alignment. T2-relaxation is the result of spin-spin interactions, in which proton magnetic moments are dephasing from each other.

One of the most important advantages of MR imaging over other imaging modalities is the ability to generate a contrast between different types of soft tissue. This is because different

types of soft tissue have different characteristic T1 and T2 relaxation times.

MR signals can be localized and encoded by applying specific magnetic field gradients. Magnetic field gradients are used to produce a change in field strength and hence a corresponding change in Larmor frequency along a particular direction. A combination of RF pulses and gradient magnetic fields are generated to produce an image. Figure 2.3 shows the different magnetic field gradients applied on the  $x$ ,  $y$  and  $z$  directions in order to encode spatial localization in a 3D acquisition.

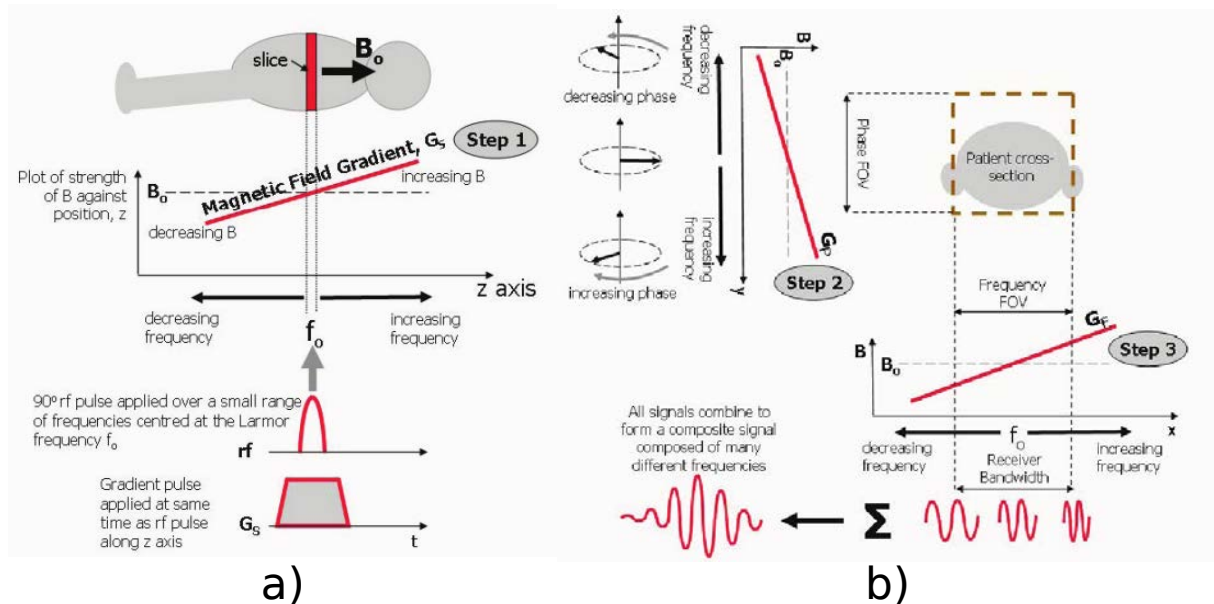


Figure 2.3: MR signals can be localized and encoded by applying magnetic field gradients. A combination of RF pulses and gradient-magnetic fields are generated to produce an image. Magnetic field gradients encode MR signals along the: a)  $z$  direction. b)  $x$  and  $y$  directions.

### 2.1.3 Echocardiography (US)

Echocardiography is the acquisition of an ultrasound image of the heart. It is a routine examination for the diagnosis and the following up of patients with suspected or known heart diseases. Echocardiographic systems are ubiquitous, present in almost every cardiac service around the world, because they are non-invasive, cheap, painless and offer different information about the heart's anatomy and function.

Cardiac ultrasound is an imaging technique that detects the frontiers between tissues with different acoustic impedances. This technique uses a beam of ultrasound to acquire an image of the heart. The image is formed from echo signals reflected by human tissues when the ultrasound propagates through. Different propagation phenomena exist that affect these echoes: absorption,

reflection, refraction and diffusion. In a US image, tissues are mainly characterized by their boundaries and moreover by speckle. Speckle arises from signal interference caused by tissue micro-inhomogeneities. Speckle distribution is quite characteristic of tissue micro-structures.

Diagnostic US imaging has undergone significant transformations. It started out with one-dimensional (1D) amplitude mode (A-mode), in which tissue structures could only be depicted along a single scanline. The introduction brightness mode (B-mode) allowed for the two-dimensional (2D) imaging. Color Doppler imaging then enabled for real-time visualization of blood flow in 2D imaging.

3D-US imaging can be obtained by using mechanical scanning probe, 2D matrix-array or free-hand techniques (Figure 2.4). A mechanical scanning 3D probe consists of a 1D array transducer and a compact motor coupled together and placed inside the probe casing. The motor translates, rotates, or wobbles the 1D transducer back and forth to insonate a 3D volume of interest. The acquired 2D images are registered using the known position and/or orientation of the transducer. Two-dimensional matrix-array transducers steer an ultrasound beam electronically into two perpendicular directions (azimuth and elevation) to insonate a typically pyramid-shaped volume. No moving parts are involved to acquire multiple scanlines for each transmitted ultrasound beam. They can achieve higher volume rates than mechanical probes, even if these come at the expense of lowered image quality, due to broader transmitted beams and artifacts arising from multiple scanline formation per transmitted beam. Freehand techniques continue to remain a less costly alternative. In sensor-based freehand acquisition, a position sensor is attached to the conventional 1D array probe. The image and sensor position are acquired simultaneously. 3D-US volumes are then visualized following geometric registration and reconstruction of the arbitrary 2D slices into 3D Cartesian coordinates.

Ultrasound transducers can be integrated into different types of probes and surgical instruments. This enables to image the heart from multiple points of view. The most commonly used US cardiac systems are:

- *Transthoracic Echocardiography (TTE)*: the US probe is placed on the thorax; thus, the US images of the heart are acquired through the chest. This is a non invasive system.
- *Intravascular Ultrasound (IVUS)*: The US probe is attached on the top of a thin catheter. This system is often used to image the arteries, i.e. for navigation purposes in a stent placement procedure (COLOMBO et al. 1995).
- *Intracardiac Echocardiography (ICE)*: The US probe is placed inside a catheter. The insertion of the catheter usually begins in the femoral vein, the right internal jugular vein or the left subclavian vein. The catheter is then guided through the vena cava into the

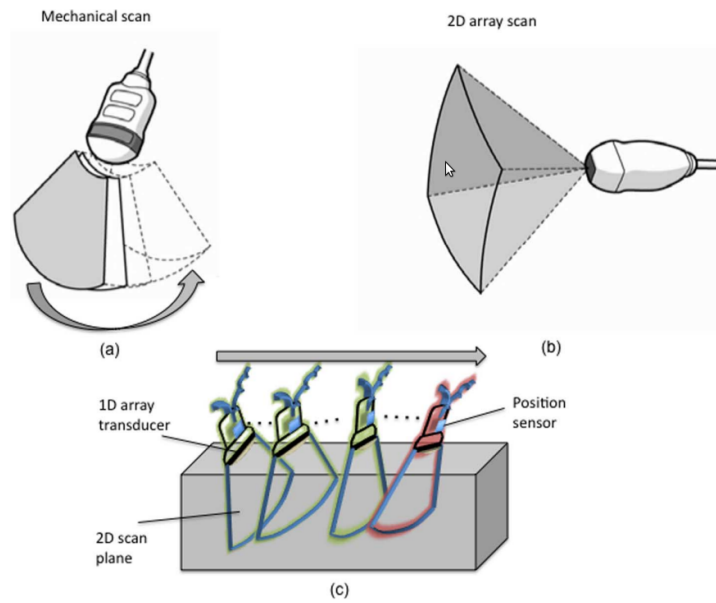


Figure 2.4: 3D-US imaging can be performed by (a) a mechanical scanning 3D probe, (b) a 2D matrix-array or, (c) freehand techniques.

heart cavities.

- *Transesophageal Echocardiography (TEE)*: US transducers are placed in the head of a probe designed to be inserted into the esophagus. Compared to transthoracic echo, TEE provides an unique access to some cardiac structures including the aorta, the heart valves and the atria (GAO et al. 2012). Moreover, TEE images are of higher quality because the transducer is located close to the heart, thus avoiding interferences from fat, lungs and ribs.

## 2.2 Image registration: Background

Image registration is the process of finding a transformation allowing to describe a pair of images using a common referential. This allows to associate their information. Let  $I_F$  and  $I_M$  be two images where subscripts  $F$  and  $M$  stand for fixed and moving, respectively. The coordinate system of  $I_F$  (fixed image) is the target referential to which  $I_M$  (moving image) will be moved to.

Let's consider that  $I_F$  and  $I_M$  are static acquisitions lying on their own spatial domain of dimension  $d$ :  $\Omega_F \subset \mathbb{R}^d$  and  $\Omega_M \subset \mathbb{R}^d$ , respectively (KLEIN et al. 2010). Let  $T_\mu(x)$  be a geometrical transform of a pixel (voxel)  $x \in \Omega_F$  with  $\mu$  the transform parameters.  $T_\mu$  maps the fixed image domain to the moving image domain, i.e.  $T_\mu: \Omega_F \subset \mathbb{R}^d \rightarrow \Omega_M \subset \mathbb{R}^d$ . Registration is the problem of finding an optimal set of parameters  $\mu'$  such that  $T_{\mu'}(x)$  aligns  $I_M(T_{\mu'}(x))$  to

$I_F(x)$ :

$$\mu' = \arg \max_{\mu} \mathcal{M}(T_{\mu}; I_F, I_M), \quad (2.1)$$

with  $\mathcal{M}(T_{\mu}; I_F, I_M)$  a similarity measure.

Figure 2.5 shows the general components of a classical registration process (IBANEZ et al. 2005). Four main components are included: the transform, the interpolator, the metric and the optimizer.

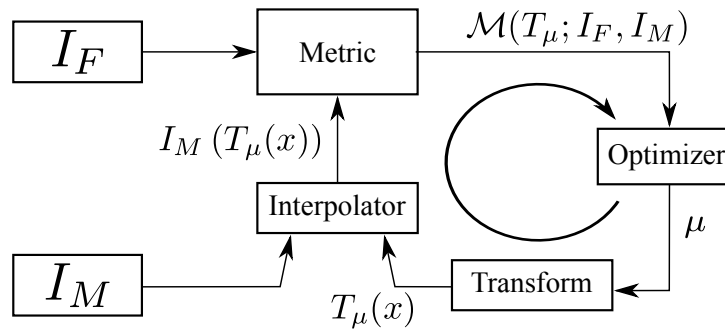


Figure 2.5: Registration of two images: searching the optimal transform parameters allowing to align the moving image in the fixed image referential.

### 2.2.1 Geometrical transform

During the registration procedure, the transform component  $T$  represents the spatial mapping of points from the fixed image space to points in the moving image space. The application problematic and the kind of images to be registered (object, intra/inter patient registration, dimensions, etc.) define the degrees of freedom of the transform to be used. This is an important aspect because it determines the type, speed and precision of the registration algorithm.

One way to classify spatial transforms is to consider linear and non-linear transforms. Linear transforms are defined by a global transformation matrix, often defined by using homogeneous coordinates, and which are applied to the whole image. Non-linear transforms (also called elastic or nonrigid transformations) are defined by a set of local transforms linked together by a regularization process (e.g using splines for the free-form deformation method or smoothing for Demon's algorithm).

The classical lineal transforms are described in the following. For all these transforms, a vector  $\mu$  containing the parameters must be defined.

**Rigid.** A rigid registration of a point  $x$  in a 3D space ( $x \in \mathbb{R}^3$ ), denoted as  $T_{\mu^R}(x) = R \cdot x + T$ , is defined by six parameters (i.e. it has six degrees of freedom), three parameters defining the translation  $T \in \mathbb{R}^3$  and three parameters for the angles of rotation ( $\theta \in \mathbb{R}^3$ ) around the axis of the coordinates system defining the rotation matrix  $R$ :  $\mu^R = (T, \theta)$ , with  $\mu^R \in \mathbb{R}^6$ . Rigid transform is also called isometric transform because it preserves distances, angles and orientation.

**Affine.** An affine transform is defined by adding anisotropic scaling (i.e. a scaling factor for each dimension) and shearing along the three axes of the rigid transform which leads to 12 parameters. It is noted as  $T_{\mu^A}(x) = A \cdot x + T$  with  $A \in \mathbb{R}^{3,3}$  a  $3 \times 3$  matrix:  $\mu^A = (a_{00}, \dots, a_{22}, T)$ , with  $a_{ij}$  the entry  $(i, j)$  of matrix  $A$ . Affine transforms preserve lines, parallel lines, and ratios of distances between points lying on a straight line.

**B-splines.** For the category of non-rigid transformations, B-splines are often used as a parametrization:

$$T_{\mu}(x) = x + \sum_{x_k \in \mathcal{N}_x} p_k \beta^3 \left( \frac{x - x_k}{\sigma} \right), \quad (2.2)$$

where  $x_k$  are the control points (defined on a regular grid),  $\beta^3(x)$  the cubic multidimensional B-spline polynomial,  $p_k$  the B-spline coefficient vectors,  $\sigma$  the B-spline control point spacing, and  $\mathcal{N}_x$  the set of all control points within the compact support of the B-spline at  $x$ . B-splines have local support ( $|\mathcal{N}_x|$  is small), which means that the transformation of a point can be computed from only a couple of surrounding control points. The parameters  $\mu$  are formed by the B-spline coefficients  $p_k$ .

### 2.2.2 Interpolator

During the registration process, a metric typically compares the intensity values of the fixed image to the corresponding values of the transformed moving image. But, because of discrete geometry, when a point is mapped from one image space to another, it will generally be mapped to a non-grid coordinate. Thus, an interpolation method is needed to obtain an intensity value for the mapped point using the information from the neighboring grid positions (Yoo 2004). There is a trade-off between the number of image values needed to interpolate a given point and the computation efficiency. The classical interpolation methods are:

**Nearest-neighbor.** This interpolator outputs the intensity of the nearest grid position. This interpolation scheme is quick and does not require floating-point calculations. It is useful for the interpolation of labeled images.

**Linear.** The returned value is a weighted average of the surrounding voxels, with the distance to each voxel taken as weight.

**B-spline.** The underlying image is represented using B-spline basis functions. The intensity of a non-grid position can then be computed by multiplying the B-spline coefficients with the shifted B-spline kernels within the support region of the requested position (YOO 2004).

### 2.2.3 Metric

The metric component is perhaps the most critical. This component quantitatively measures the similarity between the transformed moving image and the fixed image. This similarity indicates how well these two images match together. The metric is used by the optimizer to evaluate the quantitative criterion at various positions inside the transform parameter search space (YOO 2004).

Generally, two kind of information could be important in image registration: image *features* and/or the pixel (voxels) *intensities* .

On one hand, the content of an image can offer some features that could be easily detected in both images by an analysis method. These features are then used in a feature-based registration scheme. The features used in medical image are: external markers, anatomical landmarks, edges or surfaces (MAKELA et al. 2002). Anatomical landmarks are usually manually defined in both fixed and moving images. The advantages of performing the segmentation using landmarks is that it can be applied to any imaging modality and that the computation of the parameters of the geometrical transform is fast. Edges and surfaces are usually extracted using an automatic procedure that is manually initialized. The main drawback of this class of method is precisely the feature extraction step. The final registration result is highly dependent on the methods used in feature extraction and the level of interactivity of these methods.

On the other hand, all the image information is available in the distribution of its values. Some global intensity-based statistics analysis can then be used to estimate the similarity between the images. Several choices for the intensity-based similarity measure can be found in the literature:

**Mean squares** When the images to be registered come from the same imaging modality, the image intensity at corresponding positions between the two images should be similar. One of the simplest measures of similarity is the mean squared difference over all pixels, defined as:

$$\mathcal{MS}(T_{\mu}; I_F, I_M) = \frac{1}{N} \sum_i^N (I_F(x_i) - \psi(I_M(T_{\mu}(x_i))))^2 \quad (2.3)$$

with  $x_i$  a given in  $I_F$ ,  $N$  its number of voxels and  $\psi(\cdot)$  a given interpolator. The mean square metric has an ideal value of zero.

**Normalized correlation** This metric computes the pixel-wise cross-correlation between the intensities of the images to be registered, normalized by the square root of the autocorrelation of each image. When two images are identical, the measure equals one. It is defined as:

$$\mathcal{NC}(T_{\mu}; I_F, I_M) = \frac{\sum_i^N I_F(x_i) \cdot \psi(I_M(T_{\mu}(x_i)))}{\sqrt{\sum_i^N I_F^2(x_i) \cdot \sum_i^N \psi^2(I_M(T_{\mu}(x_i)))}} \quad (2.4)$$

**Mutual information** Mutual information (MI) is an information theoretic entity that qualitatively measures how much information about one random variable can be obtained from the information of another random variable (Yoo 2004). It considers the intensities of the input images as the random variable. MI is defined as (MAES et al. 1997):

$$\mathcal{MI}(T_{\mu}; I_F, I_M) = H(I_F) + H(T_{\mu}(I_M)) - H(I_F, T_{\mu}(I_M)) \quad (2.5)$$

with  $H(\cdot)$  and  $H(\cdot, \cdot)$  denoting the entropy and joint entropy, respectively, defined as:

$$H(I) = - \int p_I(i) \cdot \log(p_I(i)) \cdot di \quad (2.6)$$

$$H(I_F, I_M) = - \int p(i_F, i_M) \cdot \log(p(i_F, i_M)) \cdot di_F \cdot di_M \quad (2.7)$$

where  $i_F$  and  $i_M$  are one intensity value in  $I_F$  and  $I_M$ , respectively,  $p(i_F)$  is the probability density of the intensities in  $I_F$ , and  $p(i_F, i_M)$  is the joint probability density for  $I_F$  and  $I_M$  (the probability that  $i_F$  and  $i_M$  be at the same spatial localization).

**Normalized mutual information** There are different variants of a normalized mutual information. One of them is given by (STUDHOLME et al. 1999):

$$\mathcal{NMI}(T_{\mu}; I_F, I_M) = \frac{H(I_F) + H(T_{\mu}(I_M))}{H(I_F, T_{\mu}(I_M))} \quad (2.8)$$

**Entropy correlation coefficient** The entropy correlation coefficient is given by (MAES et al. 1997):

$$\mathcal{ECC}(T_{\mu}; I_F, I_M) = \sqrt{\frac{2 \cdot \mathcal{MI}(T_{\mu}; I_F, I_M)}{H(I_F) + H(T_{\mu}(I_M))}} \quad (2.9)$$

**Joint entropy** The original joint entropy is multiplied by  $-1$  to make the optimum a maximum instead of a minimum (MAES et al. 1997):

$$\mathcal{H}(T_{\mu}; I_F, I_M) = -H(I_F, T_{\mu}(I_M)), \quad (2.10)$$



**Point similarity measure based on MI** The point similarity measure is defined as (ROGELJ et al. 2003):

$$\mathcal{PSMI}(T_{\boldsymbol{\mu}}; I_F, I_M) = \sum_{I_F} \sum_{i_M \in T_{\boldsymbol{\mu}}(I_M)} p(i_F, i_M) \cdot \mathcal{PSMI}(i_F, i_M), \quad (2.11)$$

$$\mathcal{PSMI} = \log \left( \frac{p_{MI}(i_F, i_M)}{p_{MI}(i_F) \cdot p_{MI}(i_M)} \right), \quad (2.12)$$

$\mathcal{PSMI}$  should be initialized by defining  $\mathcal{PSMI}$  close to the global maximum. Thus, it was initialized by computed  $\mathcal{PSMI}$  at the maximum obtained by MI (2.5).

**Energy of the histogram** The energy of the histogram is defined as (BRO-NIELSEN 1997):

$$\mathcal{E}(T_{\boldsymbol{\mu}}; I_F, I_M) = \sum_{I_F} \sum_{i_M \in T_{\boldsymbol{\mu}}(I_M)} p^2(i_F, i_M), \quad (2.13)$$

**Correlation ratio** The correlation ratio is defined as (ROCHE et al. 1998):

$$\mathcal{COR}(T_{\boldsymbol{\mu}}; I_F, I_M) = \frac{\text{Var}(E(I_F|T_{\boldsymbol{\mu}}(I_M)))}{\text{Var}(I_F)} \quad (2.14)$$

**Woods criterion** The Woods criterion is defined as (WOODS et al. 1993):

$$\mathcal{WC}(T_{\boldsymbol{\mu}}; I_F, I_M) = \frac{1}{L} \sum_{i_M \in T_{\boldsymbol{\mu}}(I_M)} L_{i_F} \frac{\sigma_{i_M}}{m_{i_M}} \quad (2.15)$$

where

$$\sigma_{i_M} = \sqrt{\frac{1}{L_{i_M}} \sum_{x \in \Omega_{i_M}} I_F^2(x) - m_{i_M}^2} \quad (2.16)$$

where  $m_{i_M}$  is the average intensity in image  $I_F$  inside the subregions  $\in \Omega_{i_M} \subset T_{\boldsymbol{\mu}}(\Omega_M)$ , i.e., subregions where the image intensities in image  $I_M$  are  $i_M$ .  $L_{i_M}$  is the number of voxels in subregion  $\Omega_{i_M}$ . The original  $\mathcal{WC}$  is multiplied by  $-1$  to make the optimum a maximum instead of a minimum.

## 2.2.4 Optimizer

The role of the optimizer component is to optimize the measurements of similarity provided by the metric component, with respect to the parameters of the transform component. Starting from an initial set of parameters, the optimization procedure iteratively searches for the optimal solution by evaluating the similarity at different positions inside the parameter search space (Yoo 2004). Optimization algorithms can be broadly divided into two main classes: deterministic and stochastic methods.

Starting from an initial value, deterministic methods use simple rules, generally based on the study of the local shape of the function to minimize, to iteratively refine the solution. The local function study determines a searching direction, along which a step is selected to update the

solution. These methods can therefore be classified according to the derivative order they use to study the optimized function: (i) no derivative (e.g. downhill-simplex method or Amoeba); (ii) first-derivative (e.g. gradient descent, regular step gradient descent, conjugate gradient); (iii) second-order derivative (e.g. Broyden-Fletcher-Goldfarb-Shanno method). The use of higher order derivatives generally improves the searching direction; however, their computational cost has to be carefully considered. The strength of deterministic optimization methods is that, if the initialization is quite close to the optimum, they converge rapidly and with high precision. Their weakness is that they converge to a local minimum if the initialization is far from the optimum.

On the other hand, stochastic optimization methods rely on randomness and re-trials to better sample the parameter space in searching for an optimum solution. The three most commonly used stochastic methods are Monte Carlo, simulated annealing, and genetic algorithm. As an example, at each iteration of the simulated annealing method, a random value is generated in order to accept or reject the new guess, even if this solution is degraded compared to the previous one. These methods may avoid being trapped in local optima, but their computational cost is generally higher than that of deterministic methods.

## 2.3 Intraoperative US image registration: State of the art

From late 19th-century until now, X-ray has been the most commonly modality for image guided interventions (NOBLE et al. 2011). However, advances in ultrasound imaging from the second half of 20th century made it an alternative or a complement to be used in the operating room. US is the only imaging modality capable of imaging quickly enough the soft tissue deformations for the interventions procedure guidance. Some advantages of US against X-ray, CT and MR are: non-ionizing energy, portability, sensor miniaturization, straightforward integration in surgery, low cost, quick response in imaging tissue deformation. However, inferior image quality and constraints on its field of view make US a modality with high user dependency. Consequently, the success of interventional US imaging procedures is highly dependent on the level experience of its user.

In this context, the registration of preoperative CT/MR with intraoperative US has been studied for image-guided interventions. This approach enables: (1) the transfer of diagnostic information and the intervention planning provided by the clinician to a US-guided intervention; (2) the reduction of user dependency on the interpretation of intraoperative US images.

Navigation systems based on preoperative and intraoperative image registration reported in the literature typically follow the functional scheme in Figure 2.6 (CHEN et al. 2012). The steps involved in this scheme are: (1) US probe-tracking and 2D US acquisition; (2) 3D US image reconstruction; (3) Image registration of intraoperative US and preoperative CT/MRI; (4) Image

fusion and visualization.

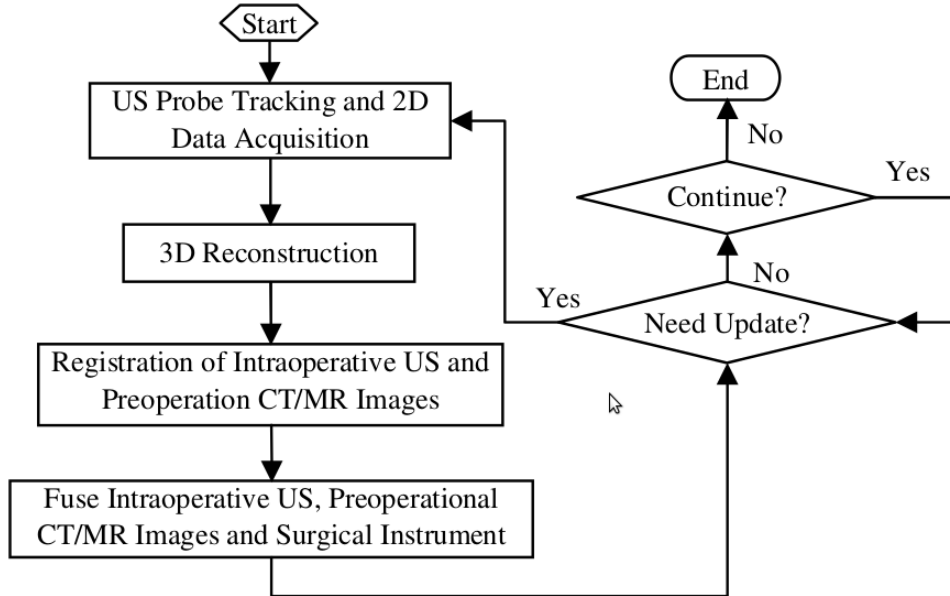


Figure 2.6: General framework for the registration between US intraoperative images and CT or MRI preoperative images (CHEN et al. 2012).

The navigation process showed in Figure 2.6 begins with the acquisition of the 2D-US images. Each image acquired has its own corresponding tracking information (i.e. position and orientation of the probe tip in an external reference coordinate system). Then, the acquired images are used to reconstruct a US volume, as described in section 2.1.3. In this way, the 2D information of the US images is positioned in a 3D space. After that, an accurate alignment of the images may be obtained using a 3D-US to 3D-preoperative image registration process (§2.2). The images are fused and displayed using the geometrical transformation resulting from the registration process.

Localizing the US-probe during the intervention is achieved using a tracking system. This system computes the spatial coordinates and rotation angles of a sensor attached to the probe with regards to a reference coordinate system. Their quick response enables the US probe to be tracked in real time. Nowadays, these tracking systems are based on optical or electromagnetic technology. The optical systems have high precision and a wide field of view. However, they require a clear line-of-sight between the tracking device and the optical sensor attached to the US-probe. Electromagnetic systems are used in cases where a line-of-sight is not available. The basic components of a tracking system using electromagnetic technology is showed in Figure 2.7. Electromagnetic sensors are small enough as be integrated into the surgical devices inserted inside the body (Figure 2.8). Unfortunately, electromagnetic systems are sensitive to metallic objects, causing a decrease in the positioning accuracy. The use of electromagnetic tracking has been reported in the literature, but none has reached wide clinical use (FRANZ et al. 2014). Some

other disadvantages of these systems include: expensive sensors, the need to connect sensors with a cable, the fact that sensors cannot be easily reused because they need to undergo a sterilization process and the fatigue of materials that causes sensors to break or provide false measurements.

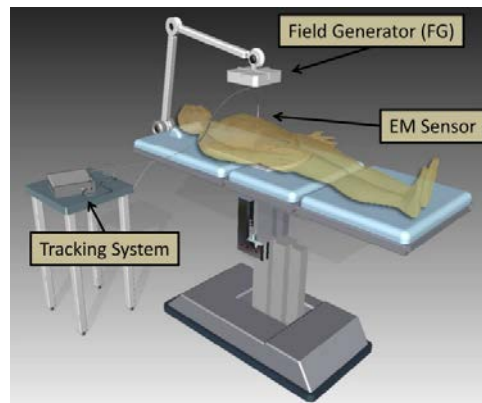


Figure 2.7: Basic components of intraoperative electromagnetic tracking (FRANZ et al. 2014).

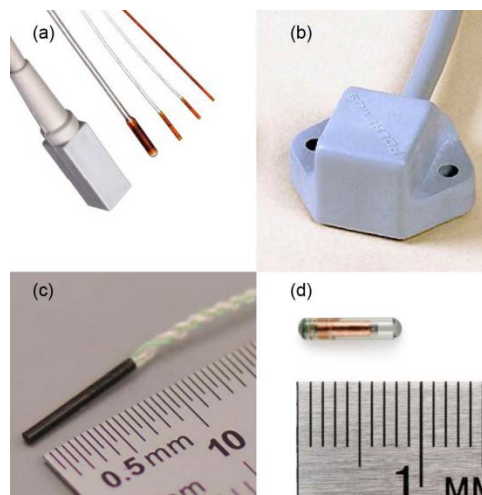


Figure 2.8: Examples of magnetic sensors for commercial electromagnetic tracking systems (FRANZ et al. 2014). (a) Ascension dc, (b) Polhemus ac, and (c) NDI Aurora ac sensors for tracking systems. (d) Passive electromagnetic transponders instead of magnetic sensors. This cannot measure the magnetic field.

A preoperative calibration process is always required using tracking systems. These calibrations help to obtain a reliable transformation that indicates the position of each pixel in the US image in the tracking tool space defined by the sensor attached to the US probe. Different calibration methods have been proposed (GOBBI et al. 1999; WANG et al. 2011).

The first studies using preoperative images and intraoperative US for image-guided interventions were reported for use in brain surgery, using optical tracking (FUERST et al. 2014; GOBBI et al. 1999).

MRI to US registration of the left ventricle images using segmentation was studied recently at LTSI (Laboratoire Traitement du Signal et de l'Image) (BETANCUR et al. 2013a; BETANCUR et al. 2013b; TAVARD et al. 2014). The developed method uses the endocardium wall information extracted manually by an expert from the US images.

#### Applications using TEE probe

A feature-based registration technique was used to align intraoperative US with the preoperative cardiac model in (LINTE et al. 2009). A 3D-US was reconstructed using an electromagnetic tracking system attached to the TEE probe. The mitral valve annuli and the aortic valve annuli are easily identifiable in both images. The edges of the annuli were segmented manually from the preoperative model and from the US reconstructed volume. The algorithm first aligns the centroids of the annuli, then it aligns the unit normal vectors corresponding to the homologous annuli, and at the end refines the registration by minimizing the overall distance between homologous annuli. The approach was tested in an in-vivo pork experiment. Both operating room and the surgical instruments were modified to minimize the accuracy errors of the tracking system.

The registration of preoperative CT and 2D-US was performed using an intensity-based measure in (HUANG et al. 2009). A US volume was reconstructed using acquired 2D images and electromagnetic tracking information. The preoperative CT was aligned with the US volume using tracking information. This preliminary registration is used to start an automatic intensity-based registration. MI was the metric used to obtain the parameters of a rigid transformation. This approach was tested in an in-vivo porcine model. The registration was performed offline after all data acquisition, and the intraoperative registration time was approximately 122 s.

CT-TEE registration of the aortic valve root was performed using a feature-based framework (LANG et al. 2013). The surface of the aortic root was extracted from both the preoperative CT and an intraoperative US. The authors used a 2D array transducer to image cross-planar US images and 3D TEE volumes from human data in order to compare both approaches. In their paper the TEE probe instrumented with magnetic tracking sensors was not available for image acquisition in humans. The edges of the aortic root were manually selected in cross-planar US images while for the 3D-CT volume the surface of the aortic root was segmented using a semi-automatic software. The use of cross-planes demonstrated better performance than for the full surface of the 3D TEE. The poor resolution and significant motion artefacts of the actual 3D US technology introduced a significant error.

The approach of (GAO et al. 2012) is a surgical navigation method using TEE. However, the registration is made with an intraoperative image. This method does not require any tracking

system; thus, it can be incorporated straightforward in to the operating room. The authors proposed to register and visualize 3D TEE and X-Ray fluoroscopy to guide cardiac interventions. Their method is based on the localization of the tip of the TEE probe in the fluoroscopic images. A preoperative CT image of the head of the probe with high resolution is acquired. The registration procedure iteratively repositions the CT to get different projection of the TEE probe tip, also called digitally reconstructed radiography (DRR). These images are then compared with one or multiple X-ray fluoroscopic images. The best alignment between the images results in acquiring information pertaining to the position of the TEE because the spatial transformation used to generate the projection is known. The algorithm was evaluated using a phantom and five clinical dataset. The experimental results proved that this method is viable because it is fast, reliable and accurate.

## 2.4 Left atrium and pulmonary veins segmentation: State of the art

The segmentation of the left atrium and pulmonary veins is performed before surgical intervention to extract the particular anatomy of the patients. Manual or semi-automatic segmentation is time-consuming and gives variable results for intra-observer and inter-observer test.

The segmentation of the myocardium in the LA and PVs is a challenging process because the myocardium wall has a variable thickness, being from 2 to 3mm in some regions (HO et al. 2012). The LA is surrounded by the aorta, right atrium, left ventricle and the coronary sinus; the automatic definition of the boundaries between the LA and these structures is challenging because they present similar intensity values. Moreover, the anatomical inter-subject variability (shape, size of the body, the number of the pulmonary veins, etc.) limits the obtention of a general automatic method.

The methods presented in the literature can be classified as: data-driven, model-based and atlas-based. Data-driven methods are not constrained by a priori specific shape information, the progress of the method is free to cover the different regions of the image. Model- and atlas-based methods use a priori shape information to constrain the progress of the method.

### 2.4.1 Data-driven methods

In data driven methods, the progress of the segmentation is constrained by data (intensity-values), rather than by intuition or a priori information. They require user interaction to initialize the algorithm and control the segmentation process. Data-driven approaches provide good results when input images have good contrast, enabling for the segmentation of anatomical variations. However, their performance is undermined by noisy images, low resolution images or when

neighbouring structures have the same intensity.

Region-growing is a simple data-driven segmentation method. In the initial stage, one or more pixels of the object of interest are designated (manually or automatically) as the initial point (seed) of a region. Then, the region is grown iteratively. In each iteration, the neighboring pixels (4- or 8-neighbors in a 2D plan or 6- or 26-neighbors in a 3D space) are added to the region if they fulfil a growth criterion. This growth criterion can be defined in terms of intensity value or by more complex rules (texture information). Rettmann et al. performed the segmentation of the LA and PVs using an approach based on region-growing (RETTMANN et al. 2008). In the first step of the technique, they used seeded region-growing to extract the entire blood pool including the four chambers of the heart, the pulmonary veins, the aorta, the superior vena cava, the inferior vena cava and other surrounding structures. Next, the left atrium and pulmonary veins were separated from the rest of the blood pool using an algorithm that searches for thin connections between user defined points in the volumetric data or on a surface rendering. Finally, the pulmonary veins are separated from the left atrium using a three dimensional tracing tool.

In watershed algorithms, the image is seen as a topographic relief, where the intensity value is interpreted as its altitude in the relief (ROERDINK et al. 2000). A drop of water on a topographic relief flows along a path to finally reach a local minimum. The watershed of the relief corresponds to the limits of the adjacent catchment basins of the drops of water. Cristoforetti et al. proposed a semi-automatic method based on watershed algorithms (CRISTOFORETTI et al. 2008). A preliminary anisotropic non-linear filtering was applied to improve the signal to noise ratio of CT images. Then, the external morphological gradient of the resulted image was extracted. Different cardiac structures and adjacent tissues were manually marked positioning some points inside of the regions. The markers controlled a watershed algorithm on the external morphological gradient image. Finally, a variable threshold method was used to obtain the final segmentation.

Region-splitting and -merging is an alternative method that does not need initialization. The idea is to subdivide the image into a set of arbitrary disjointed regions and then merge and/or split the regions in an attempt to satisfy some stated conditions. The general procedure can be summarized as: split into four disjointed quadrants any region in which the stated split predicate is not satisfied. When no further splitting is possible, merge any adjacent regions in which the merge predicate is satisfied. The procedure is stopped when no further merging is possible. John et al. presented a method based in splitting and merging to extract the heart structures from CT angiography (CTA) and MR angiography (MRA) datasets, in particular the left atrium (JOHN et al. 2005). The split-and-merge method was applied on the segmented blood pool. A simple threshold-based approach was used to extract the blood pool from the contrast-enhanced CTA and MRA data sets. With a given threshold, they separate blood pool voxels from other structures. This works fine with MRA data sets. With CTA data sets, such a threshold also segments voxels that represent bone tissue. Karim et al. presented a split-and-merge method to

segment the left atrium from MRA images (KARIM et al. 2008). In this work, the blood pool was obtained by subtracting the pre- and post-contrast scans, in this way the bone and other irrelevant structures were removed. Then, a bounding box was manually selected around the LA. A region-growing approach was initialized inside the atrium to obtain the blood pool. They also presented a method to separate the atrium body and the pulmonary veins.

The left ventricle segmentation on CT images was studied recently at LTSI (Laboratoire Traitement du Signal et de l'Image). The developed methods are based on: fuzzy connectedness algorithm (FLEUREAU et al. 2008) and multi-agent scheme combined with a supervised classification methodology (FLEUREAU et al. 2009).

### 2.4.2 Model-based methods

Model-based methods aim to deform a generic model of the organ of interest by the minimization (or maximization) of an energy function, such as that the model fits the boundary of the organ in the image that needs to be segmented.

Given that the structure of the heart is known, it is possible to incorporate prior shape knowledge into the segmentation process. The advantages are (FRANGI et al. 2001):

1. The model constrains the segmentation process when the input images are noisy, have artefacts or when the contrast between adjacent organs is low.
2. The segmentation process, the image analysis and shape modeling are simultaneously handled by a common framework.
3. Models can be as general or as detailed as needed.
4. In some approaches, the parameters of the model can be used as cardiac index.

Model-based approaches have four principal stages: generation of a generic model, positioning of the model in the region of interest, detection of organ boundaries and adaptation of the model to the boundaries.

**Generic model shape** : To compute the generic model, a representative set of images containing the delineations of the organ of interest must be defined. Different methods are then used to obtain, in an unique model (mesh), the information contained in this set of delineations, e.g. the mean shape, voting or other fusion methods. The set of images used to build the generic model must contain the variability of the application to obtain a robust model. This may include the variability of field of view (FOV), scan length, contrast, slice thickness, inter-patient shape, inter-phase shape among others.

**Initialization** : The first step to segment the organ of interest is to position the model in the area of interest, especially if the anatomy of the organ to segment is highly variable. This



aims at placing the surface of the model as close as possible to the boundaries that need to be delineated.

Automatic initialization has been used in (ECABERT et al. 2008) to position a model of the whole heart that includes the four chambers and great vessels. The parameters of the 3D transformation, which included translation and scale, were obtained using the generalized Hough transform. During a training step, the object of interest was codified using the Hough transform. This codification is disposed in a reference table. During initialization, the information of each voxel creates or increases a possible position of the shape on the reference table. At the end, the value with the highest accumulated value is used. The generalized Hough transform is a robust method to obtain the initialization; despite, its high consumption rate of memory and time consuming is high.

Another approach, based on machine learning, was proposed in (ZHENG et al. 2008). A set of possible localizations of the model is suggested, which leads a set of hypothesis. Each hypothesis suggests the parameters of a 3D similarity transformation: three rotations, three translations and three scales. Marginal space learning was used to search for the parameters of this transformation. The search is divided into three steps: translation estimation, translation-orientation estimation and full parameter estimation. A classifier is trained at each step; the search space is reduced after each step and a limited number of candidates continues on to the next step.

**Boundary detection** : Following the initial localization of the model (mesh), the shape is deformed to fit the boundary of the object. To do this a "correct" boundary must be estimated. (PETERS et al. 2010) describes a general scheme to detect the boundary using two main steps. In the first step, a set of points (landmarks) on the model are selected. In the second step, different points that may belong to the boundary (called targets), are searched in the neighborhood of these points by maximizing a match function. Generally, these targets are searched along an one-dimensional pattern that is perpendicular to the surface of the model. A review of different match functions to estimate the correct boundary is presented in (PETERS et al. 2010). Ideally, the match function must exhibit a maximum in a point that corresponds to the "correct" boundary. If the matching function does not exhibit a maximum, then all targets are discarded.

**Adaptation** : (ZHENG et al. 2008) proposed a nonrigid deformation to adapt the model in three steps. In the first step, a nonrigid deformation estimation of control points (landmarks at anatomical special characteristics) is performed. In the second step, the initial mesh is warped (thin plate spline) towards the refined control points for to improve its alignment. In the third step, other points are deformed to fit the image boundary.

In (ECABERT et al. 2008), a boundary detection function is assigned to each triangle of the mesh. This function can be based on a simple gradient or be more complex depending on the position of the triangle. The assignment of the detection function to each triangle has been optimized using simulated search. During a training procedure, the position of the triangles of a reference mesh is modified. Then, different functions (simple or complex) are used to detect the boundary. Finally, the detection function with the lowest generated error (distance) with regards to the reference boundary, is assigned to each triangle. The segmentation is then performed iteratively, alternating between two steps. During the first step, boundaries are estimated using the assigned functions. The model is modified during the second step. This process is iterated until the mesh reaches a stable state. To deform the model using a constrained form, they apply three consecutive steps of parametric and deformation adaptation are applied. Firstly, the model is modified by applying a rigid transformation to the mean shape. Secondly, it is modified using an affine transformation. Thirdly, it is modified using a elastic transformation.

### 2.4.3 Atlas-based

An atlas is a collection of images. For segmentation applications, the atlas should be a collection of pairs of images. Each pair is formed by the intensity and labeled images of one subject. The labeled image contains the segmentation of the organ of interest. The idea is to modify this segmentation to obtain the organ of interest in the image to segment. The modification information is the result of a registration process. The process can be summarized as: The transformation that aligns the intensity-image to segment and the intensity-image of one pair contained in the atlas is obtained by intensity-based registration. After, this transformation is used to modify the corresponding labeled image of the atlas. At the end, the modified label image is an approximation of the segmentation result.

The method can be single-atlas or multi-atlas. In a single-atlas the atlas is formed just for one pair of images. For multi-atlas the atlas contain more than one pair of image then the process of modification of the labeled image is repeated for all pairs of images contained in the atlas. The result of the segmentation process is the fusion of all modified labels.

Zhuang et al. present the automatic segmentation of the whole heart of cardiac MRI using a single-atlas approach (ZHUANG et al. 2010). In this approach a Locally Affine Registration Method (LARM) is proposed to obtain a robust initialization of the different structures of heart such a the four chambers and the major vessels. After, a non-rigid registration using free-form deformations with adaptive control points status is used to refine the local details. First, they employed the whole image including the surrounding structures of the heart such as the back, chest, and liver tissues. Then, they used a mask covering some structures of the heart to perform the affine registration locally. Four stages of local affine registration were adopted to obtain a

robust initialization of the non-rigid registration. Finally for the non-rigid registration, two masks were used: one with the control points onto the blood pool and the other one to activate the control points on the endocardial and epicardial surfaces. The proposed segmentation method achieved a surface-to-surface error of  $2.14 \pm 0.63$  mm (rms) and a Dice score of  $0.84 \pm 0.05$  compared to the gold standard.

Zuluaga et al. proposed a multi-atlas approach for the whole heart segmentation on CTA and MRI (ZULUAGA et al. 2013). The principal characteristic of this approach is that they used a multi-label ranking criterion, based on local normalized cross correlation, to select the best atlases for label fusion. The average whole heart segmentation Dice score was  $0.909 \pm 0.03$  for MRI and  $0.89 \pm 0.04$  for CTA images.

## 2.5 Outlines and justifications of the proposed approaches

Myocardial ablation using HIFU beamed from the esophagus is a promising procedure for mini-invasive treatment of atria fibrillation (CONSTANCIEL et al. 2013). In this therapy, a trans-esophageal HIFU probe is introduced into the esophagus and guided by ultrasound imaging towards the closest region to the posterior zone of the heart. From this location, ablation of the inner myocardial tissue of the heart is performed without damaging near tissues (such as the esophagus wall). Two types of images support this procedure: a preoperative CT/MRI volume for planning the intervention, and an intraoperative 2D-US image to carry out navigation during the intervention.

In the context of transesophageal HIFU myocardial ablation framework, the two main goals of our work in this project were 1) to improve *ablation planning* using the patient-specific preoperative CT/MRI volume, and 2) to propose solutions for the *guidance of therapy* in the intraoperative context:

1. *Planning* is a procedure that exploits high resolution information from CT or MRI concerning the anatomy of the patient (i.e. PVs branch structures, ostial and LAA position, LA thickness) to mark the desired lesion lines and also to evaluate the viability of the transesophageal approach (i.e. esophagus, bronchi and trachea location). Our contribution to therapy planning using the preoperative CT/MRI volume is three-fold: 1) the *automatic segmentation* of the left atrium and pulmonary veins to extract specific anatomy of the patient; 2), the *delineation of lesion lines* on the original volume or on LA segmentation in order to define the target of future ablation; 3) the *resampling of the CT/MRI volume* according to future 2D-US image slices orientation, *mimicking the navigation of the US probe along the esophagus*.

2. In the *intraoperative guidance* context, 2D-US images are used to guide the esophageal probe to the left atrium and also to locate the target to be ablated by the HIFU beam on the cardiac wall. As a result, these ultrasound images allow for optimal positioning of the transducer as well as verification of the absence of obstacles in the firing line of the HIFU transducer. Our contribution in the guidance step is the *registration of the intraoperative 2D-US image with the preoperative CT volume*. This registration will be used to position the HIFU beam on the left atrium, according to the planned therapy target.

In the rest of this section, these several research axes will be reviewed in terms of positioning statement and imaging particularities. The choices of the developed techniques and the justification of these choices will be stated, from these reviews.

## 2.5.1 Therapy planning

### 2.5.1.1 Segmentation of left atrium and pulmonary veins

This stage aims at automatically segmenting the left atrium and pulmonary veins in preoperative volumes for the two most common diagnostic image modalities: CT and MRI.

The myocardium wall of the LA and PVs is not uniform in thickness (6.5 – 1.5mm) (HO et al. 2012). It is challenging to identify this thin anatomical tissue even while using the highest resolution available for both modalities. Moreover, in some regions the gray level contrast is low and it is hard to separate the myocardium from the covering fat tissue. Therefore, it seems easier to segment the atrial blood pool than the myocardium wall itself, taking advantage of the high gray level contrast between the blood and the myocardium wall when the images are acquired after a contrast medium injection.

To segment the blood pool of the LA and PVs is challenging because there are different structures around them that contain blood. Adjacent structures such as the other chambers, the descending aorta or the coronary sinus are perceived with the same gray level value as the LA and PVs. Another problem comes from the contrast medium diffusion and acquisition artefacts, which produce intensity inhomogeneities in the LA cavity. Because of these problems, data-driven algorithms tend to leak towards others structures with similar gray levels or to under-segment the cavities.

The general shape of the blood pool of the LA and PVs can be roughly described as an ellipsoid with a finger-like pouch extending from the main body known as left atrial appendage (LAA) and mostly four veins (PVs) that exit the chamber at the posterior wall. Despite this general shape pattern, there is a high anatomical inter-individual variability, especially regarding the size and shape of the main cavity, the LAA and the PVs. The number and branch topology of the PVs is also highly variable (e.g. 25 % of the population have more than four PVs) (HO

et al. 2012; SCHWARTZMAN et al. 2003). We thus propose then to use a multi-atlas approach to overcome this variability. The advantage of this method is that the variability is contained in the multiple volumes that compose the atlas. The anatomical particularities of different patients in the atlas are used to obtain the desired anatomy.

Intrinsically, the result of multi-atlas methods is usually a coarse approximation of the desired segmentation. Some over-segmentation and sub-segmentation zones are observed. This is due to the fact that the deformations applied to the segmentations contained in the atlas cannot exactly fit the searched anatomy. The errors are small but significant in our application because they mainly concerns the endocardium wall, the ostial localization and/or PV branch topology. For this reason, a refined surface may be estimated from the multi-atlas result. In this way, a final method is used to obtain anatomical details that are contained in the gray level information close to the multi-atlas result.

#### **2.5.1.2 Labeling of target lesions on the preoperative volume**

The position of therapy lesions can then be marked by an expert on the 3D model of the LA and PVs. The LA and PVs segmentation obtained in previous section can be displayed as a 3D model using a visualization software as for example Slicer. The expert can then pick some points on the mesh in order to design the trajectory of the therapy. These points can be labeled in the pre-operative or in the segmented volume.

#### **2.5.1.3 Reconstructing a volume following the future navigation of the HIFU probe through the esophagus**

In order to prepare the planning of the probe navigation during the AF procedure, we propose to reconstruct the CT/MRI volumes according to the future probe positions.

As previously mentioned the HIFU probe includes a 2D-US imaging transducer at its center. This imaging transducer allows for 2D-US images to be acquired on plane relative to the probe axis, as showed in Figure 2.9. It can be noted that this plane corresponds to a zero degree angle in the classical multiplane TEE devices. Because the transducer is circular, the US image corresponds to an angular section on the axial plane in front of the probe. In our case, the 2D-US images are used to guide AF therapy during the intervention.

The position of the esophagus in the human body is constrained by its surrounding organs or tissues such as the vertebral column, trachea, carotid-jugular vascularization, aortic arch, right pulmonary artery, left main bronchus, left atrium, diaphragm and so on. We can thus make the assumption that the probe insertion does not modify the esophageal position in the body; in other

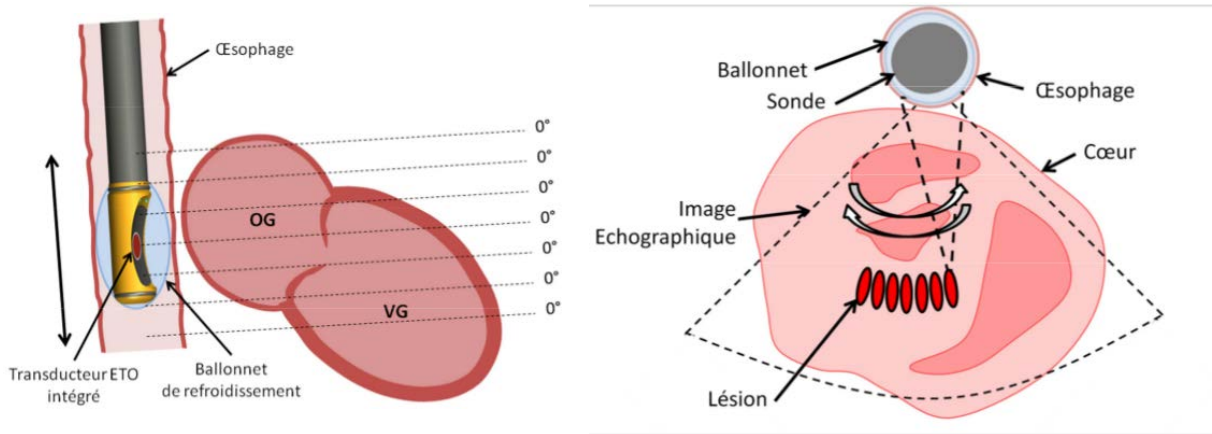


Figure 2.9: Field of view of the US imaging transducer inserted in the HIFU probe (CONSTANCIEL 2014).

words, the probe's trajectory is constrained by the esophagus. This constraint has a direct impact on the potential geometrical position of ultrasound images in the human body. For a specific US image, its origin (the apex of the image sector) is given by the position of the probe along the esophagus, the image sector is on the plane perpendicular to the esophagus centerline at a specific orientation around this centerline. We propose to integrate these geometrical constraints in our navigation planning by resampling preoperative CT volume according to the trajectory of the esophagus centerline. The resampling can be seen as a set of consecutive image planes perpendicular to the esophagus' centerline.

The goal of this resampling or reconstruction is to observe the anatomical structures in CT/MRI in the same order and orientation than the 2D-US images that would be acquired during the procedure. In other words, we want to create a procedure-adapted preoperative volume. This volume can be used to define the best localization of the HIFU probe in order to ablate a specific zone of the left atrium and to observe the anatomical obstacles in the line-of-sight of the HIFU transducer. More globally, it also allows to assess the viability of the sequence of the planned lesions.

### 2.5.2 Therapy guidance: Registration of the CT volume and 2D-US images

This stage aims to guide HIFU AF therapy by integrating high resolution anatomical preoperative information inside 2D intraoperative US cardiac images. This requires the registration of the 2D-US images with the preoperative CT volume. This is a challenging task, because the images to be registered do not have the same spatial dimensions: the preoperative is a CT volume while the intraoperative image is a slice. We have to perform a 2D-3D registration. In our specific case, the 2D-3D registration consists of finding the pose of the 2D-US image slice

inside the preoperative 3D volume. To do this, we have to search the best alignment between the US image slice with the corresponding sampled plane inside the CT volume. Here it is necessary to define: (1) the kind of alignment (rigid or elastic transform), (2) the constraints of the search (parameters of the transformation) and (3) the measure of the alignment (metric).

1. The alignment can be global (preserving the shape of the imaged objects), or elastic (modifying the shape according to local deformations). The choice of the kind of alignment is driven by the study of the movements and deformations introduced by the cardiac and respiration cycles (SRA et al. 2008).

The cardiac cycle introduces a periodic deformation of the heart. The heart can be imaged in one or several phases of the cardiac cycle using ECG-gated acquisitions. If both images to register correspond to the same cardiac phase, the movement deformation due to the cardiac cycle does not affect the registration, because the form of the heart is the same. In this case a *rigid transform* is sufficient.

As the diaphragm is close to the heart, respiration introduces some deformation and movement during the respiration cycle. The effect of this respiration is very complex, indeed, it has not yet been modelled and shows high intersubject variability (MCLEISH et al. 2002). A coarse approximation could be given as: (a) a displacement of the heart inside the human body due to respiration and (b) a deformation of the cardiac structures themselves due to the pressure or the interaction with other structures. The motion of the heart is predominantly in the cranial-caudal direction, with small displacements in the two other orthogonal planes and a rotation, especially at the apex of the heart (MCLEISH et al. 2002). The deformation of the LA and PVs is presented as a splaying of the PVs and a reduction of the diameters of the right PVs during the inspiration compared with expiration phases. However, there is little change in the overall LA size and left PVs calibre during respiration (NOSEWORTHY et al. 2005). Also, the surface-surface difference between the segmentation of the left atrium and the pulmonary veins between inspiration and expiration phases of the respiratory cycle is greater in the distal zone of the veins than in the ostial zone (NOSEWORTHY et al. 2005).

In our specific imaging case, we can make the assumption that (i) the deformations caused by respiration are small in the region of interest of the therapy, (ii) either the US probe undergoes the same translational movement as the heart or this translation can be compensated by a translation of the probe along the esophagus. Given these assumptions, we can therefore consider that a *rigid transform* is sufficient to describe the type of relationship between the 2D-US and 3D preoperative images. Another reason could be that we have not enough information to obtain a confident elastic alignment because the deformation introduced by the respiration is volumetric and the US image just shows the deformation

in 2D.

2. In our case of rigid transformation, six parameters (three translations and three rotations) have to be estimated. In the Figure 2.10, the preoperative volume is represented in the reference systems defined by  $(O_V, i, j, k)$  and the intraoperative image slice in this defined by  $(O_{US}, u, v, w)$ . The 2D-US image plane itself is defined by  $(O_{US}, u, v)$ . The six parameters define the geometrical transformation between these two coordinate systems. Without any a priori information, a brute force registration process will compare the US image with all the possible section planes of the preoperative volume in order to adjust these six parameters.

In order to reduce the number of parameters, we suggest using the assumption made in section 2.5.1.3 concerning the probe trajectory which is imposed by the esophagus topology. Using this geometrical constraint, we can reduce the number of parameters from six to two: the depth  $d$  of the US probe along the esophagus and its orientation  $\theta$  around the centerline of the esophagus (see Figure 2.10).

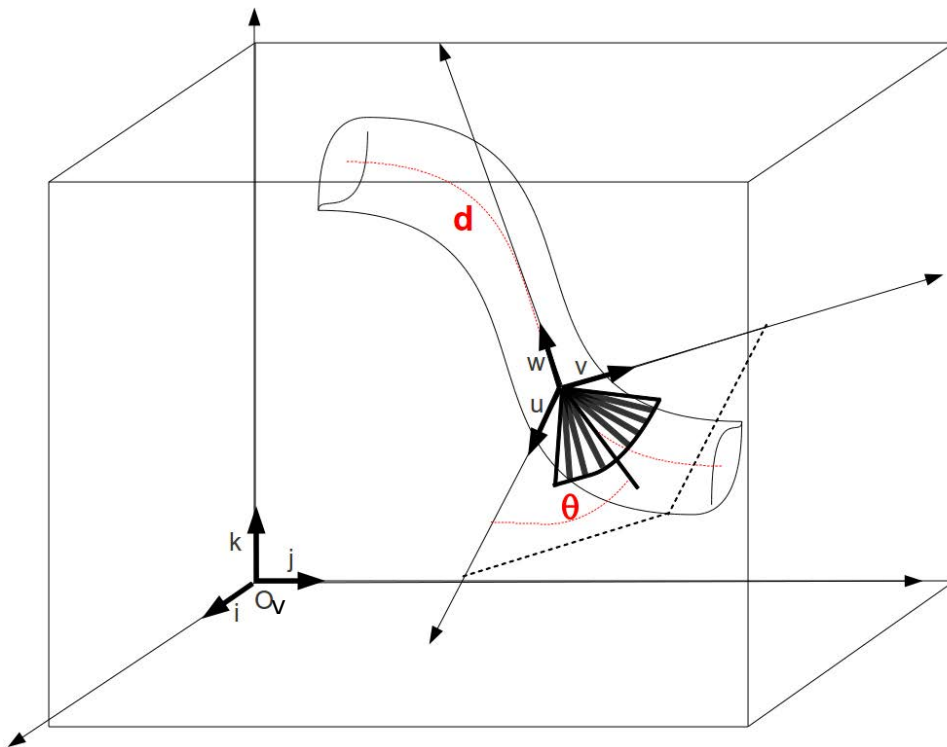


Figure 2.10: Position of the US image.

3. The nature of the image information according to the modality is a special issue. For CT the value of the voxel intensity is related to the Hounsfield scale which gives a relatively global and homogeneous information about each tissue. In contrast in US imaging, the information is mainly presented as speckle that shows some boundaries between tissues but also that



produces an inhomogeneous value distribution inside each tissue. As mentioned previously in section 2.2, there are two ways to compare image information in the process of alignment: feature-based or intensity-based. Feature-based comparison needs an additional segmentation step of the objects of interest in both image modalities. This process is usually time or computational expensive and the segmentation errors are also propagated to the posterior registration and can have a direct impact on the final accuracy. For these reasons we chose rather to use an intensity-based approach which extracts the objects information from gray levels without any additional process. The question is then, can the US image heterogeneous speckle information be used in an intensity-based approach? In cardiac imaging such a US-CT intensity-based multimodal registration has been reported by Huang et al. (HUANG et al. 2009). The authors used MI to directly (or after a simple thresholding) compare CT and US cardiac images. The question is now, can MI also be used in our own approach? If yes, other similarity metrics exist (see section 2.2.3), some of them include also some spatial information. We propose to evaluate the use of different intensity-based measures in our application and to select the optimal measure from a set of measures reported in the literature.

## 2.6 Summary: the contribution of the Thesis

As we mentioned in the introduction to this chapter, the goals of our work concerning transesophageal HIFU atrial ablation were to improve the ablation planning by using the patient-specific preoperative imaging volumes and to guide the ablation itself using the information established in the planning. For this, we propose the following framework (Figure 2.11).

### Methodological contributions

- Automatic hybrid method for the left atrium and pulmonary veins segmentation on CT/MRI images. For this we used a multiatlas method followed by a refined region growing segmentation method.
- Automatic therapy-adapted preoperative CT volume reconstruction from esophagus segmentation.
- Automatic 3D CT to 2D US image registration from therapy-adapted preoperative volume reconstruction. The originality relies in constraining the registration using the esophagus topology. The 3D/2D registration is simplified into a set of 2D/2D registrations.

### Phantom design

- Physical phantom that represents the structures and tissues of the human ventricles and esophagus used for CT and TEE acquisition.
- Digital phantom that represents the left atrium and pulmonary veins used for CT to US 2D registration evaluation.

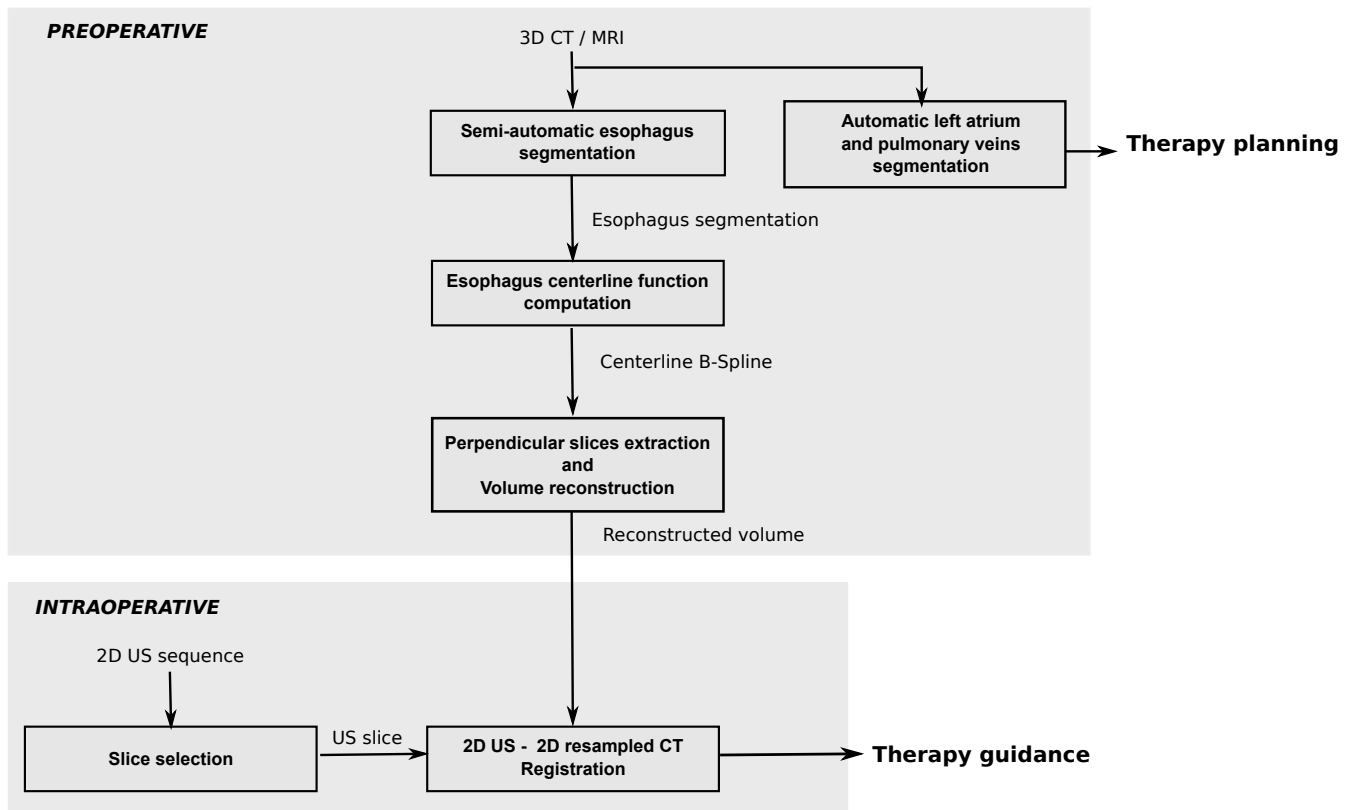


Figure 2.11: Proposed general framework for our contributions.

### Parameter studies

- Multi atlas method tuning:
  - ★ initialization,
  - ★ justified selection of the similarity measure used in affine and elastic registration,
  - ★ fusion method,
  - ★ number of images used in the fusion process.
- Similarity measure evaluation for US to CT registration.

### Evaluation methodology

In order to quantitatively evaluate the therapy-adapted preoperative CT volume reconstruction and the 2D US to 3D CT registration, we proposed a registration based evaluation scheme. One of the key point was to define by an expert, a registration ground truth. This allowed us to measure the reconstruction or registration accuracy using a Target Registration Error.

## References

- BETANCUR, J., A. SIMON, F. SCHNELL, F. TAVARD, E. DONAL, A. HERNANDEZ, and M. GARREAU (2013a). “Dynamic registration of multiple-view-US and MRI for the characterization of hypertrophic cardiomyopathy”. In: *Computing in Cardiology Conference (CinC), 2013*, pp. 237–240.
- BETANCUR, J., F. SCHNELL, A. SIMON, F. TAVARD, E. DONAL, A. HERNÁNDEZ, and M. GARREAU (2013b). “Spatio-temporal Registration of 2D US and 3D MR Images for the Characterization of Hypertrophic Cardiomyopathy”. In: ed. by S. OURSELIN, D. RUECKERT, and N. SMITH. Vol. 7945. Lecture Notes in Computer Science. Springer Berlin Heidelberg, pp. 292–299.
- BRO-NIELSEN, M. (1997). “Rigid registration of CT, MR and cryosection images using a GLCM framework”. In: *CVRMed-MRCAS’97*. Grenoble: Springer, pp. 171–180.
- CHEN, X., N. BAO, J. LI, and Y. KANG (2012). “A review of surgery navigation system based on ultrasound guidance”. In: *Information and Automation (ICIA), 2012 International Conference on*. Shenyang, pp. 882–886.
- COLOMBO, A., P. HALL, S. NAKAMURA, Y. ALMAGOR, L. MAIELLO, G. MARTINI, A. GAGLIONE, S. L. GOLDBERG, and J. M. TOBIS (1995). “Intracoronary stenting without anticoagulation accomplished with intravascular ultrasound guidance.” In: *Circulation* 91.6, pp. 1676–1688.
- CONSTANCIEL, E. (2014). “Développement d’un applicateur transoesophagien à Ultrasons Focalisés de Haute Intensité à guidage échographique intégré pour le traitement de la fibrillation atriale”. PhD thesis. Université Claude Bernard, Lyon, France.
- CONSTANCIEL, E., W. N’DJIN, F. BESSIERE, F. CHAVRIER, D. GRINBERG, A. VIGNOT, P. CHEVALIER, J. CHAPELON, and C. LAFON (2013). “Design and evaluation of a transesophageal HIFU probe for ultrasound-guided cardiac ablation: simulation of a HIFU mini-maze procedure and preliminary ex vivo trials”. In: *IEEE Transactions on Ultrasonics, Ferroelectrics, and Frequency Control* 60.9, pp. 1868–1883.
- CRISTOFORETTI, A., L. FAES, F. RAVELLI, M. CENTONZE, M. DEL GRECO, R. ANTOLINI, and G. NOLLO (2008). “Isolation of the left atrial surface from cardiac multi-detector CT images based on marker controlled watershed segmentation.” In: *Medical Engineering and Physics* 30.1, pp. 48–58.
- ECABERT, O., J. PETERS, H. SCHRAMM, C. LORENZ, J. VON BERG, M. WALKER, M. VEMBAR, M. OLSZEWSKI, K. SUBRAMANYAN, G. LAVI, and J. WEESE (2008). “Automatic model-based segmentation of the heart in CT images”. In: *IEEE Transactions on Medical Imaging* 27.9, pp. 1189–1201.
- FLEUREAU, J., M. GARREAU, D. BOULMIER, C. LECLERCQ, and A. HERNANDEZ (2009). “Segmentation 3D multi-objets d’images scanner cardiaques : une approche multi-agents”. In: *IRBM* 30.3, pp. 104–113.

- FLEUREAU, J., M. GARREAU, A. SIMON, R. HACHEMANI, and D. BOULMIER (2008). “Assessment of global cardiac function in MSCT imaging using fuzzy connectedness segmentation”. In: *Computers in Cardiology, 2008*. IEEE, pp. 725–728.
- FRANGI, A., W. NIESSEN, and M. VIERGEVER (2001). “Three-dimensional modeling for functional analysis of cardiac images, a review”. In: *IEEE Transactions on Medical Imaging* 20.1, pp. 2–5.
- FRANZ, A., T. HAIDEGGER, W. BIRKFELLNER, K. CLEARY, T. PETERS, and L. MAIERHEIN (2014). “Electromagnetic tracking in medicine: a review of technology, validation, and applications.” In: *IEEE Transactions on Medical Imaging* 33.8, pp. 1702–1725.
- FUERST, B., W. WEIN, M. MÜLLER, and N. NAVAB (2014). “Automatic ultrasound-MRI registration for neurosurgery using the 2D and 3D LC2 Metric”. In: *Medical Image Analysis* 18.8. Special Issue on the 2013 Conference on Medical Image Computing and Computer Assisted Intervention, pp. 1312–1319.
- GAO, G., G. PENNEY, Y. MA, N. GOGIN, P. CATHIER, A. ARUJUNA, G. MORTON, D. CAULFIELD, J. GILL, C. ALDO RINALDI, J. HANCOCK, S. REDWOOD, M. THOMAS, R. RAZAVI, G. GIJSBERS, and K. RHODE (2012). “Registration of 3D trans-esophageal echocardiography to X-ray fluoroscopy using image-based probe tracking”. In: *Medical Image Analysis* 16.1, pp. 38–49.
- GOBBI, D., R. COMEAU, and T. PETERS (1999). “Ultrasound probe tracking for real-time ultrasound MRI overlay and visualization of brain shift”. In: *Medical Image Computing and Computer-Assisted Intervention - MICCAI'99*. Springer, pp. 920–927.
- HERMAN, G. (2009). *Fundamentals of Computerized Tomography: image reconstruction from projections*. Advances in Computer Vision and Pattern Recognition. Springer.
- HO, S. Y., J. A. CABRERA, and D. SANCHEZ-QUINTANA (2012). “Left atrial anatomy revisited”. In: *Circulation: Arrhythmia and Electrophysiology* 5.1, pp. 220–228.
- HUANG, X., J. MOORE, G. GUIRAUDON, D. JONES, D. BAINBRIDGE, J. REN, and T. PETERS (2009). “Dynamic 2D ultrasound and 3D CT image registration of the beating heart”. In: *IEEE Transactions on Medical Imaging* 28.8, pp. 1179–1189.
- IBANEZ, L., W. SCHROEDER, L. NG, and J. CATES (2005). *The ITK Software Guide*. Second. Kitware, Inc. ISBN 1-930934-15-7. <http://www.itk.org/ItkSoftwareGuide.pdf>.
- JOHN, M. and N. RAHN (2005). “Automatic left atrium segmentation by cutting the blood pool at narrowings”. In: *Medical Image Computing and Computer-Assisted Intervention - MICCAI 2005*. Ed. by J. DUNCAN and G. GERIG. Vol. 3750. Lecture Notes in Computer Science. Springer Berlin Heidelberg, pp. 798–805.
- KARIM, R., R. MOHIADDIN, and D. RUECKERT (2008). “Left atrium segmentation for atrial fibrillation ablation”. In: *Proc. SPIE*. Vol. 6918. San Diego, 69182U–69182U–8.
- KLEIN, S., M. STARING, K. MURPHY, M. VIERGEVER, and J. P. W. PLUIM (2010). “Elastix: a toolbox for intensity-based medical image registration”. In: *IEEE Transactions on Medical Imaging* 29.1, pp. 196–205.

- LANG, P., M. CHU, D. BAINBRIDGE, G. GUIRAUDON, D. JONES, and T. PETERS (2013). “Surface-Based CT-TEE Registration of the Aortic Root”. In: *IEEE Transactions on Biomedical Engineering* 60.12, pp. 3382–3390.
- LINTE, C. A., J. MOORE, C. WEDLAKE, D. BAINBRIDGE, G. GUIRAUDON, D. JONES, and T. PETERS (2009). “Inside the beating heart: an in vivo feasibility study on fusing pre- and intra-operative imaging for minimally invasive therapy”. In: *International Journal of Computer Assisted Radiology and Surgery* 4.2, pp. 113–123.
- MAES, F., A. COLLIGNON, D. VANDERMEULEN, G. MARCHAL, and P. SUETENS (1997). “Multi-modality image registration by maximization of mutual information”. In: *IEEE Transactions on Medical Imaging* 16.2, pp. 187–198.
- MAKELA, T., P. CLARYSSE, O. SIPILA, N. PAUNA, Q. C. PHAM, T. KATILA, and I. MAGNIN (2002). “A review of cardiac image registration methods”. In: *IEEE Transactions on Medical Imaging* 21.9, pp. 1011–1021.
- MCLEISH, K., D. L. G. HILL, D. ATKINSON, J. M. BLACKALL, and R. RAZAVI (2002). “A study of the motion and deformation of the heart due to respiration.” In: *IEEE Transactions on Medical Imaging* 21.9, pp. 1142–1150.
- NOBLE, J. A., N. NAVAB, and H. BECHER (2011). “Ultrasonic image analysis and image-guided interventions”. In: *Interface Focus* 1.4, pp. 673–685.
- NOSEWORTHY, P. A., Z. J. MALCHANO, J. AHMED, G. HOLMVANG, J. N. RUSKIN, and V. Y. REDDY (2005). “The impact of respiration on left atrial and pulmonary venous anatomy: implications for image-guided intervention”. In: *Heart Rhythm* 2.11, pp. 1173–1178.
- PETERS, J., O. ECABERT, C. MEYER, R. KNESER, and J. WEESE (2010). “Optimizing boundary detection via Simulated Search with applications to multi-modal heart segmentation”. In: *Medical Image Analysis* 14.1, pp. 70–84.
- RETTMANN, M. E., D. R. HOLMES III, J. J. CAMP, D. L. PACKER, and R. A. ROBB (2008). “Validation of semi-automatic segmentation of the left atrium”. In: *Proc. SPIE*. Vol. 6916. San Diego, pp. 691625–691627.
- RIDGWAY, J. (2010). “Cardiovascular magnetic resonance physics for clinicians: part I”. In: *Journal of Cardiovascular Magnetic Resonance* 12.1, p. 71.
- ROCHE, A., G. MALANDAIN, X. PENNEC, and N. AYACHE (1998). “The correlation ratio as a new similarity measure for multimodal image registration”. In: *Medical Image Computing and Computer-Assisted Intervention - MICCAI’98*. Ed. by W. WELLS, A. COLCHESTER, and S. DELP. Vol. 1496. Lecture Notes in Computer Science. Springer Berlin Heidelberg, pp. 1115–1124.
- ROERDINK, J. B. and A. MEIJSTER (Apr. 2000). “The watershed transform: definitions, algorithms and parallelization strategies”. In: *Fundam. Inf.* 41.1,2, pp. 187–228.
- ROGELJ, P., S. KOVAČIČ, and J. C. GEE (2003). “Point similarity measures for non-rigid registration of multi-modal data”. In: *Computer vision and image understanding* 92.1, pp. 112–140.

- SCHWARTZMAN, D., J. LACOMIS, and W. G. WIGGINTON (2003). “Characterization of left atrium and distal pulmonary vein morphology using multidimensional computed tomography”. In: *Journal of the American College of Cardiology* 41.8, pp. 1349–1357.
- SRA, J. and S. RATNAKUMAR (2008). “Cardiac image registration of the left atrium and pulmonary veins”. In: *Heart Rhythm* 5.4, pp. 609–617.
- STUDHOLME, C., D. HILL, and D. HAWKES (1999). “An overlap invariant entropy measure of 3D medical image alignment”. In: *Pattern Recognition* 32.1, pp. 71–86.
- TAVARD, F., A. SIMON, C. LECLERCQ, E. DONAL, A. HERNANDEZ, and M. GARREAU (2014). “Multimodal Registration and Data Fusion for Cardiac Resynchronization Therapy Optimization”. In: *IEEE Transactions on Medical Imaging* 33.6, pp. 1363–1372.
- WANG, J., T. WANG, L. HU, H. LIAO, K. LUAN, and I SAKUMA (2011). “A fully automatic 2D ultrasound probe calibration method using a simple phantom”. In: *4th International Conference on Biomedical Engineering and Informatics (BMEI)*. Vol. 2, pp. 588–592.
- WOODS, R. P., J. C. MAZZIOTTA, and S. R. CHERRY (1993). “MRI - PET registration with automated algorithm”. In: *Journal of Computer Assisted Tomography* 17.4, pp. 536–546.
- YOO, T. S. (2004). *Insight into images: principles and practice for segmentation, registration, and image analysis*. AK Peters Ltd.
- ZHENG, Y., A. BARBU, B. GEORGESCU, M. SCHEUERING, and D. COMANICIU (2008). “Four-chamber heart modeling and automatic segmentation for 3-D cardiac CT volumes using marginal space learning and steerable features”. In: *IEEE Transactions on Medical Imaging* 27.11, pp. 1668–1681.
- ZHUANG, X., K. RHODE, R. RAZAVI, D. HAWKES, and S. OURSELIN (2010). “A registration-based propagation framework for automatic whole heart segmentation of cardiac MRI”. In: *IEEE Transactions on Medical Imaging* 29.9, pp. 1612–1625.
- ZULUAGA, M. A., M. J. CARDOSO, M. MODAT, and S. OURSELIN (2013). “Multi-atlas propagation whole heart segmentation from MRI and CTA using a local normalised correlation coefficient criterion”. In: *Functional Imaging and Modeling of the Heart, Proceedings of the 7th International Conference on. FIMH’13*. London, UK: Springer-Verlag, pp. 174–181.



## **PART II: THERAPY PLANNING**





# Left atrium and pulmonary veins segmentation

Research interest in left atrium and pulmonary veins (LA and PVs) segmentation has recently increased because the pulmonary veins and the wall of the left atrium are playing a key role in the initiation and the maintenance of the atrial fibrillation (SCHWARTZMAN et al. 2003). Preoperative MRI or CT are acquired to get high resolution information of the particular anatomical details of a specific patient when surgical AF therapy is required. Because the risk of injuring the organs close to atrium wall is high, a planning of the therapy is needed.

For the transesophageal HIFU therapy proposed by (CONSTANCIEL et al. 2013), the segmentation of the LA and PVs on the preoperative CT or MRI allows to recover the specific anatomy of the patient (i.e. PVs branch structures, ostial and left atrial appendage (LAA) position, LA thickness) in order to define the desired lesion lines on the 3D model and also to evaluate the viability of the transesophageal approach (i.e. esophagus, bronchi and trachea location).

However, it is a challenging task due to the large interindividual anatomical variations, especially regarding to the size and shape of the main cavity, the LAA and the PVs. Also the number and the branch topology of the PVs is highly variable (e.g. 25 % of the population have more than four PVs) (HO et al. 2012; SCHWARTZMAN et al. 2003).

Several methods have been proposed for LA and PVs segmentation (see section 2.4). Some of them make use of some prior knowledge of the anatomical shape such as model-based (ECABERT et al. 2008; ZHENG et al. 2012) and atlas-based (ZULUAGA et al. 2013) approaches. Other approaches, such as thresholding, region growing and active contours, use only the intensity information of the image (KARIM et al. 2008; ZHU et al. 2012).

We propose an approach that combines the use of (1) prior knowledge of the anatomical shape

to obtain a coarse first segmentation which considers interindividual anatomical variations, with (2) an intensity-based region growing algorithm to extract some particular refined anatomical details.

### 3.1 Methods

The proposed method computes a detailed segmentation of the LA and PVs from a coarse estimation of the atrium. This coarse segmentation uses a multi-atlas approach to obtain the inner region of the LA and PVs. A region growing based approach performs then a fine delineation from the inner region.

#### 3.1.1 Multi-atlas-based segmentation

Multi-atlas approaches have already been used in the segmentation of the brain (LEUNG et al. 2011), prostate (ACOSTA et al. 2011), whole heart and great vessels (ZULUAGA et al. 2013). The flowchart of the used multi-atlas approach is shown in (Figure 3.1).

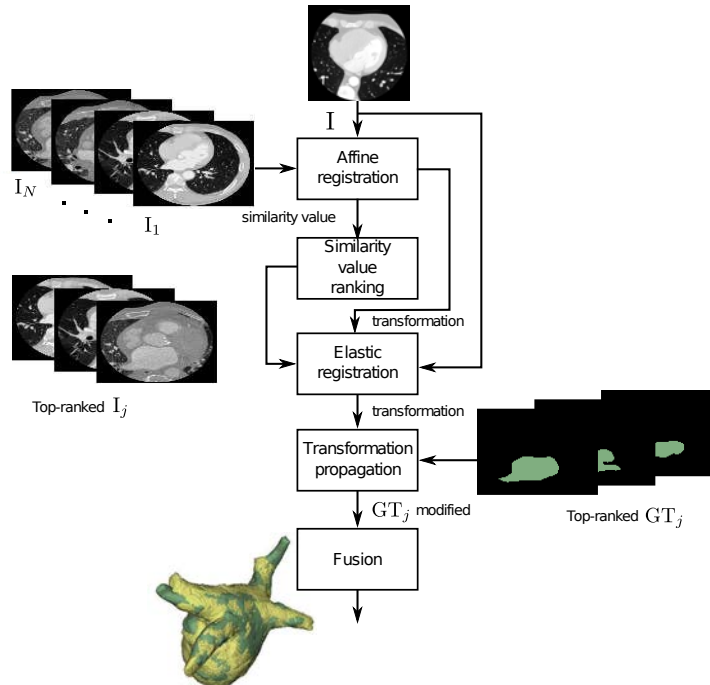


Figure 3.1: Multi-atlas-based segmentation process. The affine registration allows to evaluate the similarity between the input image and the atlas dataset. The most similar atlases are kept for the future segmentation. The elastic transformation step modifies the ground truth of the selected atlas images to adjust them to the input image. The fusion rule defines the coarse segmentation of the left atrium and pulmonary veins.

Let  $I$  be an input CT or MR image to be segmented and  $A_1, A_2, \dots, A_N$ , a set of  $N$  atlases each composed by an intensity image  $I_i$  and its corresponding ground truth  $GT_i$ , as  $A_i = (I_i, GT_i)$ ,  $i = 1, 2, \dots, N$ . The coarse segmentation of the LA and PVs is obtained with a multi-atlas approach composed of three main steps: (1) the selection of the atlases which are the most similar to  $I$ , (2) the adjustment of these atlases to  $I$  by elastic registration and (3) the fusion of the information of the adjusted atlases in order to segment  $I$ .

### 1. The atlas selection

The atlas selection step first performs an affine registration between  $I$  and each of the intensity images composing the atlas dataset  $I_i$ . The atlases  $A_i$  are then ranked according to the value of the similarity measure between  $I$  and  $I_i$ . The  $M$  top-ranked atlases are selected which gives a subset  $A_j$   $j = 1, 2, \dots, M$ .

### 2. Atlas adjustment

An elastic registration is performed between  $I$  and the top-ranked  $I_j$ . The transformation model estimated by the elastic registration is then propagated to the corresponding top-ranked  $GT_j$  in order to generate a labeled volume  $L_j$ . Each  $L_j$ s is a version of the segmentation result.

### 3. Label fusion

All the  $L_j$ s are fused together to obtain the segmentation of  $I$ . The combination rule between the  $L_j$ s is one of the key point of the method. We investigated two combination method frequently used in literature: a) the majority-voting and b) the Simultaneous Truth and Performance Level Estimation (STAPLE).

#### a) Majority-voting

A simple majority-voting fusion rule is used to merge the propagation of the labeled images of the selected atlas. This rule establishes that a voxel in  $I$  is labeled to be part of the left atrium or pulmonary vein if at least half of the corresponding voxel in the  $L_j$ s are part of the structure.

#### b) The Simultaneous Truth and Performance Level Estimation (STAPLE)

STAPLE is an algorithm that uses the Expectation Maximization to estimate simultaneous true segmentation and performance level. As input the algorithm considers a collection of segmentations. It computes then a probabilistic estimate of the true segmentation and a measure of the performance level represented by each segmentation. The probabilistic estimate of the true segmentation is formed by finding an optimal combinations of the segmentations and by weighting each segmentation depending upon the performance level. The contributions of each propagated label  $L_j$  is so

weighted according to the sensitivity and specificity (WARFIELD et al. 2004).

Consider an image of  $P$  voxels and a set of  $M$  segmentations of the image. Let  $D = P \times M$  be a matrix describing the binary decisions made for each segmentation at each voxel of the image. Let  $T$  be an indicator vector of  $P$  elements, representing the hidden binary true segmentation. Let the complete data be  $(D, T)$  and let the probability mass function of the complete data be  $f(D, T/\text{sensitivity}, \text{specificity})$ .

The goal of STAPLE is to estimate the performance level parameters of the segmentations characterized by the parameters (sensitivity, specificity) which maximize the complete data log-likelihood function :

$$(\widehat{\text{sensitivity}}, \widehat{\text{specificity}}) = \arg \max \ln f(D, T/\text{sensitivity}, \text{specificity}). \quad (3.1)$$

### 3.1.2 Region growing

The region growing process is initialized by a seed region extracted from the output of the previous multi-atlas segmentation. The seed region is set by the erosion of the result of the previous step. A spherical structuring element with a radius of 2mm is used for the erosion. This ensures that the seed region always lies inside the region of interest. The seed region is shown in Figure 3.2. In such a way, the seed region is adapted to the specificity of each patient.

From this seed region, the region growing approach adds then new voxels according to an intensity-based criterion. This criterion is based on 2 intensity thresholds. First the mean value and the standard deviation of the intensities inside the seed region are estimated. The thresholds are defined by the mean value  $\pm$  two standard deviations.

In order to avoid leakages, we also constraint the growing procedure inside a search region. This search region corresponds to the atlas-based segmentation output dilated using the same 2mm radius structuring element, as shown in Figure 3.2.

## 3.2 Experiments and results

### 3.2.1 Data and ground truth

The dataset is composed of 30 CT and 30 MRI images. These images were provided by the King's College, London, and Philips Research, Hamburg, to the participants of the Left Atrial Segmentation Challenge (LASC) carried out at the STACOM'13 workshop, in conjunction with MICCAI'13 (TOBON-GOMEZ et al. 2013). The dataset was divided into two groups:

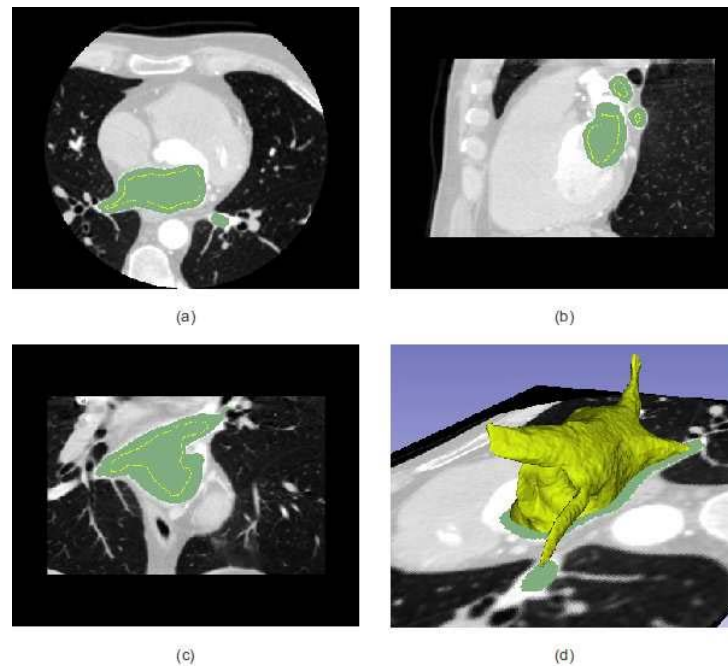


Figure 3.2: The axial (a), sagittal (b) and coronal (c) views of the intensity input image (gray level), the corresponding ground truth (green) and the contour of the seed region (yellow). The 3D view (d) of the seed region.

- (SET-A) 10 images of each modality with the corresponding delineation of the left atrium and pulmonary veins. This set is used to tune the methods and also in our case, the intensity images and corresponding ground truths of the dataset will compose the atlas for the atlas-based segmentation.
- (SET-B) the remaining 20 images without ground truth are used to evaluate the performance of the several methods in the challenge.

### 3.2.1.1 CT datasets

The CT images were acquired using Philips 16-, 40-, 64- and 256-slice scanners (Brilliance CT and Brilliance iCT, Philips Healthcare, Cleveland OH, USA). The acquisition was retrospectively ECG-gated at end-systole. All images were reconstructed using a  $512 \times 512$  matrix with an in-plane voxel resolution ranging from  $0.30 \times 0.30$  to  $0.78 \times 0.78 \text{mm}^2$  and with a slice thickness ranging from 0.33 to 1.00mm. The acquisitions were performed after the injection of 40 to 100ml of contrast media. The dataset contains images from several quality level in the following proportion : 8 high contrast, 15 moderate contrast, 3 low contrast and 4 high noise images.

### 3.2.1.2 MRI datasets

The MRI were acquired on a 1.5T Achieva scanner (Philips Healthcare, Best, The Netherlands). The sequence are non-angulated volumes covering the whole heart with a resolution of  $1.25 \times 1.2 \times 2.7\text{mm}^3$ . The acquisitions were ECG and respiratory gated. The dataset contains also images from several quality level in the following proportions: 9 high quality, 10 moderate quality, 6 with local artefacts and 5 high noise images.

### 3.2.1.3 Ground truth generation

The ground truth (GT) generation of these datasets was explained in (TOBON-GOMEZ et al. 2015). First the localization of the initial mesh was performed using the Generalized Hough Transform. Then the detection of the boundary was iteratively performed using trained boundary detectors. On this boundary, the pose of a complete model was estimated by the rigid registration which minimizes the squared distances of the model surface and the detected boundary. The model got a regional adaptation by affine transformations. At the end a local accurate segmentation was performed by a sequence of deformable adaptations. On this final model adaptation, the enclosed regions of the LA and PVs were labeled.

Two expert observers corrected manually each automatic segmentation in order to obtain the final GT segmentation. A Philips in-house editing tools and/or ITK-SNAP were the software used to perform the manual corrections. The PVs were truncated 10mm distally to the LA body or at the first branching point when there was no clear main PV to follow.

## 3.2.2 Method tuning

The goal of the following test aims to select the parameters of the method:

(1) The data subset used for the 2 registrations steps. The registration processes can be performed on all voxels of the image or on only the voxels inside of a region of interest (ROI). The region of interest is a cubic shape mask that surround the left atrium and the pulmonary veins. This mask is defined manually on each image for both moving and fixed image. The Figure 3.3 shows the two possibilities with and without ROI.

(2) The similar measure used in the 2 registration processes. We compared the results obtained by 3 different similarity measures : Mean Squares (MS), Normalized Cross Correlation (NCC) and Mutual Information (MI). The description and mathematical definitions of these metrics can be seen in section 2.2.3. We choose to evaluate these specific metrics because typically they show a good performance for mono-modality registration.

- (3) The number  $M$  of volumes used in the fusion step.

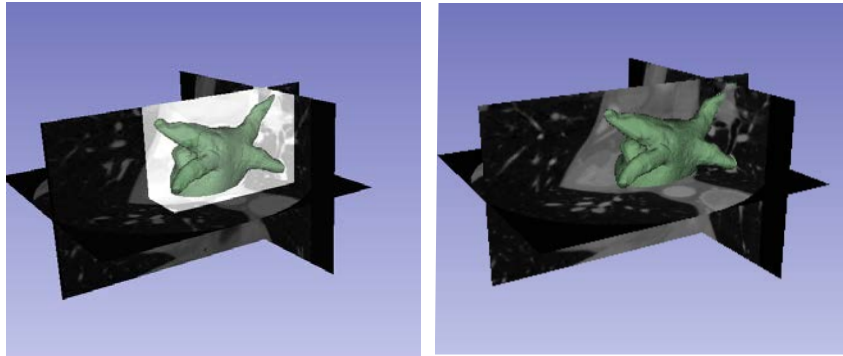


Figure 3.3: The region of interest is a cubic shaped mask that surrounds the left atrium and the pulmonary veins. This mask is set manually for both moving and fixed image.

The performance tests were performed using the leave-one-out method over the SET-1 of the CT images (section 3.2.1.1). One image is used for the test and the remaining nine images formed the atlas set. The accuracy of the registration processes was measured using the Dice score. This score depicts the overlap of two volumes  $V_1$  and  $V_2$  and is defined as:

$$Dice = \frac{2|V_1 \cap V_2|}{|V_1| + |V_2|} \quad (3.2)$$

### 3.2.2.1 Tuning the atlas selection step

In Figure 3.4, four examples of the global alignment estimated after affine registration are shown. The green model correspond to the ground truth of the image to segment. We can see the variability of the several atlas regarding to the size and shape of the LA, PVs and LAA. We can observe that the body of the LA is usually well aligned in most of the cases, however the pulmonary veins are usually miss-aligned. For some images the result of the affine registration is a good approximation of the final response. In this case, the final alignment can be refined by a posterior elastic registration. However, the bad initialization of the other registered atlas images will generate to poor results even after elastic deformations and in consequence will affect the fusion result.

At this point we can conclude that the ranking of the atlas images is needed after the global alignment to select the atlas images that are anatomically similar to the image to segment.

Table 3.1 presents the results of the ranking process when  $A_1$  the first atlas is taken from the training group as input image and the remaining nine are used as atlas set. The similarity measure and the use or not of a ROI have a direct incidence in the ranking process. Indeed, the change in the ranking is more evident when MI is used.



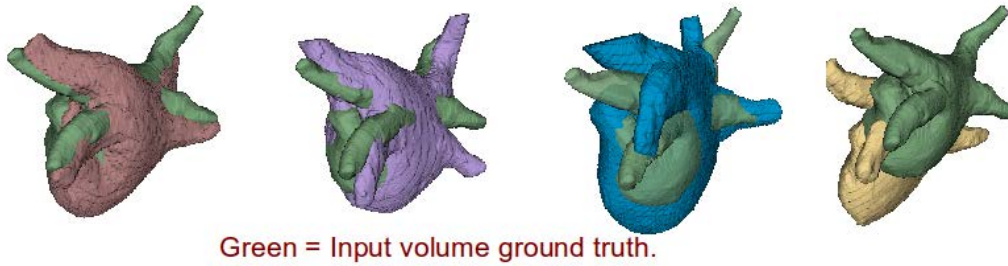


Figure 3.4: Four examples of alignments after global affine registration. The ground truth of the image to segment is presented in green.

Table 3.1: Images ranked according to the final value of the similarity measure in the affine registration from the  $A_i$ s to  $A_1$  (chosen as input image). Results for MS, NCC and MI with/without ROI are shown.

ROI	Similarity measure	1st	2nd	3rd	4th	5th	6th	7th	8th	9th
with	MS	2	3	7	6	5	4	8	9	10
	NCC	2	7	6	4	5	8	3	9	10
	MI	4	3	6	5	7	8	9	10	2
without	MS	5	2	6	3	8	9	7	10	4
	NCC	5	3	2	6	9	7	8	4	10
	MI	5	10	9	6	3	8	7	4	2

Table 3.2 presents the corresponding Dice values between  $A_1$  and the ranked images in the order of Table 3.1. In general, the affine registration reaches an average Dice score between 33% and 82%. A low Dice index would lead to a weak initialization of the next stage (elastic registration). This is the case of using MI without ROI which obtained the worst Dice. It can be observed that using a ROI improves the performance.

Table 3.2: Dice index between the ground truth of  $A_1$  and the atlas ground-truth aligned using the estimated affine transformation. Results for MS, NCC and MI with/without ROI are shown.

ROI	Similarity measure	1st	2nd	3rd	4th	5th	6th	7th	8th	9th
with	MS	82.0	80.3	64.1	79.5	72.6	74.7	67.1	77.5	66.2
	NCC	81.9	65.3	79.2	74.5	72.9	68.1	9.8	77.2	71.2
	MI	81.6	83.3	82.4	75.2	66.7	77.8	81.5	69.1	1.2
	Mean	81.8	76.3	75.2	76.4	70.7	73.5	52.8	74.6	46.2
without	MS	72.0	67.1	75.4	26.3	63.4	57.7	68.0	37.9	59.6
	NCC	70.6	68.1	66.3	75.0	58.4	65.3	63.5	58.9	37.6
	MI	54.7	35.5	41.3	67.3	21.6	51.2	67.3	0.8	10.7
	Mean	65.8	56.9	61	56.2	47.8	58.1	66.3	32.5	36

### 3.2.2.2 Elastic registration

The result of elastic registration is presented in Figure 3.5. For 3 examples, the alignment before (top) and after (bottom) elastic registration can be seen. When the images have a good initialization (example on the left) the elastic stage deformed appropriately the model. In contrary the deformation of the elastic registration could not overcome a bad initialization or a significant difference in anatomical shape or size (right).

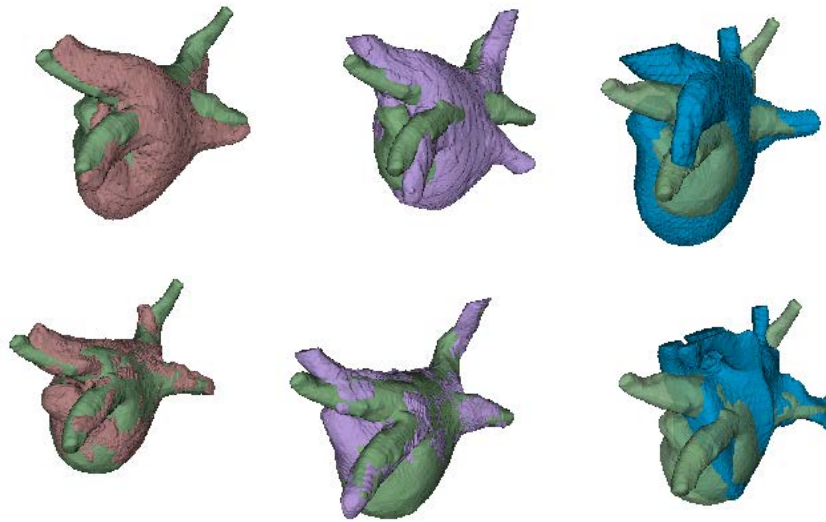


Figure 3.5: Three examples of alignments before (top) and after (bottom) elastic registration.

### 3.2.2.3 Fusion

The final registration result is obtained from the fusion of the  $M$  labeled images after elastic registration. Figure 3.6, presents an example of the fusion stage. The inputs of a fused stage are the labeled images after elastic registration. Using the fusion rule each pixel was evaluated and marked as part of the LA and PVs or as background. The example in the Figure 3.6 shows the fusion of 3 volumes by a majority voting rule. The voxels labeled as LA and PVs in more than two volumes are labeled as LA and PVs in the fusion resulting volume. We can see, that the result is a good approximation of the ground truth. With the fusion rule the remaining error introduced by some incorrect elastic registration was avoided.

The question we try to solve is about the optimal number of volumes used as input for the fusion step. Table 3.3 gives the Dice indexes when two to seven images are used in the fusion step. In general, Dice indexes are above 90% and are improved when using a ROI. The best performance was obtained for MS. Despite the low affine Dice index for MI without ROI, the fusion rule increased the index for this case to a value comparable to the other metrics.

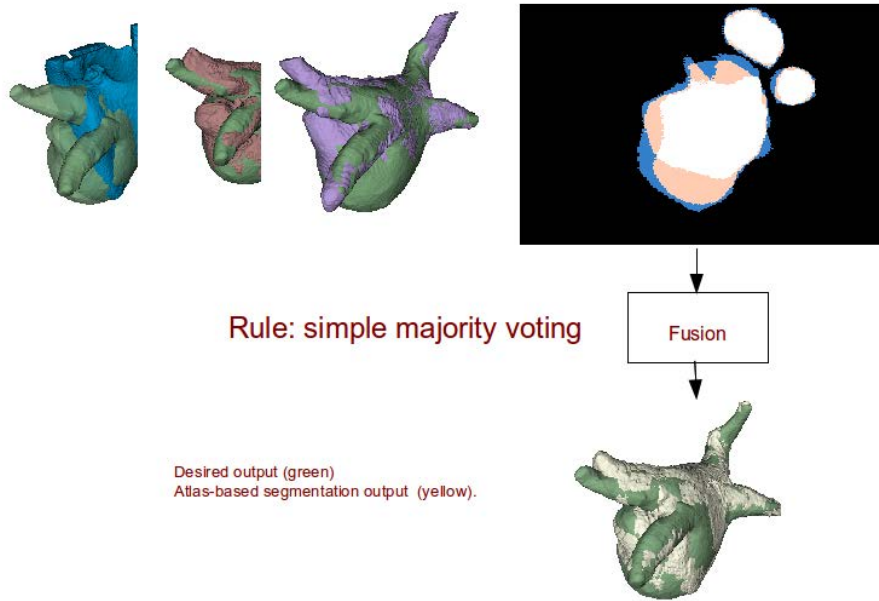


Figure 3.6: Fusion process with three images. Result using simple majority voting.

Table 3.3: Influence of the number  $M$  of images used in the fusion process. Dice index between the ground truth of  $A_1$  and the labeled result of the fusion. Results for MS, NCC and MI similarity metrics with/without ROI.

ROI	Similarity measure	Number $M$ of images used in fusion					
		2	3	4	5	6	7
with	MS	93.9	88.2	91.6	90.9	94.4	91.9
	NCC	92.7	92.5	94.2	93.5	93.4	92.0
	MI	93.2	92.1	93.3	91.5	93.0	92.3
without	MS	85.6	93.8	92.1	94.2	93.6	92.9
	NCC	89.1	92.7	93.8	88.6	89.1	88.0
	MI	91.4	84.8	88.6	86.7	89.4	86.9

### 3.2.2.4 Contribution of the region growing

The result of the atlas-based method is only a coarse approximation of the desired segmentation. Several reasons can explain this fact. Intrinsically the process of deformation of the segmentation of some subjects to obtain the desired segmentation is subject to errors. Also, the intensity-based comparison in the affine and elastic registration processes can lead to deformation overflow to other organs with the same intensity values. As said previously the region growing step is supposed to refine the segmentation within a specific search region around the atlas-based result. To obtain the limits of this region we eroded and dilated the atlas-based result. The search region is formed by all pixels located between these limits. In Figure 3.7 one example of search region is presented. We can see that the search region allowed to avoid the over- or sub-segmentations errors of the atlas-based result.

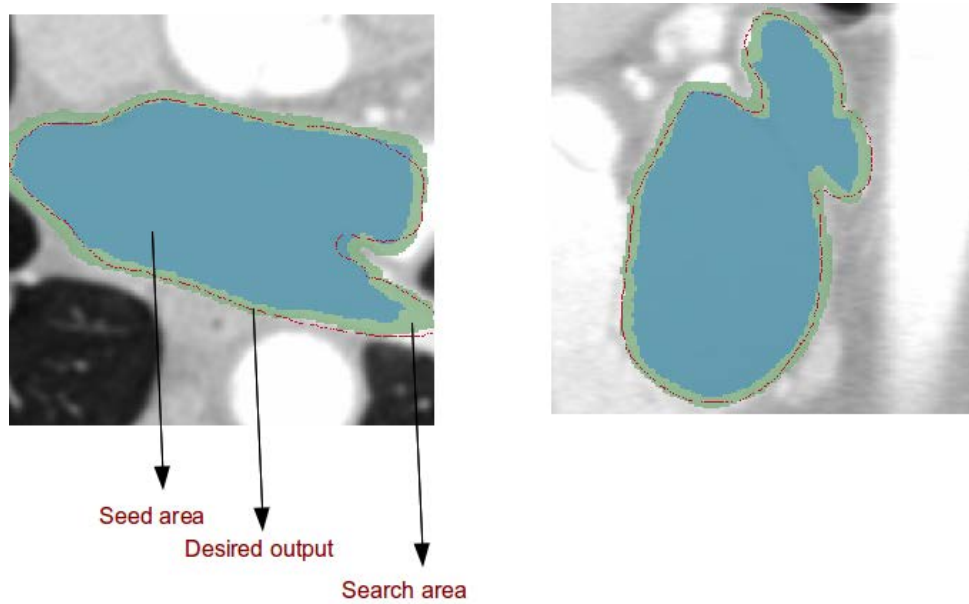


Figure 3.7: Search area for the region growing method.

In Figure 3.8, one example of the results of the region growing is presented and compared to the ground truth. We can see that the definition of a search region avoided the leakage towards close organs. The region growing process mainly refined the contour estimation in most regions even if some over- or sub-segmentation remained.

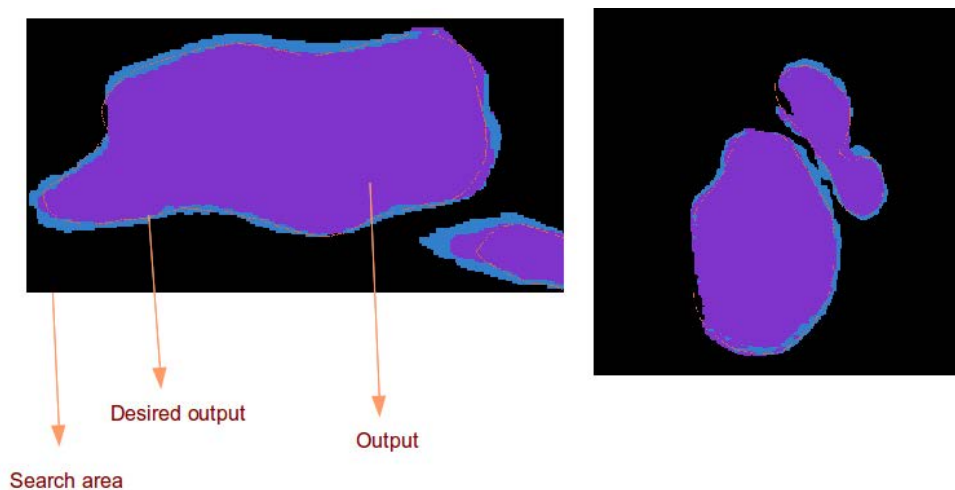


Figure 3.8: Results after region growing step.

Table 3.4 shows the influence of the region growing step. It presents the Dice indexes after the region growing step initialized by the result of the atlas-based method. Because the region growing step is directly influenced by the seed and the search area, we tried to estimate the

influence of the similarity metrics and the number  $M$  of atlases used for the fusion on the global framework. The region growing approach improved the Dice score for the tests without ROI especially when less of five images are used in the fusion. The best Dice score (95%) was obtained for MS without ROI and using five images in the fusion step. But globally, the Dice values are high no matter the number of images used in the fusion.

Table 3.4: Dice index between the ground truth of  $A_1$  and the region growing output. Results for MS, NCC and MI similarity metrics with/without ROI.

ROI	Similarity measure	Number of images used in fusion					
		2	3	4	5	6	7
with	MS	93.6	87.7	91.2	90.5	93.6	91.3
	NCC	92.7	92.0	93.4	92.9	92.7	91.3
	MI	92.8	91.2	92.3	90.6	92.0	91.4
without	MS	87.0	94.2	94.8	95.0	94.6	93.3
	NCC	90.7	93.9	94.6	88.9	89.6	88.7
	MI	93.1	84.9	89.5	87.0	90.1	87.4

### 3.2.2.5 Conclusion on the method tuning

The segmentation of LA and PVs was presented first using an atlas-based segmentation to compute an approximation of the structures and then a region growing procedure to obtain the anatomical details. Three similarity measures were tested with/without using a ROI in the registration procedures. The atlas-based segmentation reached a Dice score of 94% using the MS metric with or without ROI as seen in 3.4.

We also performed a similar tuning on the MRI dataset. The behavior of the tests was similar to this noticed for the CT data. The only main difference is that it was the Mutual Information metric which performed the best results

As a conclusion, the tuning process allows to define three parameters: (1) *registration without ROI*, (2) for CT the *Means square* and for MRI, the *Mutual Information* similarity measures will be used for affine and elastic registration and (3) we will use *the five best ranked images* for the fusion.

### 3.2.3 Evaluation of CT and MRI segmentation: left atrium and pulmonary veins challenge

We evaluated and compared our method within the framework defined by the Left Atrial Segmentation Challenge (LASC) carried out at the STACOM'13 workshop in conjunction with MICCAI'13 (TOBON-GOMEZ et al. 2013) followed by a more informal multicenter study (TOBON-

GOMEZ et al. 2015).

LASC encouraged participants to segment the LA including a short part of the LAA and the proximal section of the PVs on CT data, while the multicenter study complemented the evaluation process on MRI acquisitions. The role of the organizing committee of these 2 studies was to develop and provide the benchmark for the evaluation and comparison of the proposed algorithms: dataset, ground truth, standardization criterion and performance measures.

We participated to these 2 studies by proposing two versions of our segmentation algorithms: (1) the multi-atlas method using a multi-voting as fusion rule and after a region growing; and (2) the multi-atlas method using STAPLE as fusion rule and after a region growing. We tested these algorithms for MRI and CT modalities.

### 3.2.3.1 Evaluation framework

The evaluation data was this previously described in section 3.2.1. For each modality the organizing committee proposed a set of 20 volumes without the associated ground truth.

Each participant segmented this data with his proposed method and sent the segmentation results to the organizing committee. The committee compared and evaluated the performance of the several segmentation results to their hidden ground truth using two metrics: surface to-surface distance (S2S) and Dice coefficient (DC).

For computing S2S, the committee automatically create a standardized corresponding mesh of the ground truth and the several results. S2S is the symmetrical mean distance between corresponding points of these 2 meshes. To normalize the contribution of each case to the average S2S metric, distance measurements were subsampled to 2000 random samples (per case and per region) using a bootstrapping approach. Low values of S2S represent higher accuracy.

Dice coefficient was explained before in eq. 3.2.

These two metrics were also combined into a unified score. To equalize the contribution of both metrics, each error measurement was normalized such that:

$$Z_{reg,p} = \frac{x_p - \mu}{\sigma} \quad (3.3)$$

where  $reg$  is the anatomical region (LA *-body-* and pulmonary veins *-PVs-*),  $x_p$  is the median metric of each participant  $p$ ,  $\mu$  and  $\sigma$  are respectively the mean and the standard deviation of the median metric of all participants.

Given that S2S best reflects segmentation accuracy for the LA body, while DC best reflects the segmentation accuracy for the PVs (TOBON-GOMEZ et al. 2015), the unified score  $S_p$  for each participant  $p$  was computed as:

$$S_p = \frac{Z_{S2S_{body,p}} + Z_{(1-DC)_{PVs,p}}}{2} \quad (3.4)$$

In this score, the average accuracy of all the evaluated methods is equal to 0. So lower values represent higher accuracy.

### 3.2.3.2 Challenge results

Eleven different algorithms provided by 7 international groups were evaluated and compared. Each algorithm was different in methodology and implementation. The tendencies of this collection of algorithms were: (1) a preprocessing procedure such as histogram normalization, volume of interest selection or atrial body localization; (2) main segmentation using region growing, random decision forest, multi-atlas or shape-model; (3) optimization of the segmentation using region growing or snakes (overall or limited to PVs); (4) a post processing procedure such as hole filling or graph cuts.

#### Results on MRI database

First we compare the results obtained by the *majority voting fusion rule vs. the STAPLE fusion rule*.

Three results for each algorithm on the MRI datasets are presented in Figure 3.9. These results correspond to a high quality image with a high contrast. The ground truth is located on the superior row of the figure. We can notice that for STAPLE the surfaces seem to be under-estimated.

Figure 3.10 shows some results obtained on low quality image. The ground truth is located on the superior row of the figure. In this case, we can notice that it is sometimes difficult to separate different structures of the heart due to the low contrast on their boundaries. So the results were overflowed to other structures. One explanation could be that it is the elastic registration stage who generates this overflow instead of region growing. This because the similarity metric used in this stage is sensitive to low contrast between structures and to inhomogeneities inside the structure. Moreover, the size of the search region for the region growing approach is smaller than the irregularities noticed in the results.

Table 3.5 presents the S2S distance values between the surfaces of the ground truth and the surfaces of the result obtained by our two proposed algorithms. Both algorithms show a good performance, however S2S is below 1mm on the results obtained using the voting fusion rule. This result should be noticed because literature generally states that the segmentation MRI is

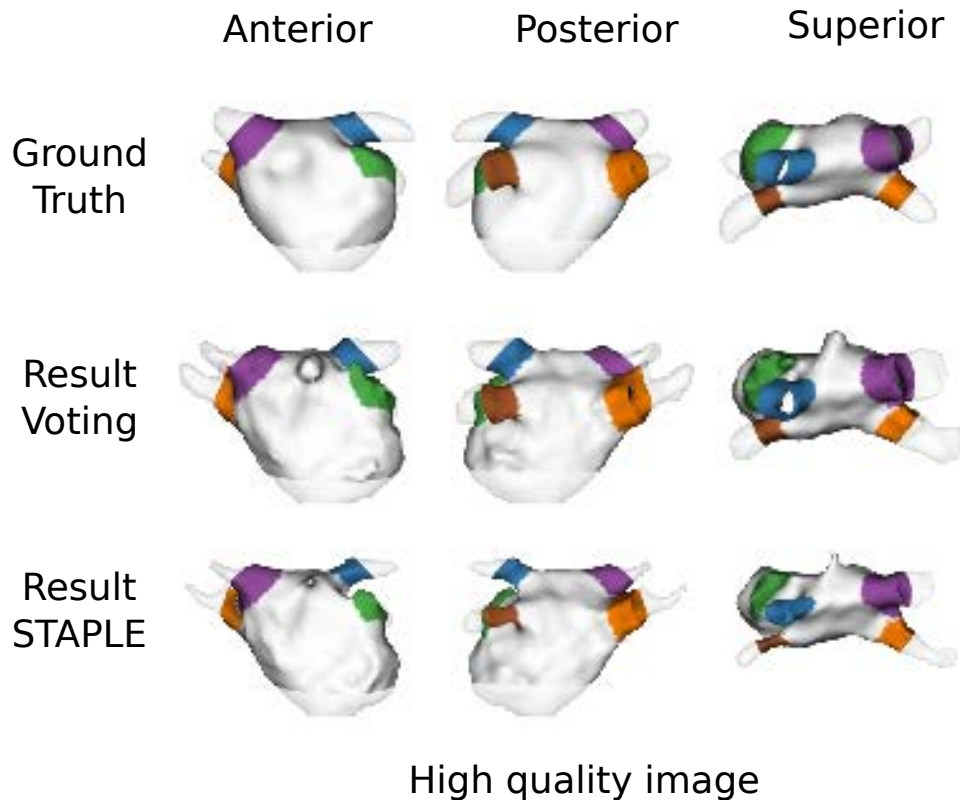


Figure 3.9: Results of our algorithms on high quality MRI data (TOBON-GOMEZ et al. 2015). The ground truth is located on the superior row of the figure.

challenging because its lower spatial resolution and intensity inhomogeneities.

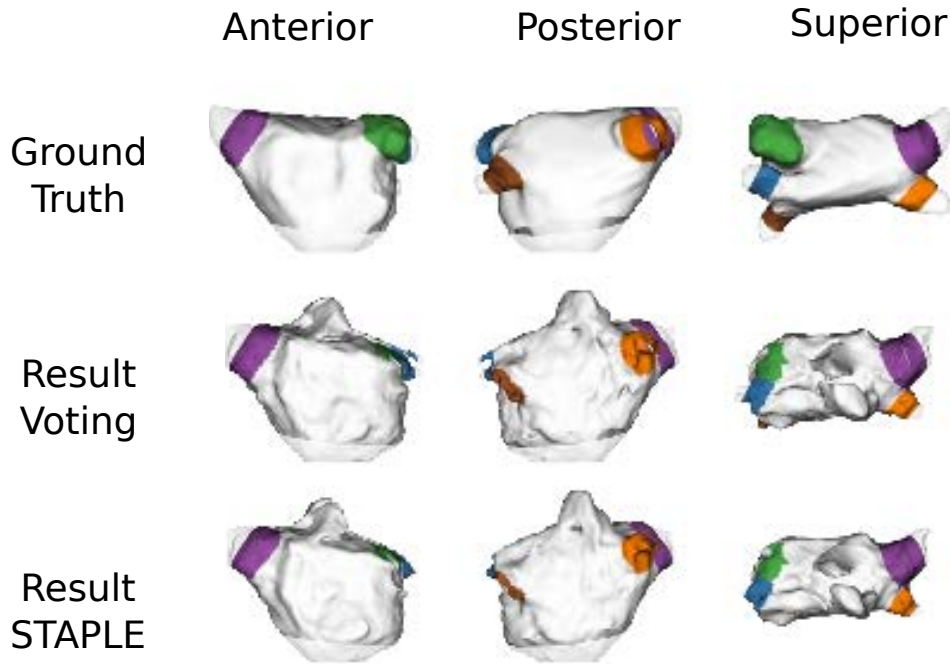
Table 3.5: Results on MRI. Median of the distance surface-to-surface (S2S) between the surface of the ground truth and the surface obtained by our algorithms for LA body and PVs. Ideally  $S2S = 0\text{mm}$ .

Method	median S2S of LA body (mm)	median S2S of PVs (mm)
Multi-atlas (Voting) + RG	$0.886 \pm 2.18$	$1.199 \pm 2.34$
Multi-atlas (STAPLE) + RG	$2.091 \pm 1.59$	$2.251 \pm 1.84$

The Dice scores between the ground truth volumes and our resulting volumes obtained by our algorithms are presented in Table 3.6. We can see the same tendency as the S2S metric. A good performance for both algorithms with a better score using the voting fusion rule. However, the error in the PVs is easier to perceive with Dice score. We can see lower performance when segmenting the PVs using STAPLE in the fusion step.

In general, the behavior of our two proposed algorithms is good. The difference between them is the method used in the fusion step. Although STAPLE is a more specialized method than the majority voting, we believe that the lower accuracy is caused by the fact that STAPLE





### Low quality image

Figure 3.10: Results of our algorithms on low quality MRI data (TOBON-GOMEZ et al. 2015). The ground truth is located on the superior row of the figure.

Table 3.6: Results on MRI. Median of the Dice scores (DC) between the ground truth volume and the volume obtained by our algorithms for LA body and PVs. Ideally  $DC = 1$ .

Method	median Dice value of LA body	median Dice value of PVs
Multi-atlas (Voting) + RG	$0.931 \pm 0.04$	$0.696 \pm 0.16$
Multi-atlas (STAPLE) + RG	$0.881 \pm 0.02$	$0.507 \pm 0.19$

is more sensitive to inputs with a big error in segmentation. This conclusion coincide with the conclusion set in (ACOSTA et al. 2011).

The Unified scores (eq. 3.3 and 3.4) is used to *compare our results to these of the other 9 algorithms*. This score combines the S2S and Dice to show a general performance (see section 3.2.3.1). In this score, zero represents the average accuracy of all evaluated methods. As lower the score as more accurate is the method.

Figure 3.11 shows the unified score of all the methods evaluated in the study. Our algorithms are labeled as *LTSI\_VRG* (using majority voting) and *LTSI\_VSRG* (using STAPLE). *OBS\_2* is the score obtained by the ground truth generation process (see section 3.2.1) using a second manual correction by an other human expert. *OBS\_2* is used to estimate interobserver variability.

If our approach using STAPLE for fusion obtained a score below the average accuracy, it can be noticed that our approach using majority voting had *the best score* among all the algorithms. In fact the score is the same as this obtained by OBS\_2.

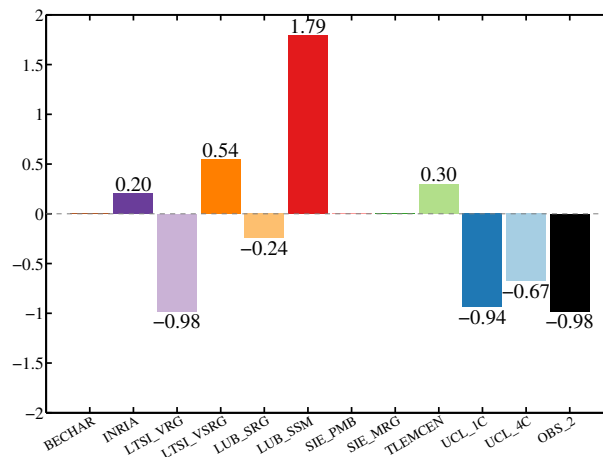


Figure 3.11: Unified scores for MRI (TOBON-GOMEZ et al. 2015). These scores combine the S2S and Dice to show a general performance of the algorithms in the segmentation of the LA body and PVs. Our algorithms are labeled as LTSI\_VRG (using majority voting) and LTSI\_VSRG (using STAPLE). OBS\_2 represents the interobserver variability.

### Results on CT datasets

We performed a similar evaluation as for MRI.

In order to compare the results obtained using majority voting to this obtained using STAPLE, Figure 3.12 and Figure 3.13 present some results obtained on respectively high quality CTs with a high contrast and low quality CTs. In both cases, the ground truth is located on the superior row of the figure. For high quality CTs, the performance for both algorithms is similar with results close to the ground truth. Some small irregularities can be perceived in the mesh obtained using STAPLE. For low quality CTs, as for the MRI case, it is difficult to separate different structures of the heart due to the low contrast in their boundaries. It can also be observed that both methods underestimate the volumes. Here also we believe that the elastic registration stage generates this under-segmentation.

The median distance value between the ground truth and the results of our both algorithms is presented in Table 3.7. The median distance value is also lower than 1mm using the majority voting, and close to 1 for STAPLE. The behavior of both algorithms is relatively similar. This can

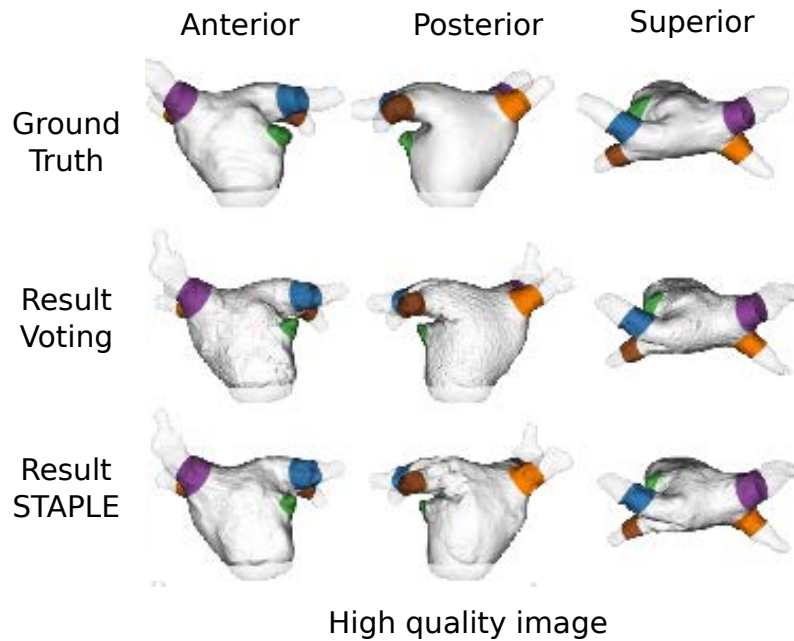


Figure 3.12: Results of our algorithms on high quality CT data (TOBON-GOMEZ et al. 2015). The ground truth is located on the superior row of the figure.

be due by the fact that the contrast and homogeneity are better on CT images than MRI. Except in the cases of poor image contrast, CT dataset gives a clear visualization of the structures. The contrast in the boundaries between the structures of the heart and the homogeneity inside the cavities are more constant in CT images. This can explain the fact that the S2S values were

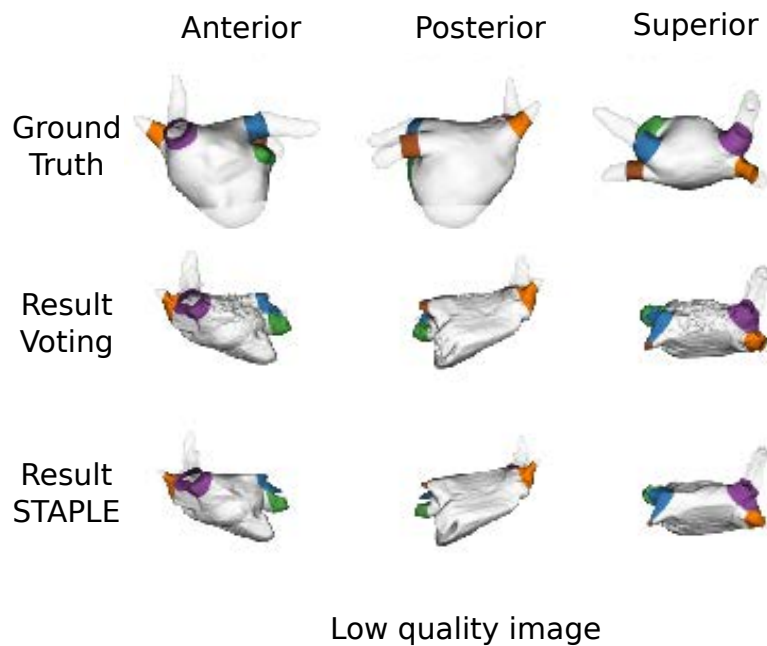


Figure 3.13: Results of our algorithms on low quality CT data (TOBON-GOMEZ et al. 2015). The ground truth is located on the superior row of the figure.

very similar for the LA body and the PVs.

Table 3.7: Results on CT data. Median of the distance surface-to-surface (S2S) between the surface of the ground truth and the surface obtained by our algorithms for LA body and PVs. Ideally  $S2S = 0\text{mm}$ .

Method	median S2S of LA body (mm)	median S2S of PVs (mm)
Multi-atlas (Voting) + RG	$0.871 \pm 3.31$	$0.89 \pm 2.44$
Multi-atlas (STAPLE) + RG	$1.264 \pm 3.32$	$1.18. \pm 2.33$

The Dice scores between ground truth and the result for our algorithms are presented in Table 3.8. These Dice scores are similar to values shown in the state of the art (see section 2.4.3). The behavior of both algorithms is relatively similar with slightly better scores using majority voting than STAPLE. Majority voting seems to be a more robust method that overtake the irregularities of the inputs.

Table 3.8: Results on CT data. Median Dice score (DC) between the ground truth volume and the volumes obtained by our algorithms for LA body and PVs. Ideally  $DC = 1$ .

Method	median Dice value of LA body	median Dice value of PVs
Multi-atlas (Voting) + RG	$0.887 \pm 0.10$	$0.769 \pm 0.22$
Multi-atlas (STAPLE) + RG	$0.865 \pm 0.12$	$0.726 \pm 0.24$

Here also we compare our methods to the others algorithms of the challenge (see Figure 3.14). In the CT case, our algorithms obtained a performance close to the average with slightly better scores using majority voting.

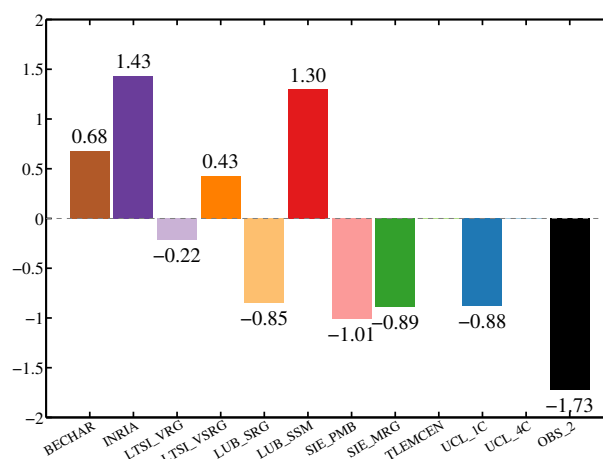


Figure 3.14: Unified scores for CT data (TOBON-GOMEZ et al. 2015). These scores combine the S2S and Dice to show a general performance of the algorithms in the segmentation of the LA body and PVs. Our algorithms are labeled as LTSI\_VRG (using majority voting) and LTSI\_VSRG (using STAPLE). OBS\_2 represents the interobserver variability.

### 3.3 Conclusion

We have proposed a refined atlas-based segmentation of the LA and PVs. This approach combines two classical methods to obtain first a coarse approximation of the structures and then a detailed delineation of the patient specific anatomy. Parameters of the atlas approach were tuned for MRI and CT cardiac images. The accuracy of our proposed method was measured using an external available evaluation tool. The quantitative results show a good performance of our method especially for MRI modality.

### References

- ACOSTA, O., A. SIMON, F. MONGE, F. COMMANDEUR, C. BASSIROU, G. CAZOULAT, R. DE CREVOISIER, and P. HAIGRON (2011). “Evaluation of multi-atlas-based segmentation of CT scans in prostate cancer radiotherapy”. In: *8th IEEE International Symposium on Biomedical Imaging (ISBI)*. Chicago, pp. 1966–1969.
- CONSTANCIEL, E., W. N’DJIN, F. BESSIERE, F. CHAVRIER, D. GRINBERG, A. VIGNOT, P. CHEVALIER, J. CHAPELON, and C. LAFON (2013). “Design and evaluation of a transesophageal HIFU probe for ultrasound-guided cardiac ablation: simulation of a HIFU mini-maze procedure and preliminary ex vivo trials”. In: *IEEE Transactions on Ultrasonics, Ferroelectrics, and Frequency Control* 60.9, pp. 1868–1883.
- ECABERT, O., J. PETERS, H. SCHRAMM, C. LORENZ, J. VON BERG, M. WALKER, M. VEMBAR, M. OLSZEWSKI, K. SUBRAMANYAN, G. LAVI, and J. WEESE (2008). “Automatic model-based segmentation of the heart in CT images”. In: *IEEE Transactions on Medical Imaging* 27.9, pp. 1189–1201.
- HO, S. Y., J. A. CABRERA, and D. SANCHEZ-QUINTANA (2012). “Left atrial anatomy revisited”. In: *Circulation: Arrhythmia and Electrophysiology* 5.1, pp. 220–228.
- KARIM, R., R. MOHIADDIN, and D. RUECKERT (2008). “Left atrium segmentation for atrial fibrillation ablation”. In: *Proc. SPIE*. Vol. 6918. San Diego, 69182U–69182U–8.
- LEUNG, K., J. BARNES, M. MODAT, G. RIDGWAY, J. BARTLETT, N. FOX, and S. OURSELIN (2011). “Automated brain extraction using Multi-Atlas Propagation and Segmentation (MAPS)”. In: *8th IEEE International Symposium on Biomedical Imaging (ISBI)*. Chicago, pp. 2053–2056.
- SCHWARTZMAN, D., J. LACOMIS, and W. G. WIGGINTON (2003). “Characterization of left atrium and distal pulmonary vein morphology using multidimensional computed tomography”. In: *Journal of the American College of Cardiology* 41.8, pp. 1349–1357.
- TOBON-GOMEZ, C., A. GEERS, J. PETERS, J. WEESE, K. PINTO, R. KARIM, M. AMMAR, A. DAOUDI, J. MARGETA, Z. SANDOVAL, B. STENDER, Y. ZHENG, M. ZULUAGA, J. BETANCUR, N. AYACHE, M. CHIKH, J. DILLENSEGER, M. KELM, S. OURSELIN, A. SCHLAEFER, T. SCHAEFFTER, R. RAZAVI, and K. RHODE (2015). “Benchmark for algorithms segmenting

- the left atrium from 3D CT and MRI datasets”. In: *IEEE Transactions on Medical Imaging* PP.99, pp. 1–1.
- TOBON-GOMEZ, C., J. PETERS, J. WEESE, K. PINTO, R. KARIM, T. SCHAEFFTER, R. RAZAVI, and K. S. RHODE (2013). “Left Atrial Segmentation Challenge: a unified benchmarking framework.” In: *Statistical Atlases and Computational Models of the Heart. Imaging and Modelling Challenges*. Ed. by O. CAMARA, T. MANSI, M. POP, K. S. RHODE, M. SERMESANT, and A. A. YOUNG. Vol. 8330. Lecture Notes in Computer Science. Nagoya: Springer, pp. 1–13.
- WARFIELD, S., K. ZOU, and W. WELLS (2004). “Simultaneous truth and performance level estimation (STAPLE): an algorithm for the validation of image segmentation”. In: *IEEE Transactions on Medical Imaging* 23.7, pp. 903–921.
- ZHENG, Y., M. JOHN, J. BOESE, and D. COMANICIU (2012). “Precise segmentation of the left atrium in C-arm CT volumes with applications to atrial fibrillation ablation”. In: *9th IEEE International Symposium on Biomedical Imaging (ISBI)*, pp. 1421–1424.
- ZHU, L., Y. GAO, A. YEZZI, R. MACLEOD, J. CATES, and A. TANNENBAUM (2012). “Automatic segmentation of the left atrium from MRI images using salient feature and contour evolution”. In: *Engineering in Medicine and Biology Society (EMBC), 2012 Annual International Conference of the IEEE*. San Diego, pp. 3211–3214.
- ZULUAGA, M. A., M. J. CARDOSO, M. MODAT, and S. OURSELIN (2013). “Multi-atlas propagation whole heart segmentation from MRI and CTA using a local normalised correlation coefficient criterion”. In: *Functional Imaging and Modeling of the Heart, Proceedings of the 7th International Conference on. FIMH’13*. London, UK: Springer-Verlag, pp. 174–181.



# Therapy-adapted preoperative volume reconstruction

The transesophageal AF therapy can only be performed under image guidance. For this, as previously mentioned in section 1.3.2.2, the transesophageal HIFU probe includes a 2D-US transducer at its center. This imaging transducer allows to acquire 2D-US images in an axial plane perpendicular to the probe axis (the same orientation of a zero degree angle in the classical multiplane TEE devices).

We assume that the probe's trajectory is constrained by the esophagus. This assumption seems to be justified because the esophagus in the human body is constrained by its surrounding organs or tissues such as the vertebral column, trachea, carotid-jugular vascularization, aortic arch, right pulmonary artery, left main bronchus, left atrium, diaphragm and so on.

The consequence of this assumption is that the cardiac volume will be explored by the TEE probe always in the same way according to the topology of the esophagus. In order to prepare the planning of the probe navigation during the AF procedure, we propose to *reconstruct the CT/MRI volumes according to the future ultrasound probe positions*.

For a specific US image, its origin (the apex of the image sector) is given by the position (the depth  $d$ ) of the probe along the esophagus, the image sector is on the plane perpendicular to the esophagus centerline at a specific orientation around this centerline (see Figure 4.1).

We propose to integrate these geometrical constraints in our navigation planning by resampling the preoperative CT volume according to the trajectory of the esophagus centerline. The resampling can be seen as a set of consecutive image planes perpendicular to the esophagus' centerline (see Figure 4.1).



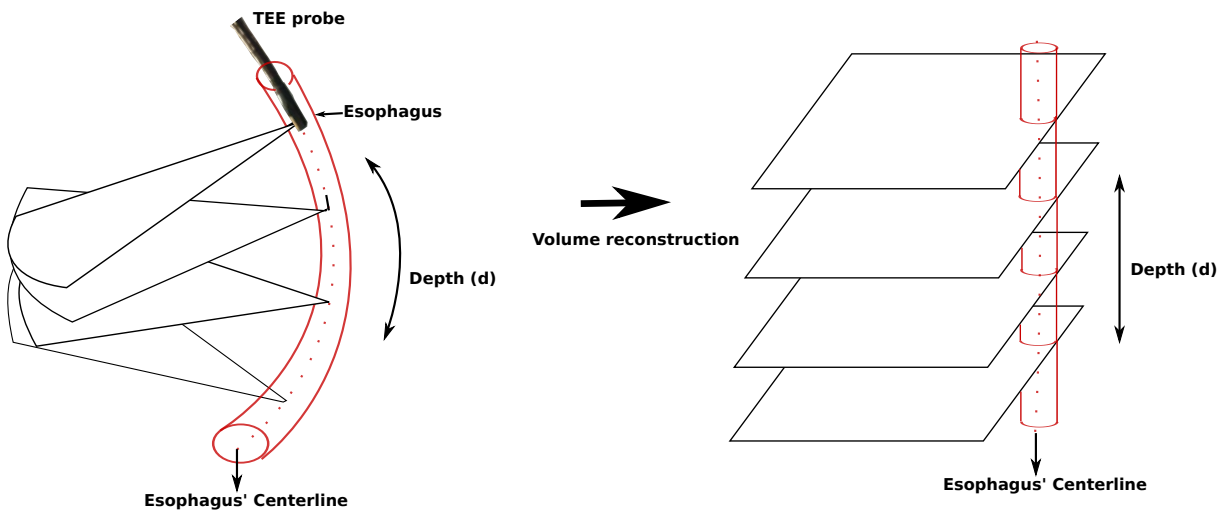


Figure 4.1: Therapy-adapted preoperative volume reconstruction.

## 4.1 Methods

The procedure to reconstruct the therapy-adapted preoperative CT/MRI image is presented in Figure 4.2. It is divided into three steps: (1) the segmentation of the esophagus from the preoperative volume; (2) the definition of the centerline as a smooth spline function; and (3) the resampling of the CT using the centerline information.

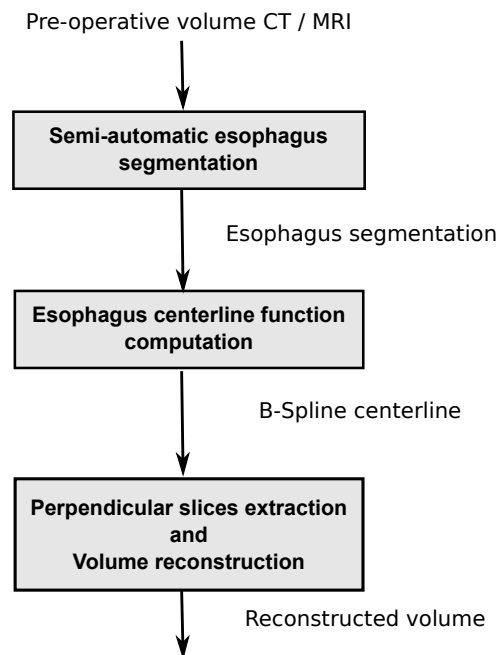


Figure 4.2: Block diagram of the therapy-adapted preoperative volume reconstruction procedure.

### 4.1.1 Semi-automatic esophagus segmentation

First, the inner surface of the esophagus is extracted from the preoperative volume using the ITKSNAP<sup>1</sup> implementation of the *active contour* segmentation (YUSHKEVICH et al. 2006). The active contour method is based on snake evolution. Snake is the name given to a closed curve (or surface) that represents the object we wish to segment. The snake is composed by a set of points  $\mathbf{C}$  linked by a curve or surface model.

Usually an initial snake is set inside the shape to segment. The snake is then governed by image forces that try to expand it towards object contours and internal forces that resist to the deformations. The evolution of the snake is governed by the front propagation equation. This equation describes the velocity of every point  $C_t$  in the snake ( $C_t \in \mathbf{C}_t$ ) at any particular time ( $t$ ) and is given by:

$$\mathbf{C}_t = (\alpha \mathbf{g}_I - \beta \mathbf{k}) \vec{\mathbf{n}} \quad (4.1)$$

where  $\alpha$  and  $\beta$  are user-defined factors weighting respectively the feature-based propagation force term and the curvature term.  $\vec{\mathbf{n}} \in \vec{\mathbf{n}}$  is the normal vector for a given point,  $g_I \in \mathbf{g}_I$  the region feature image (cf. step 2 below) component at that point and  $k \in \mathbf{k}$  the  $k$ -level curvature at that point. The value of  $k$ , which is computed at each iteration, controls the shape of the evolving snake. Sharp corners in the snake boundary have high curvature, while points where the snake is straight have low curvature. The effect of the  $-\beta k$  component is to slow down the evolution of the snake at the places of high curvature, smoothing out the sharp corners that may otherwise be formed.

The segmentation of the esophagus is performed using the following steps (Figure 4.3):

1. **ROI selection.** First, an esophageal region of interest (ROI) is interactively defined by the user.
2. **Intensity region filtering.** In Equation (4.1), we used a region competition image as the feature image instead of an edge-based one. The region competition image represents the regions with homogeneous intensity value. This feature image is computed by thresholding the intensities such that the esophagus appears in the foreground and the surrounding tissues in the background. The parameters used for the thresholding procedure are set interactively by the user.
3. **Seed region initialization.** The active contour segmentation is initialized by spherical surfaces covering the esophagus along its major axis.

---

1. <http://www.itksnap.org>

4. **Snake evolution.** This procedure is started to fit the boundaries of the initial snake (spheres) to the boundaries of the esophagus, using Equation (4.1).  $\alpha$  and  $\beta$  were set by the user (typical values were  $\alpha = 1.0$  and  $\beta = 0.3$ ).

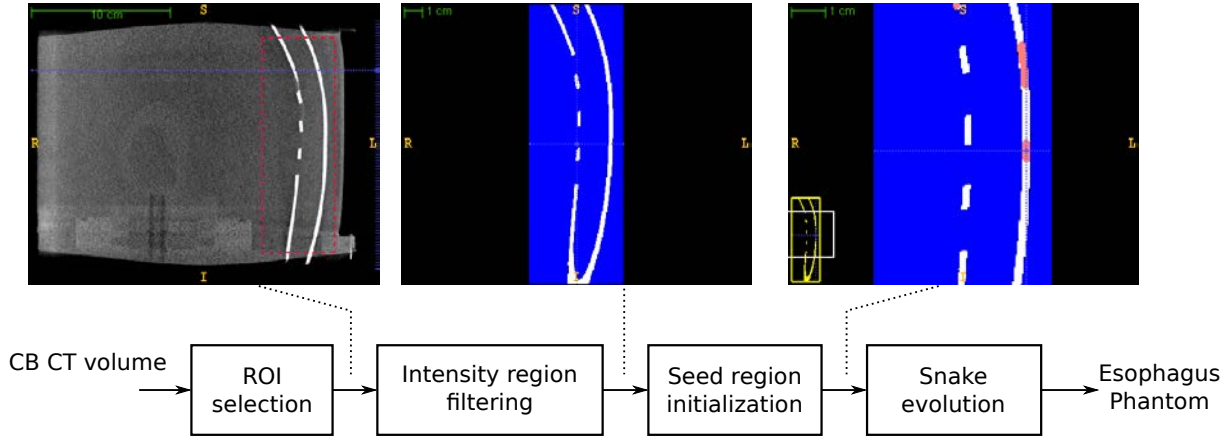


Figure 4.3: Block diagram of the esophagus segmentation process using ITKSNAP.

#### 4.1.2 Esophagus centerline curve estimation

First the segmentation of the esophagus in the CT volume is used to define a point  $E_i$  of the centerline at each axial slice of the CT volume.  $E_i$  is the mean position of the segmented esophagus at each slice of the CT volume. This gives us a set  $E = \{E_1, E_2, \dots, E_N\}$  with  $E_i = (x_i, y_i, z_i)$  a point supposed to be on centerline.

In order to obtain a smooth centerline, we fit a cubic smoothing spline functions  $f$  to the set of points defined previously. In fact, three smoothing splines  $f_x, f_y$  and  $f_z$  are fit to  $E$  (one per spatial coordinate). For instance,  $f_x$  minimizes (DE BOOR 1978):

$$p \sum_{j=0}^{N-1} |x_j - f_x(j)|^2 + (1-p) \int |D^2 f_x(t)|^2 dt \quad (4.2)$$

where  $|\bullet|^2$  stands for the sum of the squares of all the entries in  $\bullet$ ,  $D^2 f_x$  denotes the second derivative of the function  $f_x$ .  $p$  is a smoothing parameter controlling the trade-off between fidelity to the data and roughness of the function estimate.  $p$  can be a value from 0 (regression line) to 1 (go through all points).

Note that  $f_y$  and  $f_z$  are obtained by a straightforward modification of Equation (4.2).

$f_x$ ,  $f_y$  and  $f_z$  give the parametric 3D curve  $f(t)$  with  $t$  the parameter which allows to navigate along the esophagus. However, a regular variation of  $t$  can provide a non regular variation along the curve. A regular variation along the curve is given by the natural parameter  $s$  defined as:

$$s(t) = \int_{t_0}^t \|f'(u)\| du \quad (4.3)$$

In this case,  $s(t)$  is defined from the origin  $f(t_0)$ . With  $s$  we can now regularly sample the curve in order to create the "Depth" axis of the therapy-adapted preoperative volume (see Figure 4.1).

### 4.1.3 CT slices perpendicular to esophagus centerline

From the esophagus centerline function and its regular sampling, we will be able to reconstruct the therapy-adapted preoperative volume from the preoperative CT. Transformation  $T(d)$  is obtained to map the gray values from the original volume ( $V_{or}$ ) to reconstructed volume ( $V_{rec}$ ). Axis  $d$  corresponds to the esophagus centerline. For one value of  $d = d_\epsilon$ , a transformation  $T(d_\epsilon)$  is used.

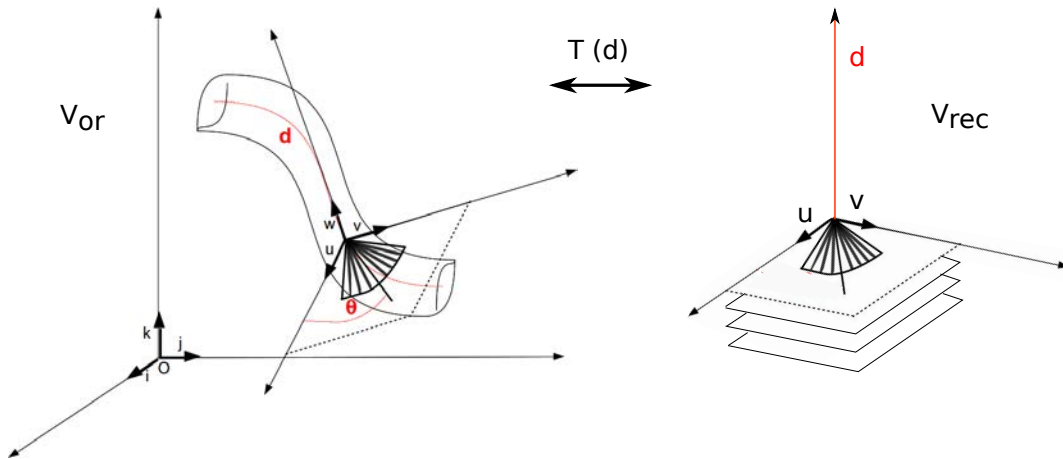


Figure 4.4: Reconstruction of the therapy-adapted preoperative volume. Transformation  $T(d)$  is obtained to map the gray values from the original volume ( $V_{or}$ ) to reconstructed volume ( $V_{rec}$ ). Axe  $d$  correspond to the esophagus centerline. For one valour of  $d = d_\epsilon$ , a transformation  $T(d_\epsilon)$  is used.

Let  $R = \{O; \vec{i}, \vec{j}, \vec{k}\}$  be the reference system of the CT volume in the physical space, with origin  $O$  and orthonormal vectors  $\vec{i}, \vec{j}, \vec{k}$  that define the system basis, see Figure 4.5. Assuming that we want to extract the plane at location  $d_1$  along the centerline. Let  $E_1$  be the 3D point which corresponds to  $d_1$ . The coordinates of  $E_1$  in  $R$  are given by:  $E_1 = (x_1, y_1, z_1)$ .

In order to extract the slice orthogonal to the centerline at  $d_1 = E_1$  we will define a new reference system  $R' = \{O'; \vec{u}, \vec{v}, \vec{w}\}$ , such that the origin  $O' = E_1$  and the vector  $\vec{w}$  be the tangent to the curve at  $E_1$  (see Figure 4.6). This new reference system correspond to the US plane acquired with the TEE probe at zero degree orientation. The goal of the reconstruction is to

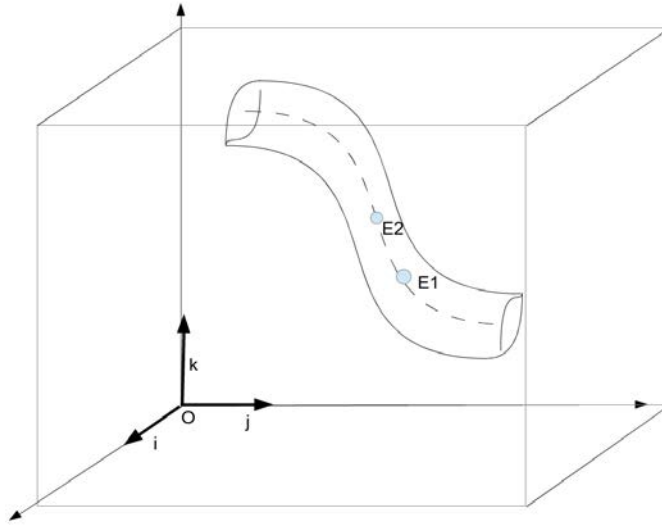


Figure 4.5: Reference system of the CT volume  $R = \{O; \vec{i}, \vec{j}, \vec{k}\}$ .  $E_1$  and  $E_2$  two consecutive points located respectively at  $d_1$  and  $d_2$  along the segmented esophagus centerline.

obtain the CT slice that correspond to the US plane acquired with the TEE probe at location  $E_1$ .

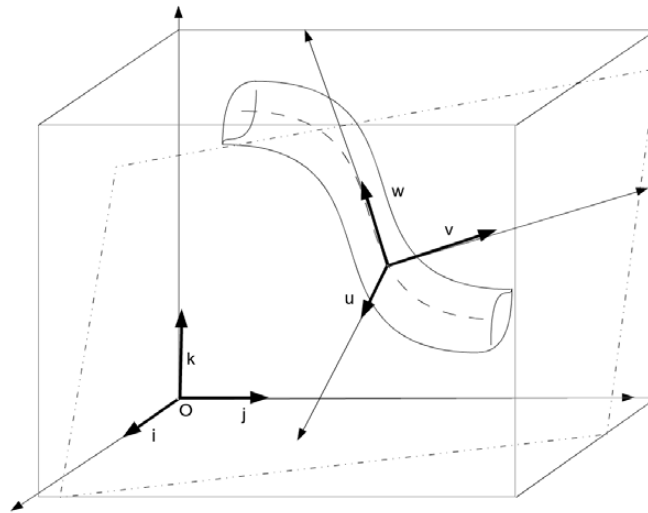


Figure 4.6: Reference systems of the reconstructed CT slice and the corresponding US acquisition at the point  $E_1$ .

The vector  $\vec{w}$  can be computed analytically by deriving  $f$  at  $E_1$  or numerically if we know a second point  $E_2 = (x_2, y_2, z_2)$  on the curve at  $d = d_2$  close to  $E_1$ . In this later case:

$$\vec{w} = \frac{(x_2 - x_1)}{N_w} \vec{i} + \frac{(y_2 - y_1)}{N_w} \vec{j} + \frac{(z_2 - z_1)}{N_w} \vec{k}, \quad (4.4)$$

where  $N_w = \sqrt{(x_2 - x_1)^2 + (y_2 - y_1)^2 + (z_2 - z_1)^2}$

The two other vectors  $\vec{u}$  and  $\vec{v}$  are perpendicular to  $\vec{w}$ . Arbitrary, we will set  $\vec{u}$  in a plane perpendicular to  $\vec{j}$ :

$$\vec{u} = \vec{w} \times \vec{j} \quad (4.5)$$

$\vec{v}$  is perpendicular simultaneously to  $\vec{u}$  and  $\vec{w}$ . It can be obtained by the following cross-product:

$$\vec{v} = \vec{u} \times \vec{w} \quad (4.6)$$

Finally, the basis defining the system  $R'$ , can be written in  $R$  as:

$$\vec{u} = a_{iu}\vec{i} + a_{ju}\vec{j} + a_{ku}\vec{k} \quad (4.7)$$

$$\vec{v} = a_{iv}\vec{i} + a_{jv}\vec{j} + a_{kv}\vec{k} \quad (4.8)$$

$$\vec{w} = a_{iw}\vec{i} + a_{jw}\vec{j} + a_{kw}\vec{k} \quad (4.9)$$

These vectors are drawn in green in the Figure 4.7.

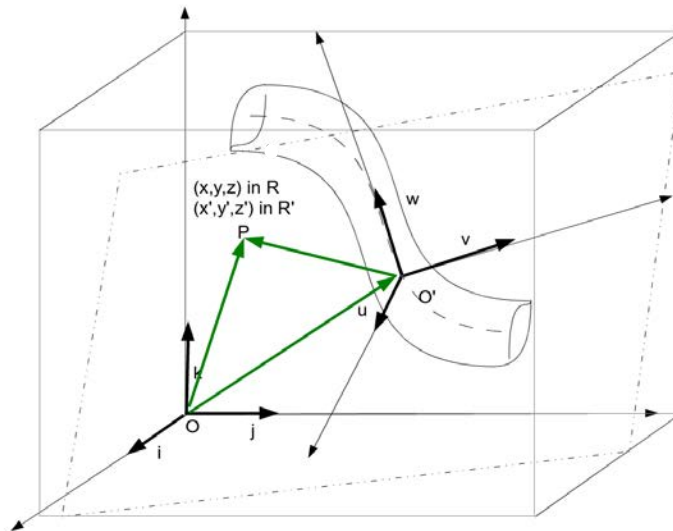


Figure 4.7: In green the three vectors that are used to obtain the corresponding position of the US-plane in the CT volume.

The plane of  $R'$  when  $\vec{w} = 0$ , corresponds to the US acquisition plane with the TEE probe at zero degree orientation positioned at location  $E_1$  inside the esophagus. We will reconstruct this plane from the preoperative CT by sampling the plane  $(x', y', 0)$  of  $R'$  and estimate the value on

these sampling points from CT value at the corresponding location in  $R$ . For each position  $P$  of the US-plane the related position in the CT volume is computed as following:

$$\overrightarrow{OP} = \overrightarrow{OO'} + \overrightarrow{O'P} \quad (4.10)$$

With :

$$\overrightarrow{OP} = x\vec{i} + y\vec{j} + z\vec{k} \quad (4.11)$$

$$\overrightarrow{O'P} = x'\vec{u} + y'\vec{v} + 0\vec{w} \quad (4.12)$$

and:

$$\overrightarrow{OO'} = \overrightarrow{OE_1} \quad (4.13)$$

$$\overrightarrow{OO'} = x_1\vec{i} + y_1\vec{j} + z_1\vec{k} \quad (4.14)$$

Equation 4.10, can be written as:

$$\begin{pmatrix} x \\ y \\ z \end{pmatrix} = \begin{pmatrix} x_1 \\ y_1 \\ z_1 \end{pmatrix} + \begin{pmatrix} a_{iu} & a_{ju} & a_{ku} \\ a_{iv} & a_{jv} & a_{kv} \\ a_{iw} & a_{jw} & a_{kw} \end{pmatrix} \begin{pmatrix} x' \\ y' \\ z' \end{pmatrix} \quad (4.15)$$

In such a way, for each plane coordinates  $x'$ ,  $y'$  and  $z' = 0$  we will obtain the intensity value in the CT volume at position  $x$ ,  $y$  and  $z$ . We can write the transformation in equation 4.15 using homogeneous coordinates as:

$$\begin{pmatrix} x \\ y \\ z \\ 1 \end{pmatrix} = T(d) \begin{pmatrix} x' \\ y' \\ 0 \\ 1 \end{pmatrix} \quad (4.16)$$

Finally, the therapy-adapted preoperative volume is obtained by : (1) sampling regularly the esophagus centerline at several depth  $d_\epsilon$  with the associated points  $E_\epsilon$ , this will give the "Depth" axis  $d$  of Figure 4.1; (2) extract the planes perpendicular to the curve at the locations  $E_\epsilon$  using the method described previously, this will give the parallel slice of the therapy-adapted preoperative volume (see Figure 4.1).

It has to be noticed that we know the transformation matrices  $T(d_\epsilon)$  (equation 4.16) between each slice of the therapy-adapted preoperative volume and the original preoperative CT volume. So any voxel of the therapy-adapted preoperative volume can be located in the original preoperative CT volume.

## 4.2 Physical phantom experiment

The goal of the reconstruction is to observe the anatomical structures in CT/MRI in the same order and orientation than the 2D-US images acquired by the probe used for the HIFU therapy. The aim of this section is to validate this fact by comparing the US image to the corresponding reconstructed CT slice. An evaluation on real images seems to be difficult because of the lack of ground truth. We choose then a *physical phantom experiment* to validate the proposed CT reconstruction.

For the experiment, we used a physical phantom that represents the structures and tissues of the human ventricles and esophagus. One CT volume of the phantom and some 2D-US images from different points of the esophagus were acquired. The reconstruction of the CT volume was performed following the esophagus trajectory. Finally, the result of the reconstruction was compared with the US images acquired with the TEE probe.

### 4.2.1 Image acquisition

The accuracy of our approach was evaluated using a physical phantom of a heart that represents some structures and tissues of the human heart and also the esophagus. We used a commercial heart model (PVAH-01 Medical Imaging Technologies, SHELLEY Automation Inc. London, Canada) limited to the ventricles. We modified it in order to include a tubular structure that simulate the esophagus (Figure 4.8). We opened some windows in the esophagus tubular structure to allow the US probe to acquire some image at some defined positions. The heart and the esophagus model were immersed in water filling the internal region of the heart cavities and inside of the esophagus. The water ensures the US wave propagation to image the heart phantom. We also fixed three rubber markers on the outer surface of the heart cavities to provide landmarks enabling to compute a spatial reference in the images.

For the TEE acquisition, we use the Vivid Q 2D real-time cardiovascular echo system with a 6VT-D 4D TEE probe (General Electric, Healthcare, Wauwatosa, USA). On this probe we fixed the orientation angle of the acquisition plane to zero degrees. In this case, the US image plane is perpendicular to the endoscope axis. This geometrical constraint is similar to the imaging device placed in the middle of the proposed therapeutic probe described in (CONSTANCIEL et al. 2013).

The preoperative volumes were acquired by a Cone Beam CT (CBCT) fixed on Artis zeego C-Arm (Siemens Healthcare, Erlangen, Germany).

The system setup of the experiment can be seen on Figure 4.9. The TEE probe was placed inside the esophagus and moved forward to image the heart phantom from three different positions of the esophagus (cf. Figure 4.8). For each three probe position, an US image and a CT volume



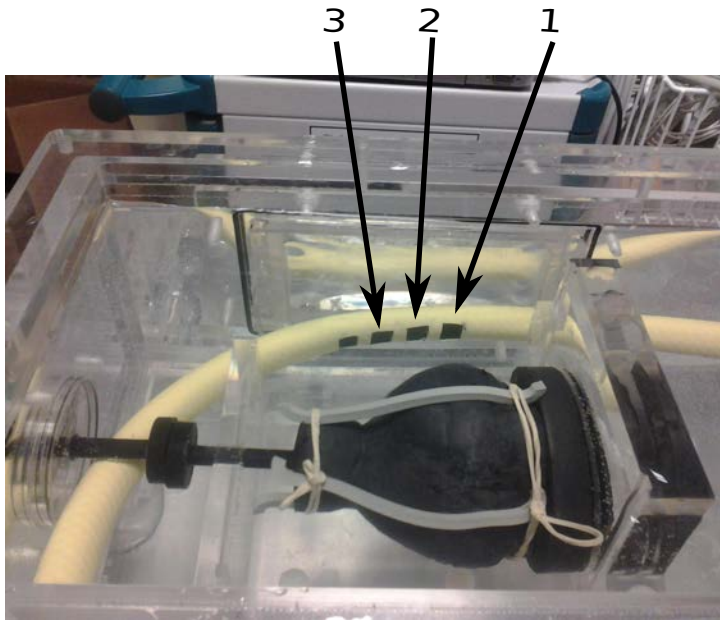


Figure 4.8: Physical phantom of the heart and esophagus. Three windows in the esophagus were opened to acquire the TEE images (1, 2, 3). Two out of the three rubber markers fixed on the heart cavities can be observed.

were acquired. The US image contains the heart anatomy and also the position of the three external referential markers. Immediately after each US acquisition, a CT volume was acquired in order to image the tip of the TEE probe at the US acquisition time. An additional CT volume imaging the phantom without markers and the TEE probe was acquired to have a scene in the same conditions as a preoperative volume. The acquired ultrasound images have a dimension of  $636 \times 422$  pixels with pixel size of  $0.4316\text{mm} \times 0.4316\text{mm}$ . The CT volumes were composed by  $512 \times 512 \times 372$  voxels, with an isotropic voxel size of  $0.4864\text{mm}$ . The experiment was performed in the Hybrid Operating Room (TherA-Image<sup>2</sup>) in the Centre Hospitalier Universitaire de Rennes, France.

#### 4.2.2 Therapy-adapted preoperative volume reconstruction of the CT phantom

For this experiment, we modified the workflow presented in section 4.1 to include a segmentation process of the myocardium, the external markers and the tip of the probe (see Figure 4.10). This information is needed to form a spatial reference for the evaluation. The segmentation process will be explained in the Results section 4.2.4.

The process for the image reconstruction from the CT phantom started as explained in section 4.1. After the acquisition of the images, the CT volume was segmented to obtain the

2. <https://esir.univ-rennes1.fr/fr/actualites/thera-image>

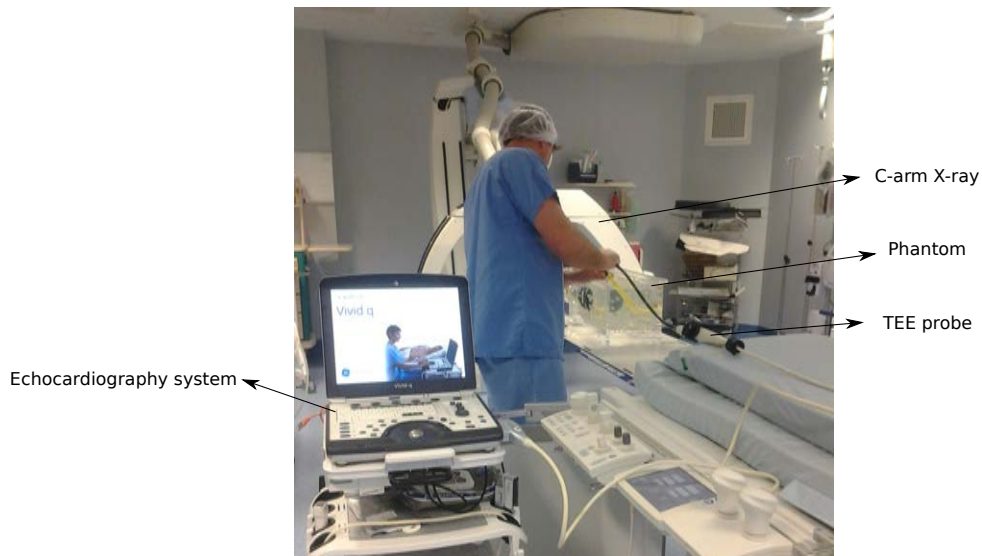


Figure 4.9: The system setup of the experiment.

esophagus (cf. § 4.1.1) and the centerline was define as a spline function (cf. § 4.1.2). The centerline was regularly sampled and the planes perpendicular to the centerline were extracted from the CT Volume. However, the extraction of the perpendicular planes was performed by resampling the segmented CT instead of the original one. This allowed to use the segmented myocardium, the external markers and the tip of the probe in the evaluation.

To summary for each US image (denoted as  $I_{US}$ ) we have:

- An original CBCT volume (denoted as  $V_{or}$ ). On this volume we know the 3D position of the US probe (which correspond to acquisition center of the US image) and the 3D positions of the 3 external markers.
- A therapy-adapted preoperative volume (denoted as  $V_{rec}$ ). On this volume, we also know the 3D position of the US probe and the 3D positions of the 3 external markers.

### 4.2.3 Evaluation of the CT reconstruction

The goal of the CT reconstruction is to observe the anatomical structures in CT/MRI in the same order and orientation than the 2D-US images acquired during the HIFU therapy. We suppose so that the parallel slices of the reconstructed volume  $V_{rec}$  has the same spatial locational as the corresponding US images  $I_{US}$ . The aim of our evaluation is to verify this assumption.

According to this assumption we think that the evaluation can be done by the comparison between:

1. The 3D pose of  $I_{US}$  estimated using the information of the reconstructed volume  $V_{rec}$ . For this we have to (a) select the slice of  $V_{rec}$  which contains the position of the US probe center along the esophagus and (b) to rotate this slice around the US probe center point to

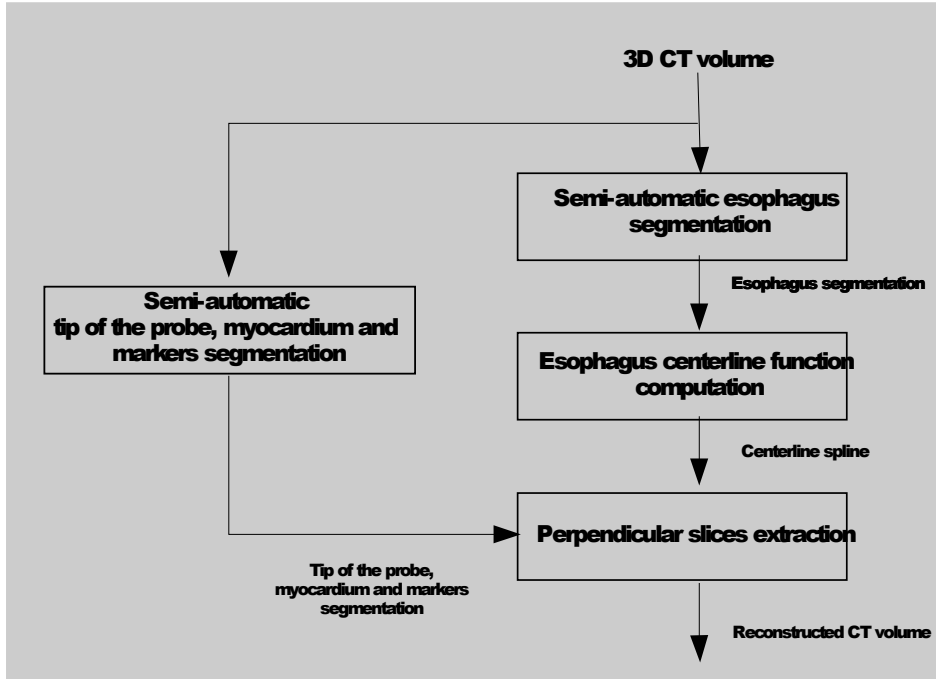


Figure 4.10: Workflow presented in section 4.1 modified to include a segmentation process of the myocardium, the external markers and the tip of the probe.

align it with  $I_{US}$ . As mentioned in the previous section, we also know the transformation matrix between each slice of  $V_{rec}$  and  $V_{or}$  (equation 4.16). By combining these several transformations, we will be able to estimate a transformation matrix  $T_{RecEval}$  between  $I_{US}$  and  $V_{or}$  based on our assumption.

2. The 3D pose of  $I_{US}$  estimated directly in the original CBCT volume  $V_{or}$ . This can be done using the phantom and acquisition information. This allows us to estimate a gold standard transformation matrix  $T_{Ref}$  that aligns the acquired  $I_{US}$  and the CBCT volume  $V_{or}$ .

The evaluation can now be done by estimating the errors between these two 3D poses of  $I_{US}$ . To quantify the error, we will define some landmarks in  $I_{US}$  and use the two transformation matrices  $T_{RecEval}$  and  $T_{Ref}$  to project this point in  $V_{or}$  as shown in Figure 4.11. The estimated error called the Target Registration Error ( $TRE$ ) will be the distance between these 2 projected points:

$$TRE(P_i) = \|T_{Ref}P_i - T_{RecEval}P_i\|, \quad (4.17)$$

where  $P_i$  denotes a landmark on the US image,  $T_{RecEval}$  is the resulted transformation matrix of our approach and the  $T_{Ref}$  is the transformation matrix of the gold standard.

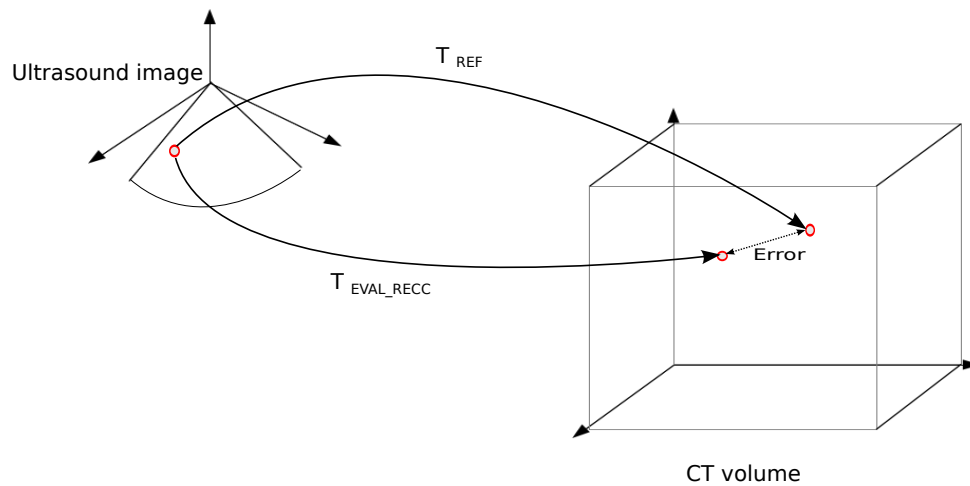


Figure 4.11: Error quantification explanation. One point in the US image is defined. The two transforms  $T_{RecEval}$  and  $T_{Ref}$  are used to project this point in the CT space. The error is the distance between these two projected points.

The global accuracy of the CT reconstruction can so be evaluated using the mean target registration error ( $mTRE$ ) defined as :

$$mTRE = \frac{1}{n} \sum_{i=1}^n TRE(P_i) \quad (4.18)$$

The key points of the evaluation will be the estimation of  $T_{RecEval}$  and  $T_{Ref}$ .

#### 4.2.3.1 Transformation matrix of the CT reconstruction evaluation: $T_{RecEval}$

$T_{RecEval}$  is the combination of 2 transformations: (1) the first is given by the pose estimation of  $I_{US}$  in  $V_{rec}$ , and (2) the second is the geometrical transformation between the chosen slice in  $V_{rec}$  and  $V_{or}$ .

The following steps were used to estimate  $T_{RecEval}$ :

1. Pose estimation of  $I_{US}$  in  $V_{rec}$ .

The reconstructed CT can be seen as a set of consecutive image planes perpendicular to the esophagus centerline. In order to identify the plane that corresponds to the US imaging transducer, we performed the reconstruction of a volume that includes the segmentation of the tip of the TEE probe. In this way, the shape of this object appeared on the corresponding resampled slices and we could so establish the slice that corresponds to the US transducer position.

In this slice, the position of the US probe center is a common point between  $I_{US}$  and  $V_{rec}$ . We have to estimate the orientation of  $I_{US}$  in the corresponding slice. The orientation is given by a rotation of  $I_{US}$  around the position of the US probe center (the US field of view - US FOV - vertex). The orientation is estimated using a 2D-2D fiducial registration procedure.

The position of the US probe center and the estimated rotation gives a 2D transformation matrix between  $I_{US}$  and the corresponding slice  $d$  in  $V_{rec}$ .

2. The link between the corresponding slice in  $V_{rec}$  and  $V_{or}$ .  $T(d)$  (equation 4.16) gives the transformation matrix between the slice of  $V_{rec}$  and  $V_{or}$ .
3.  $T_{RecEval}$  is the final transformation which is the product of the matrices obtained in 1 and 2.

#### 4.2.3.2 Gold standard reference transformation matrix: $T_{Ref}$

$T_{Ref}$  will be given by the direct estimation of the  $I_{US}$  3D pose in  $V_{or}$ . This transformation will be the gold standard of the evaluation. For this, the  $I_{US}$  3D pose will be manually estimated by an expert using the software Slicer. The procedure is the following:

1. The position of the ultrasound transducer is manually searched in the CT volume  $V_{or}$  to be designated as the center of rotation. The segmented transducer in  $V_{or}$  helps in the research.
2. The vertex of the US FOV is placed in the center of rotation defined in step 1.
3. With the 2D-US image as fixed and the CT volume as moving image, a 3D rigid transformation is obtained interactively by the variation of the six parameters (translation x, translation y, translation z, rotation x, rotation y, rotation z), in order to align the fixed US image and the moving CT volume. The fixed markers and the myocardium form are used to confirm the correct alignment.
4.  $T_{ref}$  is obtained using the inverse of the transformation obtained in step 3 and the center designated in step 1.
5. This process is repeated three times resulting in three transformation matrices. The final reference matrix  $T_{ref}$  is constructed using the mean parameters of these three matrices.

The resulting matrix  $T_{ref}$  transforms any point in the 2D-US image  $I_{US}$  to a 3D point in the 3D CT space  $V_{or}$ .

#### 4.2.4 Results

The axial, coronal and sagittal views of the acquired CT image of the phantom are presented in Figure 4.12. The images show a low contrast between the myocardium and the surrounding water. The platform that support the phantom produces some artifacts around the whole volume for both modalities CT and US.

The segmentation of the esophagus from CB CT was carry out using the method explained in section 4.1.1. The same process was repeated to obtain the segmentation of the myocardium, the markers and the tip of the probe at each one of the three probe positions. The resulting segmentation is presented in Figure 4.13. The myocardium segmentation is delineated with an

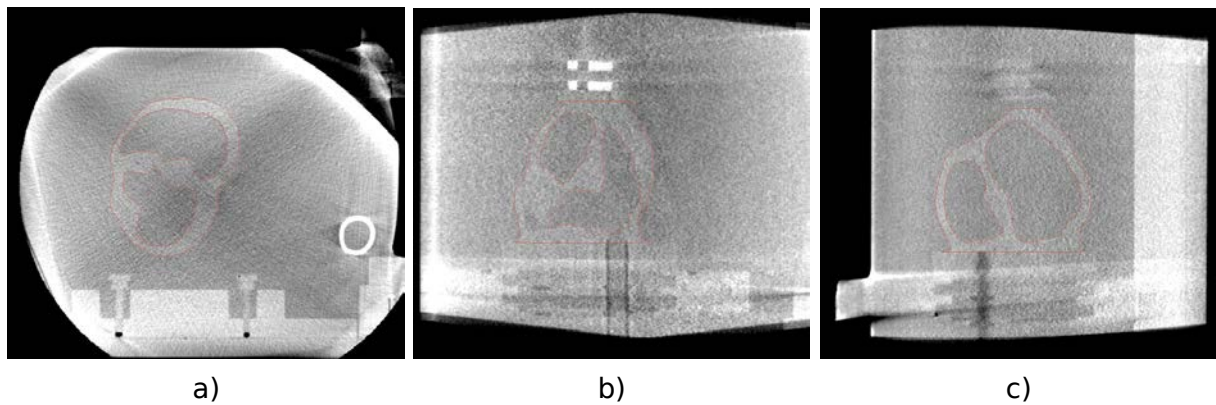


Figure 4.12: CT volume of the phantom acquired with the Artis zeego C-arm. Axial(a), coronal (b) and sagittal (c) views. The myocardium segmentation is delineated with an orange line.

orange line in Figure 4.12.

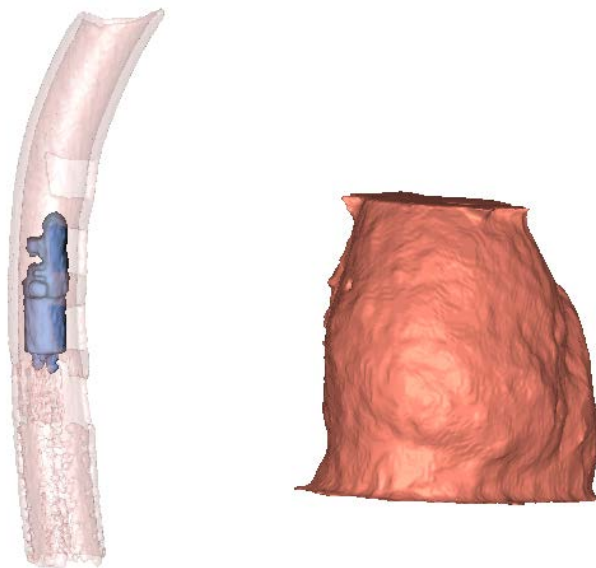


Figure 4.13: Resulting segmentation of the esophagus, the heart and the tip of the probe at the TEE acquisition time.

We used dilatation and erosion operations to fill the holes of the windows in the esophagus phantom. A spherical structuring element with a radius of 10mm was used in both dilatation and erosion. The resulting segmentation was irregular due to the artefacts generated by the probe and the platform that support the phantom, as it can be seen in Figure 4.13. A final median filter was applied to improve the segmentation. The size of the filter was 15mm.

The segmentation of the esophagus was then used to estimate the spline centerline as described previously. The segmentation of the esophagus, the centerline points on the axial slices and the corresponding spline function are presented in the Figure 4.14. 180 points of the segmentation were used to obtain the spline function. The resulting centerline was defined computing 360 points with a smoothing parameter of 0.0003. The smooth form of the resulting centerline ensures a smooth trajectory without abrupt changes and it also filters the error of the segmentation process. It has to be noticed that the smoothing parameters we used for the phantom is lower than this we will use on human data. We believe that the erosion and dilation process, the windows of the esophagus and the artefacts generated by the platform caused more irregularities than for human data.

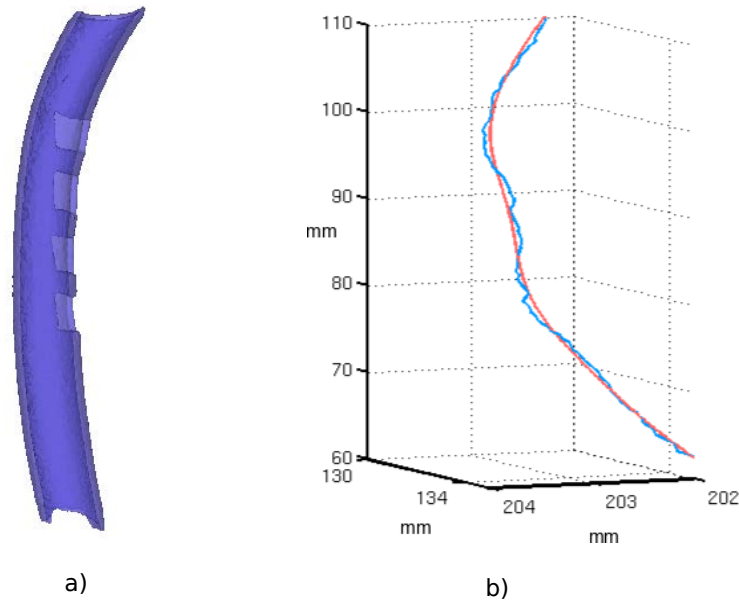


Figure 4.14: a) Resulting segmentation of the esophagus phantom. b) Estimated centerline. In blue, the mean position of the voxels labeled as esophagus on each axial slice of the CT volume. In red, the resulting centerline defined by the cubic smoothing spline.

The spline function which described the centerline was used to compute the unitary vectors that define the planes perpendicular to centerline (cf. § 4.1.2). A slice was resampled for each point of the sampled centerline (cf. § 4.1.3). The several slices which cover the whole centerline form the reconstructed volume  $V_{rec}$ . Three volumes were reconstructed, one for each position of the TEE probe (cf. Figure 4.8). The information of the heart, markers and the corresponding tip of the TEE probe segmentation was included in each reconstructed volume. In this way, we had the myocardium, the markers and the US transducer position information to select the slice that corresponds to the US image.

The positions of the three markers in the US image and in the selected resampled CT slice were defined manually. A 2D-2D fiducial registration process was used to align these

images. The center of rotation was placed in the centerline point for the resampled CT and at the vertex of the field of view for the US image. In Figure 4.15 the result of the fiducial registration is presented. The fiducial registration resulted in a rotation of more or less 10 degrees around the centerline point. We can see at the top of the images in (Figure 4.15), respectively a) the apex of the US sector field of view and b) the tip of the probe in the CT reconstruction. On these images, the apex of the US FOV and the tip of the probe in the CT reconstruction are aligned. The myocardium form in the CT reconstruction is similar to the imaged myocardium in the US image. However the acquired US has high boundary dispersion. The wall of the myocardium is perceived larger in the US image than in the CB CT volume. Moreover, the brightness of the US image seems to be too high. Although, it is difficult to see the alignment due to the quality of the US image, an error around the fiducial points is visible.

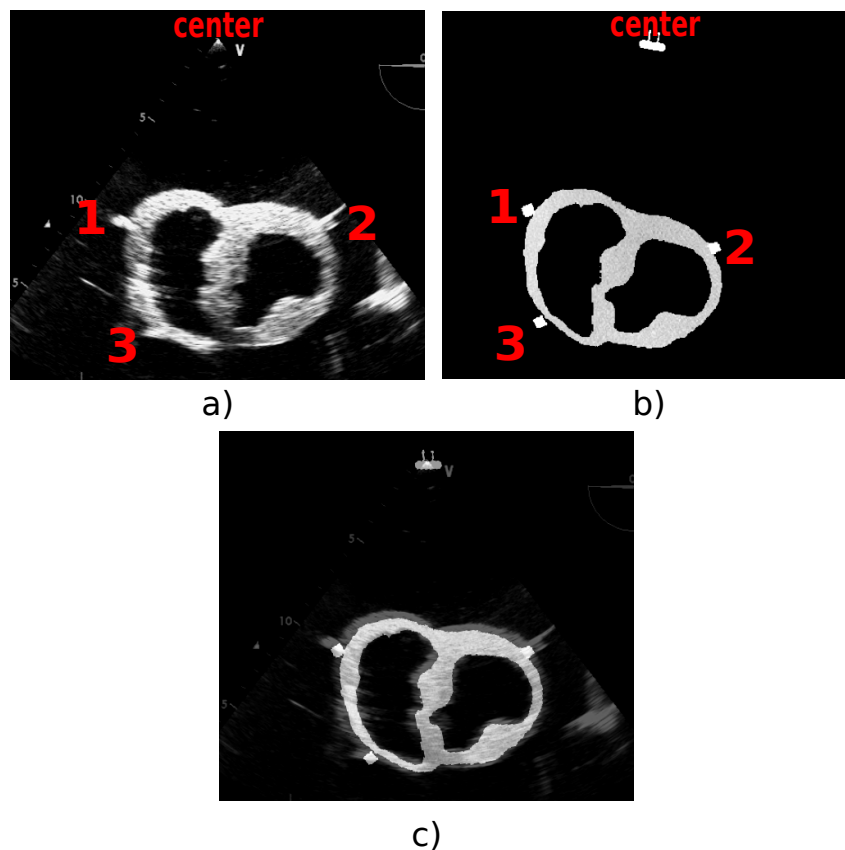


Figure 4.15: a) US image at the TEE probe position 1. b) Resampled CT image from the volume obtained after the segmentation of the heart phantom, the markers and the tip of the probe at the TEE probe position 1. c) Result of the fiducial registration. The fiducial registration has estimated a rotation of more or less 10 degrees around the centerline point.

The error was quantified using  $TRE$  (equation 4.17). The position of the US probe was established as the center of the cylinder where the transducer is located. The transducer can be seen on around 10 slices in the reconstructed volume. In order to integrate the segmentation errors we integrate a zone of five slices around of presumed transducer center. Thus, we evaluated



the  $TRE$  for these five slices.

Each fiducial points was manually selected at each TEE position ten times in order to obtain intra-subject variability. The  $TRE$  between the selected resampled CT slice and the US image was computed on these selected fiducial points.

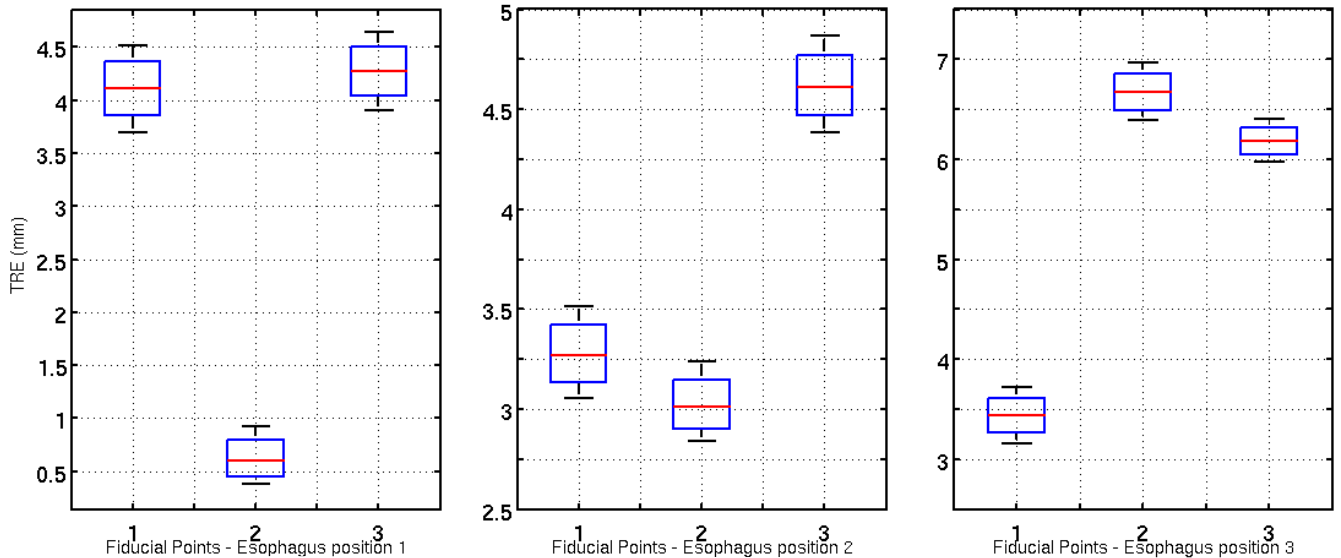


Figure 4.16: Box plots of the Target Registration Error ( $TRE$ ) for each 3 fiducial marker for a) the TEE probe position 1, b) the TEE probe position 2 and c) the TEE probe position 3.

Thus, we have the measure of error for fifty points. Figure 4.16 shows the box plots of the  $TRE$  for each fiducial points for each window. The  $mTRE$  are always lower than 5mm. For all windows or position in the esophagus, we have a minimum error lower than 3.5mm. In the window 1, fiducial point 2 is accurate while point 1 and point 3 show similar error. We can say that the image is around the gold standard position but it is oriented towards left. In the window 2, the fiducial points 1 and 2 have a small error, but point 3 is less accurate. For this window the distal zone of the slice is above the gold standard. For window 3, the fiducial point 1 is close to the gold standard, however points 2 and 3 have bigger errors. In this window, the slice is inclined to the right and the distal zone is above the gold standard. As a global tendency cannot be observed, we believe that the reconstruction is sensible to the small changes in the centerline.

The  $TRE$  by TEE probe position are shown in Figure 4.17. The  $mTRE$  is ranged between 3mm and 5.5mm. These errors are similar to those obtained by (GAO et al. 2012; LANG et al. 2013). We can see that the error is incremented as the depth. The bigger error corresponds with the farther to the insertion place. We can conclude from the measures that if the depth increases the probe moves away from the centerline.

The mean error of the all fiducial markers in all TEE probe position is 4.0247mm.

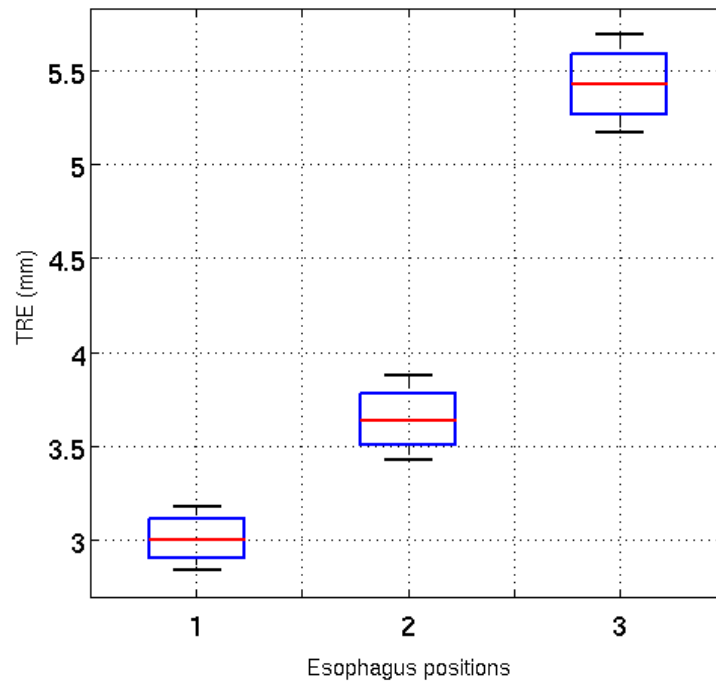


Figure 4.17: Box plots of the Target Registration Error ( $TRE$ ) for each TEE probe position.

The 3D visualization of the whole scene comparing the Gold standard plane and the selected plane of our approach is presented in Figure 4.18.

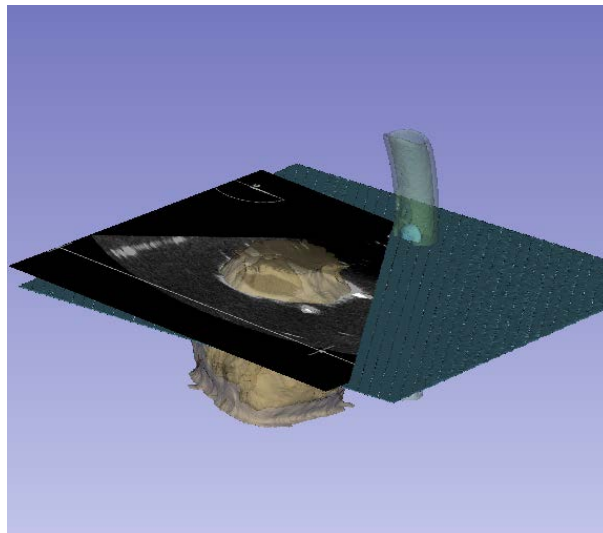


Figure 4.18: The 3D visualization of the whole scene comparing the Gold standard plane and the plane estimated by our approach.

### 4.3 Example of lesion lines definition on 3D model

In this section, we present an example of definition of the lesion lines on preoperative segmented LA and PVs. In this example, some fiducial points were picked manually on the 3D model of LA and PVs using Slicer software, as presented in the Figure 4.19. These fiducial points can be labelled on original CT or segmented volume. Using our approach, the reconstruction of these volumes can be used to observe the lesion lines in the same order and orientation than in the future navigation with the HIFU probe Figure 4.20.

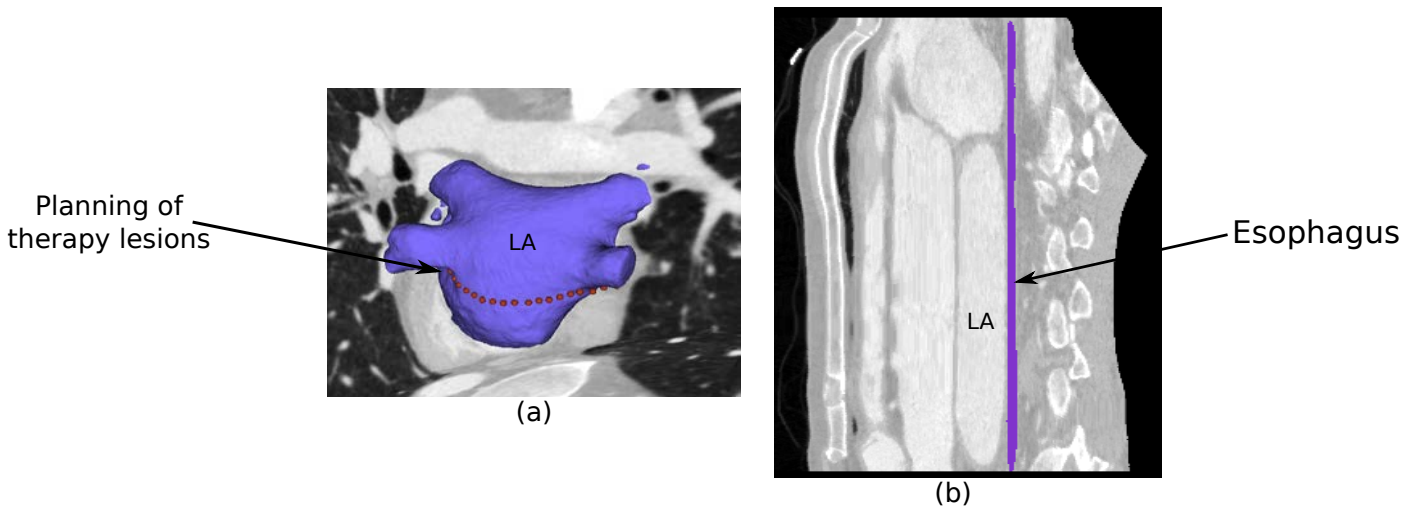


Figure 4.19: (a) Example of therapy ablation lines marked manually using Slicer on 3D model of left atrium segmentation. (b) Sagittal view of the reconstructed volume.

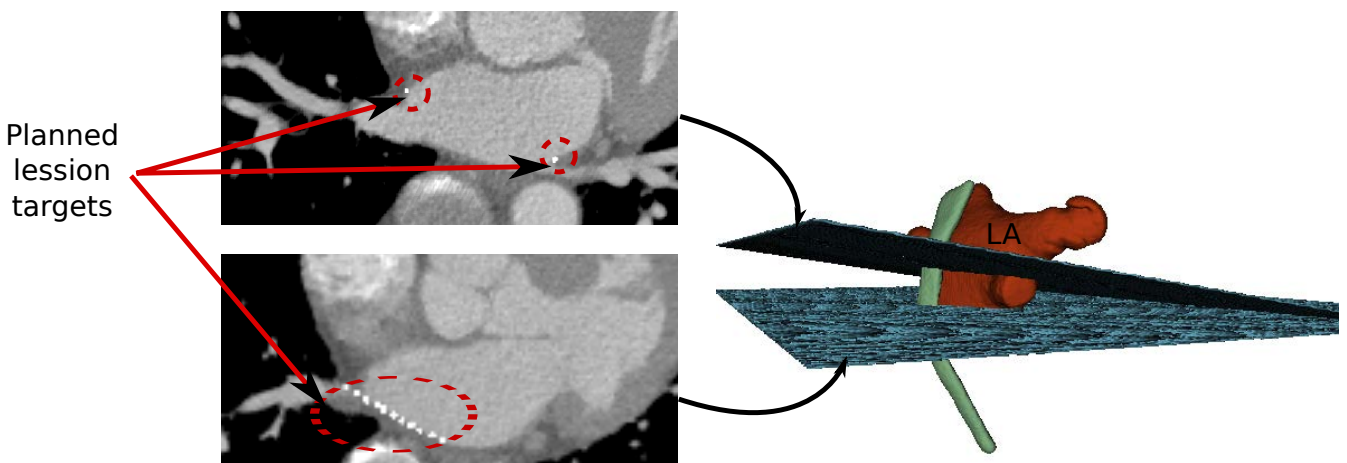


Figure 4.20: Lesion lines on two slices of the reconstructed volume. 3D visualization of these slices on the preoperative space.

## 4.4 Conclusion

Based on the assumption that the transesophageal probe trajectory will be constrained by the esophagus topology, we have proposed the reconstruction of a preoperative volume adapted to the intraoperative conditions of the HIFU therapy. This new volume is composed by the perpendicular planes to the esophagus centerline. The validity of this reconstruction has been evaluated on a physical phantom. The accuracy of the reconstruction measured as a registration issue show a precision in the same order as results of the registration methods reported in literature. In our case where therapy and imaging transducer are located in the same probe, such a reconstruction is especially useful for the planning and moreover for the future image based guidance.

## References

- CONSTANCIEL, E., W. N'DJIN, F. BESSIERE, F. CHAVRIER, D. GRINBERG, A. VIGNOT, P. CHEVALIER, J. CHAPELON, and C. LAFON (2013). "Design and evaluation of a transesophageal HIFU probe for ultrasound-guided cardiac ablation: simulation of a HIFU mini-maze procedure and preliminary ex vivo trials". In: *IEEE Transactions on Ultrasonics, Ferroelectrics, and Frequency Control* 60.9, pp. 1868–1883.
- DE BOOR, C. (1978). *A practical guide to splines*. Springer-Verlag New York.
- GAO, G., G. PENNEY, Y. MA, N. GOGIN, P. CATHIER, A. ARUJUNA, G. MORTON, D. CAULFIELD, J. GILL, C. ALDO RINALDI, J. HANCOCK, S. REDWOOD, M. THOMAS, R. RAZAVI, G. GIJSBERS, and K. RHODE (2012). "Registration of 3D trans-esophageal echocardiography to X-ray fluoroscopy using image-based probe tracking". In: *Medical Image Analysis* 16.1, pp. 38–49.
- LANG, P., M. CHU, D. BAINBRIDGE, G. GUIRAUDON, D. JONES, and T. PETERS (2013). "Surface-Based CT-TEE Registration of the Aortic Root". In: *IEEE Transactions on Biomedical Engineering* 60.12, pp. 3382–3390.
- YUSHKEVICH, P. A., J. PIVEN, H. CODY HAZLETT, R. GIMPEL SMITH, S. HO, J. C. GEE, and G. GERIG (2006). "User-guided 3D active contour segmentation of anatomical structures: significantly improved efficiency and reliability". In: *Neuroimage* 31.3, pp. 1116–1128.



## **PART III: THERAPY GUIDANCE**



# Similarity measures evaluation for CT to US registration

Beside feature-based registration methods which need a first image segmentation step, an intensity-based cardiac US to cardiac CT image registration method has been described in (HUANG et al. 2009). The authors of this paper proposed a spatio-temporal registration of the beating heart using mutual information (MI) metric to drive the spatial alignment. This technique has been improved by performing an intensity-based registration on only the relevant features of the US image after median filtering and low intensity thresholding (HUANG et al. 2006). The question of MI validity thus arises. In CT images, tissues are characterized by intensity distribution. However, in US images, each tissue is inherently characterized by a specific spatial distribution of speckle rather than a specific distribution of gray levels. Therefore, the use of an intensity-based similarity measure in a multimodal image registration problem involving US images is still an open question. Beside MI, other intensity-based similarity measures have also been proposed in the literature. Some of these metrics could be more adequate than MI in driving the registration.

We propose to validate and quantify the usability and impact of such similarity measures for US to CT registration. The evaluation of five properties of eight different intensity-based similarity measures between US and CT images is performed. This evaluation aims to find the best similarity measure or optimal combination of similarity measures to be included in our registration framework. The ability to improve the behavior of similarity measures using the pre-processing procedure proposed in (HUANG et al. 2006) is also evaluated. The protocol used in this evaluation requires a gold standard registration. We thus propose to use synthetic CT and US images with a known gold standard.



## 5.1 Materials and methods

### 5.1.1 Images

Because the evaluation requires a registration gold standard, we choose to use realistic synthetic data. Two sets of synthetic images were built for use in the evaluation:

1) a geometrical form composed of an oval on a plain background [Figure 5.1-(a) and (b)]. This image will be called "Oval" in the rest of the section.

2) a set of four synthetic phantom images of the left atrium and pulmonary veins (LAPVs), more related to our medical application. These four phantom images are composed of two images with different fields of view (FOV) from a male cryosection of the human thorax (these 2 images will be called " $LAPV_1$ " and " $LAPV_2$ " in the rest of the section) and two images with different FOV from a female cryosection of the human thorax (" $LAPV_3$ " and " $LAPV_4$ "). The cryosections were taken from the Visible Human Project<sup>1</sup>. As an example, Figure 5.1-(c) shows a slice from the male dataset. These cryosections were semi-automatically segmented and labeled into six types of tissues: air, fat, bone, muscle, water and blood (5.1-(d)).

Synthetic CT images were obtained by applying the Hounsfield value corresponding to the type of tissue modulated by Gaussian noise (Figure 5.1-(e)). For simulating US images, each tissue is first characterized by an acoustical impedance and a spatial distribution of speckle. This information is set as an input to the US image simulator (DILLENSEGER et al. 2009) (Figure 5.1-(f)).

### 5.1.2 Image simulation parameters

The LAPVs images were first segmented and labeled into six different tissue classes: air, fat, bone, muscle (including myocardium), water and blood with contrast medium.

The CT images were simulated by assigning the corresponding Hounsfield value to each tissue (see Table 5.1). We then applied an additive Gaussian noise with a standard deviation of 400 to each value.

The US images were obtained using the simulator described in (DILLENSEGER et al. 2009). In this simulator, each tissue is characterized by its acoustical impedance (see Table 5.1) and a specific spatial distribution of speckle. In this speckle model, the inter-scatterer distances are independent and randomly distributed from a gamma distribution tuned by two parameters:  $\bar{d}$  represents the mean inter-scatterer distances and  $\alpha$  a regularity parameter (see Table 5.1).

---

1. [http://www.nlm.nih.gov/research/visible/visible\\_gallery.html](http://www.nlm.nih.gov/research/visible/visible_gallery.html)

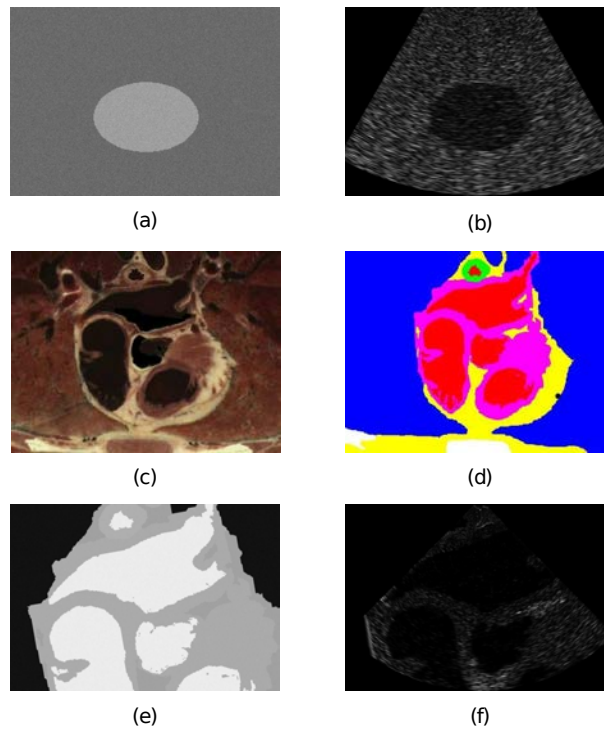


Figure 5.1: Images used for evaluation. Oval geometrical form: simulated CT (a) and US (b) images. Left atrium and pulmonary veins phantom images: cryosection of the male human thorax (c); segmentation and labeling into six different types of tissues: air, fat, bone, muscle (including myocardium), water and blood (d); corresponding simulated CT (e) and US (f) images for a US beam depth=7cm.

Table 5.1: Values of parameters used in the simulation of CT and US images.

	Acoustical impedance ( $\text{kg} \cdot \text{m}^{-2} \cdot \text{s}^{-1}$ )	Density ( $\text{g} \cdot \text{mm}^{-3}$ )	Regularity ( $\alpha$ )	Hounsfield value
Air	$4 \times 10^{-4}$	$2 \times 10^{-3}$	0.1	-1000
Water	1	$2 \times 10^{-3}$	0.1	0
Blood (contrast)	1.63	$4 \times 10^{-3}$	0.4	400
Muscle	1.65	0.03	0.4	-20
Fat	1.35	0.1	20	-80
Bone	$7.8 \times 10^6$	0.02	20	30

### 5.1.3 Registration procedure and similarity measures

The registration procedure of two images of the same scene acquired at different times, from different points of view and/or by different sensors, aims to align them into a common referential. Usually, one image is fixed as a reference and the other is moved and compared with it. The registration procedure consists of 1) applying a geometric transformation to the moving image, 2) comparing similarities between the two images by using a similarity measure and 3) optimizing the geometric transformation in order to maximize similarity between the two images. Ideally,

the similarity measure should have an optimum at the set of parameters that best align the moving image, and values that decrease monotonically with the distance to this optimum. In practice, local minima may be present close to the optimum. So the good choice of a similarity measure adapted to our medical application is crucial.

In this experiment, eight intensity-based similarity measures (cf. section 2.2.3) are evaluated. Six of these similarity measures use the information from the histogram of images while two of them use the spatial information and intensity values. They are: mutual information (MI) (MAES et al. 1997), normalized mutual information (NMI) (STUDHOLME et al. 1999), entropy correlation coefficient (ECC) (MAES et al. 1997), joint entropy (H) (MAES et al. 1997), histogram energy (E) (BRO-NIELSEN 1997) and correlation ratio (CoR) (ROCHE et al. 1998) for the histogram-based similarity measures and point similarity measure based on MI (PSMI) (ROGELJ et al. 2003) and Woods criterion (WC) (WOODS et al. 1993) for the ones based on spatial information and intensity values.

#### 5.1.4 Evaluation protocol

The protocol consists of a statistical and systematic evaluation of the similarity measure behavior around the registration gold standard. This protocol proposed by Skerl (SKERL et al. 2006) carries out a thorough performance evaluation of the similarity measures independently of the optimization method used to find the optimal alignment. The protocol needs to know the gold standard i.e., the underlying transformation between the fixed and moving images. Three steps are then needed to perform an evaluation:

1. The definition of statistical significant sample points within the parametric space around the gold standard. The parametric space is defined according to the dimensions, normalization values and amount of points used in the computation of the similarity measure. The dimension of the parametric space is defined by the amount of parameters used in the transformation (two translations and one rotation angle, in the context of 2D rigid transformation). The parametric space is normalized in such a way that a change along each axis, produces almost the same impact on the transformation magnitude. After normalization, Euclidean metrics may be used to measure the distance between the values of the similarity measure. The protocol generates a number  $M$  of sampling points equally distributed on  $N$  lines randomly localized. All these lines intersect at the origin of the parametric space, the gold standard. Sampling points lie inside of a hypersphere of radius  $R$  in the parametric space.
2. Similarity measure values around the gold standard are computed using geometrical parameters corresponding to the specific sample points defined at Step 1.

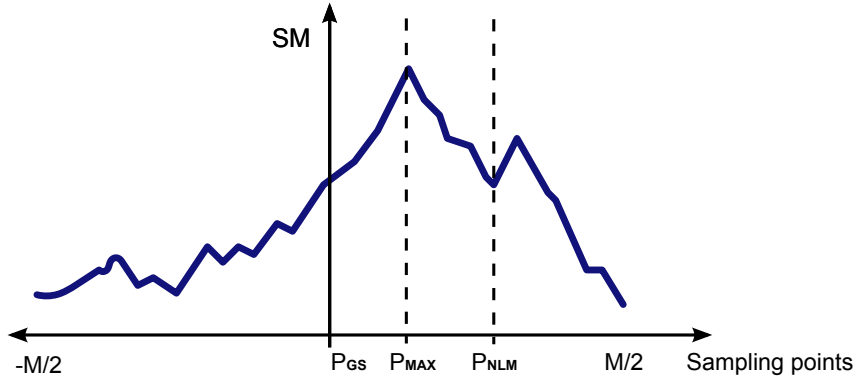


Figure 5.2: Profile of a similarity measure along one line with  $M$  sampling points, gold standard at  $P_{GS}$ , maximum value at  $P_{MAX}$  and nearest local minimum at  $P_{NLM}$ .

3. The analysis of the similarity measure behavior around the gold standard. For this, five properties are measured from the similarity measure values obtained for each line during the second step (Figure 5.2):

- a) The accuracy ( $ACC$ ) of the registration corresponds to the root-mean-square of the difference between the position of the optimum value ( $P_{MAX}$ ) and the gold standard ( $P_{GS}$ ), for all lines (equation 5.1).

$$ACC = \sqrt{\frac{1}{N} \sum_{n=1}^N \|P_{n,max} - P_{GS}\|^2} \quad (5.1)$$

- b) The distinctiveness of the optimum ( $DO$ ) measures the visibility of the maximum value against the values around it. It is calculated as the average of the difference between twice the maximum value and the sum of the two values symmetrically located at their two sides at a given distance, as is defined in (5.2).

$$DO(r) = \frac{1}{2rN} \sum_{n=1}^N 2SM(X_{n,max}) - SM(X_{n,max-k}) - SM(X_{n,max+k}), \quad (5.2)$$

with  $r = k \cdot \delta$ ,  $\delta$  the distance between two sampling points in a line ( $\delta = 2R/M$ ), and  $k$  is the number of steps ( $k = 1, 2, \dots$ ).

- c) The number of minima ( $NOM$ ) is the amount of local minima of the similarity measure around the gold standard.
- d) The capture range ( $CR$ ) of the similarity measure is the distance from the nearest local minima ( $P_{NLM}$ ) to the maximum value of the similarity measure ( $P_{MAX}$ ).
- e) The risk of non-convergence ( $RON$ ) of the registration is the average of the positive differences between the similarity measures at consecutive sampling points. It is

Table 5.2: Moving image sizes, field of view (FOV), translation and rotation units of the normalized parametric space and distance between two consecutive points along a line, for the five images ( $N = 7$  lines,  $M = 100$  sampling points and  $R = 0.3$ ).

Image	FOV	Image size (mm)		Pixel size (mm)	Trans. unit (mm)	Rot. unit (rad)	$\delta$ (mm)
<i>Oval</i>	1	98.23	141.13	0.11	9.8	0.10694	0.0588
<i>LAPV</i> <sub>1</sub>	Male1	78.14	112.26	0.0875	7.8	0.10729	0.0468
<i>LAPV</i> <sub>2</sub>	Male2	78.14	112.26	0.0875	7.8	0.10729	0.0468
<i>LAPV</i> <sub>3</sub>	Female1	74.12	106.49	0.083	7.4	0.10751	0.0444
<i>LAPV</i> <sub>4</sub>	Female2	74.12	106.49	0.083	7.4	0.10751	0.0444

defined as:

$$RON(r) = \frac{1}{2rN} \sum_{n=1}^N \sum_{P_{MAX}-k}^{P_{MAX}+k} d_{n,m}, \quad (5.3)$$

$$d_{n,m} = \begin{cases} SM(X_{n,m-1}) - SM(X_{n,m}), & \text{if } m < P_{MAX} \text{ and } SM(X_{n,m-1}) > SM(X_{n,m}) \\ SM(X_{n,m+1}) - SM(X_{n,m}), & \text{if } m > P_{MAX} \text{ and } SM(X_{n,m+1}) > SM(X_{n,m}) \\ 0, & \text{if otherwise.} \end{cases}$$

These five properties are good indicators in predicting the behavior of the similarity measure for a good registration (when  $ACC$ ,  $RON$  and  $NOM$  values are as low as possible and  $CR$  and  $DO$  values as high as possible).

## 5.2 Results

The evaluation was carried out on the the *Oval* and the four *LAPV*<sub>*i*</sub>s images. In each of these cases, we performed the registration of the CT image with the corresponding raw US images and also with the US images preprocessed as in (HUANG et al. 2006). The values used to define the sampling points were set as suggested in <sup>2</sup>:  $N = 7$ ,  $M = 100$  and  $R = 0.3$ . Using these values, the distance between two consecutive points along a line was much smaller than the smallest pixel size. Table 5.2 shows the image sizes, the normalization values, and the distances between two consecutive points along a line, for each of the images used in the test. The unit for rotation was chosen in such a way that a rotation around one corner of the image causes the mean shift of all pixels equal to a translation unit. For rotation and translation, we used a rigid transformation and a linear interpolation method. We used 256 bins in the computation of the different similarity measures.

The results of the *Oval* will be noted as *Ov* (US raw data) and *Ov1* (preprocessed US data) in the rest of the paper. The *LAPV*<sub>*i*</sub>s images had relatively similar results. We then chose to

2. <http://lit.fe.uni-lj.si/contents/tools/SimilarityEvaluation/>

Table 5.3: Value of the  $ACC$  (mm),  $RON$  ( $10^7\text{mm}^{-1}$ ),  $NOM$ ,  $CR$  (mm) and  $DO$  ( $\text{mm}^{-1}$ ) properties for the eight similarity measures evaluated on the raw *Oval* image (*Ov*) and the preprocessed *Oval* image (*Ov1*). Sampling step along a line = 0.0588mm ( $N = 7$ ,  $M = 100$ ,  $R = 0.3$ ). Best values are bolded.

	$ACC$		$RON$		$NOM$		$CR$		$DO$	
	<i>Ov</i>	<i>Ov1</i>	<i>Ov</i>	<i>Ov1</i>	<i>Ov</i>	<i>Ov1</i>	<i>Ov</i>	<i>Ov1</i>	<i>Ov</i>	<i>Ov1</i>
<i>MI</i>	<b>0.14</b>	0.14	2.8	2.8	177	177	0.059	0.059	14	15
<i>NMI</i>	<b>0.14</b>	0.16	2.7	2.8	<b>20</b>	<b>21</b>	0.059	0.059	11	11
<i>ECC</i>	0.17	0.17	2.8	2.8	100	100	0.059	0.059	11	11
<i>H</i>	0.21	0.21	3.1	3.1	38	38	0.059	0.059	0.87	0.85
<i>PSMI</i>	0.21	0.21	3.1	3.1	41	40	0.059	0.059	-0.74	-0.87
<i>E</i>	0.21	0.2	3.1	3.1	39	40	0.059	0.059	1.0	1.3
<i>CoR</i>	0.16	0.16	2.7	2.7	68	75	0.059	0.059	11	12
<i>WC</i>	0.19	<b>0</b>	<b>2.6</b>	<b>0.79</b>	77	100	0.059	<b>0.118</b>	<b>15</b>	<b>60</b>

Table 5.4: Value of the  $ACC$  (mm),  $RON$  ( $10^7\text{mm}^{-1}$ ),  $NOM$ ,  $CR$  (mm) and  $DO$  ( $\text{mm}^{-1}$ ) properties for the eight similarity measures evaluated on the raw *LAPV* image (*L*) and the preprocessed *LAPV* image (*L1*). Sampling step along a line = 0.0444mm ( $N = 7$ ,  $M = 100$ ,  $R = 0.3$ ). Best values are bolded.

	$ACC$		$RON$		$NOM$		$CR$		$DO$	
	<i>L</i>	<i>L1</i>	<i>L</i>	<i>L1</i>	<i>L</i>	<i>L1</i>	<i>L</i>	<i>L1</i>	<i>L</i>	<i>L1</i>
<i>MI</i>	0.17	0.17	<b>5.4</b>	<b>6.4</b>	100	93	0.046	0.046	6.7	8.8
<i>NMI</i>	0.21	0.19	12.7	13.0	72	58	0.046	0.046	7.5	9.5
<i>ECC</i>	0.26	0.24	12.2	12.6	89	86	<b>0.057</b>	0.057	7.1	9.3
<i>H</i>	0.29	0.29	34.2	34.7	<b>38</b>	<b>34</b>	0.046	0.046	4.8	4.3
<i>PSMI</i>	0.22	0.29	34.1	34.3	50	40	0.046	0.046	1.8	1.6
<i>E</i>	0.29	0.29	33.2	34.0	46	37	0.046	0.046	5.9	5.2
<i>CoR</i>	0.14	0.14	6.2	7.4	92	84	0.046	0.057	8.8	<b>11</b>
<i>WC</i>	<b>0.12</b>	<b>0</b>	7.7	10.4	111	100	0.046	<b>0.079</b>	<b>14</b>	4.4

present the mean values of these *LAPV* images measures and noted them as *L* (US raw data) and *L1* (preprocessed US data). Tables 5.3 and 5.4 give the  $ACC$ ,  $RON$ ,  $NOM$ ,  $CR$  and  $DO$  indicator properties of the eight similarity measures for the *Oval* and *LAPV* images respectively.

It can be observed in Tables 5.3 and 5.4 that *WC* presents a globally better performance than the other similarity measures, for both *LAPV* and *Oval* images. This is especially true for the  $ACC$  and  $DO$  indicators. *MI* and *CoR* equally give globally high performances regardless of the image content. *NMI* has a high  $ACC$  and the smallest  $NOM$  for *Oval*. The results show that *MI* can be used in the registration of CT to US images as has been done in (HUANG et al. 2006). However, the results also show that preprocessing the images does not improve the performance. If we compare the behavior between the raw and preprocessed images, it can be concluded that the performance is almost the same for all the similarity measures except for *WC*. *WC* has an optimal  $ACC$  for both *Oval* and *LAPV* preprocessed images. All similarity

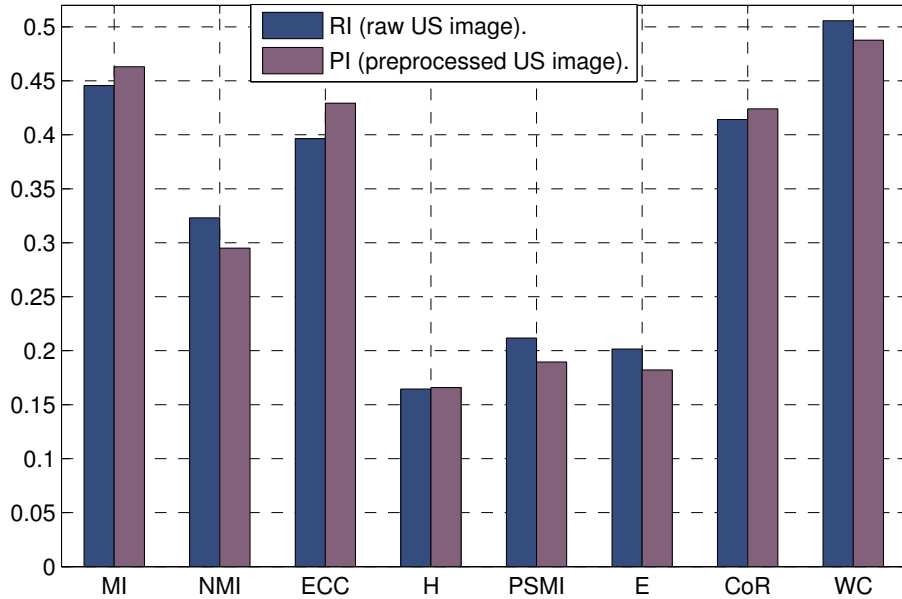


Figure 5.3: Composite index for the several similarity measures

measures have a small  $CR$ , as was expected for these modalities. This result is consistent with that reported in (SKERL et al. 2006).

However a global comparison between the several similarity measures is difficult to perform by the single analysis of Table 5.4. We propose to compute a composite index as a combination of the statistics for each similarity measure. For this we used the principal components analysis (PCA) for ranking the similarity measures. The coefficients of the first principal component give the composite index (MISHRA 2009). The coefficients of the linear combinations of the properties that generate the principal components are shown in Figure 5.3. The largest coefficients in the first principal component are  $WC$  and  $MI$  for both the real images (RI) and the preprocessed images (PI). However, the third is  $CoR$  for RI and  $ECC$  for PI.

### 5.3 Conclusion

We have evaluated the performance of different intensity-based similarity measures in the context of CT to US image registration. The analysis of the behavior of the similarity measures near of the gold standard shows that Woods Criterion and Mutual Information have globally better performances and should be used in the future 2D-US to 3D-CT registration.

## References

- BRO-NIELSEN, M. (1997). “Rigid registration of CT, MR and cryosection images using a GLCM framework”. In: *CVRMed-MRCAS'97*. Grenoble: Springer, pp. 171–180.
- DILLENSEGER, J.-L., S. LAGUITTON, and E. DELABROUSSE (2009). “Fast simulation of ultrasound images from a CT volume.” In: *Computers In Biology and Medicine* 39.2, pp. 180–186.
- HUANG, X., N. A. HILL, J. REN, and T. M. PETERS (2006). “Rapid registration of multimodal images using a reduced number of voxels”. In: *Proc. SPIE*. Vol. 6141. San Diego, pp. 614116–614116–10.
- HUANG, X., J. MOORE, G. GUIRAUDON, D. JONES, D. BAINBRIDGE, J. REN, and T. PETERS (2009). “Dynamic 2D ultrasound and 3D CT image registration of the beating heart”. In: *IEEE Transactions on Medical Imaging* 28.8, pp. 1179–1189.
- MAES, F., A. COLLIGNON, D. VANDERMEULEN, G. MARCHAL, and P. SUETENS (1997). “Multimodality image registration by maximization of mutual information”. In: *IEEE Transactions on Medical Imaging* 16.2, pp. 187–198.
- MISHRA, S. (2009). “On construction of robust composite indices by linear aggregation”. In: *The IUP Journal of Computational Mathematics* 2.3, pp. 24–44.
- ROCHE, A., G. MALANDAIN, X. PENNEC, and N. AYACHE (1998). “The correlation ratio as a new similarity measure for multimodal image registration”. In: *Medical Image Computing and Computer-Assisted Intervention - MICCAI'98*. Ed. by W. WELLS, A. COLCHESTER, and S. DELP. Vol. 1496. Lecture Notes in Computer Science. Springer Berlin Heidelberg, pp. 1115–1124.
- ROGELJ, P., S. KOVAČIČ, and J. C. GEE (2003). “Point similarity measures for non-rigid registration of multi-modal data”. In: *Computer vision and image understanding* 92.1, pp. 112–140.
- SKERL, D., B. LIKAR, and F. PERNUS (2006). “A protocol for evaluation of similarity measures for rigid registration”. In: *IEEE Transactions on Medical Imaging* 25.6, pp. 779–791.
- STUDHOLME, C., D. HILL, and D. HAWKES (1999). “An overlap invariant entropy measure of 3D medical image alignment”. In: *Pattern Recognition* 32.1, pp. 71–86.
- WOODS, R. P., J. C. MAZZIOTTA, and S. R. CHERRY (1993). “MRI - PET registration with automated algorithm”. In: *Journal of Computer Assisted Tomography* 17.4, pp. 536–546.





## 3D-CT to 2D-US registration

The aim of the thesis work is to propose a method to guide HIFU atrial fibrillation therapy by integrating high resolution anatomical preoperative information inside the 2D intraoperative US cardiac images. This requires the registration of the 2D-US images with the preoperative CT volume. This is a challenging task, because the images to be registered do not have the same spatial dimensions: the preoperative is a volume while the intraoperative image is a 2D slice.

In the bibliography, the slice to volume registration is usually achieved using an electromagnetic tracking device (HUANG et al. 2009; LANG et al. 2013; LINTE et al. 2009). However the use of the electromagnetic tracking has several disadvantages including the requirement of an additional hardware, the requirement to make some modifications to the ultrasound probe, the sensitivity of this devices to metallic interferences and the need of additional calibration and sterilization processes in the clinical procedures. The several reported approaches were evaluated during phantom or animal studies but the performance of the electromagnetic tracking in the clinical routine workflow is unclear (FRANZ et al. 2014; GAO et al. 2012). Moreover, Lang et al. (LANG et al. 2013) conclude that the use the electromagnetic tracking does not improve the results. They reported a mean registration error of 5mm for ex-vivo animal experiment using electromagnetic tracking and of 4.54mm when they evaluated their approach on human data acquired without tracking.

We propose to perform the US slice to CT volume registration without any external tracking device. However, in order to help the registration process, we will use the constraint on the probe's trajectory by the esophagus as presented in Chapter 4 on the therapy-adapted preoperative-volume. In this chapter we will present and evaluate the 2D to 3D registration process which uses the esophagus topology.

## 6.1 Global methodology

The general framework of our approach is presented in Figure 6.1. This approach is divided into a preoperative and an intraoperative stage. A therapy-adapted preoperative-volume is reconstructed during the preoperative planning stage as presented in chapter 4. This reconstruction contains the geometrical restrictions of the navigation. We have in this reconstructed volume the anatomical structures in the CT volume in the same order and orientation than the 2D-US images acquired by the probe used for the HIFU therapy. An ECG-gated 2D-US sequence is acquired during the therapy. The slice corresponding with the 75% of the cardiac cycle (R-R interval) is selected. A registration process between the reconstructed volume and the US slice can then be performed.

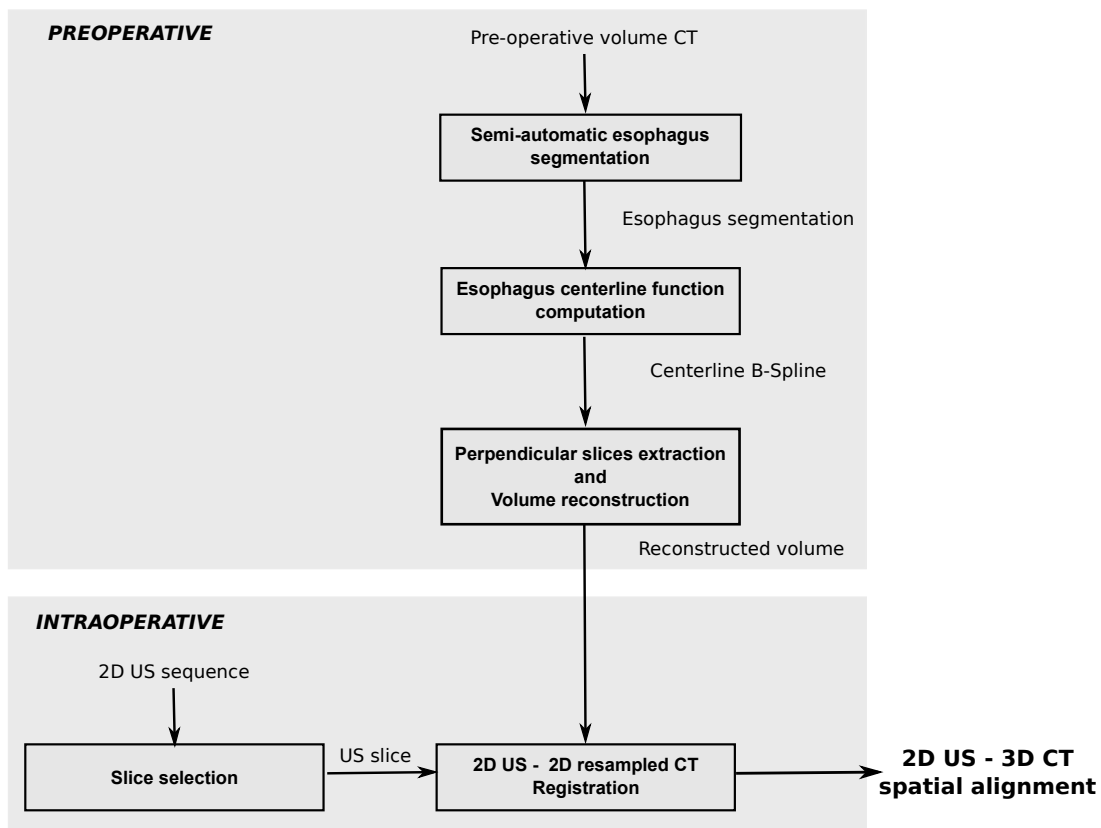


Figure 6.1: Workflow of the global methodology used for 2D-US to 3D-CT registration.

### 6.1.1 Preoperative stage

The therapy-adapted preoperative-volume construction has been presented in Chapter 4. In this chapter, we have demonstrated that the reconstruction gives an accurate information of the navigation.

### 6.1.2 Intraoperative stage

The proposed registration process between an US slice and the preoperative CT acquisition is presented in Figure 6.2. The block diagram corresponds to the classical standard registration scheme with an additional reconstruction block. To perform this procedure it is necessary to define: (1) the kind of alignment (rigid or elastic transform), (2) the constraints of the alignment research (the parameters of the transformation) and (3) the measure of the alignment (similarity metric). These points have been discussed in detail in section 2.5 and chapter 5. In summary:

1. The choice of the kind of alignment is driven by the study of the movements and deformations introduced by the cardiac and respiration cycles (SRA et al. 2008). In our specific case, the images to register correspond to the same cardiac phase, the deformations caused by respiration motion are small in the region of interest of the therapy, the movement of the heart during respiration is in the same direction than the probe insertion. For these reasons we choose to perform a *rigid registration* because the deformations caused by the cardiac cycle are mostly avoided in our application. At the other hand, we do not have enough information to obtain a confident elastic alignment because the deformations introduced by the respiration is volumetric and the US image just shows the deformations in 2D.
2. For rigid transformation, six parameters (three translations and three rotations) should be estimated. But, we made the assumption that the probe's trajectory is constrained by the esophagus. Using this geometrical constraint, we can *reduce the number of parameters from six to two*: the depth  $d$  of the US probe along the esophagus and its orientation  $\theta$  around the centerline of the esophagus (see Figure 2.10). The constraint which imposes the rotation around the centerline can be released by allowing a slight translation of the center of rotation from the centerline.
3. In chapter 5 an exhaustive evaluation of the metric performance was developed. The best similarity measures were the Woods Criterion (WC) (composite index 0.5) and the Mutual Information (MI) (composite index 0.45). In this context, MI was selected for further tests because its implementation is well established and validated in the medical image analysis community.

The data to register is the following:

1. The US image corresponds to the 75% of the cardiac cycle (R-R interval). In our case, this US image is manually selected by an expert from the acquired US sequence. The automatic selection is out of scope of this Thesis, but we suppose that in the future, such a selection will be available.

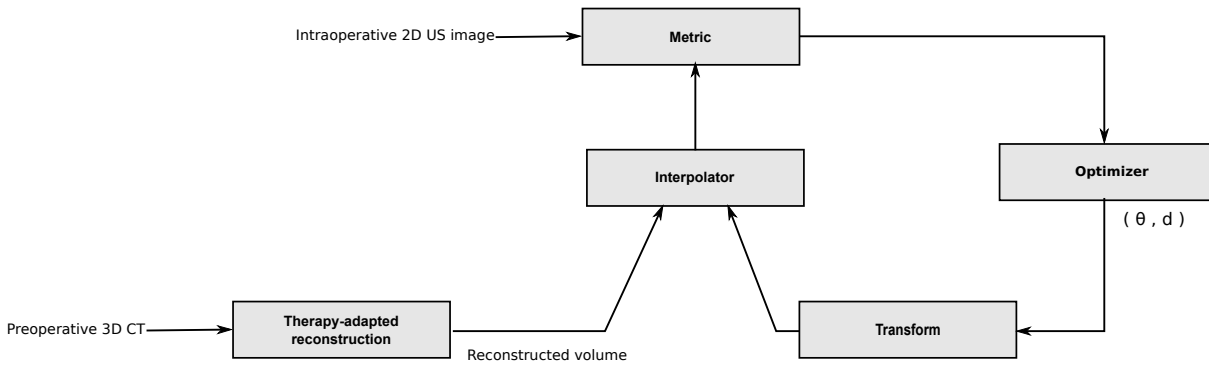


Figure 6.2: Registration process between a US slice and the preoperative acquisition. This process uses the therapy-adapted reconstructed volume performed during the preoperative stage

2. The CT sampled slices that form the reconstructed volume are loaded by the algorithm. For each slice we also know the geometrical transform  $T(d)$  (equation 4.16) to the original preoperative data.

From the choice of the registration principle and the kind of data to register we will propose the following 2D-US to 3D-CT registration scheme:

1. Initialization. We will use some information about the endoscope (inserted length, visual analysis of the image sequence during navigation, fluoroscopy, etc.) to define a candidate zone along the esophagus centerline in which the image transducer center can be. The size of this zone correspond broadly to 10mm along the esophagus. According to the depth sampling step along the esophagus, this zone can be composed by a set of 30 to 80 adjacent slices of the reconstructed volume. A 2D-2D registration will be performed for all the slices of the candidate zone.
2. 2D-2D registration. The 2D-2D registration aims at finding a transformation which is centered on the esophagus centerline. Five parameters are optimized in this 2D registration: the rotation angle, the 2D coordinate positions of the rotation center and a small 2D translation from this center. We set a scale parameters in the optimization process which holds the translation to be close to the rotation center. The results for each slice will be the estimated 2D transformation and the final value of similarity measure.
3. 2D-3D registration. After the 2D-2D registration process on all the slices of the candidate zone, the slice of depth  $d$  which presents the highest similarity value after registration will be considered as the final result of the registration scheme. The estimated 2D transform on slice  $d$  associated with the geometrical transform  $T(d)$  will give the final 2D-3D trans-

formation matrix.

The algorithm is implemented in C++ using the ITK library (IBANEZ et al. 2005).

## 6.2 Experiment: 2D-US to 3D-CT registration of human image datasets

We evaluate our approach on a human dataset acquired in a clinical environment with currently available technologies and imaging protocols. This evaluation will show the performance of our approach under clinical conditions.

### 6.2.1 Data

Three intraoperative US sequences and one preoperative 3D-CT of a patient suffering from atrial fibrillation pathology were acquired. The datasets were provided by Louis Pradel University Hospital, Lyon, France.

#### 6.2.1.1 CT datasets

An ECG-gated cardiac multislice CT image was acquired after injection of contrast agent with a Philips 64-slice scanner (Brilliance CT, Philips Healthcare) at 75% of cardiac cycle (R-R interval). The dimension of the reconstructed image was  $512 \times 512 \times 395$  voxels with an image spacing of  $0.546875 \times 0.546875 \times 0.44998169\text{mm}^3$ .

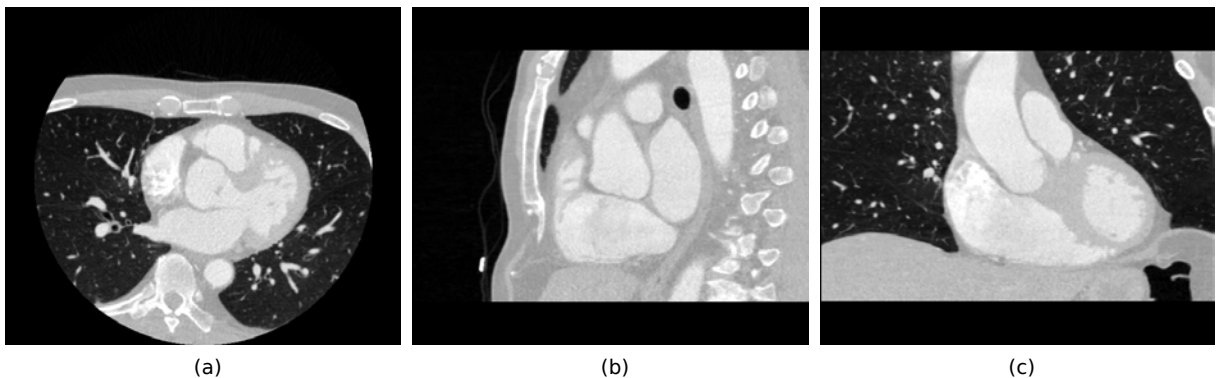


Figure 6.3: Thorax from the superior vena cava to the stomach. Axial (a), Sagittal (b) and Coronal (c) views of the CT dataset.

#### 6.2.1.2 US datasets

The US acquisition was carrying out on a Vivid-5 2D real-time cardiovascular echo system (General Electric, Healthcare, Wauwatosa, USA). One sequence of US frames imaging one cardiac

cycle (R-R interval) was acquired from three different depths in the esophagus (Figure 6.4). Each sequence was formed by 46 frames. The dimension of each frame was  $636 \times 420$  voxels with a spacing  $0.35278 \times 0.35278 \text{mm}^2$ . The acquired TEE images correspond to the plane at multiangle of zero degrees orientation. From the sequence, an expert selected manually the frame which corresponds to the 75% of the cardiac cycle (R-R interval).

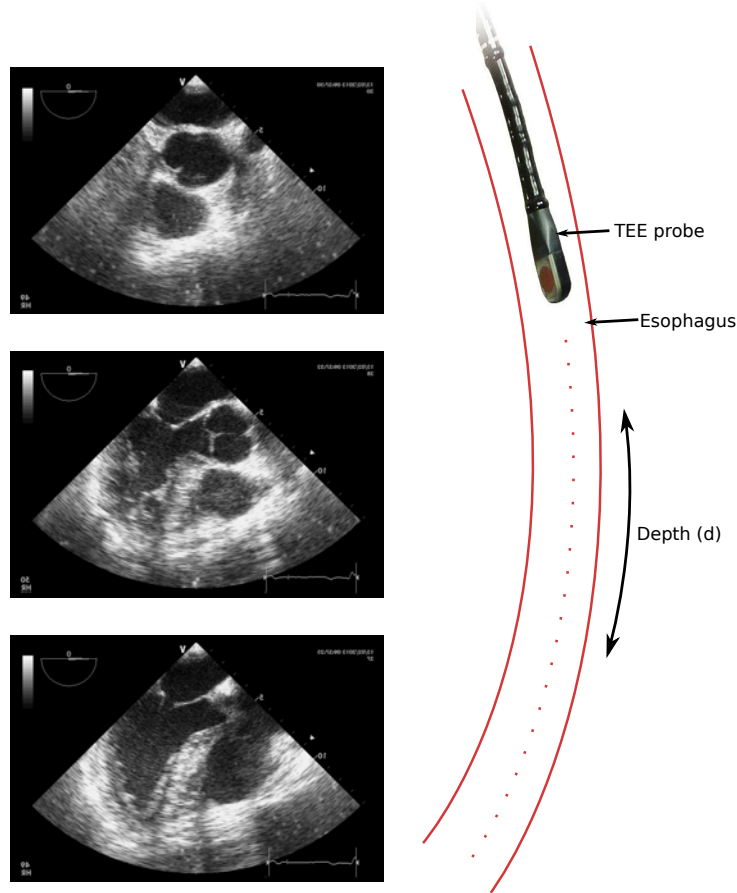


Figure 6.4: 2D-US images acquired from three different depth in esophagus.

## 6.2.2 Results

The whole procedure on the human clinical dataset was the following:

### 6.2.2.1 Preoperative stage

The inner surface of the esophagus was extracted from the preoperative volume using the ITKSNAP<sup>1</sup> implementation of the *active contour* segmentation (YUSHKEVICH et al. 2006). The segmentation of the esophagus followed the steps presented in Figure 6.5.

1. <http://www.itksnap.org>

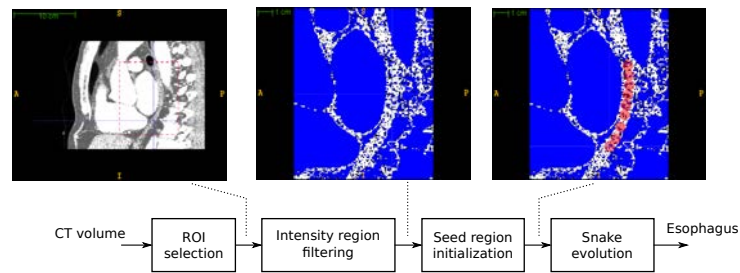


Figure 6.5: Block diagram of the esophagus segmentation process using ITKSNAP

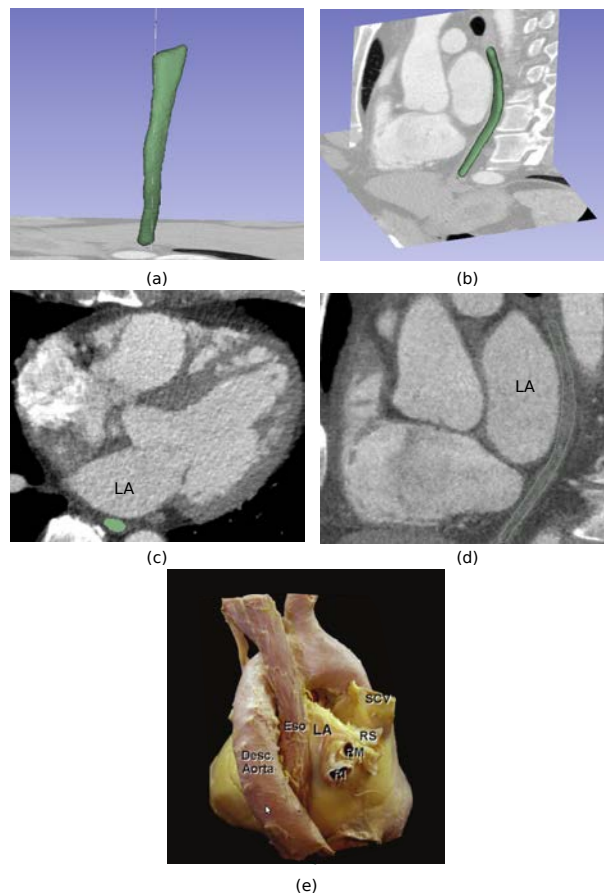


Figure 6.6: Results for semi-automatic esophagus segmentation on CT dataset. Posterior (a) and anterolateral (b) views of the resulted esophagus mesh. Axial (c) and sagittal (d) slices from the CT volume. The result of the segmentation is delineated in green. (e) Human heart viewed from the posterior perspective, to show the esophagus (HO et al. 2012). LA: Left atrium; Eso: Esophagus; SCV: Superior Caval Vein; RI: Right Inferior; RS: Right Superior Pulmonary Veins.

The seed regions were located along the esophagus because of the inhomogeneities of the intensity levels in the region to segment and a lack of edge definition of the different structures boundaries. Also, the snake evolution was supervised to avoid leakage towards other structures. A dilatation and erosion operation were performed on the resulting segmentation to fill the holes. We used a spherical structuring element with a radius of 5mm for both dilatation and erosion. A median



filter with a square window of size 5mm was used to obtain a smooth segmentation. Results for semi-automatic esophagus segmentation on CT dataset are presented in Figure 6.6.

The esophagus centerline can now be determined. For each axial slice of the CT volume, we estimate a candidate centerline point by computing the mean position of the pixels labeled as esophagus. These candidate centerline points were used to define a cubic smoothing spline that describes the esophagus centerline. The number of points and the softness of the form of the esophagus centerline is controlled by the spline function. We choosing a smoothing parameters of 0.001 for the clinical data. The mean position of the segmented region for each axial slice and the resulting spline function are presented in Figure 6.7. The spline function was defined from 247 points of the esophagus segmentation. The resulted centerline have 494 points. We can see in Figure 6.7 how the defined smoothing function have a smooth trajectory avoiding the abrupt changes produced by the segmentation process.

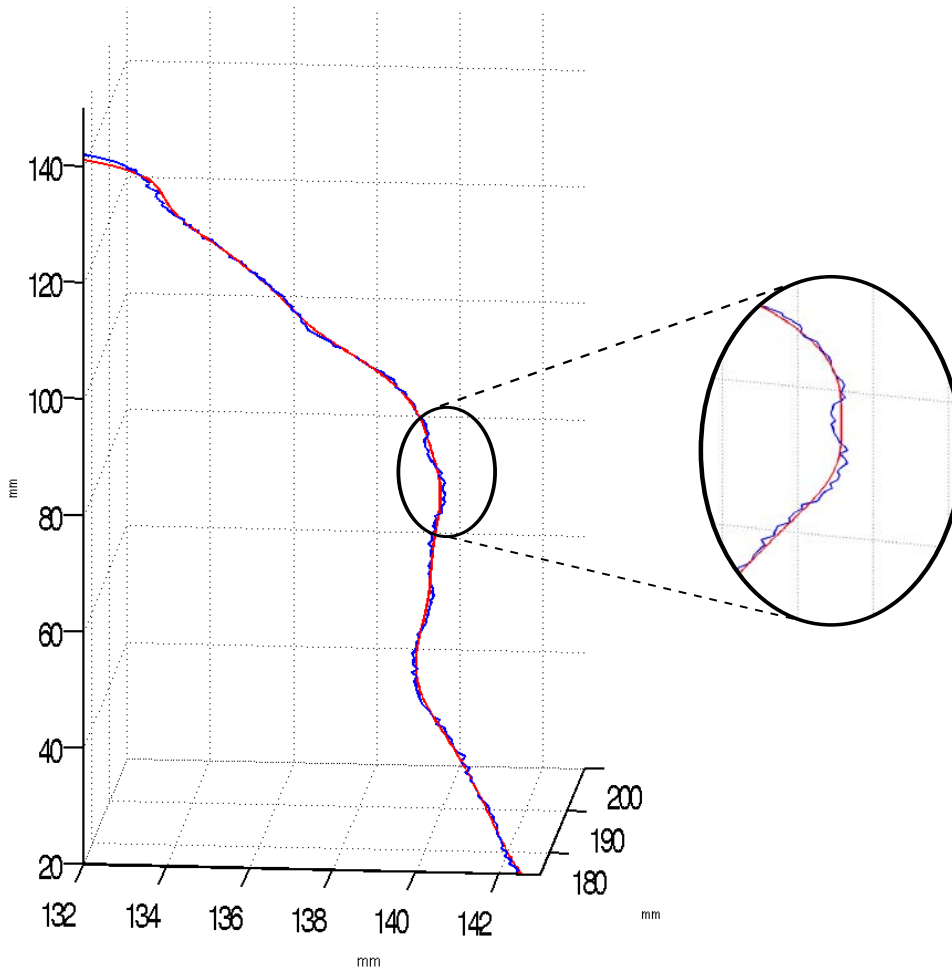


Figure 6.7: In blue, the mean position of the voxels labeled as esophagus on each axial slice of the CT volume. In red, the resulting centerline defined by the cubic smoothing spline.

The resulting centerline was used to compute the unitary vectors that define the planes perpendicular to the centerline, as was described in Chapter 4. A plane was resampled on each point of the resulting centerline. The set of planes that cover the whole centerline forms the therapy-adapted preoperative volume reconstruction.

### 6.2.2.2 Intraoperative registration

In our specific case we did not have any information about transesophageal probe insertion position for the three US images. The only information we had was the order of these images during insertion. We broadly choose the initial zone for the three images by a visual examination. However, we think in a clinical use more localization information will be available during the intervention.

The table 6.1 shows the initial and the final parameters values of the 2D-3D transformation. We can see that the proposed method converges to a final solution which is relatively far from the initialization. This is particularly true for the rotation angle and the depth. This proves that our method is not sensitive to a bad initialization. We can also see that the rotation center remains close to the esophagus centerline this validates the assumption that the transesophageal probe navigation is constraint by esophagus topology.

Table 6.1: Parameters of our proposed slice to volume registration algorithm. Comparison between initialization and resulting values for the three US images (IMA1 to IMA3). Depth (mm) is the distance to the first point of the esophagus centerline in the insertion direction. For 2D rigid registration: CenterX (mm) and CenterY (mm) are the center of rotation that correspond to the esophagus position; Angle (degrees) is the rotation angle around the center point; TransX and TransY are the translation values from the center point.

	Depth		Angle		CenterX		CenterY		TransX		TransY	
	Ini	Final	Ini	Final	Ini	Final	Ini	Final	Ini	Final	Ini	Final
IMA1	10.72	15.94	0	6.59	176.6	176.7	181.5	181.1	0	0.3	-4.9	-6.0
IMA2	57.72	62.08	0	25.39	176.6	178.5	181.5	179.5	0	-0.1	-4.9	-8.0
IMA3	72.91	78.92	0	26.83	176.6	178.1	181.5	181.6	0	3.7	-4.9	-8.1

Figure 6.8 shows the estimated 3D position of the three US slices inside the original preoperative CT acquisition. As expected the slices are perpendicular to the esophagus. Because of the esophagus topology some heart zone (eg. the aortic valve) can be examined from different orientation.

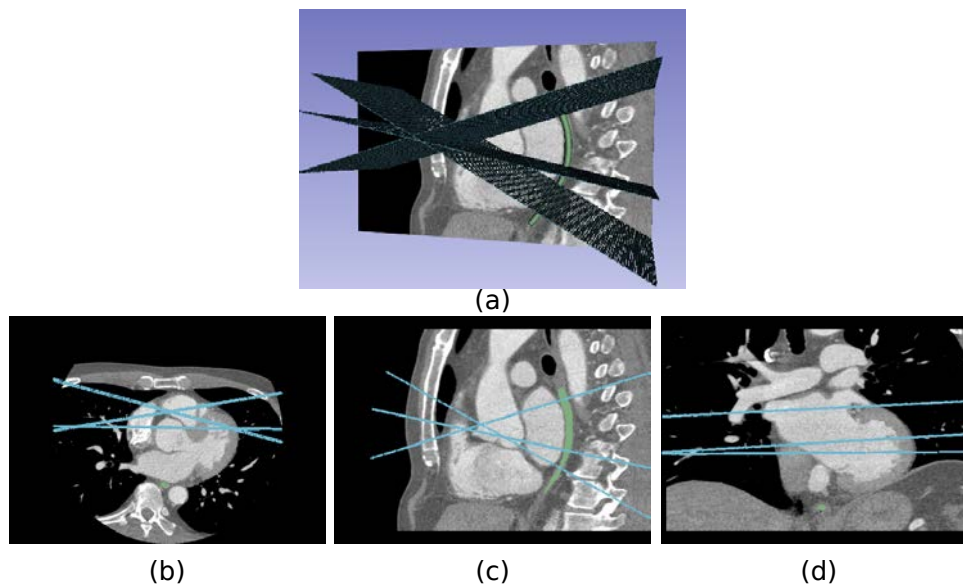


Figure 6.8: 3D visualization of the position of the US slices estimated by our method inside the preoperative CT acquisition.

Figure 6.9, 6.10 and 6.11 present the visual registration results of our proposed slice to volume algorithm for respectively Image 1, Image 2 and Image 3.

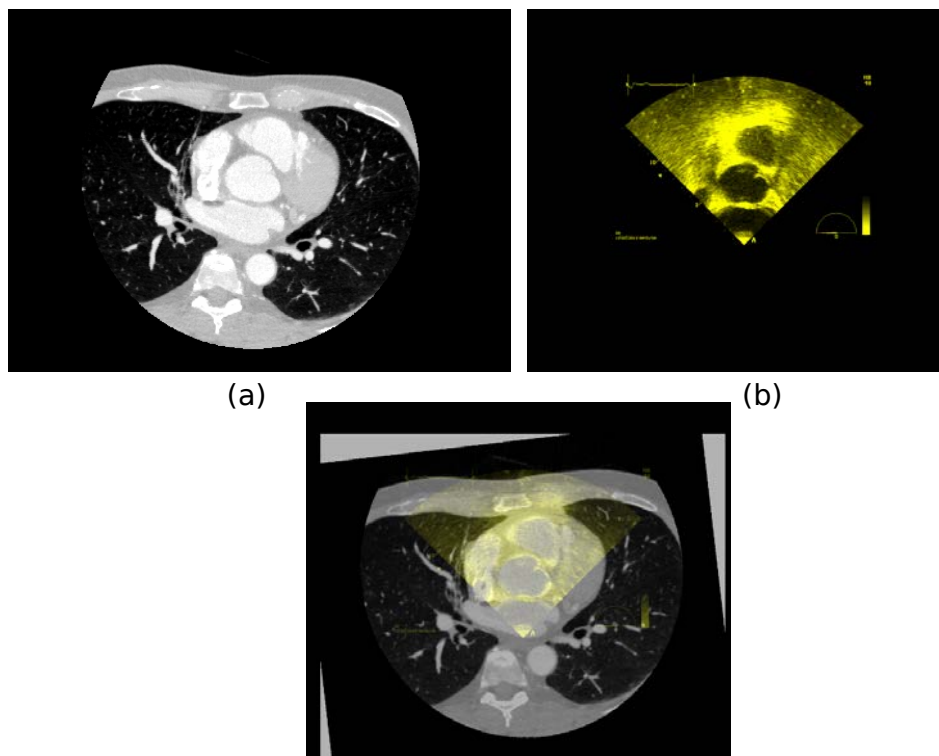


Figure 6.9: a) US Image 1. b) Resampled CT image. c) Result of the our proposed registration.

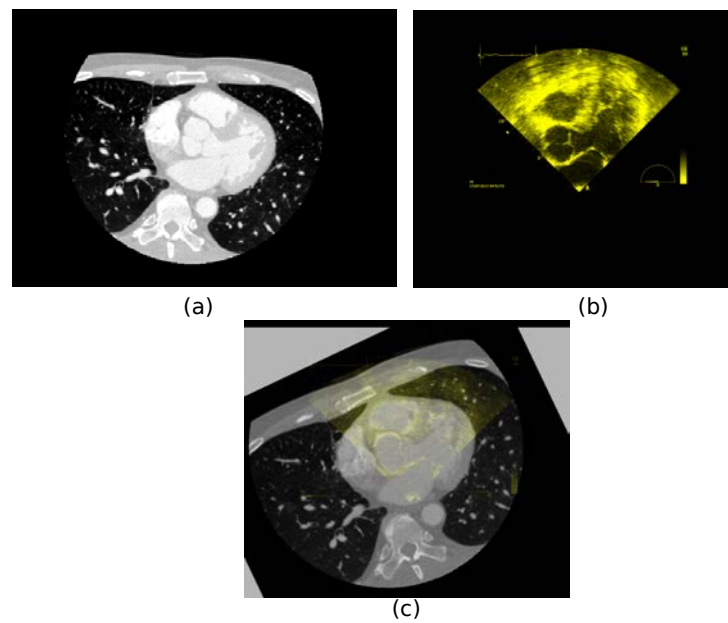


Figure 6.10: a) US Image 2. b) Resampled CT image. c) Result of the our proposed registration.

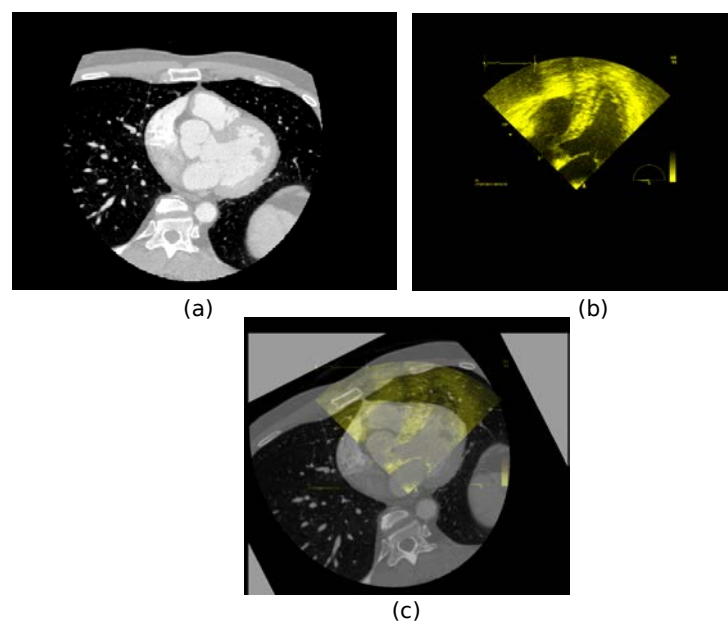


Figure 6.11: a) US Image 3. b) Resampled CT image. c) Result of the our proposed registration.

The visual examination of these three figures shows a good alignment of the two first 2D-US images with the corresponding slice in the 3D data. The results on Image 3 seems to be more difficult to interpret visually.

The mean computation time for the registration process is 5.11s with a standard deviation of 0.98s for each reconstructed image.

### 6.2.3 Evaluation

Our dataset is a clinical dataset without any gold standard. A formal evaluation of the accuracy seems to be difficult to achieve. However, we decided to use the same scheme as in Chapter 4 to assess the accuracy of our method. We will evaluate the registration accuracy using the target registration error ( $TRE$ ) defined as :

$$TRE(P_i) = |T_{Ref}P_i - T_{SliceVolRegis}P_i|, \quad (6.1)$$

where  $P_i$  denotes some landmarks or fiducial points marked on the US image, the  $T_{SliceVolRegis}$  is the resulting transformation matrix estimated by our approach and the  $T_{Ref}$  is the transformation matrix of the gold standard. The resulting error was measured in the CT physical space as shown in Figure 6.12

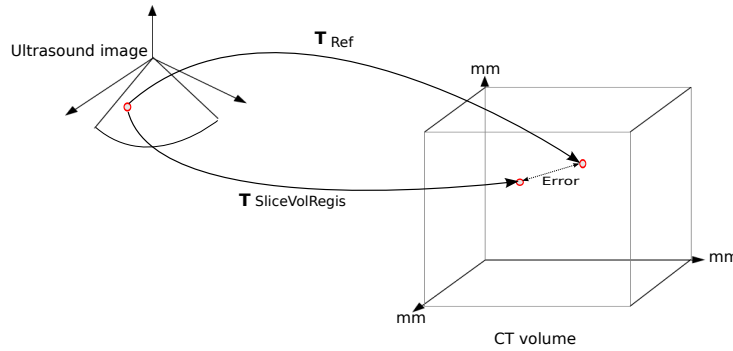


Figure 6.12: Measurement of the registration error mapping fiducial points from US image to CT physical space.

The mean value of the  $TREs$  can be used as quantitative measurement of the general registration performance. The  $mTRE$  is defined as:

$$mTRE = \frac{1}{n} \sum_{i=1}^n TRE(P_{landmark}^i) \quad (6.2)$$

#### 6.2.3.1 Transformation matrix of our slice to volume registration approach:

$T_{SliceVolRegis}$

The reconstruction can be seen as a set of consecutive image planes perpendicular to the esophagus' centerline. Thus, we can move forward in the esophagus changing the slice in the reconstruction. In our approach, we perform a rigid registration process centered on the esophagus centerline between the US slice and the slices of the reconstruction. We select the registration parameters that give the best similarity measure performing the registration for a segment of the esophagus. These parameters are: (1) the depth ( $d$ ) along the esophagus corresponding to the selected slice; (2) parameters of the 2D rigid centered registration (rotation angle and two

translation close to the center). These information is used to obtain final 3D transformation.

Following steps were used to obtain the resulting transformation of our proposed slice to volume registration:

1. A transformation matrix  $T(d)$  is known for the slice corresponding to depth ( $d$ ).
2. The 2D transformation matrix was constructed using the parameters estimated by our 2D rigid centered registration.
3. The final transformation was the product of the matrices obtained in 1 and 2.

### 6.2.3.2 Reference transformation matrix: $T_{Ref}$

For each of the three TEE probe positions one  $T_{Ref}$  was defined. These transformation matrices were obtained manually using the software Slicer following this procedure:

1. With the 2D-US image as fixed and the CT volume as moving, a 3D rigid transformation is obtained manually by the variation of the six parameters (translation  $x$ , translation  $y$ , translation  $z$ , rotation  $rx$ , rotation  $ry$ , rotation  $rz$ ), in order to align the fixed US image to the moving CT volume. Some fiducial points were marked by an expert in both US image and 3D CT as presented in Figure 6.13. These fiducial points and the heart structures are used to confirm the correct alignment.

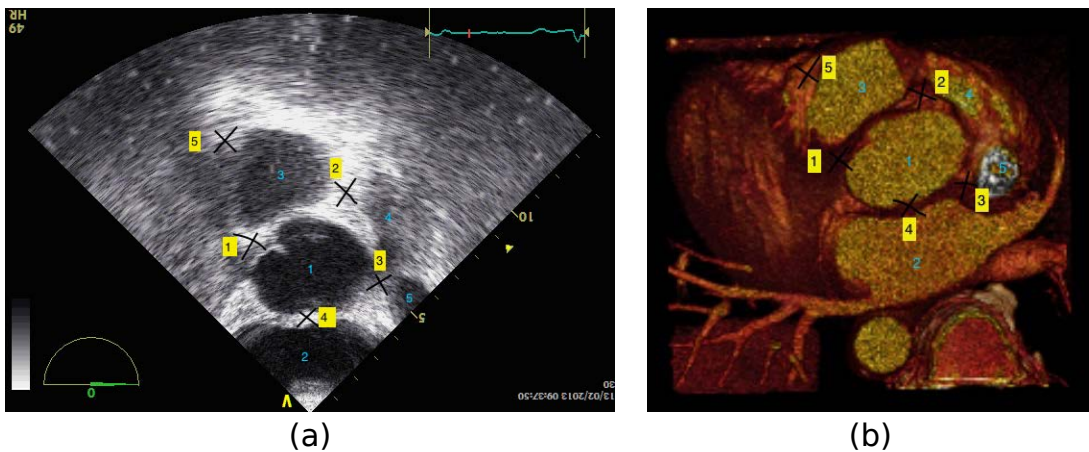


Figure 6.13: Fiducial points marked by an expert. In Yellow, the fiducial Points. In Blue, Aorta(1), left atrium (2), pulmonary artery (3), right atrial appendage (4), superior vena cava (5).

2.  $T_{ref}$  is obtained using the inverse of the transformation obtained in the previous step.

The process was repeated three times resulting in three transformation matrices. The reference matrix  $T_{Ref}$  was constructed using the mean parameters of these three matrices. The resulting matrix transforms a point in the 2D-US space to a 3D point in the 3D-CT space.

### 6.2.3.3 Results of the evaluation

For each image five fiducial points were selected by the experts. Each fiducial points is selected ten times to obtain intra-subject variability.

The box plots of the  $TRE$  values for each fiducial points of Image 1, Image 2 and Image 3 are presented respectively in Figure 6.14, 6.15 and 6.16.

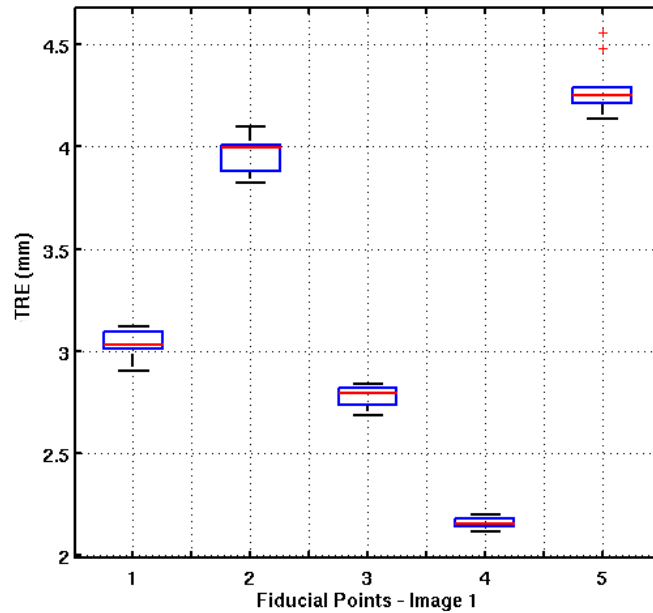


Figure 6.14: Box plots of Target Registration Error ( $TRE$ ) computed for each fiducial point of Image 1. The selection of the pixel position corresponding to the anatomical fiducial point was repeated 10 times to obtain the variability of the anatomical landmarks location.

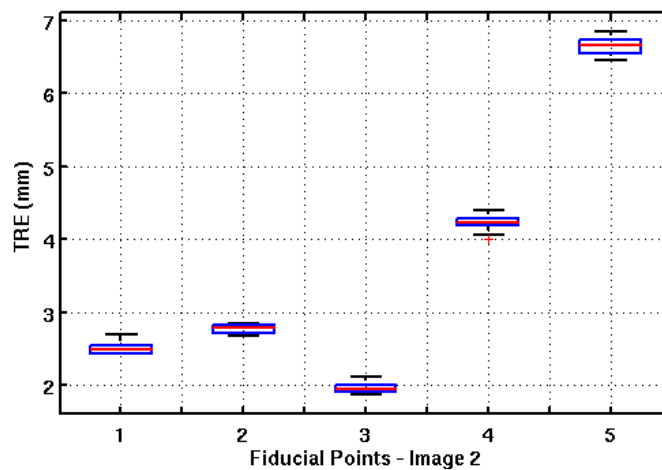


Figure 6.15: Box plots of Target Registration Error ( $TRE$ ) computed at each fiducial point of Image 2. The selection of the pixel position corresponding to the anatomical fiducial point was repeated 10 times to obtain the variability of the anatomical landmarks location.

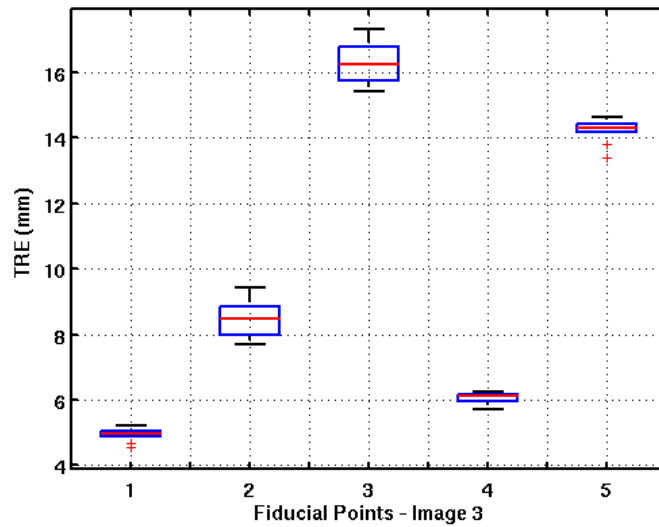


Figure 6.16: Box plots of Target Registration Error ( $TRE$ ) computed at each fiducial point of image 3. The selection of the pixel position corresponding to the anatomical fiducial point was repeated 10 times to obtain the variability of the anatomical landmarks location.

The box plot of the global  $TRE$  for each image is presented in Figure 6.17.

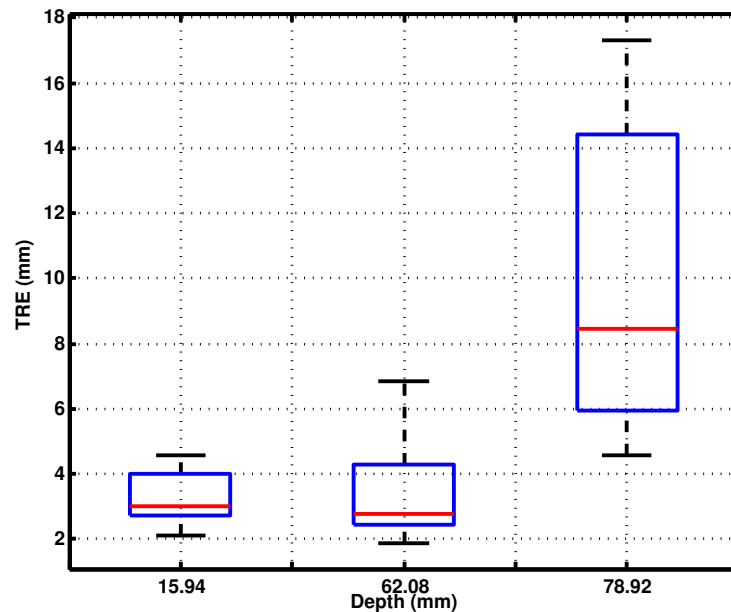


Figure 6.17: Box plots of the Target Registration Error ( $TRE$ ) for a) Image 1, b) Image 2 and c) Image 3

Quantitative results show a mean target registration error of 5.6mm for all images. For the two images close to the insertion point of the TEE (Image 1 and 2), the mean error was 3.5mm, and for the third image which was farther from the insertion point, the mean error increased to 9.5mm. We can observe that the error increases while the TEE tip is progressing in the esophagus. We believe that the probe tip gains some freedom thus it can move away from the



estimated esophagus centerline.

Our results have the same order of magnitude as the results obtained by the other approaches reported in literature evaluated on human datasets: 1.5-4.2mm for (GAO et al. 2012) and less than 5mm for (LANG et al. 2013). However, in their approaches more information was available than in our case. They used a combination of two cross sections or/and 3D-TEE images to perform the registration. Also, a manual selection of the cross section was needed for a good initialization.

#### 6.2.4 Conclusion

We have proposed a novel 2D-US to 3D-CT registration approach adapted to the guidance of the AF transesophageal HIFU therapy. This method was successfully evaluated on a human dataset acquired from a patient with cardiac arrhythmia pathology. US images were acquired by TEE with a multiangle of zero degree orientation to have the same geometrical condition as the US imaging transducer inserted in the middle of the HIFU probe. The final evaluation showed that our method have good performances in the same order of magnitude as the results obtained by the other approaches reported in literature. However, in our case less information was available for the registration.

## References

- FRANZ, A., T. HAIDEGGER, W. BIRKFELLNER, K. CLEARY, T. PETERS, and L. MAIER-HEIN (2014). “Electromagnetic tracking in medicine: a review of technology, validation, and applications.” In: *IEEE Transactions on Medical Imaging* 33.8, pp. 1702–1725.
- GAO, G., G. PENNEY, Y. MA, N. GOGIN, P. CATHIER, A. ARUJUNA, G. MORTON, D. CAULFIELD, J. GILL, C. ALDO RINALDI, J. HANCOCK, S. REDWOOD, M. THOMAS, R. RAZAVI, G. GIJSBERS, and K. RHODE (2012). “Registration of 3D trans-esophageal echocardiography to X-ray fluoroscopy using image-based probe tracking”. In: *Medical Image Analysis* 16.1, pp. 38–49.
- HO, S. Y., J. A. CABRERA, and D. SANCHEZ-QUINTANA (2012). “Left atrial anatomy revisited”. In: *Circulation: Arrhythmia and Electrophysiology* 5.1, pp. 220–228.
- HUANG, X., J. MOORE, G. GUIRAUDON, D. JONES, D. BAINBRIDGE, J. REN, and T. PETERS (2009). “Dynamic 2D ultrasound and 3D CT image registration of the beating heart”. In: *IEEE Transactions on Medical Imaging* 28.8, pp. 1179–1189.
- IBANEZ, L., W. SCHROEDER, L. NG, and J. CATES (2005). *The ITK Software Guide*. Second. Kitware, Inc. ISBN 1-930934-15-7. <http://www.itk.org/ItkSoftwareGuide.pdf>.
- LANG, P., M. CHU, D. BAINBRIDGE, G. GUIRAUDON, D. JONES, and T. PETERS (2013). “Surface-Based CT-TEE Registration of the Aortic Root”. In: *IEEE Transactions on Biomedical Engineering* 60.12, pp. 3382–3390.

- LINTE, C. A., J. MOORE, C. WEDLAKE, D. BAINBRIDGE, G. GUIRAUDON, D. JONES, and T. PETERS (2009). “Inside the beating heart: an in vivo feasibility study on fusing pre- and intra-operative imaging for minimally invasive therapy”. In: *International Journal of Computer Assisted Radiology and Surgery* 4.2, pp. 113–123.
- SRA, J. and S. RATNAKUMAR (2008). “Cardiac image registration of the left atrium and pulmonary veins”. In: *Heart Rhythm* 5.4, pp. 609–617.
- YUSHKEVICH, P. A., J. PIVEN, H. CODY HAZLETT, R. GIMPEL SMITH, S. HO, J. C. GEE, and G. GERIG (2006). “User-guided 3D active contour segmentation of anatomical structures: significantly improved efficiency and reliability”. In: *Neuroimage* 31.3, pp. 1116–1128.



# Conclusion

This Thesis was developed in the context of a minimally-invasive treatment of the atrial fibrillation using transesophageal HIFU ablation. In this context, image processing methods were proposed to improve the planning and the guidance of the therapy. In particular, our contributions were more specifically focused on defining a planning adapted to the patient-specific anatomy and on an appropriate intraoperative guidance of the HIFU probe and therapy.

One of the goal of the planning was to define the ablation zone on the left atrium wall of the patient. According to this objective, we have proposed a left atrium and pulmonary veins segmentation approach. This approach combined two classical methods, multi-atlas and region growing, to obtain a refined segmentation result. Multi-atlas is a robust method that integrates the inter-subject anatomical variability in the set of images that form the atlas. In addition, the region-growing stage is able to delineate more precisely the anatomical details. Our proposed method had the advantage to be completely automatic. The performance of our method was evaluated and compared to other methods proposed by other teams in the context of a multicenter study. This study showed that our approach, compared to other methods, had very good results on MRI data and correct ones on CT.

The planning phase can also be used to prepare the data that will be useful to physician during the future intervention. In this spirit, we have proposed to represent the CT preoperative volume according to the several pose (position and orientation) that will take the future ultrasound images provided by the transesophageal probe. This representation corresponded to the reconstruction of a therapy-adapted volume. This reconstruction is based on a semiautomatic delineation on the esophagus centerline. The original preoperative volume is then resampled according to the geometry of the estimated esophagus centerline. The validity of this reconstruction has been evaluated on a physical phantom. The accuracy of the reconstruction, measured as a registration issue, showed a precision in the same order as the results of conventional registration methods reported in literature.

In the intraoperative stage, the therapy guidance needs to incorporate the planning information inside the 2D ultrasound (US) images used during the intervention. This information integration can be carried out by the registration of the 2D-US to the 3D preoperative CT volume. In order to solve this 2D-3D registration problem, we first performed a systematic study to select

the most effective similarity measures to compare the information provided by the US and CT modalities. The best similarity measure has then be integrated within an original 2D-US to 3D CT registration scheme. The innovative part of this method consisted to use the therapy-adapted preoperative volume as a reference for the research process. We applied this method for the registration of a clinic dataset. The qualitative results have shown a good alignment of the information given by US and CT modalities. This good behavior has been confirmed on a first quantitative evaluation which estimated the accuracy level of our method to be similar to conventional US-CT registration methods reported in literature but with less needed information and less manual intervention.

## List of associated publications

### International journals

- SANDOVAL, Z. and J.-L. DILLENSEGER (2013b). “Intensity-based similarity measures evaluation for CT to ultrasound 2D registration”. In: *IRBM* 34.4–5, pp. 278–282.
- TOBON-GOMEZ, C., A. GEERS, J. PETERS, J. WEESE, K. PINTO, R. KARIM, M. AMMAR, A. DAOUDI, J. MARGETA, Z. SANDOVAL, B. STENDER, Y. ZHENG, M. ZULUAGA, J. BETANCUR, N. AYACHE, M. CHIKH, J. DILLENSEGER, M. KELM, S. OURSELIN, A. SCHLAEFER, T. SCHAEFFTER, R. RAZAVI, and K. RHODE (2015). “Benchmark for algorithms segmenting the left atrium from 3D CT and MRI datasets”. In: *IEEE Transactions on Medical Imaging* PP.99, pp. 1–1.

### International conferences

- SANDOVAL, Z. and J.-L. DILLENSEGER (2013c). “Evaluation of computed tomography to ultrasound 2D image registration for atrial fibrillation treatment”. In: *Computing in Cardiology Conference (CinC)*. Zaragossa, pp. 245–248.
- SANDOVAL, Z., J. BETANCUR, and J.-L. DILLENSEGER (2014). “Multi-atlas-Based Segmentation of the Left Atrium and Pulmonary Veins”. In: *Statistical Atlases and Computational Models of the Heart. Imaging and Modelling Challenges*. Vol. 8330. Lecture Notes in Computer Science. Nagoya: Springer Berlin Heidelberg, pp. 24–30.

### National conferences

- SANDOVAL, Z. and J.-L. DILLENSEGER (2013a). “Intensity-based similarity measures evaluation for CT to Ultrasound 2D registration”. In: *RITS*. Bordeaux.
- SANDOVAL, Z. and J.-L. DILLENSEGER (2015). “Thorax tissues segmentation: a first step for a dynamic beating heart digital phantom”. In: *RITS*. Dourdan.



# List of Figures

1	Approche « minimize » pour le traitement des fibrillations auriculaires par ablation (Cox 2004). . . . .	vi
2	Approche transœsophagienne pour le traitement des fibrillations auriculaires. . . . .	viii
3	Prototype de sonde transœsophagienne pour le traitement des fibrillations auriculaires (CONSTANCIEL et al. 2013). . . . .	viii
4	Objectifs des travaux liés à la Thèse. . . . .	x
5	Méthodes étudiées durant la Thèse. . . . .	xii
6	Approche de segmentation multi-atlas. 1) Choix des atlas les plus proches du volume à segmenter après un recalage affine, 2) l’ajustement des atlas les plus proches par recalage élastique et 3) la fusion entre les atlas ajustés. . . . .	xv
7	Exemples de recalage affine de différents atlas (en vert la vérité terrain). . . . .	xvi
8	Trois exemples d’alignements avant (haut) et après (bas) le recalage élastique. . . . .	xvi
9	Processus de fusion avec 3 volumes. Résultat de la majorité après vote. . . . .	xvii
10	Région de recherche pour la croissance de régions. . . . .	xvii
11	Résultats de la segmentation sur une IRM de bonne qualité. La vérité terrain est sur la ligne supérieure (TOBON-GOMEZ et al. 2015). . . . .	xx
12	Résultats de la segmentation sur une IRM de basse qualité. La vérité terrain est sur la ligne supérieure (TOBON-GOMEZ et al. 2015). . . . .	xxi
13	Score unifié pour l’IRM. Comparaison entre méthodes (TOBON-GOMEZ et al. 2015). Les scores les plus faibles (les plus négatifs) sont les meilleurs. Nos méthodes sont : LTSI_VRG pour la variante avec fusion par vote majoritaire et LTSI_VSRG pour la fusion par STAPLE. OBS_2 est un second observateur humain qui permet de définir la variabilité inter-observateurs. . . . .	xxi
14	Volume préopératoire adapté à la thérapie. . . . .	xxiii
15	Systèmes de référence entre le volume scanner X et les coupes le long de l’œsophage. . . . .	xxiv
16	Fantôme physique du cœur et de l’œsophage. Trois fenêtres (1, 2 et 3) sont ouvertes dans l’œsophage pour permettre l’acquisition échographique. Deux des 3 marqueurs externes de référence sont également visibles sur la face externe du cœur. . . . .	xxv
17	a) Image échographique. b) Coupe du volume reconstruit à l’aide de notre méthode et présentant le myocarde et les marqueurs segmentés. c) Résultat du recalage en rotation 2D autour de la position du centre de l’échographe. . . . .	xxvi



18	Boîtes à moustaches des <i>TREs</i> pour les 3 fenêtres d'échographies transoesophagiennes. La fenêtre 1 est la plus proche du cœur et la fenêtre 3 la plus éloignée. . . . .	xxvii
19	Images des fantômes numériques. Ellipse: images simulées de scanner X (a) et d'échographie (b). Coupe de l'oreillette gauche et des veines pulmonaires : section du thorax de l'homme du Visible Human (c); image segmentée et étiquetée : air, graisse, os, muscle (dont le myocarde), eau et sang (d); images simulées de scanner X (e) et d'échographie (f). . . . .	xxx
20	Indice de composition des différentes mesures de similarité. . . . .	xxxii
21	Schéma fonctionnel de la technique de recalage 2D/3D. . . . .	xxxiii
22	Volume préopératoire, vues a) axiale, b) sagittale et c) coronale. Échographies per-opératoires à 3 positions (d-f) de l'endoscope. . . . .	xxxiv
23	Segmentation de l'œsophage. . . . .	xxxv
24	Exemple de recalage 2D/3D. a) Coupe scanner X correspondante du volume reconstruit. b) Image échographique 1. c) Superposition des images après recalage. . . . .	xxxvi
25	Visualisation 3D de la pose des 3 images échographiques dans le volume préopératoire. . . . .	xxxvii
26	Boîte à moustaches de l'erreur de recalage ( <i>TRE</i> ) pour a) Image 1, b) Image 2 et c) Image 3. . . . .	xxxviii
1.1	Membrane potential over time for a cardiomyocyte. The phases of a complete cycle and the refractory and absolute periods are shown (GAZTANAGA et al. 2012). . . . .	8
1.2	Action potential for a cell in the sinus node (A) and a muscle cell (B) (GAZTANAGA et al. 2012). . . . .	8
1.3	The electrical function of a healthy heart, showing the electrical conduction system from the sinus node in the right atrium to the ramifications of the Purkinje fibers in both ventricles. . . . .	9
1.4	Re-entry loop caused by an anatomical blocking of electrical conduction in one direction (GAZTANAGA et al. 2012). . . . .	10
1.5	Atrial fibrillation is a consequence of wave fronts being propagated in the stimulated atrial tissue (FERNÁNDEZ 2006). . . . .	12
1.6	Atrial fibrillation is caused and maintained by a focus located in the pulmonary veins (FERNÁNDEZ 2006). . . . .	13
1.7	Atrial fibrillation is caused by extrasystoles generated in the pulmonary veins, but it is maintained by a rotor generated in the body of the atrium (FERNÁNDEZ 2006). . . . .	14
1.8	Five left atrial lesions as per maze III standard, surgical procedure for atrial fibrillation (COX 2003). . . . .	15
1.9	The mini-maze procedure for atrial fibrillation (COX 2003). . . . .	16
1.10	Transesophageal approach for atrial fibrillation treatment. . . . .	20
1.11	The prototype: (a) schematic view of the prototype. (b) Photography of the probe head. (c) Geometrical characteristics of the HIFU transducer (CONSTANCIEL et al. 2013). . . . .	22

1.12	Closest and farthest points of the mini-maze therapy from the oesophagus (CONSTANCIEL 2014). . . . .	22
2.1	Our contributions to the project concerning cardiac arrhythmia treatment using a transesophageal HIFU probe guided by ultrasound imaging. . . . .	30
2.2	Computed tomography. . . . .	32
2.3	MR signals can be localized and encoded by applying magnetic field gradients. A combination of RF pulses and gradient-magnetic fields are generated to produce an image. Magnetic field gradients encode MR signals along the: a) $z$ direction. b) $x$ and $y$ directions. . . . .	33
2.4	3D-US imaging can be performed by (a) a mechanical scanning 3D probe, (b) a 2D matrix-array or, (c) freehand techniques. . . . .	35
2.5	Registration of two images: searching the optimal transform parameters allowing to align the moving image in the fixed image referential. . . . .	36
2.6	General framework for the registration between US intraoperative images and CT or MRI preoperative images (CHEN et al. 2012). . . . .	42
2.7	Basic components of intraoperative electromagnetic tracking (FRANZ et al. 2014). . . . .	43
2.8	Examples of magnetic sensors for commercial electromagnetic tracking systems (FRANZ et al. 2014). (a) Ascension dc, (b) Polhemus ac, and (c) NDI Aurora ac sensors for tracking systems. (d) Passive electromagnetic transponders instead of magnetic sensors. This cannot measure the magnetic field. . . . .	43
2.9	Field of view of the US imaging transducer inserted in the HIFU probe (CONSTANCIEL 2014). . . . .	53
2.10	Position of the US image. . . . .	55
2.11	Proposed general framework for our contributions. . . . .	57
3.1	Multi-atlas-based segmentation process. The affine registration allows to evaluate the similarity between the input image and the atlas dataset. The most similar atlases are kept for the future segmentation. The elastic transformation step modifies the ground truth of the selected atlas images to adjust them to the input image. The fusion rule defines the coarse segmentation of the left atrium and pulmonary veins. . . . .	66
3.2	The axial (a), sagittal (b) and coronal (c) views of the intensity input image (gray level), the corresponding ground truth (green) and the contour of the seed region (yellow). The 3D view (d) of the seed region. . . . .	69
3.3	The region of interest is a cubic shaped mask that surrounds the left atrium and the pulmonary veins. This mask is set manually for both moving and fixed image. . . . .	71
3.4	Four examples of alignments after global affine registration. The ground truth of the image to segment is presented in green. . . . .	72
3.5	Three examples of alignments before (top) and after (bottom) elastic registration. . . . .	73
3.6	Fusion process with three images. Result using simple majority voting. . . . .	74
3.7	Search area for the region growing method. . . . .	75

3.8	Results after region growing step. . . . .	75
3.9	Results of our algorithms on high quality MRI data (TOBON-GOMEZ et al. 2015). The ground truth is located on the superior row of the figure. . . . .	79
3.10	Results of our algorithms on low quality MRI data (TOBON-GOMEZ et al. 2015). The ground truth is located on the superior row of the figure. . . . .	80
3.11	Unified scores for MRI (TOBON-GOMEZ et al. 2015). These scores combine the S2S and Dice to show a general performance of the algorithms in the segmentation of the LA body and PVs. Our algorithms are labeled as LTSI_VRG (using majority voting) and LTSI_VSRG (using STAPLE). OBS_2 represents the interobserver variability. . . . .	81
3.12	Results of our algorithms on high quality CT data (TOBON-GOMEZ et al. 2015). The ground truth is located on the superior row of the figure. . . . .	82
3.13	Results of our algorithms on low quality CT data (TOBON-GOMEZ et al. 2015). The ground truth is located on the superior row of the figure. . . . .	82
3.14	Unified scores for CT data (TOBON-GOMEZ et al. 2015). These scores combine the S2S and Dice to show a general performance of the algorithms in the segmentation of the LA body and PVs. Our algorithms are labeled as LTSI_VRG (using majority voting) and LTSI_VSRG (using STAPLE). OBS_2 represents the interobserver variability. . . . .	83
4.1	Therapy-adapted preoperative volume reconstruction. . . . .	88
4.2	Block diagram of the therapy-adapted preoperative volume reconstruction procedure. . . . .	88
4.3	Block diagram of the esophagus segmentation process using ITKSNAP. . . . .	90
4.4	Reconstruction of the therapy-adapted preoperative volume. Transformation $T(d)$ is obtained to map the gray values from the original volume ( $V_{or}$ ) to reconstructed volume ( $V_{rec}$ ). Axe $d$ correspond to the esophagus centerline. For one valour of $d = d_\epsilon$ , a transformation $T(d_\epsilon)$ is used. . . . .	91
4.5	Reference system of the CT volume $R = \{O; \vec{i}, \vec{j}, \vec{k}\}$ . $E_1$ and $E_2$ two consecutive points located respectively at $d_1$ and $d_2$ along the segmented esophagus centerline. . . . .	92
4.6	Reference systems of the reconstructed CT slice and the corresponding US acquisition at the point $E_1$ . . . . .	92
4.7	In green the three vectors that are used to obtain the corresponding position of the US-plane in the CT volume. . . . .	93
4.8	Physical phantom of the heart and esophagus. Three windows in the esophagus were opened to acquire the TEE images (1, 2, 3). Two out of the three rubber markers fixed on the heart cavities can be observed. . . . .	96
4.9	The system setup of the experiment. . . . .	97
4.10	Workflow presented in section 4.1 modified to include a segmentation process of the myocardium, the external markers and the tip of the probe. . . . .	98
4.11	Error quantification explanation. One point in the US image is defined. The two transforms $T_{RecEval}$ and $T_{Ref}$ are used to project this point in the CT space. The error is the distance between these two projected points. . . . .	99

4.12	CT volume of the phantom acquired with the Artis zeego C-arm. Axial(a), coronal (b) and sagittal (c) views. The myocardium segmentation is delineated with an orange line.	101
4.13	Resulting segmentation of the esophagus, the heart and the tip of the probe at the TEE acquisition time. . . . .	101
4.14	a) Resulting segmentation of the esophagus phantom. b) Estimated centerline. In blue, the mean position of the voxels labeled as esophagus on each axial slice of the CT volume. In red, the resulting centerline defined by the cubic smoothing spline. . .	102
4.15	a) US image at the TEE probe position 1. b) Resampled CT image from the volume obtained after the segmentation of the heart phantom, the markers and the tip of the probe at the TEE probe position 1. c) Result of the fiducial registration. The fiducial registration has estimated a rotation of more or less 10 degrees around the centerline point. . . . .	103
4.16	Box plots of the Target Registration Error ( $TRE$ ) for each 3 fiducial marker for a) the TEE probe position 1, b) the TEE probe position 2 and c) the TEE probe position 3.	104
4.17	Box plots of the Target Registration Error ( $TRE$ ) for each TEE probe position. . .	105
4.18	The 3D visualization of the whole scene comparing the Gold standard plane and the plane estimated by our approach. . . . .	105
4.19	(a) Example of therapy ablation lines marked manually using Slicer on 3D model of left atrium segmentation. (b) Sagittal view of the reconstructed volume. . . . .	106
4.20	Lesion lines on two slices of the reconstructed volume. 3D visualization of these slices on the preoperative space. . . . .	106
5.1	Images used for evaluation. Oval geometrical form: simulated CT (a) and US (b) images. Left atrium and pulmonary veins phantom images: cryosection of the male human thorax (c); segmentation and labeling into six different types of tissues: air, fat, bone, muscle (including myocardium), water and blood (d); corresponding simulated CT (e) and US (f) images for a US beam depth=7cm. . . . .	113
5.2	Profile of a similarity measure along one line with $M$ sampling points, gold standard at $P_{GS}$ , maximum value at $P_{MAX}$ and nearest local minimum at $P_{NLM}$ . . . . .	115
5.3	Composite index for the several similarity measures . . . . .	118
6.1	Workflow of the global methodology used for 2D-US to 3D-CT registration. . . . .	122
6.2	Registration process between a US slice and the preoperative acquisition. This process uses the therapy-adapted reconstructed volume performed during the preoperative stage	124
6.3	Thorax from the superior vena cava to the stomach. Axial (a), Sagittal (b) and Coronal (c) views of the CT dataset. . . . .	125
6.4	2D-US images acquired from three different depth in esophagus. . . . .	126
6.5	Block diagram of the esophagus segmentation process using ITKSNAP . . . . .	127

6.6	Results for semi-automatic esophagus segmentation on CT dataset. Posterior (a) and anterolateral (b) views of the resulted esophagus mesh. Axial (c) and sagittal (d) slices from the CT volume. The result of the segmentation is delineated in green. (e) Human heart viewed from the posterior perspective, to show the esophagus (HO et al. 2012) . LA: Left atrium; Eso: Esophagus; SCV: Superior Caval Vein; RI: Right Inferior; RS: Right Superior Pulmonary Veins. . . . .	127
6.7	In blue, the mean position of the voxels labeled as esophagus on each axial slice of the CT volume. In red, the resulting centerline defined by the cubic smoothing spline.	128
6.8	3D visualization of the position of the US slices estimated by our method inside the preoperative CT acquisition. . . . .	130
6.9	a) US Image 1. b) Resampled CT image. c) Result of the our proposed registration.	130
6.10	a) US Image 2. b) Resampled CT image. c) Result of the our proposed registration.	131
6.11	a) US Image 3. b) Resampled CT image. c) Result of the our proposed registration.	131
6.12	Measurement of the registration error mapping fiducial points from US image to CT physical space. . . . .	132
6.13	Fiducial points marked by an expert. In Yellow, the fiducial Points. In Blue, Aorta(1), left atrium (2), pulmonary artery (3), right atrial appendage (4), superior vena cava (5). . . . .	133
6.14	Box plots of Target Registration Error ( $TRE$ ) computed for each fiducial point of Image 1. The selection of the pixel position corresponding to the anatomical fiducial point was repeated 10 times to obtain the variability of the anatomical landmarks location. . . . .	134
6.15	Box plots of Target Registration Error ( $TRE$ ) computed at each fiducial point of Image 2. The selection of the pixel position corresponding to the anatomical fiducial point was repeated 10 times to obtain the variability of the anatomical landmarks location. . . . .	134
6.16	Box plots of Target Registration Error ( $TRE$ ) computed at each fiducial point of image 3. The selection of the pixel position corresponding to the anatomical fiducial point was repeated 10 times to obtain the variability of the anatomical landmarks location. . . . .	135
6.17	Box plots of the Target Registration Error ( $TRE$ ) for a) Image 1, b) Image 2 and c) Image 3 . . . . .	135

# List of Tables

1	Scores médians de DICE et S2S entre le résultat de la segmentation et la vérité terrain pour l'oreillette et les veines pulmonaires (TOBON-GOMEZ et al. 2015). Idéalement S2S = 0mm et le score de Dice = 1. . . . .	xx
1.1	Classification of atrial fibrillation in terms of the duration of the episodes according to the 2014 AHA/ACC/HRS Guideline for the Management of Patients with Atrial Fibrillation (JANUARY et al. 2014). . . . .	11
3.1	Images ranked according to the final value of the similarity measure in the affine registration from the $A_i$ s to $A_1$ (chosen as input image). Results for MS, NCC and MI with/without ROI are shown. . . . .	72
3.2	Dice index between the ground truth of $A_1$ and the atlas ground-truth aligned using the estimated affine transformation. Results for MS, NCC and MI with/without ROI are shown. . . . .	72
3.3	Influence of the number $M$ of images used in the fusion process. Dice index between the ground truth of $A_1$ and the labeled result of the fusion. Results for MS, NCC and MI similarity metrics with/without ROI. . . . .	74
3.4	Dice index between the ground truth of $A_1$ and the region growing output. Results for MS, NCC and MI similarity metrics with/without ROI. . . . .	76
3.5	Results on MRI. Median of the distance surface-to-surface (S2S) between the surface of the ground truth and the surface obtained by our algorithms for LA body and PVs. Ideally S2S = 0mm. . . . .	79
3.6	Results on MRI. Median of the Dice scores (DC) between the ground truth volume and the volume obtained by our algorithms for LA body and PVs. Ideally DC = 1. . . . .	80
3.7	Results on CT data. Median of the distance surface-to-surface (S2S) between the surface of the ground truth and the surface obtained by our algorithms for LA body and PVs. Ideally S2S = 0mm. . . . .	83
3.8	Results on CT data. Median Dice score (DC) between the ground truth volume and the volumes obtained by our algorithms for LA body and PVs. Ideally DC = 1. . . . .	83
5.1	Values of parameters used in the simulation of CT and US images. . . . .	113

5.2	Moving image sizes, field of view (FOV), translation and rotation units of the normalized parametric space and distance between two consecutive points along a line, for the five images ( $N = 7$ lines, $M = 100$ sampling points and $R = 0.3$ ). . . . .	116
5.3	Value of the $ACC$ (mm), $RON$ ( $10^7\text{mm}^{-1}$ ), $NOM$ , $CR$ (mm) and $DO$ ( $\text{mm}^{-1}$ ) properties for the eight similarity measures evaluated on the raw <i>Oval</i> image ( <i>Ov</i> ) and the preprocessed <i>Oval</i> image ( <i>Ov1</i> ). Sampling step along a line = 0.0588mm ( $N = 7$ , $M = 100$ , $R = 0.3$ ). Best values are bolded. . . . .	117
5.4	Value of the $ACC$ (mm), $RON$ ( $10^7\text{mm}^{-1}$ ), $NOM$ , $CR$ (mm) and $DO$ ( $\text{mm}^{-1}$ ) properties for the eight similarity measures evaluated on the raw <i>LAPV</i> image ( <i>L</i> ) and the preprocessed <i>LAPV</i> image ( <i>L1</i> ). Sampling step along a line = 0.0444mm ( $N = 7$ , $M = 100$ , $R = 0.3$ ). Best values are bolded. . . . .	117
6.1	Parameters of our proposed slice to volume registration algorithm. Comparison between initialization and resulting values for the three US images (IMA1 to IMA3). Depth (mm) is the distance to the first point of the esophagus centerline in the insertion direction. For 2D rigid registration: CenterX (mm) and CenterY (mm) are the center of rotation that correspond to the esophagus position; Angle (degrees) is the rotation angle around the center point; TransX and TransY are the translation values from the center point. . . . .	129

## Abstract

The work presented in this document aims at developing new image-processing methods to improve the planning and guidance of transesophageal HIFU atrial fibrillation therapy. This document is divided into two parts, namely therapy planning and therapy guidance. We first propose novel therapy planning methods that exploit high-resolution pre-operative CT or MRI information to extract patient-specific anatomical details and to define future therapeutic procedures. Our specific methodological contributions concern the following: an automatically-refined atlas-based segmentation approach to extract the left atrium and pulmonary veins; the delineation of the lesion lines on the original or segmented volume; and the reconstruction of a volume adapted to future intraoperative transesophageal navigation. Secondly, our proposal of a novel registration approach for use in therapy guidance aligns intraoperative 2D ultrasound with preoperative 3D-CT information. This approach first carries out a systematic statistical evaluation to select the best similarity measure for our application and then takes advantage of the geometrical constraints of the transesophageal HIFU probe to simplify the registration process. Our proposed methods have been evaluated on digital and/or physical phantoms and on real clinical data.

## Résumé

L'objectif des travaux présentés dans ce document est de développer de nouvelles méthodes de traitement d'images pour améliorer la planification et le guidage d'une thérapie par voie transœsophagienne de la fibrillation auriculaire à l'aide d'Ultrason Focalisé Haute Intensité. Le document est divisé en deux parties : la planification du traitement et le guidage de la thérapie. Pour la planification de la thérapie, l'idée est d'exploiter l'information acquise au stade préopératoire par un scanner X ou IRM afin de retrouver l'anatomie spécifique du patient et à y définir le futur geste thérapeutique. Plus particulièrement, nos différentes contributions ont porté sur une approche multi-atlas de segmentation de l'oreillette gauche et des veines pulmonaires ; le tracé des lignes de lésions sur le volume initial ou segmenté ; et la reconstruction d'un volume adapté à la future navigation transœsophagienne. Pour le guidage de la thérapie, nous proposons une nouvelle approche de recalage qui permet d'aligner les images échographiques peropératoires 2D et l'information 3D CT préopératoire. Dans cette approche, dans un premier temps nous avons sélectionné la mesure de similarité la plus adaptée à notre problématique à l'aide d'une évaluation systématique puis nous avons tiré profit des contraintes imposées à la sonde transœsophagienne par l'anatomie du patient pour simplifier la procédure de recalage. Toutes ces méthodes ont été évaluées sur des fantômes numériques ou physiques et sur des données cliniques.